MICROMETEOROLOGICAL MODELING OF AN IDEALIZED CAVE AND APPLICATION TO CARLSBAD CAVERN, NM

by

Setsuko Shindo

Submitted in Partial Fulfillment

of the Requirements for the Degree of

Master of Science in Hydrology

New Mexico Institute of Mining and Technology
Department of Earth and Environmental Science

Socorro, New Mexico

December, 2005

ABSTRACT

Air–filled caves are subsurface, semi-closed systems with their own poorly understood internal micrometeorology. Cave micrometeorological processes may contribute to the formation and subsequent enlargement of caves and control some of the details of secondary mineral deposition. In this work, we consider some aspects of the internal fluid-thermal dynamics of caves, especially buoyancy and natural convection due to geothermal heating, characterized by a Rayleigh number defined for cave conditions. Two-dimensional steady state computer models of idealized caves were created using FEMLAB multiphysics computer software. The thermal properties of limestone and air, and geothermal flux were incorporated into the models. Limestone was considered an impermeable material. The models couple the incompressible Navier-Stokes equations (air phase only) with the thermal energy convection and conduction equation using the finite element method.

Although the constructed models are limited in scale and have highly simplified geometries compared to real caves, they have identified some important factors that influence internal cave dynamics. Air-filled caves act as insulators. Geothermal heat produces convection cells in the deeper parts of caves, where there is less influence from the surface. These internal dynamics can induce the flow of surface air into caves largely due to thermally-induced buoyancy forces, the conservation of mass of essentially incompressible air, and cave geometries (e.g., the presence of multiple entrances).

Humidity is an important factor frequently cited as influencing cave features. However, Rayleigh number and instability analyses indicate that humidity has less impact on flow dynamics in moderate cave meteorological conditions (e.g., cave air temperature of 20˚C); on the contrary, humidity may be affected by fluid flows. Future studies on subjects such as latent heat transport, evaporation and condensation, will be required.

Unlike our steady state models, real cave systems could be transient and, thus, the rate of escaping of air could be different from the rate of incoming air. Since cave air moves in order to conserve air mass, if caves temporarily have excess air mass, a high air pressure area may be created locally, triggering the movement of this air to areas of lower pressure. As a result, if a cave entrance is large enough, inflow and outflow components can be observed at a single entrance. The models were applied to help explain several observed phenomena within Carlsbad Cavern, NM. This cave is an extremely large and geometrically complex cave; however the simple models constructed in this study help to shed light on the interpretation of observations.

To our knowledge, this modeling effort is the first attempt to capture the behavior of such cave micrometeorological systems in a quantitatively rigorous manner. We believe that computer modeling can be very useful to assist understanding of the dynamics of cave interiors and possible effects on the enlargement and subsequent mineralogical decoration of caves. Modeling combined with detailed and continuous site monitoring in real caves, and attempts to include the vertical variations of humidity, cave pressure fluctuations, and salient aspects of cave geometries, will be especially fruitful.

ACKNOWLEDGEMENTS

I would like to thank all the people who have helped me to complete this thesis. Penelope J. Boston (NMT) who has conducted the interdisciplinary study of caves provided this research opportunity and supported the entire work; H. Jake Turin (Los Alamos National Laboratory) provided the original research idea; Paul Berger (Carlsbad Caverns National Park) guided us within Carlsbad Cavern and provided his precious meteorological data; Rakhim Aitbayev (NMT) generously spent time to teach me the finite element method; Glenn Spinelli (NMT) always gave me great advice, especially making me aware of the importance of the Rayleigh number; Joshua S. Stein (Sandia National Laboratory) provided references of the geothermal data for the WIPP site; Enrique R. Vivoni (NMT) evaluated FEMLAB and provided funding for FEMLAB; Susan L. Bilek (NMT) also provided funding for FEMLAB; Leigh Soutter and Peter Georén (COMSOL AB) gave me technical support; Robert S. Bowman (NMT) first gave me the idea that moist air is lighter than dry air based on the ideal gas law; John L. Wilson (NMT) gave me great advice on modeling as well as on this entire thesis, and I could not have completed this without his help; Gus Frederick (Oregon Public Education Network) gave me a nice cave diagram; Xiaobing Zhou (NMT) provided the remote sensing data of surface temperature of the Carlsbad Cavern region; Hongji Xie (NMT) taught me how to create GIS maps of Carlsbad Cavern; Marshall Reiter (New Mexico Bureau of Mines and Mineral Resources) provided the geothermal data for the AEC-8 in

WIPP site and his geothermal research reports; Val Werker provided the photograph of Carlsbad Cavern Natural Entrance; John McLean provided his research report of Carlsbad Cavern micrometeorology; Connie Apache, her kindness rescued me when I had a difficult time; Renee Sandvig, Catherine Jones, Sung-Ho Hong, Bayani Cardenas, Elizabeth Bryant, Geoffrey Marshal, Samuel Ndur, Suzanne Mills, Shasta McGee, and all my friends at NMT who have encouraged this research work; and my family, especially Norio Shindo (my husband) and Tama Ishibashi (my mother) have supported my entire study in the U.S.

This research has been funded by the National Cave and Karst Research Institute.

TABLE OF CONTENTS

Page

LIST OF TABLES

LIST OF FIGURES

CHAPTER 1

INTRODUCTION

1.1 Cave Micrometeorology

Cave micrometeorology can be defined as the study of cave weather systems, involving heat, air, and materials flow. The relevant flow materials are water, air, solid particles and microorganisms [Rowling, 2001]. Of course, flow requires energy. Caves are subsurface semi-closed systems, in which the energies and materials from surface and subsurface interact and flow very slowly, creating their own distinctive meteorology. Cave micrometeorology may control aspects of the formation and subsequent enlargement of caves and details of secondary mineral deposition.

An important ultimate application of cave studies is to “Protect caves as natural resources.” The study of cave micrometeorology is an important part of realizing this goal. For example, Neville [Bat Conservation International, 2001, 2 and 21-23] studied cave micrometeorology to help restore a once large hibernating population of endangered Indiana bats.

Other researchers have investigated some additional aspects of cave micrometeorology. Several interesting questions arise from their investigations that provide the inspiration for this thesis research. McLean [1971] measured the vertical variations of air velocity in the Natural Entrance of Carlsbad Cavern, NM (a map of

Carlsbad Cavern is found in Figure 1.1), and he observed inflow and outflow components in the single entrance [Hill, 1987, 29]. We are interested in mechanisms that can produce the two flow directions in a single entrance.

According to Hill [1987, 27], the temperature in Carlsbad Cavern ranges from 12.4°C to 19.6 °C, and averages 13.3 °C. The highest temperature was observed in the Lake of the Clouds located about 312 m below the surface, which is the deepest point in the cave. Based on this study, Hill points out that the temperature of the Lake of the Clouds (19.6°C) is too high even if we consider the effect of geothermal heating, and that there could be unknown factors contributing to the anomalous temperature. About 30 years after the McLean study, Forbes [2000] also collected temperature data within Carlsbad Cavern. The two investigations appear to agree. The Lower Cave in Carlsbad Cavern is located about 260 m below the surface. Its temperature ranges from 14°C to 15°C, which is slightly lower than the temperatures in the system above. Temperatures tend to increase with depth due to geothermal heating (see Figures 2.2 and 2.6). If we consider the geothermal heating effect, the temperatures may be higher in the deeper parts of a cave. Geothermal heating alone may not be sufficient to explain the observed slightly lower temperatures in the Lower Cave section of Carlsbad Cavern.

Buecher [1999] conducted intensive micrometeorological investigations in Kartchner Caverns, AZ. He also observed temperature anomalies within that cave. In general, the average temperature of a cave is expected to be similar to the average surface temperature at the cave's elevation [Moore and Sullivan, 1978]. Buecher argues, "While geothermal heating explains why the cave is warmer than expected, it does not explain the variations in temperature in different sections of the cave." We are interested in the unknown factors that are causing this temperature variability.

Forbes [1998] conducted air temperature and relative humidity studies in Torgac Cave, NM. He investigated the existence of large vertical variations in time–averaged relative humidity from floor to ceiling of the cave passage. He infers that the lowest humidity zone probably corresponds to the zone of maximum airflow. Wind Cave, located in the southern Black Hills of South Dakota, exhibits strong airflow at its entrances (winds in excess of 33 m s^{-1} have been recorded). Nepstad and Pisarowicz [1989] report results of a micrometeorology study in this cave. According to these investigators, "Summer Avenue is an interesting place along the tour route in Wind Cave. No matter which direction the air is moving at the Walk-In Entrance, the air movement is always from east to west through this passage. The reason behind this unusual air flow is not currently understood and has not been addressed in any literature about Wind Cave." The permanent airflow direction may imply internal factors are playing a role. We would like to understand the internal mechanisms that produce permanent airflow directions inside caves.

To understand the atmospheric condition of the Historical Section of Mammoth Cave, KY, Jernigan and Swift [2001] investigated the behavior of a mathematical model that predicts cave air temperature as a function of the distance from a cave entrance. The Historical Section extends approximately 500 m from the Natural Entrance, except for the area of Wright's Rotunda which is about 1500 m from the Natural Entrance. The atmospheric conditions of this area have been disturbed by alterations made to the Natural Entrance over the past two centuries. The most drastic of these alterations was clearance of large rockfall debris piles, which enhanced air exchange between the surface and the subsurface. This area was once a major bat hibernation site, but today, few bats are found. Jernigan and Swift modified the Bernoulli equation to include the effects of energy loss due to the presence of other cave passages between two points and heat exchange between the cave strata and air. They assumed that airflow between the two points in the cave system is driven by the temperature difference between those two points. The coefficients of the modified Bernoulli equation were found by the regression analysis of atmospheric data. The model accurately predicted air temperature at sites near Houchins Narrows (located 103 m from the Natural Entrance) during winter. The model accuracy decreased in summer months, and with an increase in the distance from the Natural Entrance (e.g., the value of R-squared in Wrights Rotunda is 0.32). The internal mechanisms may play an important role in determining air temperatures in the deeper parts of the cave.

1.2 Natural Convection in Enclosures

Air movement inside caves due to the force of buoyancy is called natural convection. Yang [1987] provides a definition of natural convection in enclosures, “By definition, enclosures are finite space bounded by walls and filled with fluid media. Natural convection in such enclosures is induced by buoyancy caused by a body force, such as gravity, together with density variations within the fluid. Such density variations may be due to external heating or cooling through the bounding walls, to the presence of internal heat sources or sinks, to concentration changes in the fluid as a result of mass transfer, or to any combination of these processes.” There are many possible applications for the study of natural convection in enclosures including nuclear reactor insulation, ventilation of rooms, solar-energy collection and crystal growth in liquids [Markatos and Pericleous, 1984]; and of course, micrometeorological modeling of cave systems.

Study of natural convection in enclosures is a challenging subject [Bejan, 1995]. It has been extensively investigated in the mechanical engineering fields in the past decades using simple geometries including: rectangular enclosures heated from the sides; rectangular enclosures heated from below; triangular enclosures; and inclined enclosures [*e.g.* Yang, 1987; Bejan 1995 and 2000; and Ghassemi, 2003]. Among the geometries, the case of rectangular enclosures heated from below may be the most useful to study natural convection inside caves coupled to geothermal heating [Blake et al., 1984; Catton, 1978; Paul and Catton, 2004; and Busse, 1978].

Some of the main objectives of the study of natural convection in the mechanical engineering field appears to be: 1) to identify the critical Rayleigh number, depending on different geometry, especially geometries with different aspect ratios, and different fluid materials [Blake et al., 1984; Catton, 1978; and Busse, 1978]; 2) to solve the coupling problem between boundary layers and core flows [Markatos and Pericleous, 1984]; and 3) to investigate appropriate numerical methods including accuracy and grid generation problems for the natural convection simulation [Christon et al., 2002; and Gelfgat, 2004]. The *Rayleigh number* is based on the ratio of thermally induced buoyancy forces (which drive convective fluid flow) to the viscous forces inhibiting fluid movements [Furbish, 1997, 428-429]; and above the critical Rayleigh number, flow will be unsteady (see Section 2.5.2). Typical Rayleigh numbers that have been applied to these studies range from 10^3 to 10^6. If we assume that the fluid is air with thermal properties at 17°C and heat flux of 0.05 Wm^{-2}, the characteristic length (e.g. height of the model) within this range of Rayleigh numbers would be from 0.04 m to 0.25 m (calculation methods are found in Section 2.5.2). The studies conducted by those in the mechanical engineering fields often focus on relatively small scales (e.g., electronics component). Flow equations are extremely non-linear, so at this moment large scale, transient simulations require very large computer capacities with a very long simulation time. At present, these limitations constrain our own modeling attempts, and the caves we simulate are relatively small with steady flow conditions. We are looking forward to having more efficient computer codes to simulate non-linear flow equations in larger scale models in the future.

1.3 Yucca Mountain Project

Drift scale studies of micrometeorology at the Yucca Mountain project in Nevada are relevant analogies to cave micrometeorology. Recent projects at this possible future radioactive waste repository have studied natural convection at the field scale [Valentine et al., 2002]. Consideration of the impact of radioactive waste heat is essential for many aspects of potential repository design. For example, waste heat in the emplacement drifts (the mined horizontal opening that would contain the waste canisters) affects the relative humidity, temperature and subsequent dripping water on the waste packages, all of which control the corrosion rate [Buscheck et al., 1996]. On a large scale, waste heat might alter the mineralogy of the host rock [Bish, 1995] or it could impact on the above-ground ecosystem from increases in soil temperature [CRWMS M&O, 1999]. Hao et al. [2004] have challenged the state of thermohydrologic modeling, coupling Navier-Stokes models of gas, moisture, and heat flow in the Yucca Mountain project emplacement drifts, with a finite-element scheme using the NUFT code. Their study aims to develop a method of coupling the Navier-Stokes equations (see Section 3.2) for the drift and porous flow equations for the walls to reach a more accurate representation of all major flow and transport processes in underground tunnels and surrounding fractured host-rocks. Porous-medium Darcy-flow approximations are applied to the thermohydrologic processes in the host-rock, and the Navier-Stokes modeling is applied to model in-tunnel flow behavior (natural convection, turbulent flow conditions, etc.). We anticipate that these types of innovative methods will be available in the near future, although they are currently still under development and not available for this study.

Or and Ghezzehei [2000] studied water dripping into subterranean cavities with fractured porous media in order to improve estimates of dripping rates, sizes, and chemical composition of droplets that could affect long-term integrity of waste disposal canisters. They studied the effect of evaporation from the drop surface during drop formation. The authors concluded, “The competing effect of evaporation renders drop size, dripping rate (detachment times), and chemical composition of drops very sensitive to minute changes in ambient conditions.” We may be able to apply these studies to formation and growth of stalactites in the future.

The amount of water that flows through the mountain and into drifts is considered to be controlling the corrosion rates of waste packages, as well as mobilization and transport of radionuclides. Salve and Kneafsey [2005] report the results of their continuous measurements of relative humidity and temperature and periodic observations of liquid water in the unheated Cross Drift (a 5-m-diameter, 2.7-km-long tunnel) at Yucca Mountain. According to these authors, the formation surrounding the drift is able to provide and transport large amounts of water vapor over a relatively short period. This vapor is able to condense, resulting in liquid water accumulating in an initially dry drift. Water condensation in drifts from vapor flow can impact the performance of the repository. These authors suggest, “The key information necessary to understand and properly model the air motion in drifts is the measurement of the internal gas flow.”

1.4 Purpose and Scope of Thesis

Compared with the surface weather conditions, cave meteorological conditions may be relatively constant over time, especially in deeper parts of caves, but caves are complicated miniature worlds, and the mechanisms of cave meteorology are poorly understood. Many researchers have tried to explain the temperature anomalies or airflow patterns relating to the surface influences, such as cooling effects of flooding water [Buecher, 1999] or change in surface barometric pressures. However, we think that cave internal elements such as geothermal heating, relative thermal properties of air and rock, and cave geometry may also contribute to cave micrometeorology. We apply these internal elements to our computer models in this study to observe air and heat flow behaviors.

To our knowledge, this effort is the first attempt to conduct micrometeorological modeling of cave systems. Applying the study of natural convection to cave micrometeorology is a difficult task because caves are sites of large-scale processes, complex geometries, and have at least two materials (rock and air). Although there are many difficulties, we hope that this study provides some convincing possible explanations for the behavior of flow systems inside caves.

This thesis first delineates the factors that affect air and heat flow inside caves in Chapter 2. Next, we discuss the computer modeling issues, such as the computer software used, governing equations, and boundary and initial conditions in Chapter 3. Chapter 4 focuses on the various problems and limitations associated with the computer models. Chapters 5 and 6 provide the constructed computer models, focusing on the geothermal heating, cave geometry, and thermal properties of materials. Chapter 7 summarizes the modeling and discusses the important factors for cave micrometeorology based on the results of modeling. Following that, the possible applications of the computer models are considered in Chapter 8. Finally, we draw conclusions from this work in Chapter 9.

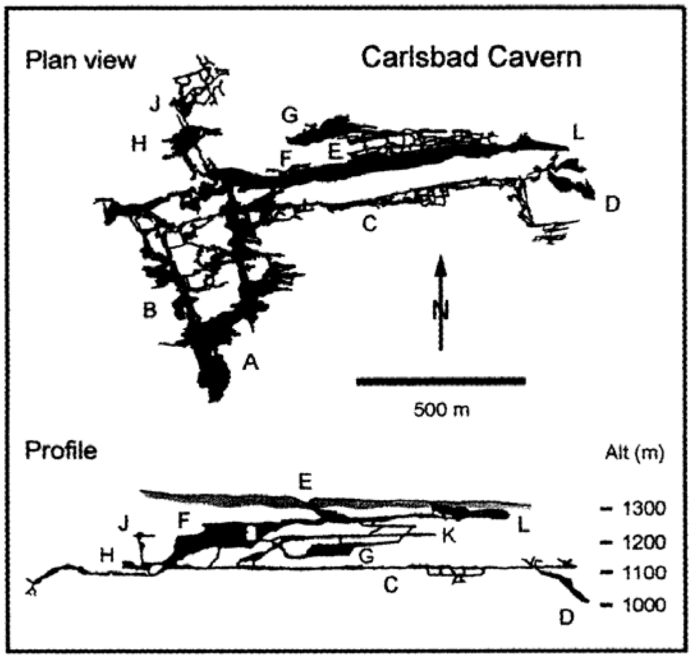

Figure 1.1: Carlsbad Cavern, NM. A = Big Room; B = Lower Cave; C = Left Hand Tunnel; D = Lake of the Clouds; E = entrance; F = Main Corridor; G = Guadalupe Room; H = New Mexico Room; J = Chocolate High; K = New Section; L = Bat Cave [Palmer, A., and Palmer, M., 2000; and Cave Research Foundation, 1992].

CHAPTER 2

FACTORS OF CAVE MICROMETEOROLOGY

Air and heat flow are the result of multiple factors acting on the atmospheric systems inside caves. Study of each factor is important to understand flow dynamics, and it is a necessary step in constructing and applying computer models. We must select factors that are critical for model fidelity and determine those that can be ignored. The following sections describe the possible factors that affect cave micrometeorology and provide an assessment of their relative importance for the model.

2.1 Surface Weather System

If a cave has one or more entrances, then outside air may enter. Surface meteorological conditions are changing all the time. When there is a high-pressure system at the surface, a wind forms that is downward and outward wind with respect to the center of the whirlwind and air may enter into a cave regardless of whether the air is cold or warm, and regardless of the season. When there is a low-pressure system at the surface, an upward and inward wind forms with respect to the center of the whirlwind [Earth Observatory, 2004] and some cave air may be sucked out to the surface. When the surface is in a calm weather pattern, airflow may also occur between the surface and the subsurface due to the difference of air density. Cold and dry air is denser than warm and wet air. Denser fluids sink and lighter fluids rise in a gravitational field.

If the cave has enough air mass originally, the introduced or departed air mass may render the remaining cave air unstable, and will induce airflow in order to maintain the appropriate air mass with respect to temperature, elevation, and volume of caves. When we think of the conservation of mass with respect to cave air, we generally make the simplifying assumption that air is an incompressible fluid (see Section 2.4).

Of course, the surface weather conditions are important, and while constructing the computer models, we can consider these conditions to some extent by imposing inflow or outflow conditions at the cave entrance boundary (see Chapter 6). However, researchers often observe the relatively constant temperature or permanent airflow in the deeper parts of caves, and the surface influence appears to be limited to the vicinity of cave entrances [e.g., Forbes, 2000; and Nepstad and Pisarowicz 1989]. The relatively constant meteorological state in deeper parts of caves is analogous to the constant temperature in deeper parts of soil profiles. For example, Figure 2.1 shows the soil temperature profile at Argonne, Illinois in 1953, which tells us that the fluctuations of the surface temperature gradually become small with depth, reaching approximately the average surface temperature at depths of around 3 m. Figure 2.2 shows the six air temperature logs (borehole filled with air) across the deep vadose zone taken during a 2-week period (May 26 to June 3, 2003) at the Tome piezometer site about 35 km south of Albuquerque, NM. Logs are offset 0.5˚C so they can be compared. In the figure, there are temperature fluctuations within a 10 m depth, but below 20 m, the temperature gradients appear to be stable, and there are no obvious temperature fluctuations.

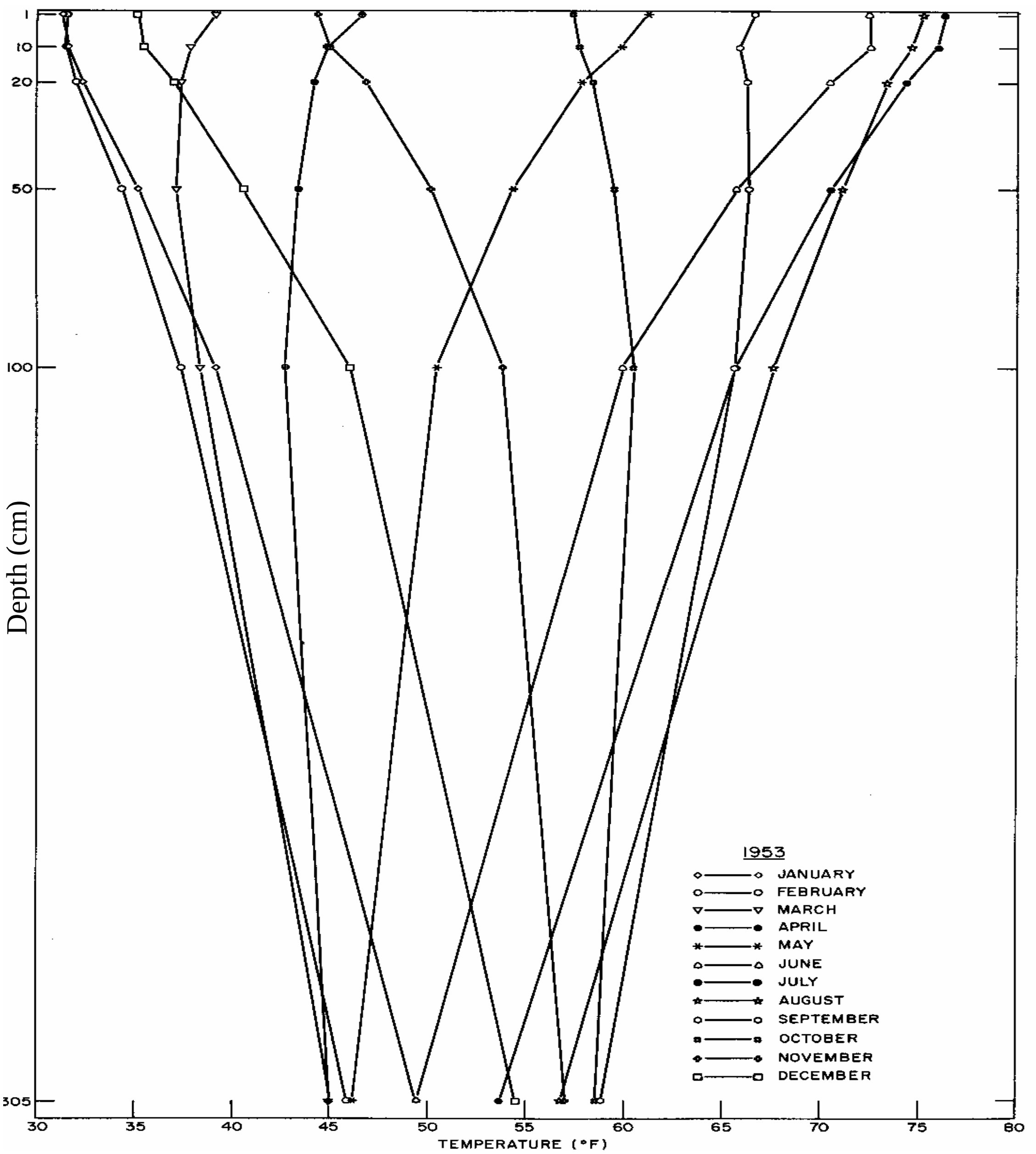

Figure 2.1: Soil-temperature profile for 1953 based in monthly averages at Argonne, Illinois [Carson, 1961, 120].

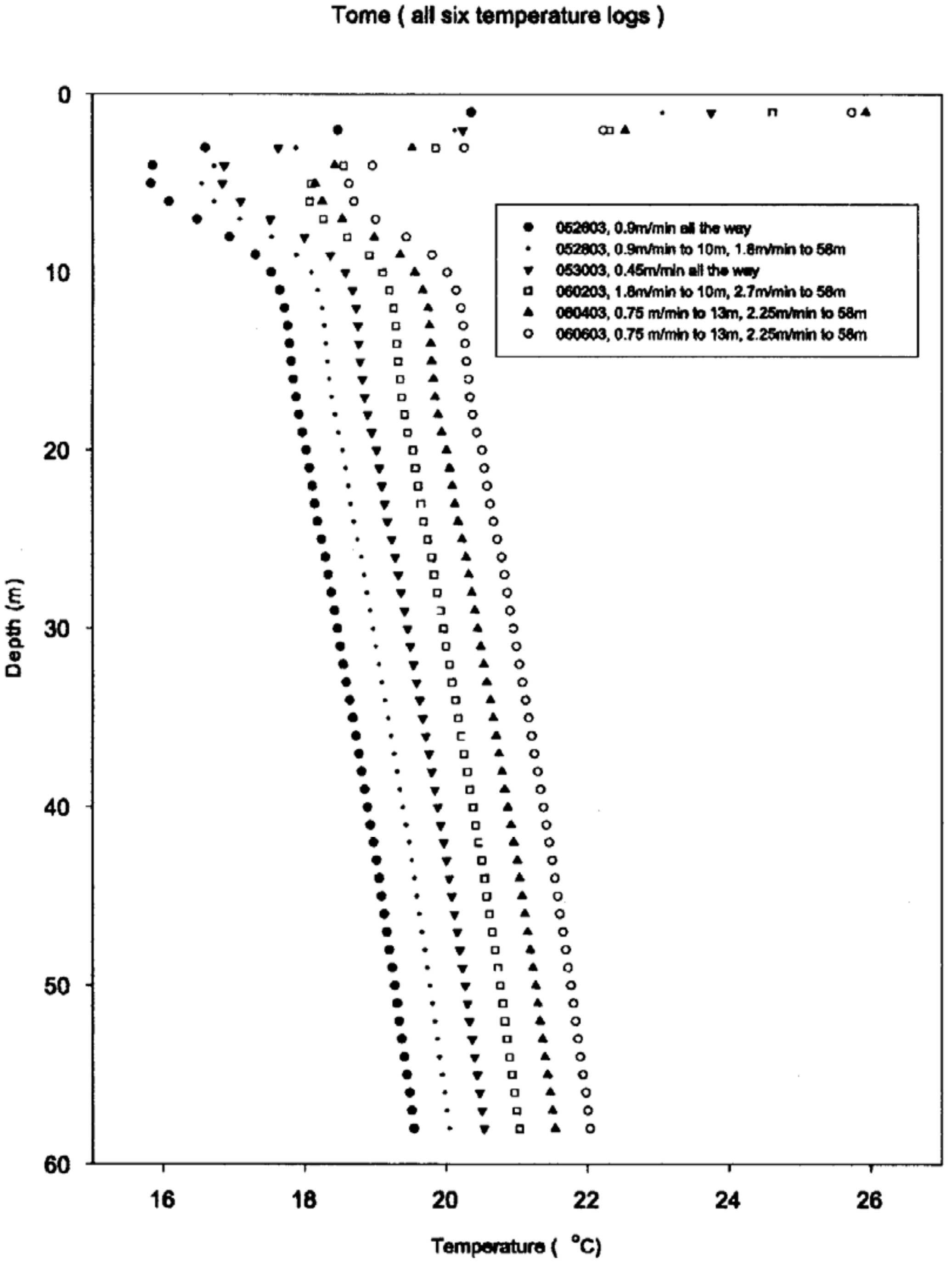

Figure 2.2: Temperature vs. depth data, temperature logs, for six different days measured at the Tome piezometer site about 35 km south of Albuquerque, NM. Dates logged (month, day, year) and logging speed are given in legend. Logs are offset 0.5˚C so they can be compared [Reiter, 2004].

Internal cave air and heat flow patterns are relatively constant in time, but there are small micrometeorological variations in the different parts of caves (details on temperature variations observed within Carlsbad Cavern are found in Chapter 8), which may contribute to the uniqueness of secondary mineral deposits. For example, in Figure 2.3, subaerial speleothems (speleothems that are created within air) in the upper part of the chamber are different from those of in the lower parts. Different micrometeorology between the upper and lower parts of this chamber may create these unique speleothems. Although we cannot ignore the effects of fluctuations of the surface weather conditions, we hypothesize that the small micrometeorological variations in the different sections of deeper parts of caves are mainly due to internal factors, and we try to identify these important internal factors.

Figure 2.3: Ogof Draenen Cave, Wales, UK. Different micrometeorology between the upper and lower parts of this chamber may create unique subaerial spleothems with distinct dividing lines. Photo by Jon Jones.

2.2 Viscosity of Air

Air is a viscous fluid having very low viscosity. Viscosity can be considered as the internal stickiness of a fluid. It accounts for the energy losses associated with the transport of fluids in ducts, channels, and pipes. In addition, viscosity has a primary role in the generation of turbulence [Potter and Wiggert, 1997, 13]. Viscous fluids exhibit resistance to shearing motions, thus, mechanical treatments of such flows must involve a consideration of frictional forces associated with this viscous behavior [Furbish, 1997, 261].

McPherson [1993, 28-29] explains the difference in the viscous behavior of liquids and gases with respect to temperature. There are at least two effects that produce the phenomenon of viscosity: the attractive forces that exist between molecules, and the molecular inertia effect. In liquids, the molecular attraction effect is dominant. Heating a liquid increases the internal kinetic energy of the molecules and also increases the average intermolecular spacing. As the attractive forces diminish with distance, the viscosity of a liquid decreases with respect to temperature. In a gas, the molecular attractive force is negligible, and the viscosity of gases is much less than that of liquids. The viscosity of gases is dominated by the molecular inertia effect. If molecules from the faster moving layer stray sideways into the slower layer, then the inertia that they carry would impart kinetic energy to that layer. The increased velocity of molecules of gases caused by heating will tend to enhance their ability to transmit inertia across streamlines and, thus, the viscosity of gases increases with respect to temperature. McPherson [1993, 29] provides the equation of viscosity for air:

$$\mu_{air} = (17.0 + 0.045T)\ x\,10^{-6} \quad \left(\frac{Ns}{m^2}\right) \qquad (2.1)$$

where T is the temperature in the range 0°C – 60°C.

Viscosity of air increases with respect to temperature, but under the same pressure, an increase in temperature leads to a decrease of air density (ρ) based on the ideal gas law: $\rho = p/(RT)$, where p is pressure, R is the gas constant, and T is temperature. The Reynolds number (Re) is the ratio of inertial force and viscous force, described by:

$$\mathrm{Re} = \frac{\rho U L}{\mu} \tag{2.2}$$

where U is the velocity (m s^{-1}), L is the characteristic length (m) [Furbish, 1997, 126]. We expect more turbulent flow in the larger values for Re. It is interesting that from equation (2.2), an increase of temperature appears to decrease the Reynolds number, thus, less turbulent flow, if we assume that the velocity remains constant.

The viscosity of air is one of the very important internal factors involved in flow mechanisms inside caves. The mechanical energy of incoming air is reduced by frictional heat loss when it passes through the complex cave ducts and channels. Eddies are formed when airflow hits complex speleothems or in the nooks and corners of a cave, which also convert mechanical energy to thermal energy. Because air is a viscous fluid, the frictional force changes flow patterns. Because of the low viscosity of air, the resistance to convective movements becomes low, which promotes the creation of convection cells (see description of Rayleigh number in Section 2.5.2).

Navier-Stokes equations are the governing equations of fluid flow modeling, in which the viscosity is treated as one of the important parameters in flow systems (Navier-Stokes equations are described in Chapter 3). The equation can treat the viscosity of air as a dependent variable with respect to temperature. However, we treat the viscosity as a constant value. Using equation (2.1), we determined a viscosity of 1.78 x10^{-5} N s m^{-2} with respect to the initial temperature of 17°C, the average surface temperature of Carlsbad Cavern's region, NM [Carlsbad Caverns Bat Cave Draw Weather Station, 2004]. The variation of viscosity with respect to the range of temperature observed in real cave systems is negligible. For example, in January of 1995, at Carlsbad Cavern, Forbes [2000] observed temperatures of 10.7°C at Devils Spring (about 100 m below the Natural Entrance), and 19.9°C at Lake of the Clouds (312 m below the Natural Entrance), which yields the maximum temperature difference in this entire set of observations; corresponding viscosities are 1.75 x 10^{-5} N s m^{-2} and 1.79 x 10^{-5} N s m^{-2}, respectively based on equation (2.1). The difference is negligible. The models have no slip boundaries (velocity is zero) at the air and cave wall interface due to the viscosity of air. In the case of steady, laminar flow in a circular tube, the velocity distribution at any cross section becomes parabolic (zero at the walls and maximum at its center) also due to the fluid viscosity [Young et al., 2004, 258].

2.3 Cave Geometry and Size of Caves Associated with the Steady Flow Energy Equation

Cave geometry and size should exert significant influences on air and heat flow inside caves. Lower Cave of Carlsbad Cavern, NM is located about 260 m below the Natural Entrance, and about 30 m below the Big Room. This author visited that area in May 2003. Lower Cave and Big Room are connected in a complex way, but there are two known positions of interest, Entrance of Lower Cave (it is a small opening and there are narrow ladders), and Jumping Off Place.

Jumping Off Place, located in the southeast relative to the Entrance of Lower Cave, is a wide cliff, and the bottom of the cliff is a part of Lower Cave. This geometry may contribute to the creation of air circulation. When our team descended the narrow ladders, we clearly felt air flowing into Lower Cave. (Details of downward flow observed at the Entrance of Lower Cave are found in Section 8.1.)

Whatever the reasons are for this flow, clearly, a certain mass of air was being introduced into Lower Cave from the Big Room. The flow appeared to cease before we reached the bottom of the ladder. The process can be expressed in an expanded version of the steady state flow energy equation for dry air, also called the advanced Bernoulli's equation [McPherson, 1993, 60]:

$$\frac{u_1^2 - u_2^2}{2} + (z_1 - z_2)g = \int_1^2 v\,dp + F_{12} = H_2 - H_1 - q_{12} \quad \left(\frac{J}{kg}\right) \tag{2.3}$$

where subscripts indicate stations, u is the velocity (m s^{-1}), z is the elevation (m), g is the gravitational acceleration (m s^{-2}), v is the specific volume (m^3 kg^{-1}), F is the frictional conversion of mechanical to heat energy (J kg^{-1}), H is the enthalpy (J kg^{-1}), and q is the heat input from external sources (J kg^{-1}). Enthalpy (H) is the sum of the internal energy U ($J\ kg^{-1}$), a molecular or 'internal' kinetic energy, and the pv product (p is pressure and $v = 1/\rho$ is specific volume; the pv product is known as *flow work*) [McPherson, 1993, 25]. As a parcel of air moves forward, the air must overcome the resistance of air that already exists in the flow passage. Flow work is the work performed to move the air in the cave.

The total mechanical energy is the sum of kinetic energy, potential energy, and flow work. If there are neither frictional effects nor heat input from external sources, the total mechanical energy must remain constant throughout the airway [McPherson, 1993, 24-26]:

$$\frac{u_1^2 - u_2^2}{2} + (z_1 - z_2)g + \int_2^1 v dp = 0 \qquad (2.4)$$

Any frictional effects will reduce the mechanical energy terms:

$$\frac{u_1^2 - u_2^2}{2} + (z_1 - z_2)g + \int_2^1 v dp = F_{12} \qquad (2.5)$$

(the mechanical energy is smaller at station 2), and increase the internal energy:

$$F_{12} = H_2 - H_1 - q_{12} + \int_2^1 v dp = U_2 - U_1 - q_{12} \qquad (2.6)$$

(the internal energy is larger at station 2), but will have no influence on the overall energy balance. $H_2 - H_1 = C_p (T_2 - T_1)$ for an ideal gas, where C_p is the specific heat of dry air (1005 J kg^{-1} K^{-1}) and T is temperature (K). In equation 2.3, a friction term appears in the middle, and no friction term is present in the left hand and right hand parts, which indicate that the change in temperature ($T_2 - T_1$) is independent of frictional effects. "In case of the steady flow of perfect gases, the frictional conversion of mechanical work to heat through viscous shear produces a higher final specific volume and a lower pressure than the ideal process, but exactly the same temperature [McPherson, 1993, 67]."

Figure 2.4 shows the schematic diagram of the steady flow energy equation. Assume that a certain mass of air is moving from stations 1 to 2, for example, from the top to the bottom of the ladders at Lower Cave. Due to frictional effects, the mechanical energy is reduced, and internal energy is increased. The frictional effects increase the specific volume and lower the pressure, but they may not affect temperature in the case of a perfect gas. Although air at atmospheric pressure approximates the behavior of an ideal gas, air is not an ideal gas, so the frictional effects could affect temperature very slightly.

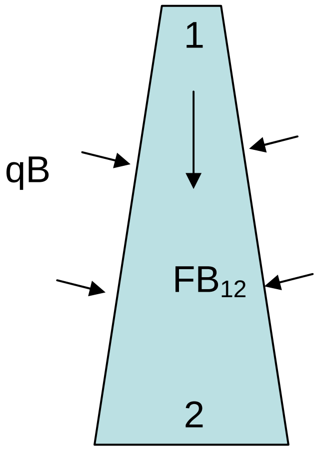

Energy state at station 1

$$\frac{u_1^2}{2} + z_1 g + H_1 \qquad H_1 = U_1 + p_1 v_1$$

Δmechanical energy$_{1\text{-}2}$ = F_{12} = $\Delta U_{2\text{-}1}$ - q_{12}

Energy state at station 2

$$\frac{u_2^2}{2} + z_2 g + H_2 \qquad H_2 = U_2 + p_2 v_2$$

H is a thermal property of state and is independent of any previous process path [McPherson, 1993, 58].

Figure 2.4: Schematic diagram of the steady flow energy equation.

Cave geometry is very complicated. The presence of stalactites, stalagmites, and other secondary mineral deposits (know as speleothems) may produce eddies and promote frictional effects, resulting in reduction of the speed of the parcel of air. The larger the cave size or the more complicated the cave geometry, the greater the frictional effects, and the greater the reduction in mechanical energy and the greater the increase in the internal energy.

We hypothesize that cave geometry and size are very important internal factors of cave micrometeorology because of the frictional effects. To construct the computer models, we dealt with the effects of cave geometry in a highly simplified way. To consider the effects of cave size, we have tried to make the models as large as possible, but it is difficult to approach typical sizes of real caves. The reasons for the difficulty are: 1) Navier-Stokes equations coupled with the heat equation solve non-linear systems, and sometimes computer simulations produce multiple solutions or no solution for computational reasons; and 2) an extremely large computer capability is necessary to produce models that approximate realistic cave sizes. Although there are many limitations, we hope that the simple and small models presented in this study can provide some explanations applicable to real systems.

2.4 Incompressible Airflow Associated with the Steady State Pressure Equation

The steady state flow energy equation (2.3) can be converted to the steady state pressure equation by multiplying the equation by the mean density of air (ρ_m):

$$\rho_m \frac{u_1^2 - u_2^2}{2} + \rho_m (z_1 - z_2) g = p_2 - p_1 + \rho_m F_{12} = \rho_m (H_2 - H_1) - \rho_m q_{12} \quad \left(\frac{N}{m^2}\right) \quad (2.7)$$

Now we can analyze the flow system from the pressure balance perspective. The first term of the left hand side of the equation (LHS) is the change in dynamic pressure, the pressure required for fluid flow [Furbish, 1997, 232]. The second term of LHS is the change in static pressure due to the column of air between z_1 and z_2. Usually the change in dynamic pressure is very small, and sometimes it is negligible compared with the change in static pressure. In the middle of the equation, $p_2 - p_1$ is the change in barometric fluid pressure, and $\rho_m F_{12}$ is the frictional pressure drop (the frictional effect increases the specific volume and decreases the pressure) [McPherson, 1993, 67-68]. Because q is the heat source term and the H_2-H_1 equals $C_p (T_2-T_1)$, both $\rho_m (H_2-H_1)$ and $\rho_m q$ indicate the pressure change associated with change in temperature.

When a parcel of air descends or ascends in the cave passage, the change in static pressure and thus, the resulting change in the weight of the air column, produces gravitational compression or decompression of the parcel of air. This results in the change in temperature of that parcel. The increase in temperature due to depth is known as the *adiabatic lapse rate*. When the dynamic pressure and frictional pressure drop are negligible, and no heat is added from the strata, equation (2.7) describes only gravitational compression [McPherson, 1993, 553-556 and 589]. The adiabatic lapse rate for dry air is about 0.98°C per100m. The moist adiabatic lapse rate varies with temperature, initial vapor pressure, and elevation, but is typically about 0.5°C to 0.65°C per 100m [Dingman, 2002, 590]. The lesser difference in temperature change of moist air is due to heat released in the process of condensation and heat utilized in the evaporation process; these processes are not included in equation (2.7).

Air is a compressible fluid when we think of it in terms of gravitational compression. However, when we consider the compressibility of air due to flow, it can be treated as an incompressible fluid. Furbish [1997, 58] explains that the flow of a gas can be treated as incompressible if the relative change in density induced by flow is small, that is, $d\rho/\rho << 1$. Elasticity (E) is expressed by:

$$E = -\frac{dp}{dV/V} = \frac{dp}{d\rho/\rho} \tag{2.8}$$

Bernoulli's equation tells us that: $p + \frac{1}{2}\rho u^2$ = constant for a frictionless system within the same elevation (the gravitational pressure gradient is negligible). The change in pressure dp induced by flow is of the order of the dynamic pressure, $\frac{1}{2}\rho u^2$. Substituting this into (2.5) and rearranging yields:

$$\frac{d\rho}{\rho} \approx \frac{\rho u^2}{2E} \approx \frac{1}{2}\left(\frac{u}{c_s}\right)^2 \tag{2.9}$$

where $c_s = (E/\rho)^{0.5}$ is the speed of sound (about 335 m s^{-1}), and u/c_s is called the *Mach number*, *M*. Thus, the compressibility can be neglected when $\frac{1}{2}M^2 << 1$. The relative change in density $d\rho/\rho$ for a flow velocity of 50 m s^{-1} is about 0.01. McLean [1971] observed air current speeds of about 0.05 m s^{-1} in the Lunch Room of Carlsbad Cavern [Hill, 1987, 29]; corresponding $d\rho/\rho$ is about 1.11 x 10^{-8}. We should be able to safely treat cave air as an incompressible fluid in the flow system.

In our daily life, however, we sometimes observe the phenomenon that air is compressed at a given elevation (a condition of gravitational compression is negligible). A swamp cooler that uses the evaporative cooling effect is commonly used in New Mexico. To use the swamp cooler, we need to open the window because the relatively large amount of cool air is continually introduced into a room from the upper parts of the room. For example, this author usually opens the window about 10 cm. In this situation, some resistance is created when the entrance door of the author's house is opened inward. When the window is opened widely, the entrance door can be opened normally. Obviously there is an imbalance between the amount of introduced air and outgoing air when the escape space for the exiting air is too small. The air inside the room thus appears to be compressed due to the excess amount of cool air. According to the ideal gas law ($pV = nRT$, where R is a gas constant), the increase in the number of molecules (n) causes an increase in pressure (p), if the volume (V) remains the same. We think that air acts as essentially incompressible in a flow system, but when we see its behavior at a local scale such as a room that has multiple entrances, obviously the air can be compressed temporarily (the transient state) due to excess air accumulation. Eventually the excess air in the room escapes and the room air returns to the steady state condition.

The example above may be heuristic with respect to cave systems. Caves are local, semi-closed systems. As long as a cave is connected with the surface, excess air may try to move out from the cave to maintain appropriate mass of air with respect to temperature, volume of cave, and elevation. The flow system could be transient, if caves are connected to the surface in multiple ways (such as the presence of multiple entrances or fractures), or if caves have a single large entrance. Temporary imbalance between incoming and outgoing air masses can be created, producing excess air pressure or less air pressure inside caves. In the process of the exploration of Lechuguilla Cave, NM, investigators have sometimes experienced strong cave winds coming through the cracks in the floor. According to those investigators, "The wind howled insistently through several large cracks in the floor. Usually the cave exhaled, blasting sand and dirt into the digger's face. Today it was inhaling. In fact, it was like a vacuum cleaner sucking dirt and loose rocks down through a couple of screaming holes in the floor [Reames et al., 1999, 20]". Those strong winds could be produced by the direct response of cave air to the surface weather conditions as ascribed in a commonly employed idea; but it could also come from excess or less cave air pressure caused by that the flow system is transient, creating imbalance of cave air mass (an indirect response to the surface weather fluctuation).

Navier-Stokes equations describe momentum balance for fluid flow. If a fluid is incompressible, the non-linear equations become much simpler and computer simulation model convergence is more likely. Although air could be a compressible fluid in the transient state, in our models we treat it here as an incompressible fluid for the steady state flow system, and the air mass is conserved. This treatment may not be too far afield from a real situation if an entrance is large enough or the surface weather condition is calm. Because we consider air as incompressible, the air density is treated as a constant, and change in density due to change in temperature is dealt with as a thermally induced buoyancy force in the momentum equation, associated with gravitational acceleration and the thermal expansion coefficient of air. This is the so-called *Boussinesq approximation* (see Section 3.3), and we use it in our simulations.

Our models simulate the density-driven flow due to thermally-induced buoyancy forces. The models ignore the change in temperature and pressure due to gravitational compression. Temperature in the models is determined by the cave size and geometry, the geothermal heat flow (bottom boundary), the average surface temperature (top boundary), thermal properties of materials, and thermally-induced buoyancy force. Neglecting the effects of gravitational compression is not a serious problem, because the change in temperature due to gravitational compression can be compensated by the increased resistance to flow. In addition, in the density-driven flow, air moves because of the difference in density among neighboring parcels of air, in which the gravitational pressure gradient is negligible. Neglecting the gravitational pressure gradient has let us focus on the cave internal dynamics. Details of the buoyancy force, gravitational compression, and the Boussinesq approximation are discussed in Chapter 3.

2.5 Geothermal Heat Flow and Thermal Properties of Rocks and Air

Many cave researchers may anecdotally agree that geothermal heat flow can be an important factor in controlling of cave air temperatures, but there are no studies that we have found that discuss the relationship between the geothermal heat flow and convection of cave air. We believe that computer modeling may help to uncover this possible relationship. As a first step, we wish to understand the nature of the geothermal heat flow. Next, we must examine the relevant Rayleigh numbers (the ratio of thermally-induced buoyant forces to the viscous forces), and consider whether or not geothermal heat flow can induce convective airflow.

2.5.1 Geothermal Heat and Thermal Properties of Rock and Air

(1) Geothermal Heat

The mean conductive heat flow measured very near the Earth's surface is approximately 0.07W m^{-2} [e.g., Chapman and Pollack, 1975]. The sources of this heat are not completely determined, but the radioactive decay of isotopes of uranium, thorium, and potassium is definitely the most significant. Prior to the discovery of radioactivity, many scientists believed that all of the current heat loss from the Earth was due to its continued cooling from an originally molten state [Ingebritsen and Sanford, 1998, 176-177]. Cooling of an initially hot Earth and the gravitational energy released by its density segregation may or may not be important sources. On a global scale, there is a reasonably good correlation between the age of the Earth's crust and crustal heat flow, and there is a distinguishable relationship between the timing of the most recent tectonic activity and heat flow [Sclater et al., 1980]. Average oceanic heat flow values range from about 0.05W m^{-2} in the oldest oceanic crust to over 0.30W m^{-2} in young crust near the mid-ocean ridges. Mean continental heat flow ranges from 0.04W m^{-2} on the stable cratons to 0.07W m^{-2} in Tertiary tectonic provinces [Ingebritsen and Sanford, 1998, 176-177].

Groundwater flow also affects geothermal heat flow. For example, heat flow of 0.09W m^{-2} observed in Pecos River near Artesia in southeast New Mexico is interpreted to be associated with upward groundwater movement that convects heat upward from depth [Reiter and Jordan, 1996]. The Socorro geothermal area is located in central New Mexico. Extremely high temperature gradients have been measured within the Socorro mountain block, including a heat flow of 0.49W m^{-2}. According to Barroll and Reiter [1990], although upper crustal magma in the Socorro area may contribute heat to the system, the Socorro geothermal system is greatly influenced by groundwater flow. By finite difference modeling of the hydrogeology of the Socorro area, Barroll and Reiter [1990] found that the forced convection of groundwater alone, without anomalous heat sources, could produce the observed geothermal anomalies.

In the 1970's, Sandia National Laboratories and D' Appolonia Consulting Engineers [1983] collected various geologic data for borehole AEC-8, Eddy County, New Mexico. Borehole AEC-8 is one of several exploratory wells drilled in eastern Eddy County to evaluate the stratigraphy, structure, and lithology of the rock units in and around the site proposed for the Waste Isolation Pilot Plant (WIPP), about 50 km east-southeast of Carlsbad. In early 1977, temperatures were measured in the borehole AEC-8 and three zones were identified with distinct temperature gradients (Table 2.1). These zones of distinct temperature gradients correspond well to the site lithology, and the low temperature gradient in the middle zone is probably due to the high thermal conductivities of Castile evaporites. The estimated geothermal heat flow at AEC-8 is 0.045W m^{-2} [Mansure and Reiter, 1977]. We rounded this value up as 0.05W m^{-2} and selected it for our modeling. Figure 2.5 shows the temperature profile at AEC-8, in which we can see that although there are some small fluctuations of temperature gradient, overall the temperature increases with depth at the large scale (also see Figure 2.1).

Table 2.1: Zone of temperature gradient in the borehole AEC-8 [Sandia National Laboratories and D’ Appolonia Consulting Engineers, 1983, 98].

Depth	Temperature Gradient
50 – 1035 ft (15 – 315 m)	0.85 °F / 100 ft (1.55 °C / 100 m)
1056 – 4247 ft (322 – 1294 m)	0.43 °F / 100 ft (0.78 °C / 100 m)
4306 – 4810 ft (1312 – 1466 m)	0.91 °F / 100 ft (1.66 °C / 100 m)

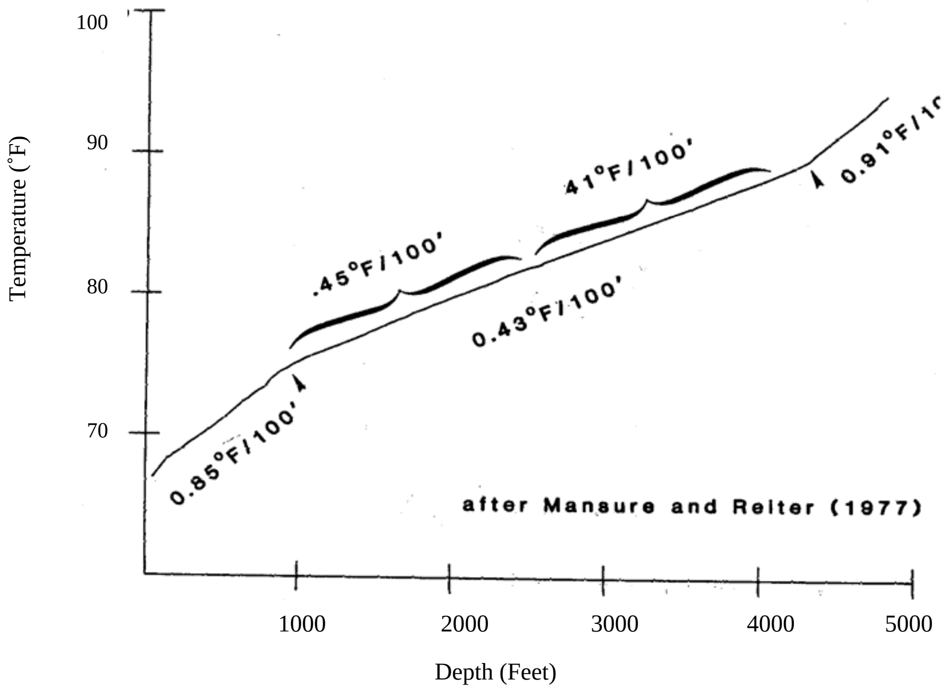

Figure 2.5: Temperature profile for AEC-8 [Sandia National Laboratories and D’ Appolonia Consulting Engineers, 1983, 115].

Figure 2.6 is the same data as Figure 2.5, but it shows the temperature profile from the surface to the depth of 304.8 m. The surface elevation of this site is 1077 m. Temperature at the depth of 69.8 m (elevation 1007 m) is 20.5°C [Mansure and Reiter, 1977]. Lake of the Clouds in Carlsbad Cavern is located at the same elevation (1007 m) and its air temperature ranges from 19.4°C to 19.7°C [Forbes, 2000]. AEC-8 is a small well filled with groundwater, so the collected temperature data are considered to be equilibrium temperatures of the surrounding rocks [Reiter, personal communication, 2005]. Using the average temperature gradient (1.55 °C / 100 m) observed at AEC-8, Hill [1987, 27] estimated rock temperature at the same elevation of the Lake of the Clouds as 18°C, and considered that the air temperature at Lake of the Clouds is too high to be in direct agreement with the calculations. However, actual data [Mansure and Reiter, 1977] show that air temperature of Lake of the Clouds (19.4°C to 19.7°C) is slightly lower than the rock temperature observed at the Lake of Clouds elevation in borehole AEC-8 (20.5°C).

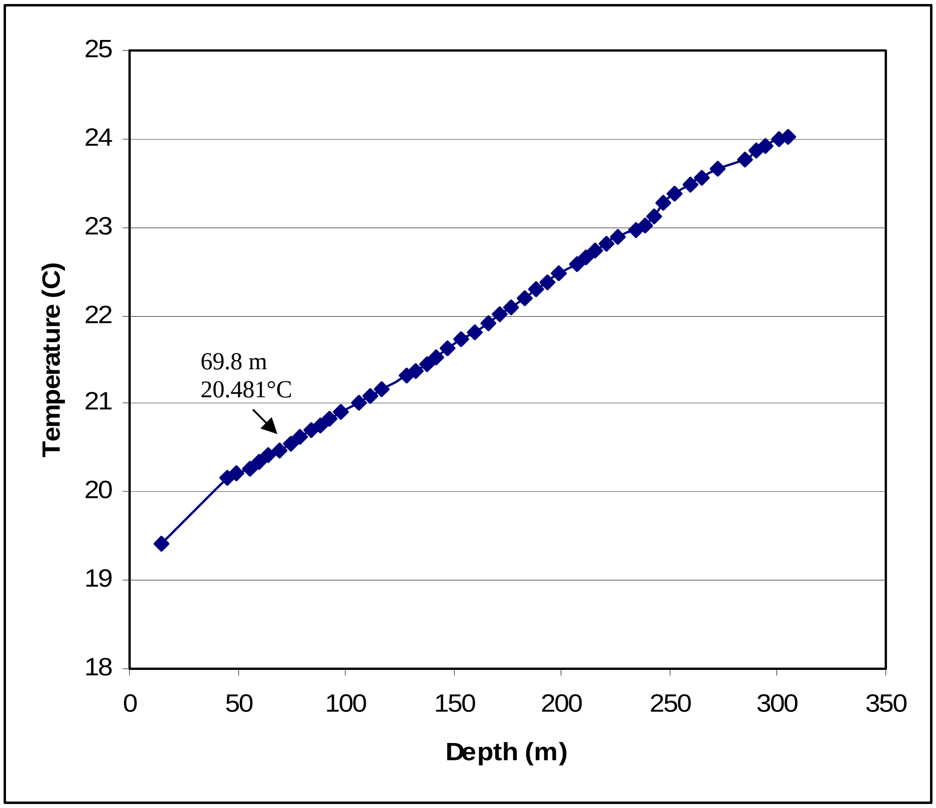

Figure 2.6: Temperature profile for AEC 8 (from the surface to the depth of 304.8 m). The elevation of the surface is 1076.8 m [Mansure and Reiter, 1977].

Lithologies of the WIPP site and the Lake of the Clouds area of Carlsbad Cavern are the evaporite rocks of the Gypsum Plain and the reef limestones, respectively [Hill, 1987, 27]. In addition, the groundwater flow regime could be different between these two sites. Therefore, the geothermal heating may also be different between these two sites, although elevations are the same. If we assume that water temperature of Lake of the Clouds is the equilibrium temperature of surrounding rocks, the rock temperature of this area would range from 18.5°C to 19.0°C based on Forbes [2000], which is slightly lower than the air temperature of this area.

(2) Thermal Properties of Rock and Air - Caves as Insulators

The caves considered in this study are surrounded by rocks and filled with air. Thermal properties of rocks and air are very different. We are interested in the difference in the heat flow behavior when geothermal heat passes through these different materials. We expect that convection cells will appear inside caves due to both geothermal heat flow, and the low viscosity (1.78×10^{-5} N s m^{-2}) and the low thermal conductivity of air (0.0255 W m^{-1} K^{-1}).

Figure 2.7 shows the temperature contour plot when heat flows by conduction only through limestone. The top has a constant temperature of 290 K, and a constant heat flux of 0.05 Wm^{-2} was applied to the bottom boundary. Figures 2.8 and 2.9 show the temperature contour plots of an idealized cave with the same boundary conditions. Detailed descriptions of the models are discussed in Chapters 3 thru 6. In Figure 2.8, air (the inner layer) is not allowed to move as a fluid, so the heat transfer occurs only by conduction. The outer layer of the model is limestone. Thermal conductivity of air is 0.0255 W m^{-1} K^{-1}, which is much smaller than that of limestone (2.5 W m^{-1} K^{-1}) and, hence, air in the cave acts as an insulator. In Figure 2.9, air is treated as a fluid, so heat transfer occurs by convection (heat is transferred by fluid flow) and conduction. In both models, temperature gradient within the air-filled cave becomes steep. Regardless of occurrence of convection cells, an air-filled cave acts as an insulator due to its low thermal conductivity.

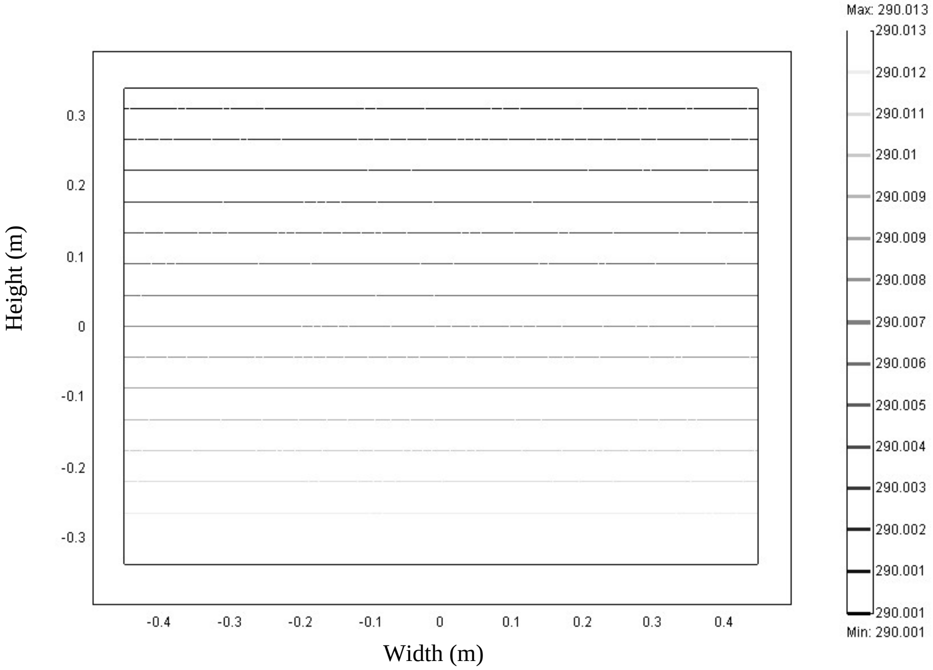

Figure 2.7: Conduction model with rock material showing contour lines for temperature (K). Heat flows through limestone by conduction.

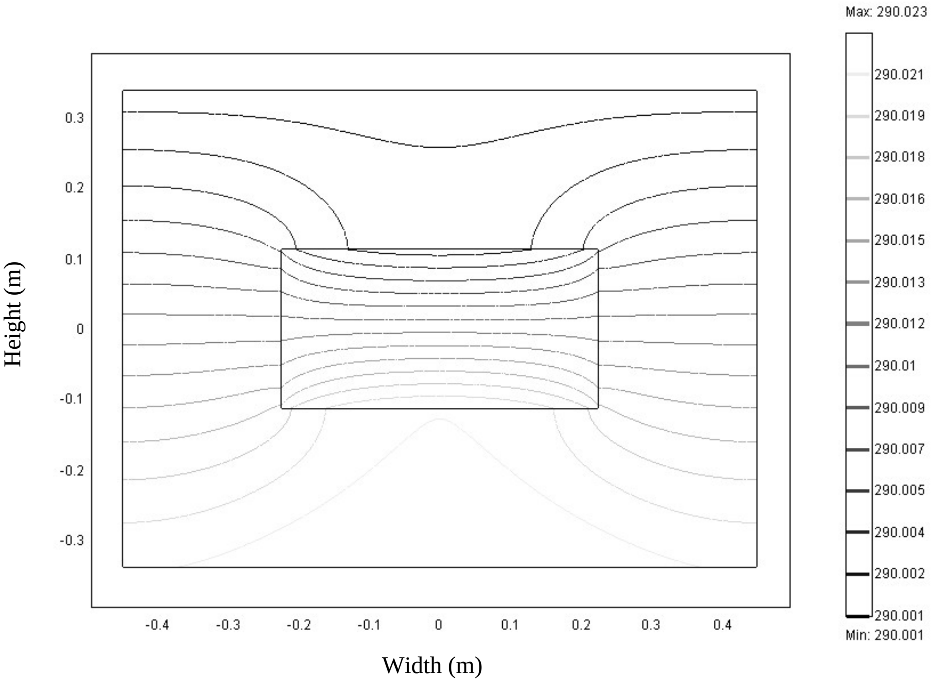

Figure 2.8: Conduction model with air and rock materials showing contour lines for temperature (K). Heat is transferred from bottom to top boundaries by conduction through limestone (outer layer) and air (inner layer).

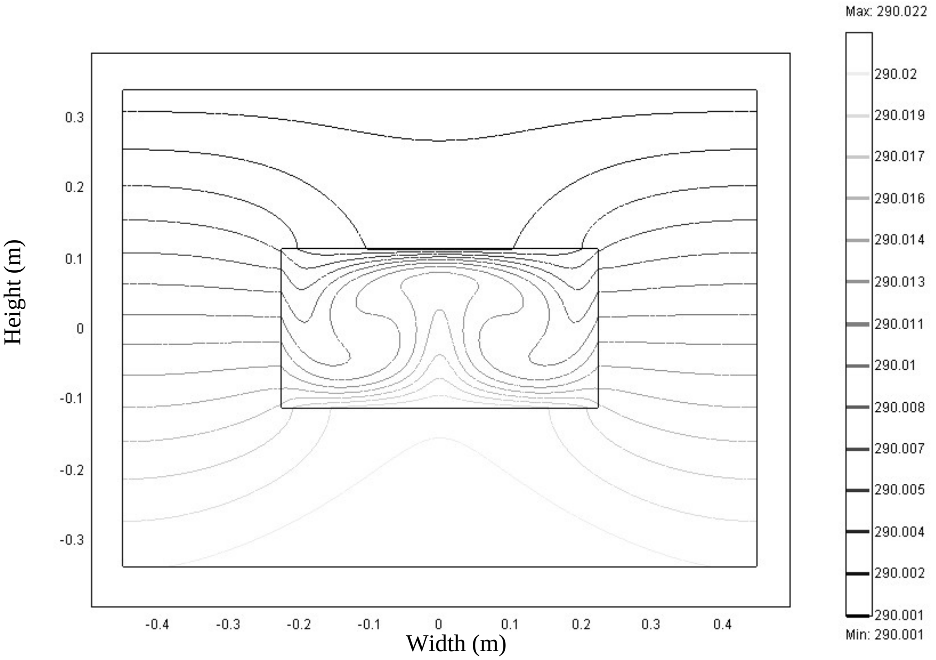

Figure 2.9: Convection and conduction model with air and rock materials showing contour lines for temperature (K). Heat is transferred by conduction through limestone and by convection and conduction through air.

2.5.2 Rayleigh Number and Free Convection

The Rayleigh number (*Ra*) is based on the ratio of thermally-induced buoyancy forces (which drive convective fluid flow) to the viscous forces inhibiting fluid movements:

$$Ra = \frac{\rho^2 \; g \; C_p \; \alpha \; \Delta T \; L^3}{\mu \, k} \tag{2.10}$$

where ρ (kg m^{-3}) is the fluid density, g is the gravitational acceleration (m s^{-2}), C_p is the specific heat at constant pressure (J kg^{-1} K^{-1}), α is the coefficient of thermal expansion (K^{-1}), ΔT is the temperature difference (K) between the top and bottom boundaries, L is the characteristic length (m), μ is the dynamic fluid viscosity (N s m^{-2}), and k is the thermal conductivity of the fluid (W m^{-1} K^{-1}) [Farnetani and Samuel, 2003].

Equation (2.10) is applied to models that have one fluid material and constant temperatures at the top and bottom boundaries and, thus the temperature difference between the boundaries is known. In our case, the models have both rock and air (Figure 2.9). Heat travels through the rock and when it reaches the air, heat is transferred by convection and conduction. Our models have constant heat flux at the bottom and constant temperature at the top boundaries of rock material (details of boundary conditions are found in Section 3.4). Temperature differences between the top and bottom walls of the component air (ΔT_a) are determined by many factors and, thus, are unknown.

Wilson [unpublished note, 2004] has proposed replacement of this unknown difference ΔT_a by what we do know, but which still represents the thermal forcing, that is,

ΔT for rock (ΔT_r). Applying Fourier's Law, the temperature difference for a cavity of height L (when the cavity is replaced by the same homogeneous rock) will become:

$$\Delta T_r = \frac{q_r L}{k_r} \tag{2.11}$$

where the subscript $_r$ refers to the rock, q_r is the uniform heat flux (Wm^{-2}) at the bottom, L is the height of the cavity, and k_r is the thermal conductivity of the rock. Substituting this expression for ΔT in equation 2.10, we get a new Ra to which we have given a subscript $_1$ to distinguish it:

$$Ra_1 = \frac{\rho_a^2 \; g \; c_{pa} \; \alpha_a \; q_r \; L^4}{\mu_a \; k_a \; k_r} \tag{2.12}$$

where the subscript $_a$ refers to air. In the numerator, buoyancy becomes more sensitive to the length scale than in Ra ($Ra \propto L^3$ and $Ra_1 \propto L^4$). The denominator expresses diffusion (momentum or heat) that decreases the effects of buoyancy. Ra_1 inherits this dependence on air viscosity and air thermal conductivity from Ra, but now the denominator also connotes the term for rock thermal conductivity, k_r. Ra_1 decreases with increase in k_r, because more heat can diffuse through the rock and around the cavity, which effectively reduces buoyancy.

We will use Ra_1 to examine the convective force of our models. Applying the same theory as Ra_1, in the case of models that have only an air-filled cavity and no rock, but with constant heat flux and temperature on the bottom and top boundaries, respectively, Ra with subscript of $_2$ is:

$$Ra_2 = \frac{\rho_a^2 \; g \; c_{pa} \; \alpha_a \; q_a \; L^4}{\mu_a \; k_a \; k_a} \tag{2.13}$$

Equation (2.13) was used to estimate the characteristic lengths for $Ra_2 = 10^3$ and 10^6 in Section 1.2.

Fluid in an infinite horizontal layer will begin moving at a critical Rayleigh number ($Ra = Ra_c$). However, Ra_c is different depending on the boundary conditions (bcs). A rigid boundary has a no slip condition (velocity is zero at a rigid boundary). If cave passages are bounded by rocks, then the rigid-rigid (top bc – bottom bc) condition obtains, but if their top boundaries are the surface (physically there is no boundary, like a cave entrance), then the condition is the free-rigid state. If we focus on convection cells in a certain part of the atmosphere, it is then in the free-free condition. Laboratory experiments and theoretical analyses give the values for Ra_c depending on these boundary conditions: the free-free case = 657.5, the free-rigid case = 1101, and the rigid-rigid case = 1708. Furbish [1997, 417-418] explains the reasons for the increased values for Ra_c in the rigid boundary, "This increasing value of Ra_c reflects a stabilizing influence provided by viscous friction at the boundaries; that is, an increasing temperature variation is required to destabilize the fluid column when one, then both, of the boundaries are rigid."

Both rigid-rigid and free-rigid conditions may be appropriate to describe cave systems. However, Ra_c for these scenarios assumes that the horizontally extended layer has constant temperatures at the top and bottom boundaries, so the effects of side boundaries are negligible. In our models, the effects of side boundaries are important.

Our models also have constant heat flux at the bottom boundary and, hence, Ra_c may be different from these values discussed in the previous paragraph. We will present the values for Ra_c for cave models in Chapter 5.

Figure 2.10 shows the relationship between Rayleigh number and Prandtl number for a horizontally extensive fluid with constant temperatures at the bottom and top boundaries. Prandtl number is expressed as $Pr = C_p \mu / k$ [Hirsch, 1988, 268] or $Pr = \nu / \kappa$ with ν the kinematic viscosity (μ/ρ) and κ the thermal diffusivity ($k / C_p \rho$). Prandtl number can be viewed as the ratio of the vertical thermal diffusion time $t_v = d^2/\kappa$ to the vertical viscous relaxation time $t_\mu = d^2/ \nu$ where the d is height of the horizontal fluid layer [Bodenschatz et al., 2000]. At a given temperature, each fluid has a unique Prandtl number. For example, a typical value for the Prandtl number for air is 0.7. When the Rayleigh number (Ra) is greater than 10^4, the flow is categorized as turbulent for this Prandtl number.

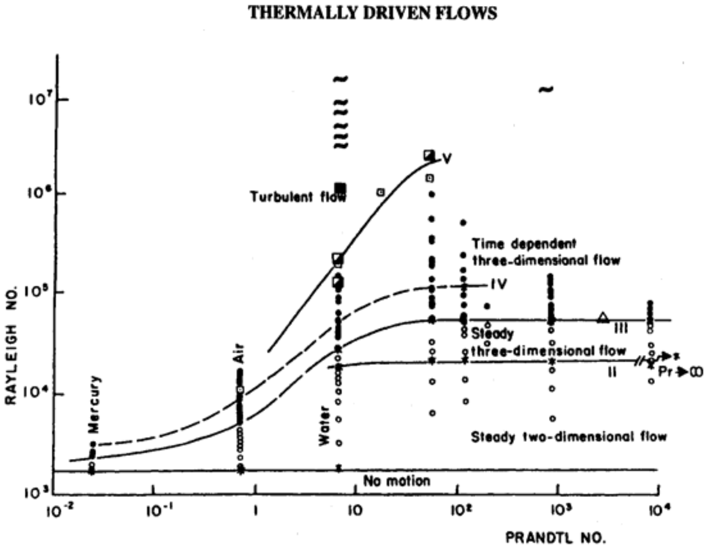

Figure 2.10: Regime diagram of Prandtl number *Pr* versus Rayleigh number *Ra* for Bénard convection (a form of convection observed in a horizontal layer of fluid heated from below with constant temperatures at the top and bottom boundaries) [Furbish, 1997, 422].

If we assume that a small model has characteristic length L = 0.5 m and the material thermal properties at 17°C, then the resulting Rayleigh number Ra_1 will be:

$$Ra_1 = \frac{(1.201)^2(9.8)(1005)(3.45e-3)(0.05)(0.5)^4}{(1.78e-5)(0.0255)(2.5)} = 134973 = 10^{5.13}.$$

If the height of a cave is 10 m, then the Rayleigh number Ra_1 will be:

$$Ra_1 = \frac{(1.201)^2(9.8)(1005)(3.45e-3)(0.05)(10)^4}{(1.78e-5)(0.0255)(2.5)} = 21595688786 = 10^{10.3}.$$

Geothermal heat is more than enough to produce convection cells, and the resulting flow should be turbulent. Hence, we think that geothermal heat flow and the thermal properties of rocks and air are critical internal factors controlling air and heat flow inside caves.

2.6 Humidity

Around the surface of the Earth, air that is not affected by pollution has a composition that is surprisingly constant [McPherson, 1993, 491]. The composition of dry air is given on both a volume and mass basis in Table 2.2. However, there is another gas present in the free atmosphere, namely water vapor. The weight of a mole of water is 18 g, which is lighter than that of dry air (28.966 g). Water vapor is rather different from the other components in that its concentration varies widely from place to place and with time. This is because the pressures and temperatures in the atmosphere encompass the ranges over which water may exist in the gaseous, liquid or solid forms [McPherson, 1993, 491].

Table 2.2: Composition of dry air. Equivalent molecular weight of dry air is 28.966 (g) [McPherson, 1993, pp492].

Gas	Volume (%)	Mass (%)	*Molecular weight (g)*
Nitrogen	78.03	75.46	28.015
Oxygen	20.99	23.19	32.000
Carbon dioxide	0.03	0.05	44.003
Hydrogen	0.01	0.0007	2.016
Monatomic gases	0.94	1.30	39.943
	100	100	

Most caves are extremely moist environments, and changes in phase of water are particularly important in cave micrometeorology. Condensation and evaporation may appear alternately by small changes in temperature, which may have important influences on cave formations or secondary cave decorations. Fogging in the subsurface occurs in two situations: when the strata are cooler than the dew point temperature of the incoming air; or as a result of decompressive cooling of humid, ascending cave air [McPherson, 1993, 514].

An interesting question is how the presence of moisture changes the Rayleigh number, thus altering the convection cells. McPherson [1993, 497-498] provides an equation for the moist air density:

$$\rho_m = \frac{p}{R_a T}(1 - 0.608X) \qquad \left(\frac{kg_{moist\ air}}{m^3}\right) \tag{2.14}$$

where ρ_m is the density of moist air (kg m^{-3}), p is the pressure (N m^{-2}), R_a is the gas constant for dry air (287.04 J kg^{-1} K^{-1}), T is the temperature (K), and X is the moisture content (kg/kg$_{\text{dry air}}$). From equation (2.14), we realize that moist air density is less than the density of dry air under the same pressure and temperature.

The presence of moisture in air affects other parameters. For example, the specific heat capacity for moist air (C_{pm}) is calculated by:

$$C_{pm} = \frac{C_{pa} + XC_{pv}}{1 + X} \qquad \left(\frac{J}{kg^{\circ}K}\right) \tag{2.15}$$

where C_{pa} is the specific heat of dry air at constant pressure (1005 J kg^{-1} K^{-1}), and C_{pv} is the specific heat at constant pressure for water vapor (1884 J kg^{-1} K^{-1}) [McPherson, 1993, 497-498]. From the expression of equation (2.15), we can see that the presence of water vapor appears to increase the specific heat.

Let's apply the same principle of equation (2.15) to estimate the dynamic viscosity of moist air:

$$\mu_m = \frac{\mu_a + X\mu_v}{1 + X} \qquad \left(\frac{Ns}{m^2}\right) \tag{2.16}$$

where μ_m is the dynamic viscosity of moist air, μ_a is the dynamic viscosity of dry air, and μ_v is the dynamic viscosity of water vapor. The dynamic viscosity of water vapor at 20°C is 9.52 x 10^{-6} Ns m^{-2} [Schmidt and Grigull, 1979]. Using equation (2.1), the dynamic viscosity of dry air at 20°C is 1.79 x 10^{-5} Ns m^{-2}. The dynamic viscosity of water vapor is less than that of dry air, and from the expression of equation (2.16), the presence of moisture in air appears to reduce the dynamic viscosity.

Figure 2.11 shows the thermal conductivity of moist air [Lasance, 2003] with respect to relative humidity and temperature. The presence of moisture in air produces a non-liner relationship between thermal conductivity and temperature. The thermal conductivity of moist air decreases with an increase of relative humidity. However, the decrease of thermal conductivity appears to be essentially negligible within the temperature range 0 – 40°C that can be observed in real caves.

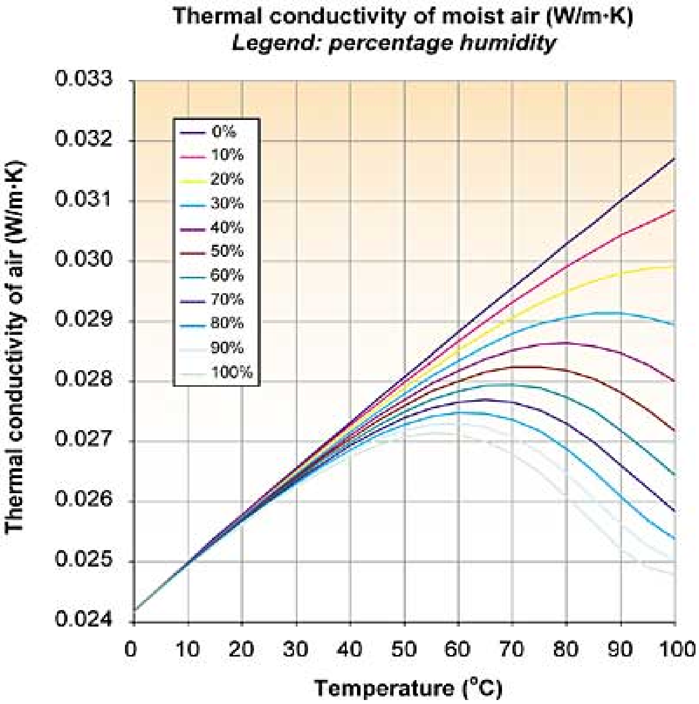

Figure 2.11: Relationship between thermal conductivity and moist air with respect to relative humidity and temperature [Lasance, 2003].

Moreover, we do not expect large values for moisture content *X*. The saturation vapor pressure is calculated by [McPherson, 1993, 494-496]:

$$e = 610.6 * \exp\left(\frac{17.27 * T}{T + 237.3}\right) \qquad (Pa) \tag{2.17}$$

where *T* is in °C, and the moisture content is estimated by:

$$X = 0.622 * \frac{e}{P - e} \qquad \left(\frac{kg}{kg_{dry\,air}}\right) \tag{2.18}$$

If we assume a relative humidity of 100% at temperature of 20°C and pressure of 100 kPa, then using equations (2.17) and (2.18), the saturation vapor pressure *e* is 2337.5 Pa, and the moisture content *X* becomes 0.0149 (kg/ $kg_{\text{dry air}}$); corresponding specific heat capacity is 1018 J kg^{-1} K^{-1}, air density is 1.178 kg m^{-3} (density of dry air is 1.189 kg m^{-3}), and dynamic viscosity is 1.78 x 10^{-5} Ns m^{-2}. Even if we consider the saturated situation, the effects of moisture on thermal properties of air are relatively small.

The thermal expansion coefficient α for ideal gas is obtained by [Furbish, 1997, 98]:

$$\alpha = \frac{1}{\rho}\frac{p}{R_a T^2}; \quad \rho = \frac{p}{R_a T}; \quad \alpha = \frac{1}{T} \tag{2.19}$$

Let's apply the same principle to obtain the thermal expansion coefficient for moist air (α_m) using moist air density (ρ_m):

$$\alpha_m = \frac{1}{\rho_m}\frac{p}{R_a T^2}\ ; \quad \rho_m = \frac{p}{R_a T}(1-0.608X)\,; \quad \alpha_m = \frac{1}{(1-0.608X)\,T} \tag{2.20}$$

Using equations (2.19) and (2.20), and the moisture content X = 0.0149 (kg/ kg $_{\text{dry air}}$), the thermal expansion coefficients for dry air and saturated air at 20°C with pressure of 100 kPa become 3.41 x 10^{-3} (K^{-1}) and 3.44 x 10^{-3} (K^{-1}), respectively.

Now we shall calculate the value for the Rayleigh number of our small models with saturated air (Ra_{1m}) at temperature 20°C and pressure 100 kPa. We assume that the thermal conductivity of saturated air is the same as that of dry air.

$$Ra_{1m} = \frac{(1.178)^2(9.8)(1018)(3.44e-3)(0.05)(0.5)^4}{(1.78e-5)(0.0255)(2.5)} = 131151 = 10^{5.12}\,.$$

The Rayleigh number for dry air (Ra_{1d}) at temperature 20°C and pressure 100 kPa is:

$$Ra_{1d} = \frac{(1.189)^2(9.8)(1005)(3.41e-3)(0.05)(0.5)^4}{(1.79e-5)(0.0255)(2.5)} = 130025 = 10^{5.11}\,.$$

The Rayleigh number for dry air is slightly smaller than that of saturated air when the other conditions are kept the same.

Furbish [1997, 155 - 156] provides a useful criterion for the temperature gradient required for an ideal gas column to spontaneously overturn, the so-called *autoconvective lapse rate*:

$$\frac{dT}{dZ} < -\frac{g}{R} = -0.0341 \quad \left(\frac{K}{m}\right) \tag{2.21}$$

where g is the gravitational acceleration 9.8 m s^{-2}, and R is the gas constant for dry air 287.04 J kg^{-1} K^{-1}. McPherson [1993, 497] gives an equation for the gas constant for moist air (R_m):

$$R_m = 287.04 \frac{p}{p - 0.378e} \quad \left(\frac{J}{kg\ K}\right) \tag{2.22}$$

Assume p = 100 kPa and e = 2337.5 Pa (saturation vapor pressure at 20°C), the value for R_m becomes 289.60 J kg^{-1} K^{-1}. Then, the estimated autoconvective lapse rate for moist air is - 0.0338 K m^{-1}. The magnitude of the autoconvective lapse rate for saturated air at 20 °C is slightly less than in the case of dry air and, thus, moist air requires slightly less temperature difference to spontaneously overturn than in the dry case. The Rayleigh number and the autoconvective analyses agree. At the surface, because moist air is lighter than dry air, the humidity may assist in the upward movement of air, accompanied by higher temperatures of air or water bodies and, hence, we appreciate global water circulation.

In deep cave systems, humidity tends to be high and its fluctuation is small, except near the entrance area, where the surface and subsurface systems interface. Colder atmospheric air selectively sinks into caves through their entrances, for example, in winter time or at night. The gradients of temperature and humidity may be steep in the vicinity of cave entrances, which may have a significant impact on cave micrometeorology.

Humidity is an important factor in cave meteorology. However, in this study, we are focusing on internal dynamics, and seeking the internal factors that create cave micrometeorological processes. Due to technical difficulties, the direct effects of humidity due to latent heat effects are ignored in our computer models. The indirect effects, by influencing physical properties, could be considered in our models, but we neglected them, too. (Our investigation of this influence suggests that it is not important for cave conditions.) Although it is only a rough estimation, based on Rayleigh number and the autoconvective lapse analyses with dry and moist air, we suggest that humidity does not have an important indirect role in altering the internal convection cells; rather, the airflow created by cave geometries or other factors may affect the local humidity [e.g., Forbes, 1998].

2.7 Others

The presence of liquid water is an important factor in cave micrometeorology. For example, if the temperature of a cave pool is lower than the wet bulb air temperature (temperature at which unsaturated air becomes saturated), the water will provide a cooling effect on the airflow [McPherson, 1993, 563]. Chemical reactions can also be associated with heat exchanges as exothermic or endothermic effects. Human activities in commercial caves may also add heat or introduce airflow. For example, visitors and lights may add heat to cave air, and an elevator may pump surface air into caves effectively. There may be other unknowns. All these factors are not considered in our computer models developed here.

CHAPTER 3

MODELING CAVE AIR AND HEAT FLOW

3.1 FEMLAB Computer Software

FEMLAB, a computer software package developed by COMSOL AB, is a powerful interactive environment for modeling and solving all kinds of scientific and engineering problems based on partial differential equations [COMSOL AB, 2004a, 5]. As our primary purposes in this research are to observe the effects of geothermal heat flow, cave geometry, and thermal properties of rock and air on cave micrometeorology, the flow equations and heat balance equation are strongly coupled. FEMLAB has been chosen because it performs equation-based multiphysics modeling using the finite element method and, thus, it can solve the coupled Navier-Stokes (fluid flow) and heat balance equations (convection and conduction equation).

3.2 Navier-Stokes and Heat Balance Equations

The governing equations for our modeling are the incompressible Navier-Stokes equations and the heat balance (convection and conduction) equation. The incompressible Navier-Stokes equations are applied to the air-phase only. The heat balance equation is applied to both the air-phase (caves) and the rock that surrounds the caves. The incompressible Navier-Stokes equations consist of the momentum balance equation (3.1) and the equation for the conservation of mass (the continuity equation) (3.2):

$$\rho \frac{d\mathbf{u}}{dt} - \nabla \cdot [\mu(\nabla \mathbf{u} + (\nabla \mathbf{u})^T)] + \rho(\mathbf{u} \cdot \nabla)\mathbf{u} + \nabla p = F \tag{3.1}$$

$$\nabla \cdot \mathbf{u} = 0 \tag{3.2}$$

The steady state heat balance equation is expressed by:

$$\nabla \cdot (-k \nabla T + \rho C_p T \mathbf{u}) = 0 \tag{3.3}$$

where μ is the dynamic viscosity; ρ is the density; $\mathbf{u}$ is the velocity field which contains velocity components that depend on the dimensions of the geometry (e.g. 2D or 3D); p is the pressure; F is a volume force field such as the gravitational force; k is the thermal conductivity; T is the temperature; and C_p is the specific heat capacity [COMSOL, 2004b, 53]. Equation (3.1) is a generalized version of the momentum equation that FEMLAB uses to allow variable viscosity. Equations (3.1) and (3.2) describe incompressible flow, so the density is assumed to be constant.

The dimension of the equation (3.1) is force per unit volume for 3 D, so if we multiply equation (3.1) by the volume, dimension of all terms becomes the product of mass and acceleration, that is, force, or the rate of change in momentum. In a frictionless system, if there is no force acting on the fluid, the velocity of that fluid is not accelerating. On the left hand side of equation (3.1), the first term is the rate of change in momentum with respect to time (M_1); the term inside the brackets of the second term is called the *viscous stress tensor* (τ); the third term is the rate of change in momentum with respect to space (M_2); and the fourth term is pressure gradient (∇p). The expression of $- pI + \tau$, where I is the identity matrix, is called the *total stress tensor* (σ) that is a sum of normal stress ($-pI$) and tangential stress (τ) acting on the fluid surface [Reddy and Gartling, 2001, 150].

The pressure gradient arises due not only to gravitational pressure gradient, but also due to changes in internal energy caused by fluid movements. The models in this study ignore the gravitational pressure gradient, so ∇p describes only the change in pressure caused by fluid movement. Work performed against friction alters internal energy, resulting in the change in pressure [Furbish, 1997, 267-268]. The right hand side of the equation represents the body forces (F). The body force in our models is a buoyancy force that acts in the opposite direction to the gravitational force. Equation (3.1) tells us that $M_{(1+2)} = \nabla \cdot \sigma + F$: the rate of change in momentum (time + space) equals the sum of surface force and body force [Furbish, 1997, 266]. The term $\rho(\mathbf{u} \cdot \nabla)\mathbf{u}$ shows non-linearity, in which the components of vector **u** (solutions of the equation) are multiplied by a function of themselves [Valentine et al., 2002].

The continuity equation shows that fluid mass flowing into a control volume, such as a cave, must be compensated by mass flowing out of the control volume, or by a change in the density of the fluid within the volume, or some combination of both [Furbish, 1997, 178-179]. Equation (3.2) is the continuity equation for the case of incompressible fluid flow that assumes that the density of fluid is constant. Thus, the volumetric flow in equals the volumetric flow out.

Ideally, we would like to use density as a function of temperature, but density variation makes models more complicated. In that case, equations (3.1) and (3.2) would be replaced with more sophisticated non-linear coupled conservation equations, which could be difficult to solve. Assuming that air is incompressible, and using the Boussinesq approximation (see Section 3.3) the change in air density with respect to temperature is considered by the calculation of the thermally-induced buoyancy body forces (F_y) expressed by:

$$F_y = \rho\, g\, \alpha\, (T-T_0) \tag{3.4}$$

where α is the thermal expansion coefficient (K^{-1}), T is the temperature (K), and subscript $_y$ denotes the vertical direction (y axis for 2D models). The buoyancy force is applied only in the vertical direction. Models are run assuming a steady state in which the force does not change with respect to time, so the change in fluid momentum associated with time (M_1) vanishes in steady state simulations.

Equation (3.3) is a steady state heat balance equation, applied in both air and rock phases. The first term inside the bracket of the left hand side is a conductive term and the second is a convective term. The dimension of the equation is watts per unit volume for 3D. The theory of the equation is analogous to the theory of conservation of mass, that is, the heat energy flowing into the control volume must be compensated by the heat energy flowing out of the control volume. Equations (3.1), (3.2), and (3.3) are strongly coupled: a change in temperature induces a change in velocity, a change in velocity in one direction changes the velocity of other directions, and change in velocity changes the temperature. FEMLAB is capable of computing a solution for equations (3.1) thru (3.4) using the finite element method. However, the equations are extremely non-linear, and sometimes, for computational reasons, there are multiple solutions or no solution.

3.3 Boussinesq Approximation

The Boussinesq approximation for coupled fluid flow and heat transfer represents two important ideas. First, any fluctuations in density that arise with the onset of fluid motion are formed mainly by thermal effects rather than by pressure effects. Second, all variations in fluid properties, except density, may be neglected; and variations in density may be neglected except to the extent that they are coupled with buoyancy forces. Spiegel and Veronis [1960] point out that the important objective in justifying the Boussinesq approximation is "to demonstrate that the equations governing convection of an ideal gas are equivalent to those for an incompressible fluid, modified to consider that the important temperature gradient is that in excess of the adiabatic lapse rate." Thus, the approximation depends on two conditions: (1) the vertical dimension of the fluid system must be much less than any characteristic scale height; and (2) any fluctuations in pressure and density induced by fluid motions must not exceed the total variations in these quantities in the static state [Furbish, 1997, 406]. For our application, we must determine whether we can apply the Boussinesq approximation to a real cave system like Carlsbad Cavern.

(1) The Vertical Dimension of the Fluid System must be Much Less than Any Characteristic Scale Height

The characteristic scale heights z_p, z_T, and z_ρ are defined by:

$$z_p = \left| \frac{1}{p_m} \frac{dp_s}{dz} \right|^{-1}; \qquad z_T = \left| \frac{1}{T_m} \frac{dT_s}{dz} \right|^{-1}; \qquad z_\rho = \left| \frac{1}{\rho_m} \frac{d\rho_s}{dz} \right|^{-1} \tag{3.5}$$

where p_m, T_m, and ρ_m denote constant, spatially averaged values; and p_s, T_s, and ρ_s are variations about the average state in the absence of motion (static condition). Each scale height is a measure of the distance over which the defining state variable is vertically uniform. For instance, z_ρ is a measure of the distance over which the density of the fluid varies by a fraction of order of unity. The vertical dimension of fluid system z should be much less than z_ρ, which provides the expression of $1/z_\rho << 1/z$. Substituting the definition of z_ρ (3.5) into the expression of $1/z_\rho << 1/z$, and integrating these over the height z leads to the condition of $\Delta\rho_s / \rho_m << 1$, in which $\Delta\rho_s$ is the maximum variation over the distance z [Furbish, 1997, 407]. Therefore, the condition (1) necessitates that the maximum variations (Δp_s, ΔT_s, and $\Delta\rho_s$) over the distance z are very small compared to the spatially averaged values (p_m, T_m, and ρ_m).

The elevation of the Lunch Room in Carlsbad Cavern is 1113m [Hill, 1987, 27] and that of the Lake of Clouds (the deepest point of the cave system) is 1007m [Hill, 1987, Sheet 2]. In September of 1969, the temperatures around the Lunch Room and the Lake of Clouds areas were 14.5 °C and 19.6°C, as observed by McLean [1971]. McLean also observed airflow velocity of 0.05 m s^{-1} in Lunch Room [Hill, 1987, 29]. Using the available information, the values for p_m, T_m, ρ_m, p_s, T_s, and ρ_s in the case of Carlsbad Cavern were estimated assuming dry air (Table 3.1 and 3.2). The dry air pressure and density were estimated using the 1976 Standard Atmospheric Calculator developed by Digital Dutch [2003].

Table 3.1: Dry air density, dry air pressure and airflow velocity in Lunch Room and Lake of Clouds of Carlsbad Cavern in September 1969.

	Elevation (m)	*Airflow ($m\ s^{-1}$)*	*Temperature (K)*	*Pressure ($N\ m^{-2}$)*	*Density ($kg\ m^{-3}$)*
Lunch Room	1113	0.05	14.5 + 273	88.65 x10^3	1.074
Lake of Cloud	1007	-	19.6 + 273	89.80 x10^3	1.069

Table 3.2: Parameters for the characteristic scale heights.

dz (m)	*dT_s (K)*	*T_m (K)*	*dp_s ($N\ m^{-2}$)*	*p_m ($N\ m^{-2}$)*	*$d\rho_s$ ($kg\ m^{-3}$)*	*ρ_m ($kg\ m^{-3}$)*
106	5.1	290.05	1.15 x10^3	89.23 x10^3	0.005	1.072

$$Z_p = \left| \frac{1}{p_m} \frac{dp_s}{dz} \right|^{-1} = \left| \frac{1}{89.23e3} \frac{1.15e3}{106} \right|^{-1} = 8225\,m \ \ >> dz = 106\,m$$

$$Z_T = \left| \frac{1}{T_m} \frac{dT_s}{dz} \right|^{-1} = \left| \frac{1}{290.05} \frac{5.1}{106} \right|^{-1} = 6028\,m \ \ >> 106\ m\text{, and}$$

$$Z_\rho = \left| \frac{1}{\rho_m} \frac{d\rho_s}{dz} \right|^{-1} = \left| \frac{1}{1.072} \frac{0.005}{106} \right|^{-1} = 22726\,m >> 106\ m$$

The vertical distance between the Lunch Room and Lake of the Clouds (106 m) is much less than any characteristic scale heights. Thus, we consider that real cave systems adequately satisfy the condition (1) of the Boussinesq approximation.

(2) Any Fluctuations in Pressure and Density Induced by Fluid Motions Must Not Exceed the Total Variations in these Quantities in the Static State

Using equation (2.4) we can calculate the fluctuation of pressure within the Lunch Room due to a change in velocity from 0.05 m s^{-1} to 0 m s^{-1}, assuming a frictionless system:

$$\rho_m \frac{u_1^2 - u_2^2}{2} = 1.063 \frac{0.05^2 - 0}{2} = 0.00133 \ \ N\,m^{-2} << \ dP_s = 1.11x10^3 \ N\,m^{-2}.$$

Modifying equation (2.11) and applying the calculated fluctuation of pressure, we can estimate the fluctuation of density due to the change in velocity from 0.05 m s^{-1} to 0 ms^{-1}:

$$\Delta\rho = \frac{\Delta P}{R_a T_m} = \frac{0.00133}{287.04 * 290.05} = 1.597x10^{-8} \ kg\,m^{-3} << \ d\rho_s = 0.005 \quad kg\,m^{-3}.$$

The fluctuation of pressure and density induced by fluid motions observed within Carlsbad Cavern are much less than those in the static state. Real cave systems satisfy condition (2) of the Boussinesq approximation.

Thus, we can apply the Boussinesq approximation to describe airflow in real cave systems, that is, air density is assumed to be constant, except when it is coupled with buoyancy forces.

3.4 Model Conditions

The schematic diagram of model conditions is shown in Figure 3.1. The following subsections describe the details of these conditions.

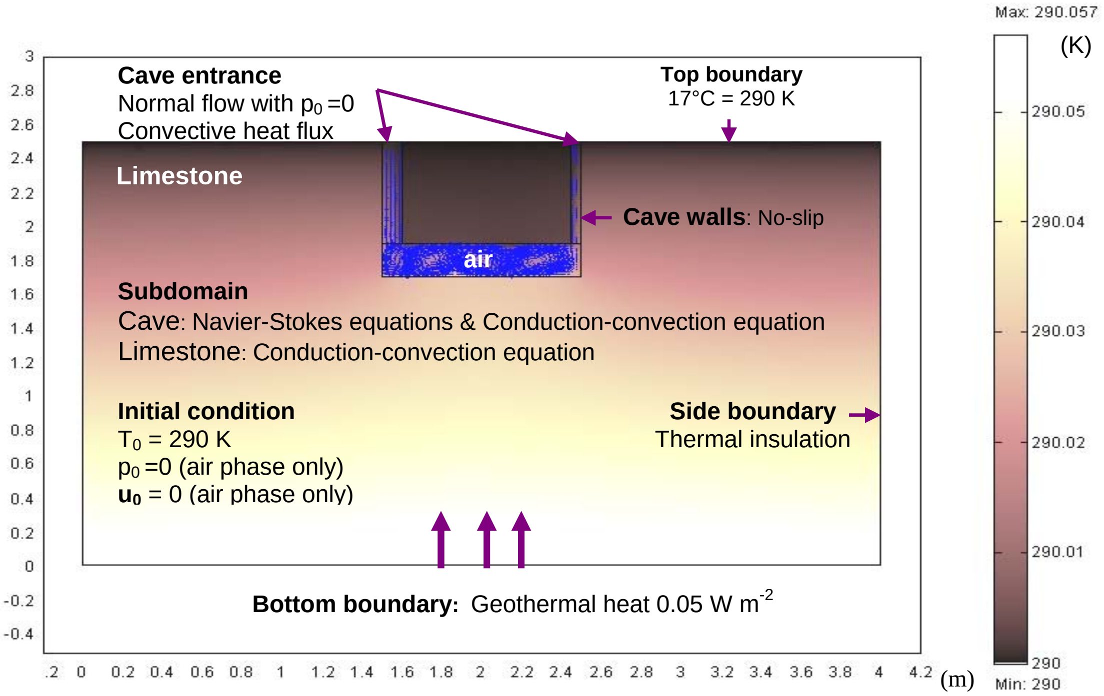

Figure 3.1: Schematic diagram of model conditions for a horizontal cave with two vertical entrances. The diagram shows surfaces indicating temperature (K), and arrows indicating the velocity field (m s^{-1}).

3.4.1 Material Properties

Table 3.3 shows material properties assigned to the subdomains of the air and limestone components of the models (see equations 3.1 thru 3.3).

Table 3.3: Thermal properties of air and limestone

Material	ρ (kg m^{-3})	μ (N s m^{-2})	k (W m^{-1} K^{-1})	C_p (J kg^{-1} K^{-1})	α (K^{-1})
Air	1.201	1.78 x10^{-5}	0.0255	1005	3.45x10^{-3}
Limestone	2500	-	2.5	834	-

Air density (ρ) was obtained using equation (2.8) assuming dry air with an absolute temperature of 290 K and static pressure of 100 kPa. Dynamic viscosity of air (μ) was calculated by equation (2.1) assuming temperature of 17°C. Thermal conductivity of air (k_a) was calculated by:

$$k_a = 2.2348 \times 10^{-4} \times T^{0.8353} \tag{3.6}$$

where T is an absolute temperature of 290°K [Hemp, 1982]. The specific heat capacity (C_p) of dry air has been determined by McPherson [1993, 498]. According to McPherson [1993, 54], "Although no real gas conforms exactly to [the definition of the ideal gas], the mixture of gases that constitute air behaves in a manner that differs negligibly from an ideal gas within the ranges of temperature and pressure found in subsurface ventilation engineering." Hence, we treat air as an ideal gas. The thermal expansion coefficient (α) was obtained by $\alpha = 1/T$ (assuming air as an ideal gas), where T is 290 K [Furbish, 1997, 98]. In the air-phase model components, the volume force was assigned to the vertical direction (y axis) as a thermally-induced buoyancy force expressed by $F_y = \rho\ g\ \alpha\ (T-T_0)$, where g is the gravitational acceleration (9.8 m s^{-2}).

According to Turcotte and Schubert [1982, 432], the density of limestone ranges from 2200 kg m^{-3} to 2800 kg m^{-3}; and the thermal conductivity of limestone ranges from 2.0 Wm^{-1} K^{-1} to 3.4 Wm^{-1} K^{-1}. According to Spinelli [class note, 2004], the typical values for the density and thermal conductivity of limestone are 2500 kg m^{-3} and 2.5 W m^{-1} K^{-1}, respectively. Here we use a limestone density estimate of 2500 kg m^{-3} and assign the thermal conductivity of limestone as 2.5 W m^{-1} K^{-1}. The specific heat capacity of limestone was calculated based on the specific heat capacity of calcite [Dean, 1999, 3.21 and 6.87]:

$$\frac{83.5J}{K\ mol} \cdot \frac{1\,mol\ CaCO_3}{0.1\,0009kg} = 834 \quad \left(\frac{J}{K\ kg}\right)$$

The typical value for heat capacity of limestone is 800 (J K^{-1} kg^{-1}) [Spinelli, class note, 2004], and that of Indiana limestone is 900 (J K^{-1} kg^{-1}) [Bejan, 1995, 587], so the above calculation is a close enough value for our purpose.

3.4.2 Initial and Boundary Conditions

(1) Incompressible Navier-Stokes Equations As Applied to Cave Model Components

a. Initial condition

$u(t_0) = 0$, $v(t_0) = 0$, and $p(t_0)=0$.

As an initial condition of the subdomain of air-filled components, the airflow velocities in both the horizontal (*u*) and vertical (*v*) directions are zero. The models in this study are two dimensional, so the third velocity component (*w*) is neglected. The initial pressure is also assumed to be zero. Airflow and pressure change occur as a result of the buoyant force acting in the vertical direction. Here, the static pressure variation is ignored based on the Boussinesq approximation (see Section 3.3).

b. Boundary conditions

(i) Cave walls: No slip $\mathbf{u} = 0$

Airflow velocity at the cave walls is zero, because air is a viscous fluid.

(ii) Cave and atmosphere interface and boundary of a side passage

Normal flow /Pressure

$\mathbf{t} \cdot \mathbf{u} = 0$

$$p = p_0$$

$$\mathbf{n} \cdot \tau = 0$$

Normal vector (**n**) is in a direction perpendicular to the boundary, towards the outside is positive and towards the inside is negative, relative to the domain. Basically, there is no resistance at either a cave entrance or the boundary of a side passage, thus air can move in or out depending upon the pressure gradient relative to the reference pressure assigned, namely zero. The tangential components (**t**) of velocity are also zero, which means that air flows only in the normal direction. Further, the normal component (**n**) of the viscous forces tensor (τ) is zero [COMSOL AB, 2004b, 56-58].

(2) Convection-Conduction Equation – As Applied to Both Air and Limestone

a. Initial condition

$$T(t_0) = T_0 = 290\ K$$

Both air and limestone are at a temperature of 290 K as an initial condition. The temperature can then be changed by convection and conduction of geothermal heat.

b. Boundary conditions

(i) Top boundary

$$T = T_0 = 290\ K$$

A temperature of 290 K was chosen based on the average surface temperature of the region in the vicinity of Carlsbad Cavern [Carlsbad Caverns Bat Cave Draw Weather Station, 2004].

(ii) Bottom boundary: Normal heat flux boundary

$$\mathbf{q}_0 = 0.05\ W\ m^{-2}$$

$$-\mathbf{n} \cdot \mathbf{q} = \mathbf{q}_0$$

$$\mathbf{q} = -k\nabla T + \rho C_p T\mathbf{u}$$

The normal heat flux of 0.05 Wm^{-2} was estimated from information in Section 2.5. The negative sign of the normal flow component indicates that heat flows into the domain. The third equation tells us that heat flow could occur both by conduction and convection, although convection only occurs if the fluid is in direct contact with boundary, as would be the case for a cavity only model.

(iii) Cave entrance boundaries: Convective flux boundaries

$$\mathbf{n} \cdot \mathbf{q} = 0$$
$$\mathbf{q} = -k\nabla T$$

A cave entrance is signified by the case where convection across a boundary is much greater than heat diffusion. The convective flux boundary sets the diffusive flux at the boundary to zero, but it allows convective flux to exit the domain [COMSOL AB, 2004b, 149].

(ix) Side boundaries: Thermal insulation boundaries

$$-\mathbf{n} \cdot \mathbf{q} = 0$$
$$\mathbf{q} = -k\nabla T + \rho C_p T \mathbf{u}$$

When the cave is isolated inside the rock mass, as it almost always is in these simulations, there is no convection at the boundaries. In that case, the convective term, $\rho\ Cp\ T\ \mathbf{u}$ vanishes. In that case, the conditions that describe thermal insulation occur when the gradient across the boundary is zero and, thus, the temperature on one side of the boundary must equal the temperature on the other side. Heat cannot transfer across the boundary, because there is no temperature difference across it [COMSOL AB, 2004b, 144].

3.4.3 Nonlinear, Parametric Nonlinear, and Time-Dependent Solvers

The nonlinear solver of FEMLAB solves non-linear equations, but sometimes the models do not converge with the solver; in such cases we then try the parametric nonlinear solver or the time-dependent solver of FEMLAB [COMSOL AB, 2004a, 227-236, 240-241].

The parametric nonlinear solver of FEMLAB also helps us find the solution to a sequence of nonlinear stationary partial differential equations. The parametric nonlinear solver in FEMLAB specifies a parameter vector of increasing or decreasing value (e.g., 0:0.1:1) [COMSOL AB, 2004a, 240-241]. We have specified the name of the parameter as 'damp', and assigned its values as 0:0.1:1. The parameter 'damp' was applied to the buoyancy force, such as $F_y = damp\ \rho\ g\ \alpha\ (T-T_0)$. By doing this, the buoyancy force is applied gradually from zero to 100% with a step size of 10%. In each step, the models solve the equations by iteration. When the damp parameter reaches the value of 1, then 100% of the buoyancy force is applied to the models and the models then hopefully converge.

Sometimes the time-dependent solver or the parametric solver of FEMLAB can work in relatively large models. When the time-dependent solver was used, we applied it for a sufficiently long period of time so that results could be considered steady state. However, this author experienced file breakdown in the time-dependent solver when a model was too large. The time-dependent solver appears to use a very large amount of computer memory. When a model was run with the time-dependent solver, the file size tended to be larger than 100 MB (e.g., the file size of the model in Figure 6.9 is 106 MB when run with the time-dependent solver), whereas the file is only about 1 MB with the non-linear solver and similar geometry as the model (e.g., the file size of the model in Figure 5.37 is 987 KB when run with the non-linear solver).

3.4.4 Incompressible Navier-Stokes, Non-Isothermal, and k-ε Modes of FEMLAB

There are three options in FEMLAB that deal with incompressible fluid flow: the incompressible Navier-Stokes mode, the non-isothermal flow mode, and the k-ε mode. The non-isothermal flow mode is almost identical to the incompressible Navier-Stokes mode, except that the continuity equation and the time-derivative in the flow equation include the density term [COMSOL AB, 2004c, 48]. If we set a constant density, the governing equations of the two modes should be the same. The k-ε mode deals with turbulent flow ($Ra > 10^4$ based on the general Rayleigh number, equation 2.7) closure, and adds two more equations in addition to the Navier-Stokes equations: the equation for the turbulent kinetic energy (k), and the equation for dissipation rate of turbulence energy (ε) [COMSOL AB, 2004c, 85-104]. In high *Ra*, heat transfer takes place only in the vicinity of walls, in the boundary layer, and the temperatures far from walls or inside convection cells are relatively uniform due to mixing by turbulence [Bejan, 1995, 252-256]. The k-ε mode identifies the height of the boundary layer and allows us to choose a logarithmic wall function instead of a no-slip boundary for walls, which accounts for the fluctuations resulting in turbulence in the thin boundary layer near the walls. The k-ε mode is an attractive approach for studying turbulent flows, but it has limitations, such as in the description of rotating flows where the model often shows poor agreement with experimental data [COSOL AB, 2004c, 107]. Figures 3.2 thru 3.4 are example models that have very similar conditions but were run by the three different modes of FEMLAB:

the incompressible Navier-Stokes mode, the non-isothermal mode, and the k-ε mode, respectively. In the models, the height of the caves (*H*) is 1m, the width 3*H*, and the top, side and bottom boundaries are located at 2*H*, 4*H*, and 4*H* from the caves, respectively. The positions of the side and bottom boundaries were chosen so that these boundaries do not have influence from the insulation effects of the caves. The top boundary was selected so that the depths of the caves are twice as much as the heights of the caves. Figures 3.2 thru 3.4 show contour lines for temperature and surfaces for velocity fields in the vicinity of caves. The Ra_1 (based on *H)* is $10^{6.33}$ which suggests that turbulent flow should likely be present. This cave size is the maximum that we can simulate using FEMLAB 3.1 at this moment. (Later in Chapter 5, the same model as Figure 3.3 is used to consider the effects of speleothems.)

Flow patterns are slightly different from each other. In Figures 3.2 and 3.3, velocity at the walls is zero because the no-slip condition is applied there, whereas in Figure 3.4, flows are also observed very near the walls (the minimum velocity greater than zero). However, there is a reason to believe that the wall functions in the k- ε model are inappropriate for this problem. The other two models produced organized convection cells without additional visible eddies. It is difficult to identify whether the flow is turbulent or laminar from two dimensional models. If we see the organized convection cells without additional eddies in the models, the models appear to create laminar flow fields, despite the relatively high Ra_1. If we focus on the temperature contour lines, especially in Figure 3.3, they appear to be well mixed, and temperature inside the cave domain appears to be relatively uniform, indicating the produced flow fields could be turbulent.

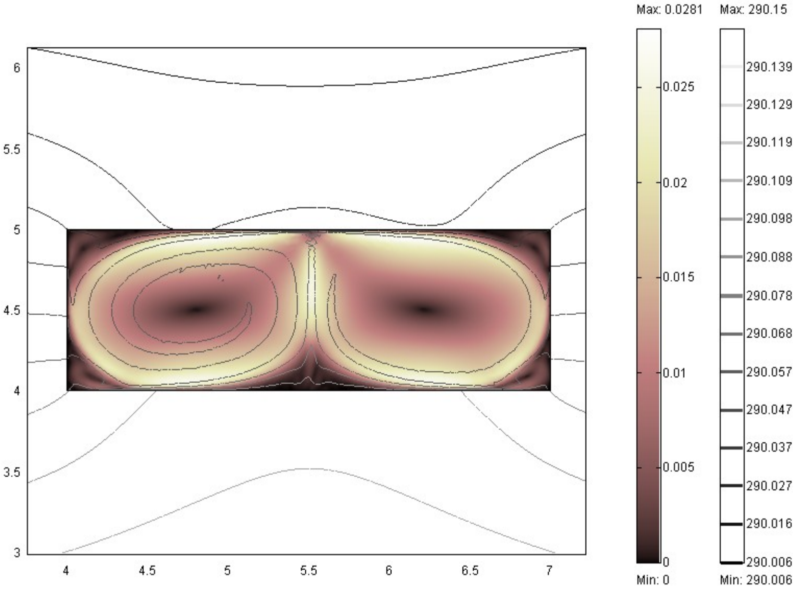

Figure 3.2: Flow simulation using the incompressible Navier-Stokes mode. The cave height *H* = 1m, and width is 3*H*. The Ra_1 based on *H* is $10^{6.33}$. The cave walls have a no-slip condition. The model shows contour lines indicating temperature (K) and surfaces indicating velocity field (m s^{-1}).

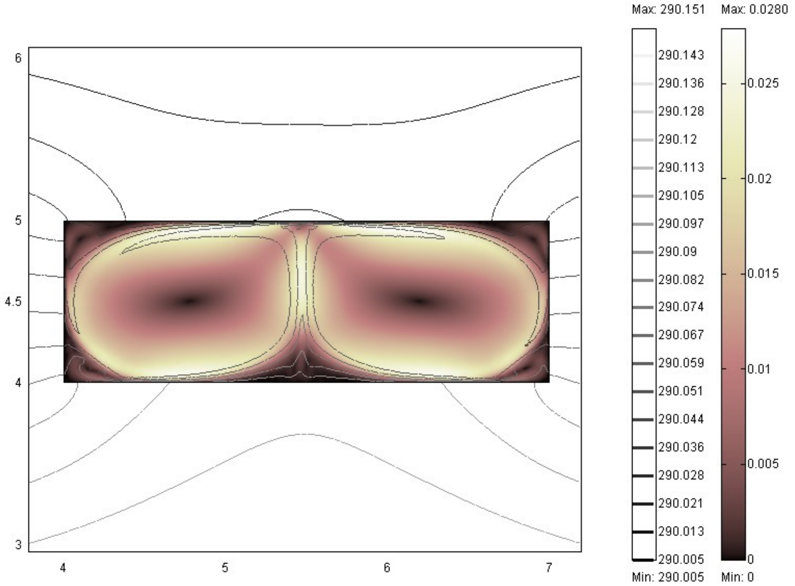

Figure 3.3: Flow simulation using the non-isothermal mode. The cave height *H* = 1m, and width is 3*H*. The Ra_1 based on *H* is $10^{6.33}$. The cave walls have a non-slip condition. The model shows contour lines indicating temperature (K) and surfaces indicating velocity field (m s^{-1}).

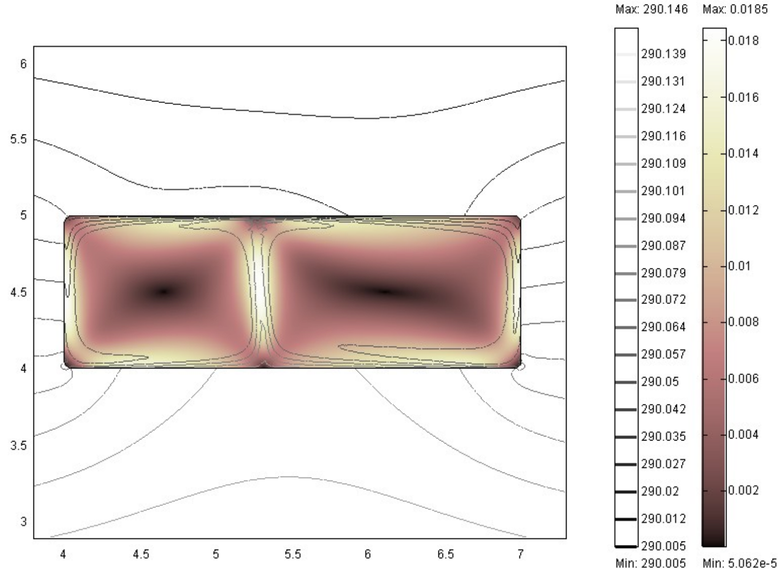

Figure 3.4: Flow simulation using the k-ε mode. The cave height H = 1m, and width is 3H. The Ra_1 based on H is $10^{6.33}$. The cave walls have a logarithmic wall function. The four corners of the cave structure were rounded with a radius of 0.05m so that the logarithmic wall function could work. The model shows contour lines indicating temperature (K) and surfaces indicating velocity field (m s^{-1}).

Table 3.4: Flow simulations by different modes of FEMLAB. L is the length of the bottom boundary (11H, where H = 1m), and q is the heat flux of 0.05 Wm^{-2}. InNS, NonIso, and k-ε stand for the incompressible Navier-Stokes, non-isothermal and k-ε modes, respectively.

Model	*mode*	*Num. of elements*	*Deg. of freedom*	*Simula. time (s)*	[1]*Avg. velocity (m s^{-1})*	[2]*Avg. temp. (K)*	[3]*Boundary integration (Bi) (Wm^{-1})*	[4]*Error* $\left\|\frac{Bi}{qL}\right\|100(\%)$
F 3.1	InNS	5981	28390	266	1.234×10^{-2}	290.058	-8.568×10^{-5}	1.558×10^{-2}
F 3.2	NonIso	5961	28332	258	1.233×10^{-2}	290.058	1.165×10^{-3}	2.118×10^{-1}
F 3.3	k-ε	5969	35907	1243	7.693×10^{-3}	290.059	-2.557×10^{-2}	4.648

1. Average velocity is the spatial average velocity that is calculated by integrating the velocity field in the cave domain, and dividing the value by the area of the cave domain.
2. Average temperature is the spatial average temperature that is calculated by integrating the temperature in the cave domain, and dividing the value by the area of the cave domain.
3. *Bi* is the normal total heat flux integrated over the entire model boundary. When models do not have entrances, the normal total heat flux is essentially the same as the normal conductive heat flux. When models have entrances, the normal total heat flux includes both convective and conductive heat fluxes. Because the continuity equation is applied to our models, *Bi* should be zero if there is no error, that is, all heat introduced to models move out of the models. Thus, the values of *Bi* reflect the total heat flux errors.
4. The error was calculated by taking the total heat flux error (as the boundary integration *Bi*) and dividing by the total applied heat flux (*qL*).

Table 3.4 provides a summary of the models. In the following, all average velocities and temperatures, boundary integrations, and errors are calculated in the same manner as in Table 3.4, except when models have entrance passages (see the explanations presented following Table 5.9).

The k-ε mode requires a longer simulation time with larger degrees of freedom and, thus, the computational cost of the k-ε mode is much higher than the other modes. The average temperatures amongst the three models are very similar. On the other hand, the average velocity field of the k-ε mode is slightly lower than the other cases. The following models (which are smaller than above examples) are run using the non-isothermal mode or the incompressible Navier-Stokes mode, both of which appear to be more flexible than the k-ε mode: they work better for complicated geometries, such as those that include speleothems or entrance passages; the parametric non-linear solver works well in the incompressible Navier-Stokes mode; and the time-dependent solver works well in the non-isothermal mode.

CHAPTER 4

PROBLEMS ASSOCIATED WITH MODELING

4.1 Two Dimensional Models with Highly Simplified Geometries

Two dimensional models (e.g., Figure 4.1) assume that the entire 2D geometry has the same, sufficiently large width (e.g., Figures 4.2). However, real caves have irregular shapes with a variety of widths. Ideally, we would like to create 3D models, but it is impossible at this moment, because it requires very large computer memory currently unavailable to us. Although, 2D models cannot represent real cave geometries, they may give us valuable clues to understand the effects of some particular factors, such as the effects of side passages on flow patterns.

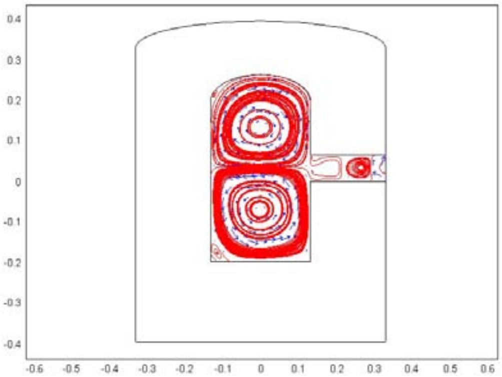

Figure 4.1: An example of a 2D model.

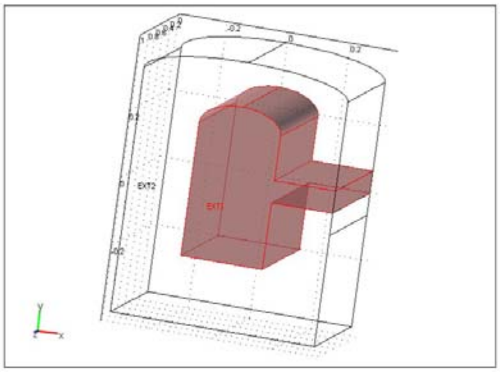

Figure 4.2: The 3D image of the 2D model in Figure 4.1.

Geometries of real cave systems are extremely complicated, and it is a very difficult task for computer models to approach the geometries of real systems. The constructed models in Chapter 5 and 6 have highly simplified geometries, which could produce some serious problems when we interpret them. However, the highly simplified models also provide a chance to focus on some specific aspects of real systems, such as the effects of the presence of stalactites or stalagmites on temperature and velocity as well as flow patterns. We would like to treat the 2D and simple models as an exercise that allows us to focus on particular factors acting on cave meteorology.

4.2 Small Size

Because of software limitations, the constructed models are very small compared to real cave sizes of interest. Therefore, it is difficult to predict the real flow patterns from the small-scale computer models. However, in terms of airflow velocity fields, we may be able to approximate the velocity field in the larger caves using dynamic similitude. For example, the essential force of our models is the buoyancy force, which is a gravitational force. If the gravitational force is important in the system, we can assume that the ratio of inertial force to the gravitational force is constant.

The Froude number (*Fr*) is a dimensionless number defined as the ratio of inertial and gravitational forces expressed by:

$$Fr = \frac{\rho U^2 L^2}{\rho L^3 g} = \frac{U^2}{Lg} \tag{4.1}$$

[Furbish, 1997, 127] in which ρ is the density of fluid, U is characteristic velocity, L is the characteristic length, and g is the gravitational acceleration. The Froude number is relevant in cases of forced convection, such as a forced pressure gradient [Wilson, unpublished note, 2004]. Our models here simulate natural convection. Although more detailed study is needed, if we assume that cave geometries create the forced convection or pressure gradient, we may be able to use the Froude number to roughly approximate the velocity field of larger models that we cannot yet construct. In order to use this approach, we must construct small models considering geometric similitude, that is, the model should have the similar aspect ratios to real cave systems to which modeling results apply. We can find the value for *Fr* from the small models, treat it as a constant, and then find the velocity (*U*) with different characteristic length (*L*). If the obtained velocity is close to the velocities observed in real systems, then this may be a valid approach. For example, assume that a model of small scale with characteristic length of 0.5 m yields the velocity of 4 x 10^{-3} m s^{-1}, then the value for *Fr* becomes 3.265 x 10^{-6}. The velocity with characteristic length of 10 m will be 1.79 x 10^{-2} m s^{-1}. The estimated velocity would then be in the appropriate range to describe air flow velocity in a cave with a height of 10 m. For example, McLean [Hill, 1987, 29] reported airflow velocity as somewhat less than 0.05 m s^{-1} in the Lunch Room area of Carlsbad Cavern, and Wilkening and Watkins [1976] reported airflow of 0.3 m s^{-1}- 0.4 m s^{-1} in the Devil's Spring region of Carlsbad Cavern. In an example from another cave, the Blowhole is the known route for airflow in Kartchner Caverns, AZ. The average airflow rate observed at Blowhole during 12/23/89 to 01/16/90 was 9.8 x 10^{-2} m s^{-1} [Buecher, 1999].

Because the Froude number described above is basically applied to the forced convection, we must find better dimensionless numbers (such as the ratio of buoyancy forces to inertial forces, or buoyancy forces to gravitational forces) that we can use for thermally-induced buoyancy-driven flow systems. There is another Froude number that we should consider in our future work that is known as the *turbulent Froude number*. The inertial-buoyancy force balance for motions of velocity scale u' and the length scale l is expressed by the turbulent Froude number $Fr_T = u' / N l$, where N is the buoyancy frequency $N = [-g / \rho \, (\partial \rho / \partial z)]^{1/2}$ and $l = u'^3 / \varepsilon$ (where ε is the turbulent kinetic energy dissipation rate)[Huq and Stretch, 1995]. This turbulent Froude number could be one of our future options for dimensionless numbers to upscale the velocities obtained from small computer models.

Bejan [1995, 254 - 256] describes the heat transfer of fluid layers heated from below with high Rayleigh number ($Ra > 10^3$). When Ra is orders of magnitude greater than the critical value, convection in the bottom-heated fluid layer is turbulent. The core of the fluid layer is almost at the average temperature $(T_h + T_c)/2$, while temperature drops of size $(T_h - T_c)/2$ occur across thin fluid layers that line the two horizontal walls (Figure 4.3). Based on both theoretical and empirical results, the actual heat transfer rate does not depend on H (the height of cavities). Although cave models are more complicated as described in Section 2.5, Bejan's explanation would help us approximate the heat flow of the large models from results of the small models.

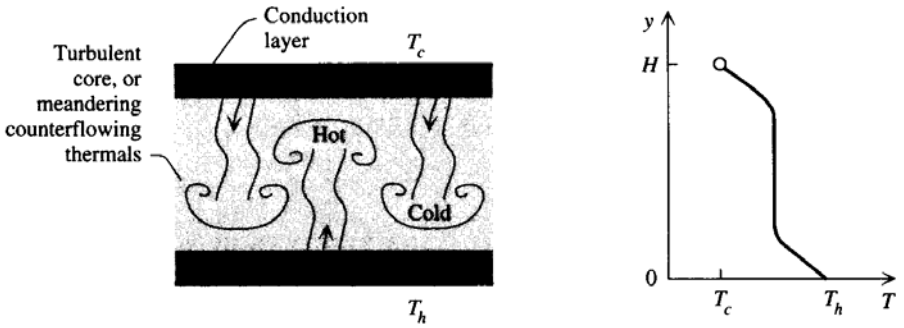

Figure 4.3: The structure of a fluid layer heated from below in the high Ra regime [Bejan, 1995, 255].

Although size issues remain problematic, we can still interpret the models to identify important factors acing on internal dynamics.

4.3 Cave Position Relative to the Side, Bottom and Top Boundaries

Caves act as insulators, so the presence of caves changes the thermal regime of surrounding rocks. In models, we need to assign certain thermal conditions (constant heat flux, constant temperature, or thermal insulation) to the boundaries. In this section, we will consider how the cave position relative to the boundaries affects the thermal regime of the entire model, and we will estimate the positions of the bottom and side boundaries that have less influence from the isolation effects of cave structures. The following models assume a cave with height (*H*) = 0.225 m and width = 2*H*. The bottom boundary has a normal heat flux value of 0.05 $\mathrm{Wm^{-2}}$. The unit length *H* = 0.225 m, and we assign the distances from the cave to the side (*s*), bottom (*b*), and top (*t*) boundaries, such as *s* = 2*H*, *b* = 2*H*, and *t* =1*H*, respectively. The modeling software produces contour lines for temperature and surfaces for velocity fields (i.e. the magnitude of velocity).

4.3.1 Position of Side Boundaries

In Figures 4.4 thru 4.6, the *b* and *t* are kept at 3*H* and 1*H*, respectively, but the side*s* varies as 1*H*, 2*H* and 3*H*, respectively. We will see how the distances between the cave and the side boundaries affect each entire model.

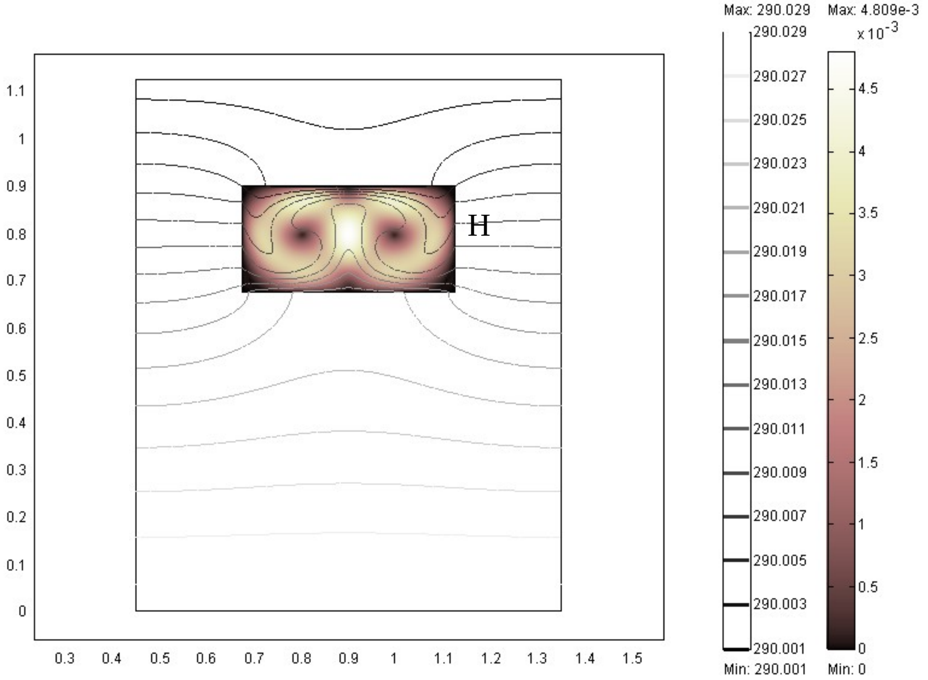

Figure 4.4: Temperature (K) and velocity field (m s^{-1}). The distances from the cave to the boundaries are: s = 1H, b = 3H and t =1H, where H = 0.255 m.

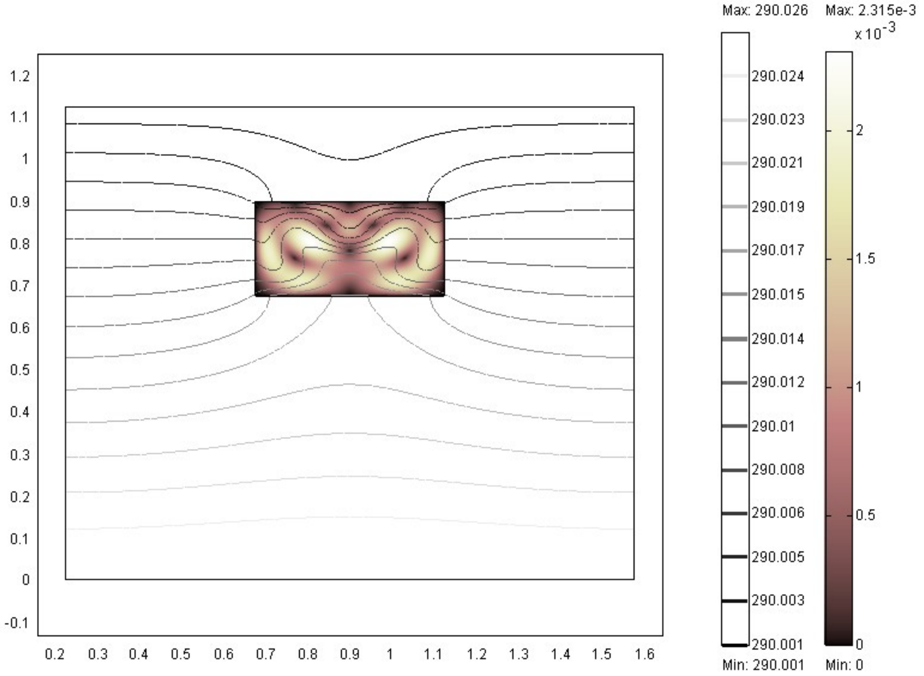

Figure 4.5: Temperature (K) and velocity field (m s^{-1}). The distances from the cave to the boundaries are: s = 2H, b = 3H and t = 1H, where H = 0.255 m.

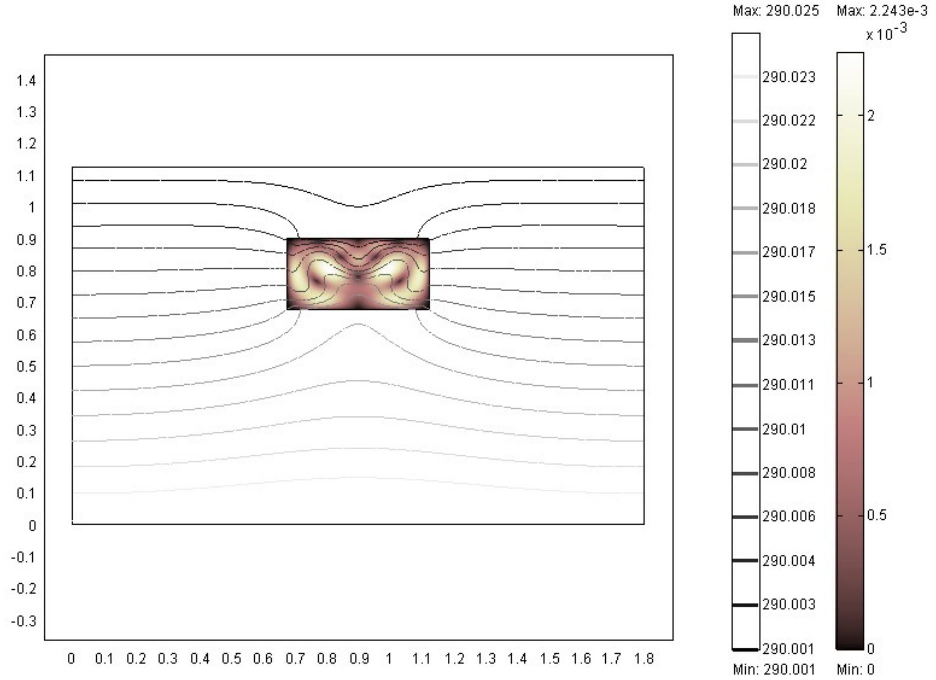

Figure 4.6: Temperature (K) and velocity field (m s^{-1}). The distances from the cave to the boundaries are: *s* = 3*H*, *b* = 3*H* and *t* = 1*H*, where *H* = 0.255 m.

Table 4.1: Side boundary effects: where *s*, *b* and *t* are the distances from the side, bottom, and top boundaries to a cave; *L* is the length (m) of the bottom boundary; and *q* is the heat flux of 0.05 Wm^{-2}.

Model	s : b : t *x* H (m) H =0.225	Numb. of elements	L *x* H (m)	Numb. of cells	Avg. temp. (K)	Avg. velocity (m s^{-1})	Boundary integration (Bi) (W m^{-1})	Error $\left\lvert\frac{Bi}{L\,q}\right\rvert$100(%
F 4.4	1 : 3 : 1	2320	4	2	290.011	$2.158x10^{-3}$	9.603×10^{-5}	$2.134x10^{-1}$
F 4.5	2 : 3 : 1	2475	6	4	290.010	$1.015x10^{-3}$	-1.435×10^{-5}	$2.126x10^{-2}$
F 4.6	3 : 3 : 1	2408	8	4	290.009	$9.831x10^{-4}$	-3.106×10^{-5}	$3.451x10^{-2}$

Table 4.1 displays evaluations of the models. The average values for temperature and velocity decrease as *s* increases. The side boundary is a thermal insulator, which for this geometry, assumes the same temperatures across the boundary. Thus, the temperature contour lines are perpendicular to the side boundary. When side boundaries are too close to the cave, the resulting temperatures and velocities of models could be

exaggerated, because the side boundaries force more of the heat flux through the cave. The significantly high average velocity in Figure 4.4 may be attributed to the smaller number of convection cells compared with Figures 4.5 and 4.6.

4.3.2 Position of Bottom Boundary

In Figures 4.7 and 4.8, *t* is 1*H*, *s* is 3*H*, but *b* varies from 1*H* to 2*H*, and along with Figure 4.6 in which *b* = 3*H*, the effects of the position of the bottom boundary are considered.

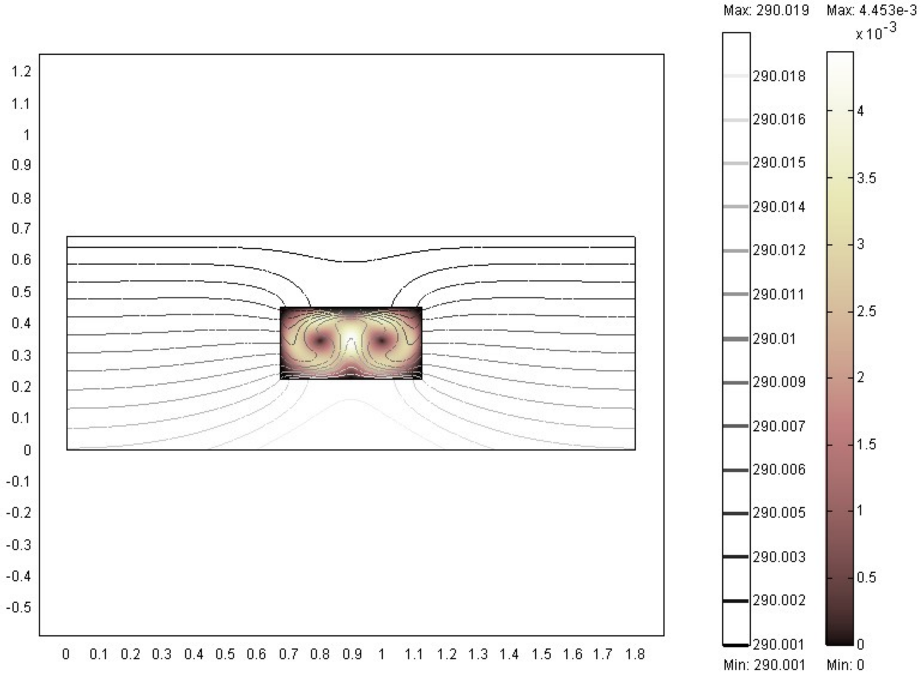

Figure 4.7: Temperature (K) and velocity field (m s^{-1}). The distances from the cave to the boundaries are: *s* = 3*H*, *b* = *t* =1*H*, where *H* = 0.255 m.

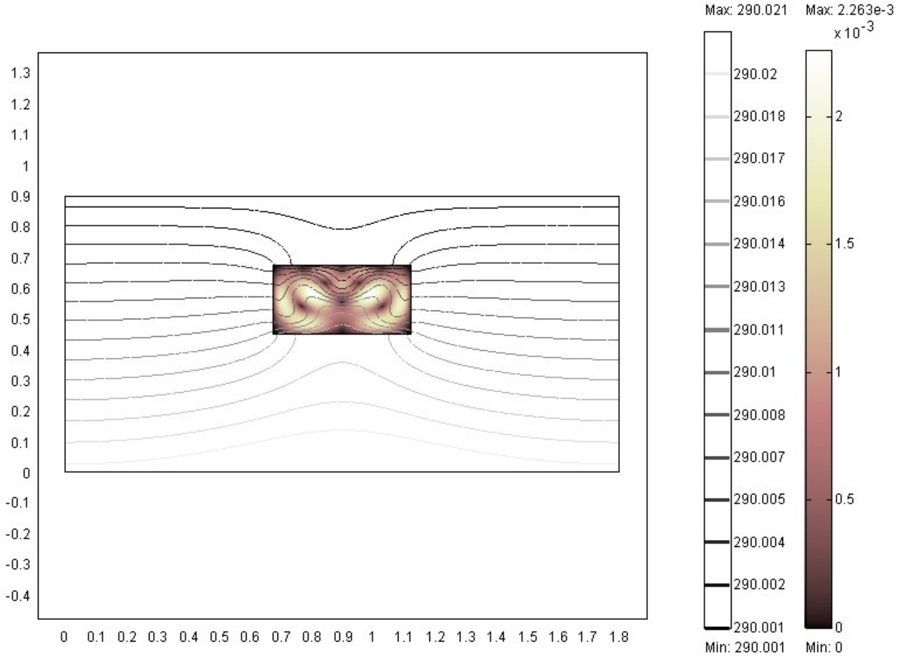

Figure 4.8: Temperature (K) and velocity field (m s^{-1}). The distances from the cave to the boundaries are: $s = 3H$, $b = 2H$ and $t = 1H$, where $H = 0.255$ m.

Table 4.2: Bottom boundary effects: where *s*, *b* and *t* are the distances from the side, bottom, and top boundaries to a cave; *L* is the length (m) of the bottom boundary; and *q* is the heat flux of 0.05 Wm^{-2}.

Model	s : b : t *x* H (m) H =0.225	Numb. of elements	L *x* H (m)	Numb. of cells	Avg. temp. (K)	Avg. velocity (m s^{-1})	Boundary integration (Bi) (W m^{-1})	Error $\left\|\frac{Bi}{Lq}\right\|100(\%)$
F 4.7	3 : 1 : 1	2198	8	2	290.009	$2.018\text{x}10^{-3}$	$-6.208 \text{ x } 10^{-5}$	$6.898\text{x}10^{-2}$
F 4.8	3 : 2 : 1	2294	8	4	290.009	$9.928\text{x}10^{-4}$	$6.080 \text{ x } 10^{-6}$	$6.755\text{x}10^{-3}$
F 4.6	3 : 3 : 1	2408	8	4	290.009	$9.831\text{x}10^{-4}$	$-3.106 \text{ x } 10^{-5}$	$3.451\text{x}10^{-2}$

The position of the bottom boundary does not have significant influence on the average temperature for the simulated conditions (Table 4.2). The bottom boundary maintains a constant heat flux, along which temperature can vary depending on the model conditions. The relatively constant temperature in a cavity could be mostly determined by the constant temperature on top, constant flux on bottom boundaries, and values for *s* and *t*. The average velocity decreases as *b* increases. The significantly high average velocity in Figure 4.7 may be attributed to the smaller number of convection cells compared with Figures 4.8 and 4.6. The position of the bottom boundary exerts influence on the average velocity in a cave, but the magnitude of influence appears to be smaller than that of side boundaries (Table 4.1).

4.3.3 Position of Top Boundary and Summary

When we set the top boundary, the distance from the top to the cave interior can be taken as the relative length with respect to the height of a cave, so its absolute size may not be problematic. Unlike the top boundary, the side or bottom boundaries can be arbitrarily located. In Figures 4.6, 4.9 and 4.10, the *s* and *b* are kept at 3*H*, but *t* varies as 1*H*, 2*H* and 3*H*, respectively. We will see how the depth of a cave affects the entire model.

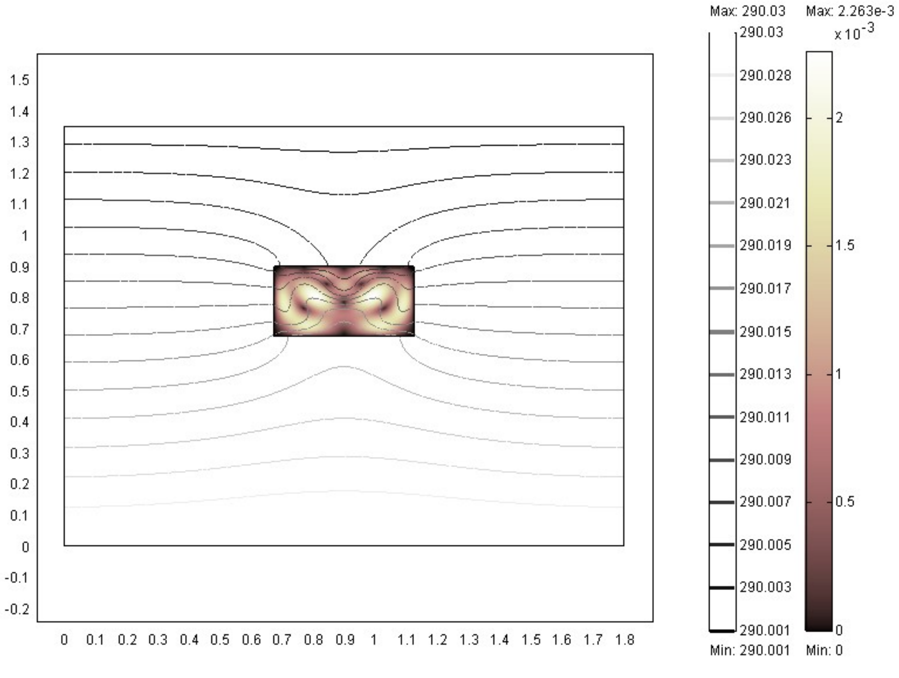

Figure 4.9: Temperature (K) and velocity fields (m s^{-1}). The distances from the cave to the boundaries are: s = b = 3H and t =2H, where H = 0.255 m.

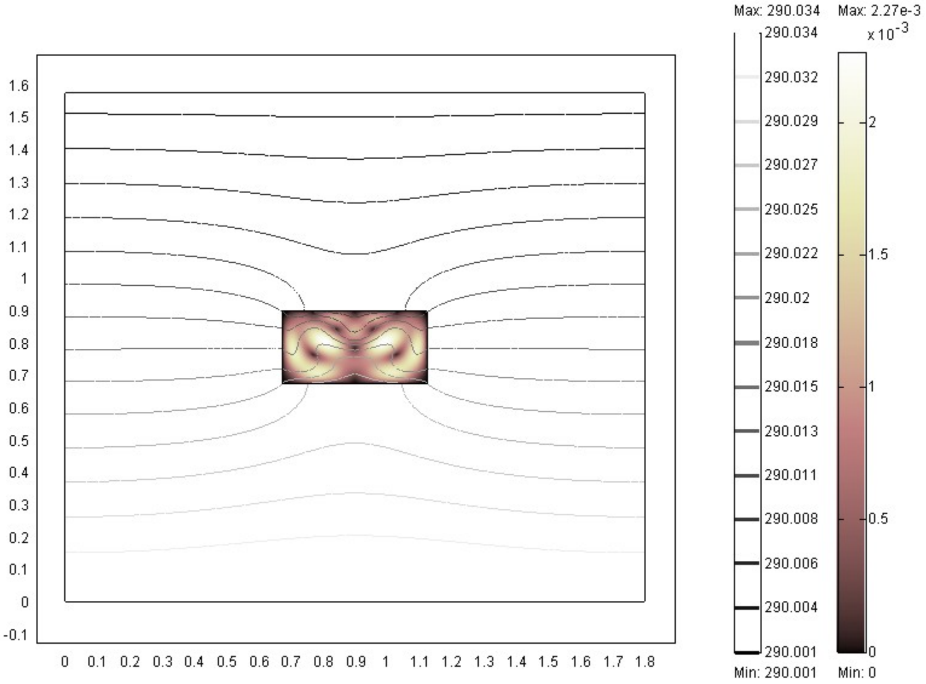

Figure 4.10: Temperature (K) and velocity fields (m s^{-1}). The distances from the cave to the boundaries are: $s = b = t = 3H$, where $H = 0.255$ m.

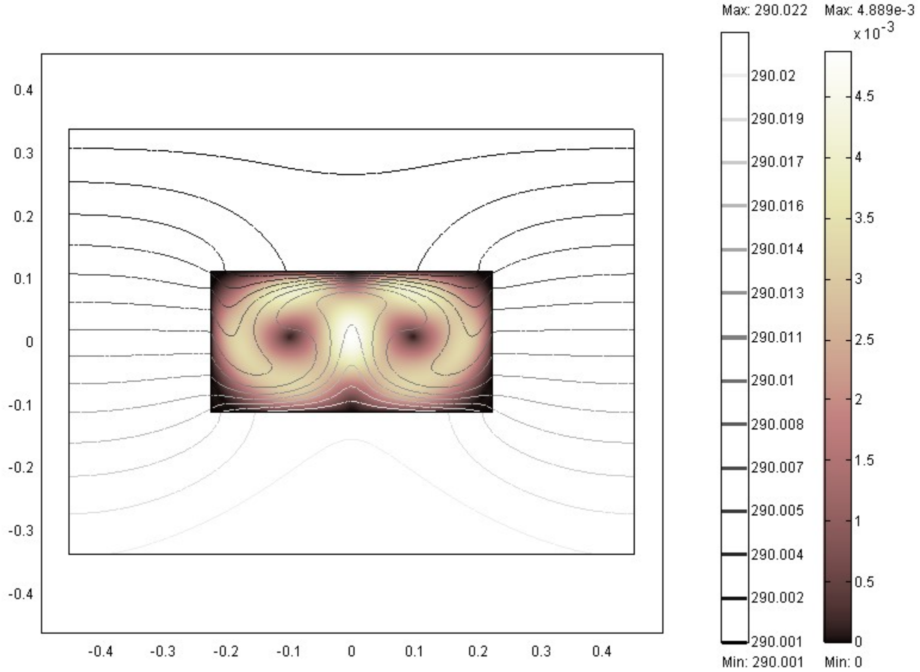

Figure 4.11: Temperature (K) and velocity fields (m s^{-1}). The distances from the cave to the boundaries are: $s = b = t = 1H$.

Figure 4.11 is an example model in which $s = b = t = 1H$. Table 4.3 and Figures 4.12 and 4.13 summarize the model results. When the side boundaries are too close to a cavity (e.g., $D/H = 1$), the average temperature and velocity in the cavity are exaggerated. The effects of the position of the bottom boundary are not significant compared to that of the side boundaries, but the velocity can be exaggerated if the bottom boundary is too close to the cave structure. The bottom boundary has a constant heat flux, so temperature can vary along the boundary depending on the values for constant temperature at the top boundary and the material properties in which heat flows. Thus, temperature and velocity inside cave structures may not depend heavily on the position of the bottom boundary. The deeper the cave location, the higher the average temperature and the average velocity, as long as the side and bottom boundaries are located far enough from the cavity (e.g. 3*H*). We need to consider these relationships when we construct computer models, but since they were derived from the very small and simple models, we cannot treat them as absolute relationships.

Table 4.3: Top boundary effects: where *s, b* and *t* are the distances from the side, bottom, and top boundaries to a cave; *L* is the length (m) of the bottom boundary; and *q* is the heat flux of 0.05 Wm^{-2}.

Model	s : b : t *x* H (m) H =0.225	Numb. of elements	L *x* H (m)	Numb. of cells	Avg. temp. (K)	Avg. velocity (m s^{-1})	Boundary integration (Bi) (W m^{-1})	Error $\left\lvert \frac{Bi}{L\ q} \right\rvert 100(\%$
F 4.6	3 : 3 : 1	2408	8	4	290.009	9.831x10^{-4}	-3.106 x 10^{-5}	3.451x10^{-2}
F 4.9	3 : 3 : 2	2550	8	4	290.014	9.921x10^{-4}	9.266 x 10^{-6}	1.030x10^{-2}
F 4.10	3 : 3 : 3	2674	8	4	290.018	9.941x10^{-4}	7.744 x 10^{-6}	8.605x10^{-3}
F 4.11	1 : 1 : 1	2338	4	2	290.011	2.198x10^{-3}	8.877 x 10^{-6}	1.973x10^{-2}

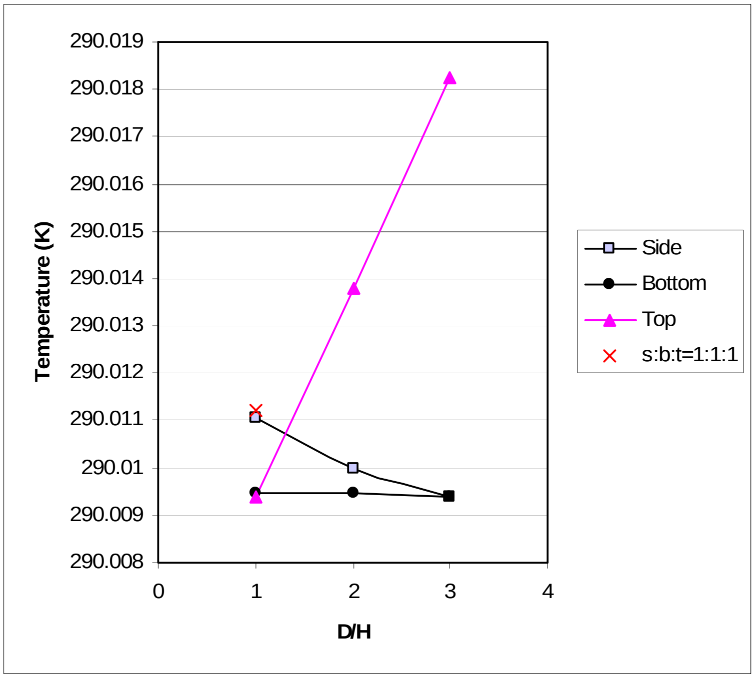

Figure 4.12: Average temperature in a cavity versus distance between boundaries and the cavity, where *D* represents the distance and *H* is cavity height (0.225m).

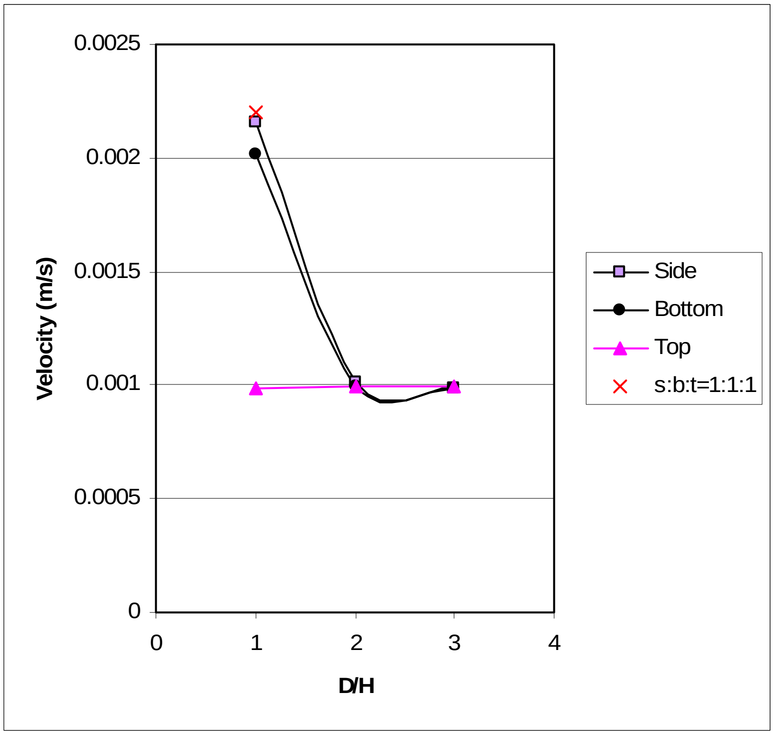

Figure 4.13: Average velocity fields in a cavity versus distance between boundaries and the cavity, where *D* represents the distance and *H* is cavity height (0.225m).

4.4 Grid Resolution

Solutions vary with different grid or mesh resolutions even if the other conditions are kept the same. The fine grids are necessary to find reliable solutions of the non-linear flow equations. We need to optimize grid resolution for models that are achievably accurate within the capacity of our computers. Modelers have pointed out the need for grid resolution studies [e.g. Christon et al., 2002]. For example, in Yucca Mountain projects that are attempting a large scale numerical simulation, Valentine et al. [2002] suggest that standard practice in simulating complex, non-linear behavior must include grid resolution studies. In this study, we have selected sufficiently fine grids to minimize the errors. Figure 4.14 shows grid resolution for Figure 4.10, in which finer grids are applied to the interior cave component. Finer grids are applied to the cavities of all following models to solve multiphysics, non-linear flow equations within those cavities.

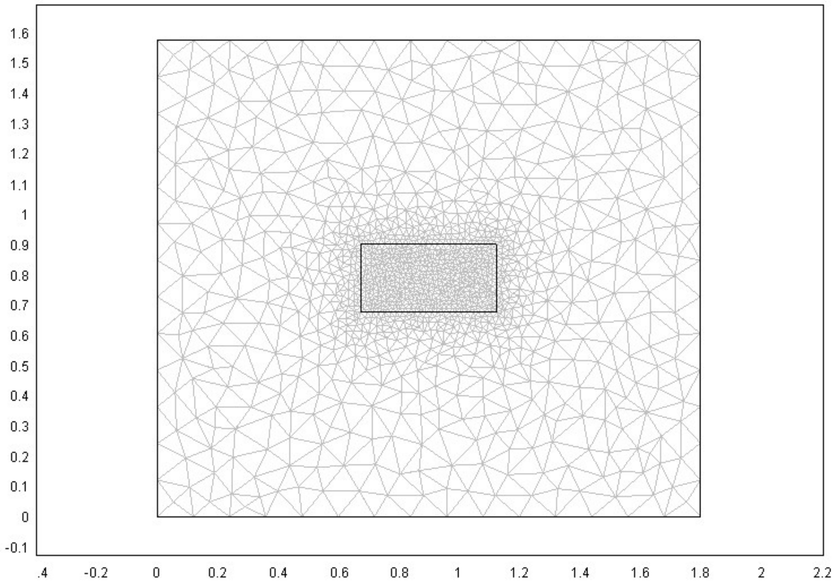

Figure 4.14: Grid resolution for Figure 4.10. The cave component has a finer grid in order to solve non-linear flow equations. The number of grid elements is 2674.

FEMLAB allows us to adjust grid size and grid growth rate within subdomains and along boundaries [COMSOL AB**,** 2004d, 246-286]. It is important to check the model accuracy. If a model has not been verified by other means (using other sources of data), convergence test is useful to determine if the grid density is sufficient. We can refine the grid and run the analysis again, and then we see if the solution is converging to a stable value as the grid refined [COMSOL AB, 2004d, 440].

4.5 Other Factors

Other factors discussed in Section 2.7 that potentially have significant impacts on cave meteorology are difficult to include in the models, namely the effects of water movement, chemical reactions, and human activities. These are discussed in Section 2.7. However, we think that these other factors are probably minor compared to the effects of geothermal heating, thermal properties of materials, and cave geometries.

CHAPTER 5

MODELS – INTERNAL DYNAMICS

This chapter displays the computer models that focus on the internal factors affecting air and heat flow. Here we assume that there is no influence from the surface weather conditions and if flows are observed in models, it would only be due to internal factors.

5.1 Critical Rayleigh Number

5.1.1 Critical Rayleigh Number for Cave Systems

The critical Rayleigh number (Ra_c) of 1708, the convection onset criterion, refers strictly to an infinite horizontal layer with rigid (no-slip) and isothermal top and bottom boundaries [Bejan, 1995, 254]. Air-filled caves are surrounded by rocks. This section first examines Ra_c for an air-filled cavity only with isothermal top, constant heat flux bottom and thermal insulation side boundaries. Next we consider Ra_c for a cave situation with isothermal top, constant heat flux bottom and thermal insulation side boundaries that are located far from an air-filled cave.

(1) Critical Rayleigh Number for Air-Filled Cavity with Heat Flux at the Bottom Boundary

In Figures 5.1 and 5.2, air-filled cavities have the height (H) of 0.054 m and 0.053 m, respectively, and widths of $2H$. The models are air-phase only, and there is no surrounding rock. Simulations with a variety of cave heights have been conducted, and here, the cavity heights of 0.054 m and 0.053 m have been chosen because the onset of fluid motion was observed in the simulations that used those heights. The top boundary has a constant temperature of 290 K and a constant heat flux of 0.05 Wm^{-2} is applied to the bottom boundary. The values for the Rayleigh number Ra_2 in Table 5.1 are calculated using equation 2.10 (*Ra* for models that have an air-filled cavity with heat flux at the bottom boundary).

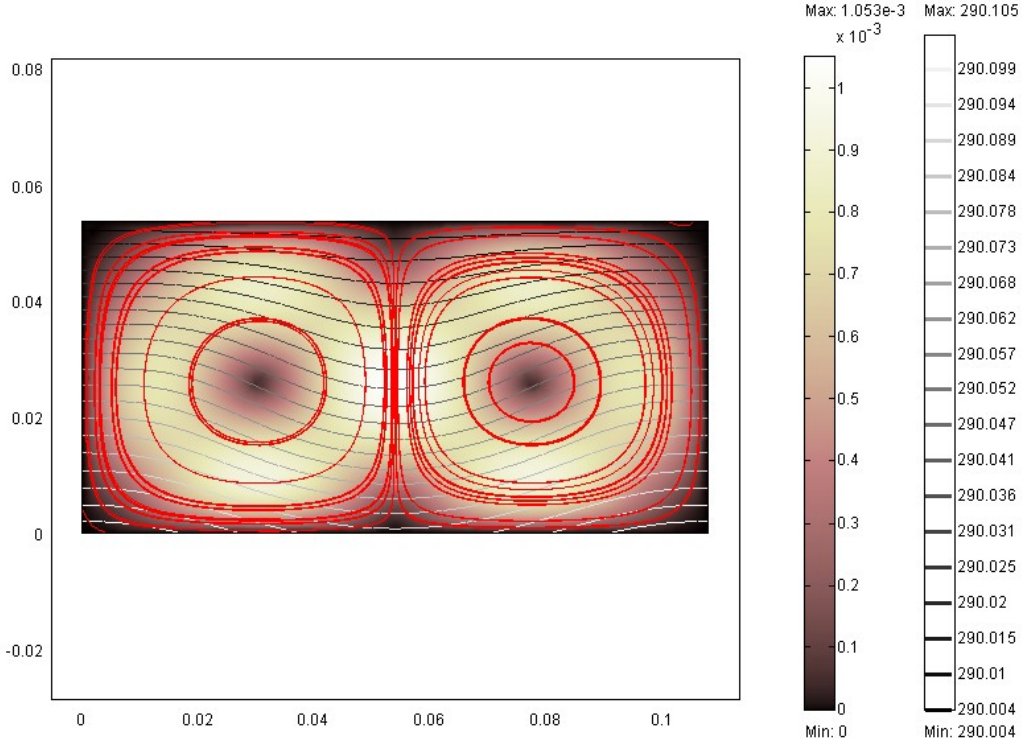

Figure 5.1: Air-filled cavity with contour lines indicating temperature (K), and surfaces and streamlines, indicating the velocity field ($m\ s^{-1}$). $Ra_2 = 1800$. The cavity height H = 0.054 m, cave width $W = 2H$, cave area = 2 H^2, and the length of the bottom boundary $L = 2H$.

The streamlines for the velocity field in Figure 5.1 are not symmetric. The finite element method computes the fluid velocity by subdividing the given domain into a set of subdomains, and by generating the approximation functions required in the solution of differential equations [Reddy and Gartling, 2001, 33]. Errors are always associated with model approximations and, thus, models may not produce perfectly symmetrical streamlines.

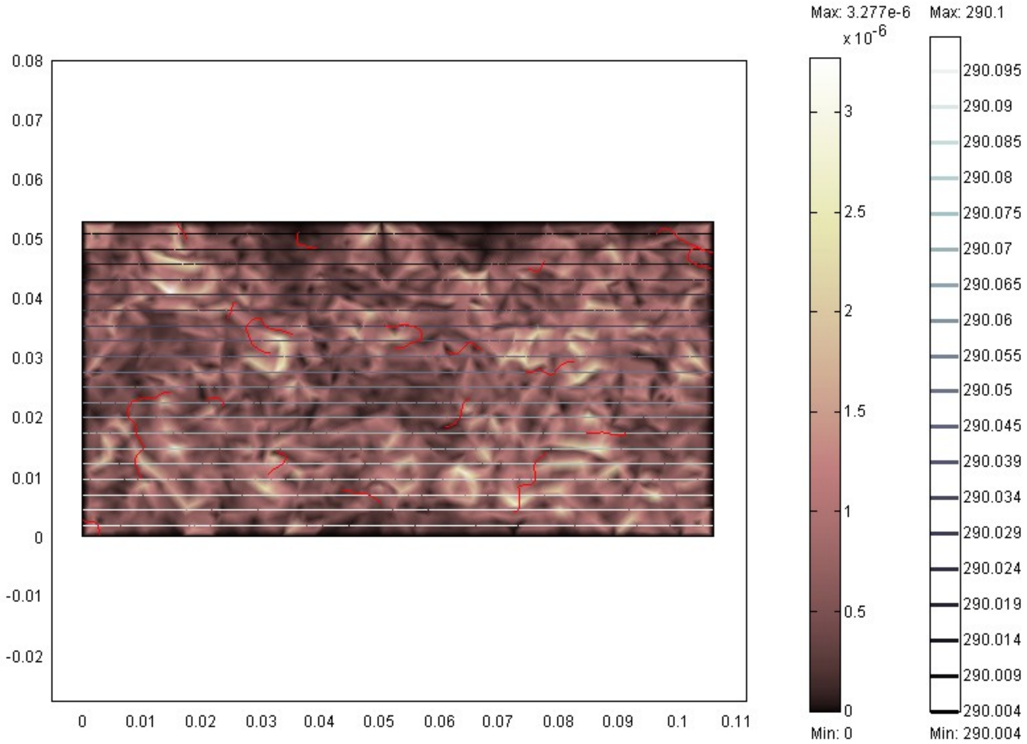

Figure 5.2: Air-filled cavity model with contour lines indicating temperature (K), and surfaces and streamlines indicating the velocity field (m s^{-1}). $Ra_2 = 1670$. The cavity height $H = 0.053$ m, cave width $W = 2H$, cave area = 2 H^2, and the length of the bottom boundary $L = 2H$.

Table 5.1: Critical Rayleigh number for models with air-filled cavities only and heat flux from the bottom. L is the length of the bottom boundary of $2H$ (m), and q is the heat flux of 0.05 Wm^{-2}.

Model	*H (m)*	*Ra_2*	*Number of elements*	*Number of convec. cells*	*Avg. velocity (ms^{-2})*	*Avg. temp. (K)*	*Boundary integration (Bi) (Wm^{-1})*	*Error* $\left\lvert\frac{Bi}{L\,q}\right\rvert 100(\%)$
F 5.1	0.054	1800	740	2	$5.374\text{x}10^{-4}$	290.050	$1.022\text{x}10^{-5}$	$1.892\text{x}10^{-3}$
F 5.2	0.053	1670	744	0	$6.016\text{x}10^{-7}$	290.052	$-1.582\text{x}10^{-8}$	$2.986\text{x}10^{-6}$

Convection cells are observed at Ra_2=1800 (Figure 5.1), but they disappear at Ra_2 = 1670, in which streamlines for velocity fields no longer form constant flow patterns. The critical Rayleigh number Ra_{2c} appears to be between these values ($1670 < Ra_{2c} < 1800$). Although the bottom boundary of the models is set at a constant heat flux instead of constant temperature, the results are consistent with the theoretical Ra_c (1708) for an infinite horizontal layer with rigid (no-slip) and isothermal top and bottom boundaries [Bejan, 1995, 254].

(2) Critical Rayleigh Number for Cave Systems with Heat Flux at the Bottom Boundary

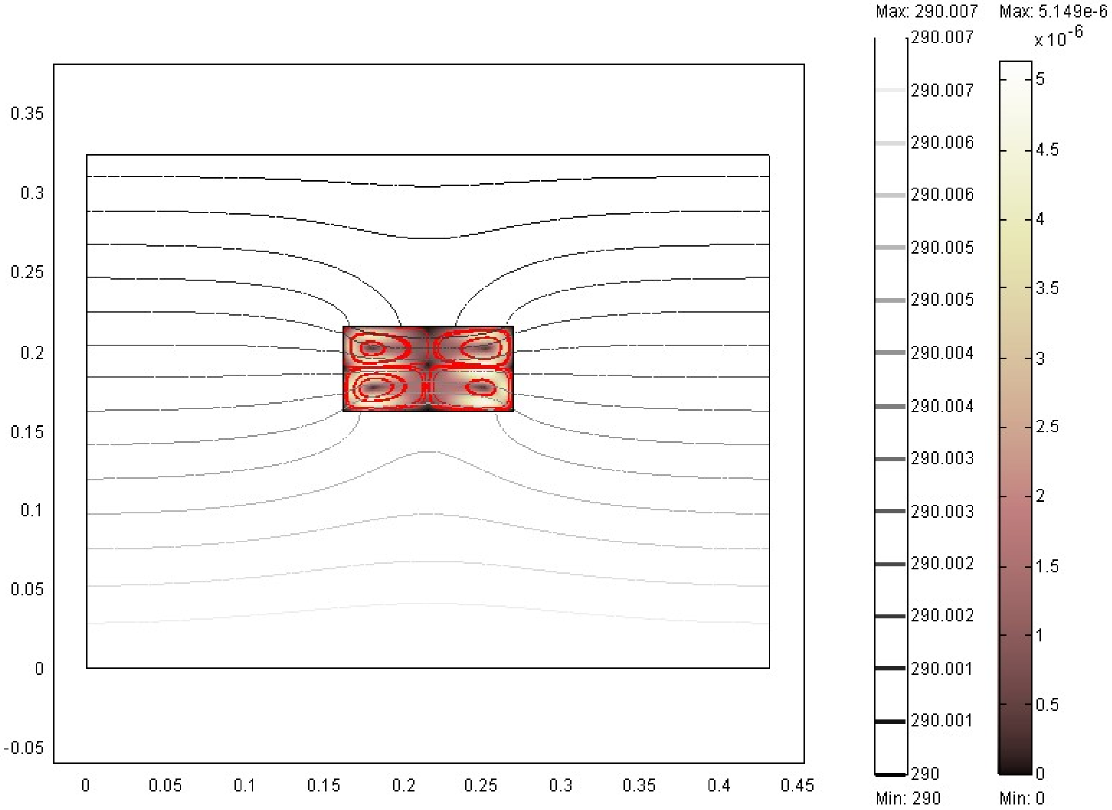

Figure 5.3: Cave model with contour lines indicating temperature (K), and surfaces and streamlines indicating the velocity field (m s^{-1}). Ra_1 =18. Cave height H = 0.054 m, cave width $W = 2H$, cave area = 2 H^2, and the length of the bottom boundary $L = 8H$.

Figures 5.3 thru 5.6 describe cave systems with a cavity located within a rock mass. A cave is located 2*H* below the surface, and the side and bottom boundaries are placed 3*H* from the cave, in which *H* is the height of the cave. Width of the cave is 2*H*. Various values for *H* were applied to find critical Rayleigh numbers (Ra_{1c}). Figure 5.3 shows the case of $H = 0.054$ m. Figures 5.4 and 5.5 are the enlarged images of the cave vicinities with *H* of 0.053 m and 0.0053 m, respectively. The cavity heights of 0.054 m and 0.053 m were selected to compare with the air-filled cavity only models that have the same heights described in the previous section. The height of 0.0053 m was selected to observe whether or not the model still produces streamlines for the velocity field in such a small cavity. Applying equation (2.9), the corresponding Ra_1 are 18, 17, and 0.0017, respectively; the values for Ra_1 are small compared to Ra_2 for the same cavity heights (see Table 5.1). Clear convection cells are observed in all models even when the velocity fields are extremely small (e.g., Figure 5.5). We will examine the reasons for this phenomenon in the next section.

If we consider the constant streamline patterns in the models, even small spaces in the subsurface could conceivably have convection cells (Figure 5.5). However, their average velocity fields (magnitude of velocity) are extremely small. For example, in Lower Cave at Carlsbad Cavern, NM, there is clearly perceivable airflow that can tilt the angle of a handheld handkerchief approximately 15 - 30°; this author measured a velocity of 0.4 m s^{-1} in December 2004. The velocities of 10^{-6} or 10^{-9} m s^{-1} (Table 5.2) are 5 to 8 orders less than that observed at Lower Cave. Such small velocities could be negligible with respect to Ra_{1c}. Therefore, the contour lines for temperatures of these models do not show the convection.

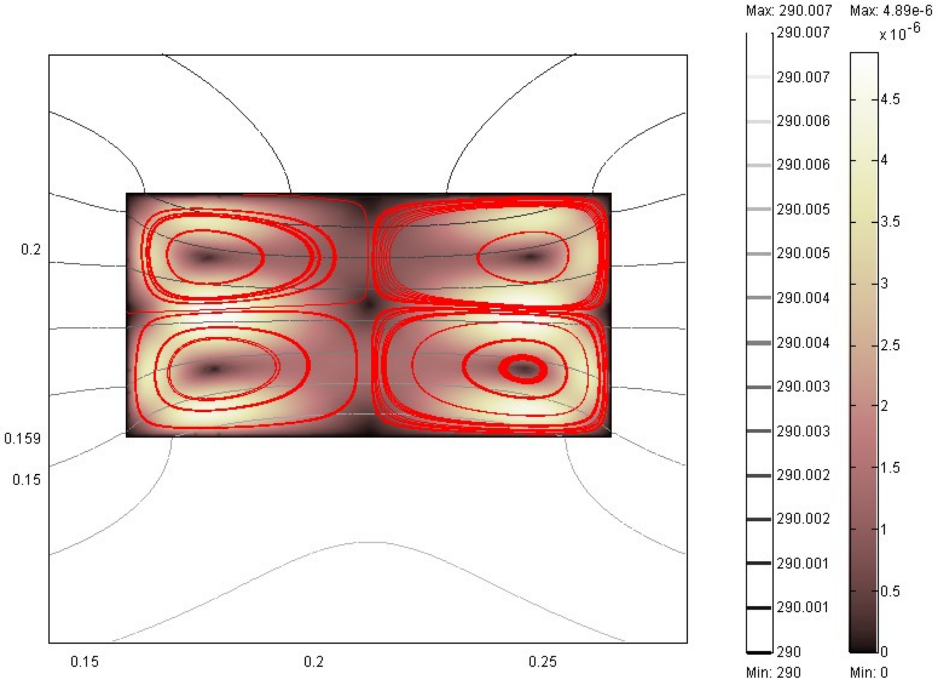

Figure 5.4: Cave model with contour lines indicating temperature (K), and surfaces and streamlines indicating the velocity field (m s^{-1}). The vicinity of the cave is enlarged. Ra_1 =17. Cave height H = 0.053 m, cave width W = 2H, cave area = 2H^2, and the length of the bottom boundary L = 8H.

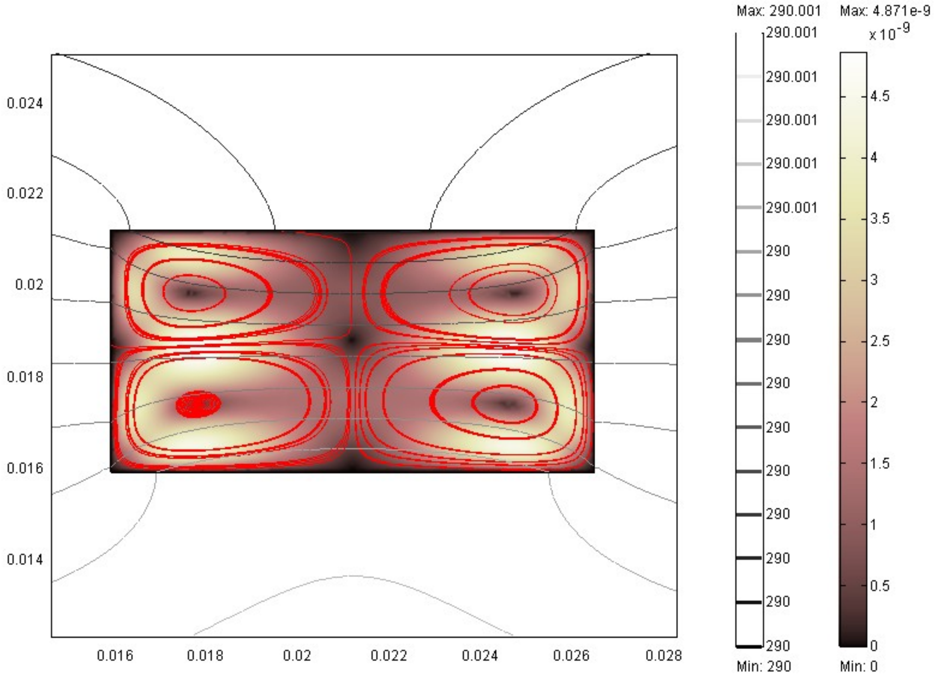

Figure 5.5: Cave model with contour lines indicating temperature (K), and surfaces and streamlines indicating the velocity field (m s^{-1}). The vicinity of the cave is enlarged. Ra_1 =0.0017. Cave height H = 0.0053 m, cave width W = 2H, cave area = 2H^2, and the length of the bottom boundary L = 8H.

Table 5.2: Critical Rayleigh number for cave models. The length of the bottom boundary $L = 8H$ (m), and the heat flux $q = 0.05$ Wm^{-2}.

Model	*H (m)*	Ra_1	*Number of elements*	*Number of cells*	*Avg. velocity (m s^{-1})*	*Avg. temp. (K)*	*Boundary integration (Bi) (Wm^{-1})*	*Error* $\left\lvert\frac{Bi}{L\,q}\right\rvert 100(\%)$
F 5.3	0.054	18	2728	4	2.218×10^{-6}	290.003	5.507×10^{-7}	2.549×10^{-5}
F 5.4	0.053	17	2626	4	2.097×10^{-6}	290.003	-4.823×10^{-7}	2.275×10^{-5}
F 5.5	0.0053	0.0017	2614	4	2.093×10^{-9}	289.996	-1.602×10^{-8}	7.559×10^{-6}

The magnitude of the average velocity field in Figure 5.2 is 10^{-7} m s^{-1}, in which there is no convection observed; and that in Figure 5.1 is 10^{-4} m s^{-1}, in which air begins moving. We shall assume that at Ra_{1c} the order of the average velocity field shifts to 10^{-4} m s^{-2} from lower orders such as 10^{-5} or 10^{-6} m s^{-2}, based on the examples of Figures 5.1 and 5.2. We simulated model cases with various cave heights to find those with which the average velocity field shifts to the magnitude of 10^{-4} m s^{-1} from the lower magnitude.

The values for H in Figures 5.6 and 5.7 are 0.13 m and 0.14 m, and corresponding Ra_1 are 617 and 830, respectively. The evaluations for the models are shown in Table 5.3. In Figure 5.7, the average velocity field shifts from the order of 10^{-5} m s^{-2} (Figure 5.6) to 10^{-4} m s^{-2}, and the contour lines for temperature clearly form curved lines. Thus, Ra_{1c} could be between 617 and 830 in this geometry whose aspect ratio is $W/H = 2$.

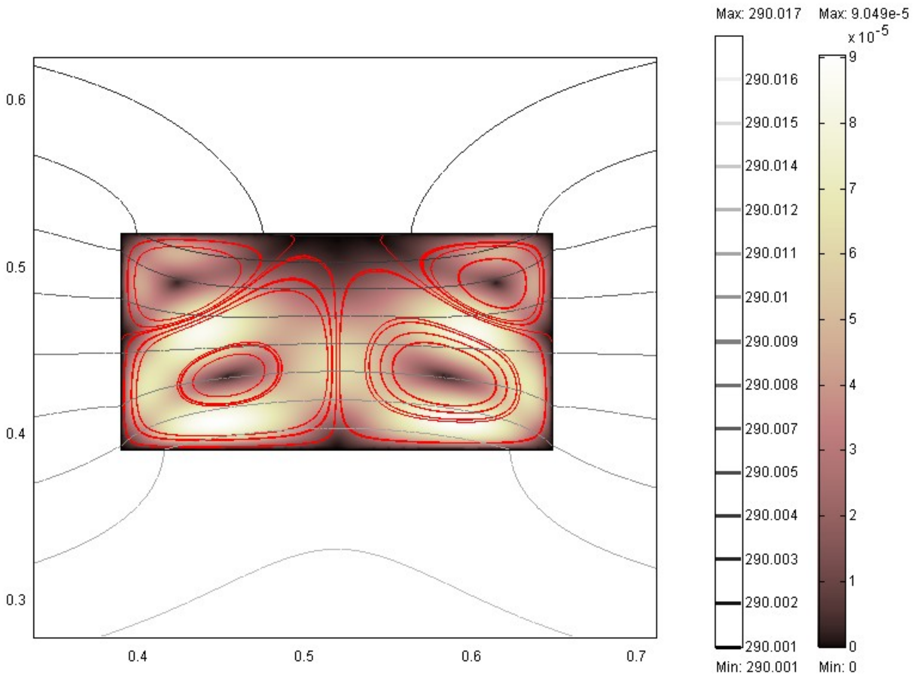

Figure 5.6: Cave model with contour lines indicating temperature (K), and surfaces and streamlines indicating the velocity field (m s^{-1}). The vicinity of the cave is enlarged. Ra_1 =617. Cave height H = 0.13 m, cave width W = 2H, cave area = 2H^2, and the length of the bottom boundary L = 8H.

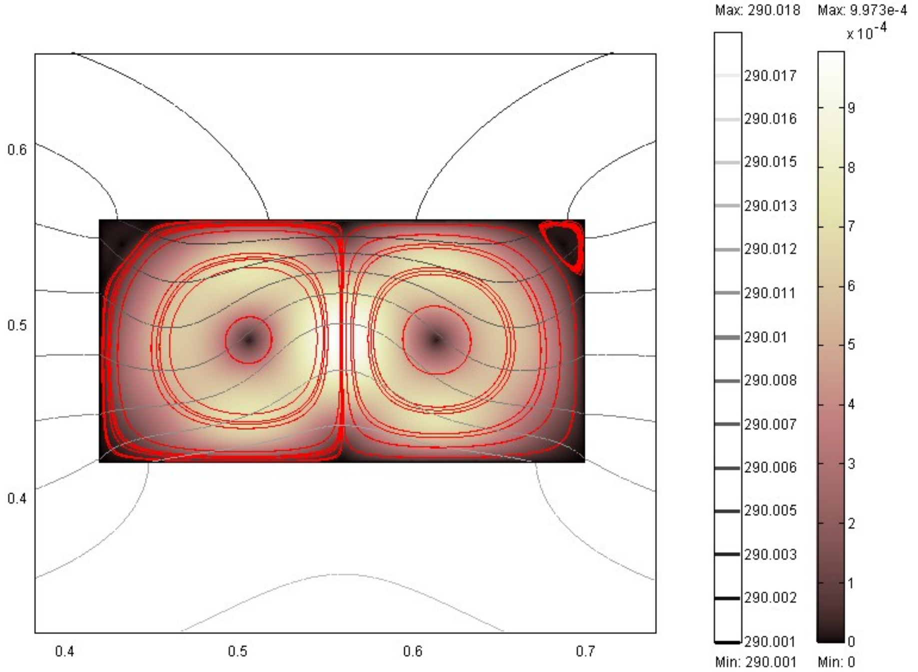

Figure 5.7: Cave model with contour lines indicating temperature (K), and surfaces and streamlines indicating the velocity field (m s^{-1}). The vicinity of the cave is enlarged. Ra_1 = 830. Cave height H = 0.14 m, cave width W =2H, cave area = 2H^2, and the length of the bottom boundary L = 8H.

Table 5.3: Critical Rayleigh number based on velocity for cave models. The length of the bottom boundary $L = 8H$ (m), and q is the heat flux of 0.05 Wm^{-2}.

Model	*H (m)*	*Ra_1*	*Number of elements*	*Number of cells*	*Avg. velocity (m s^{-1})*	*Avg. temp. (K)*	*Boundary integration (Bi) (Wm^{-1})*	*Error* $\left\lvert\frac{Bi}{L\,q}\right\rvert 100(\%)$
F 5.6	0.13	617	3820	4	4.097×10^{-5}	290.008	1.806×10^{-6}	3.473×10^{-5}
F 5.7	0.14	830	4230	2	4.280×10^{-4}	290.008	2.353×10^{-6}	4.201×10^{-5}

5.1.2 Organized Flow Patterns in Caves under the Low Ra_1

Cave model streamlines form organized flow patterns even if the average velocity field is negligibly small. We shall consider why this phenomenon could happen. The difference between the models of air-filled cavity-only and the models of cave systems is the position of boundaries. In cave systems, the boundaries are located far from a cave and, thus, temperature or heat flux is not constant on the walls of the cave, whereas a constant temperature or heat flux is assigned to the walls of the air-filled cavity models.

The plot in Figure 5.8 describes the normal total heat flux of the boundaries of Figure 5.2 (the air-filled cavity model with H = 0.053 m that has no convection cell) clockwise starting from the left-bottom corner (left, top, right and bottom boundaries). The plot of Figure 5.9 shows the normal total heat flux of the boundaries of Figure 5.4 (the cave system with H = 0.053m). The unit of conductive heat flux is Wm^{-2} and it does not have a sign as it describes magnitude. In contrast, the unit of normal heat flux is also Wm^{-2}, but it does have a sign. A normal heat flux has the flow direction perpendicular to a boundary. A negative sign indicates that heat enters a domain and a positive sign means that heat leaves a domain.

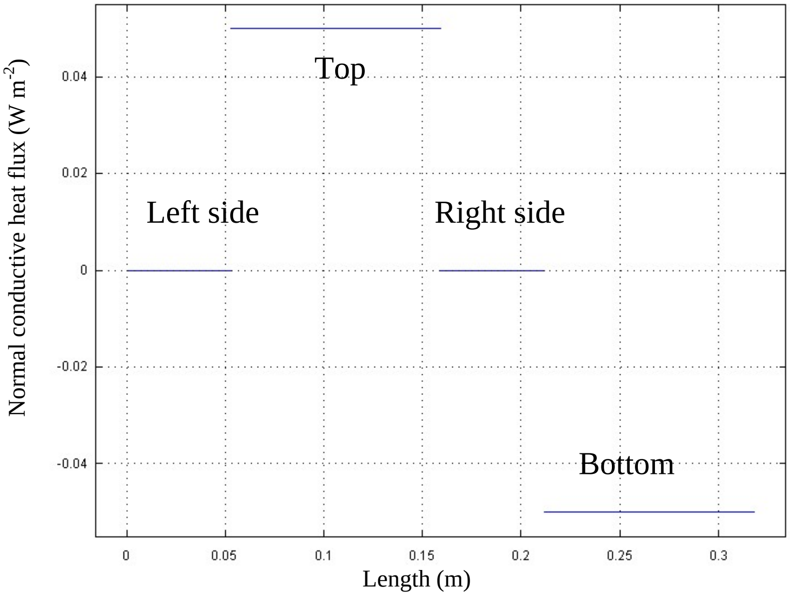

Figure 5.8: Normal conductive heat flux (Wm^{-2}) of the boundaries of Figure 5.2 (H = 0.053 m), from the left side, top, right side and bottom boundaries.

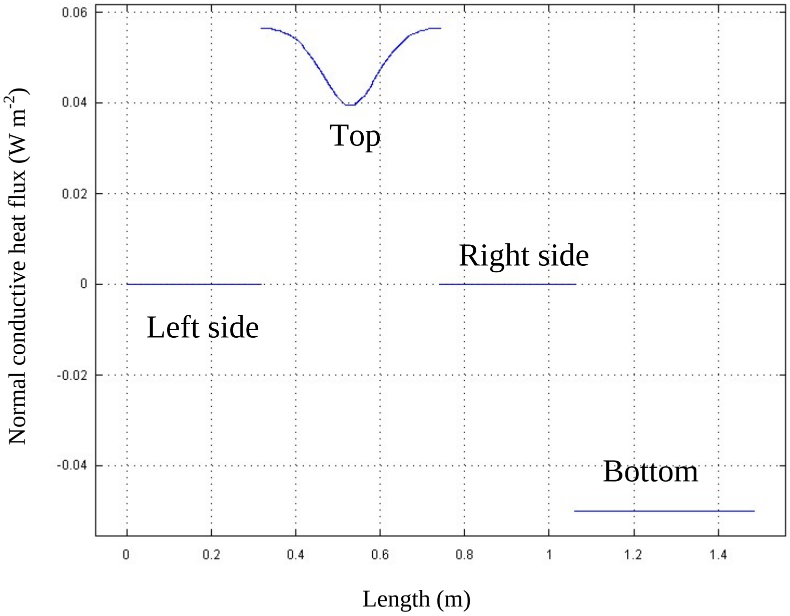

Figure 5.9: Normal conductive heat flux (Wm^{-2}) of the boundaries of Figure 5.4 (H = 0.053 m) clockwise starting from the left of the bottom boundary of the entire model (they are not cave walls).

In Figure 5.8, the boundaries are at a constant condition; side boundaries have 0 Wm^{-2}, and bottom and top boundaries have about -0.05 Wm^{-2} and 0.05 Wm^{-2}, respectively. In contrast, in Figure 5.9, the total flux at the top boundary is not constant along the boundary, and shows the effects of the presence of the cave structure. The lowest heat flux is observed at the center of the top boundary.

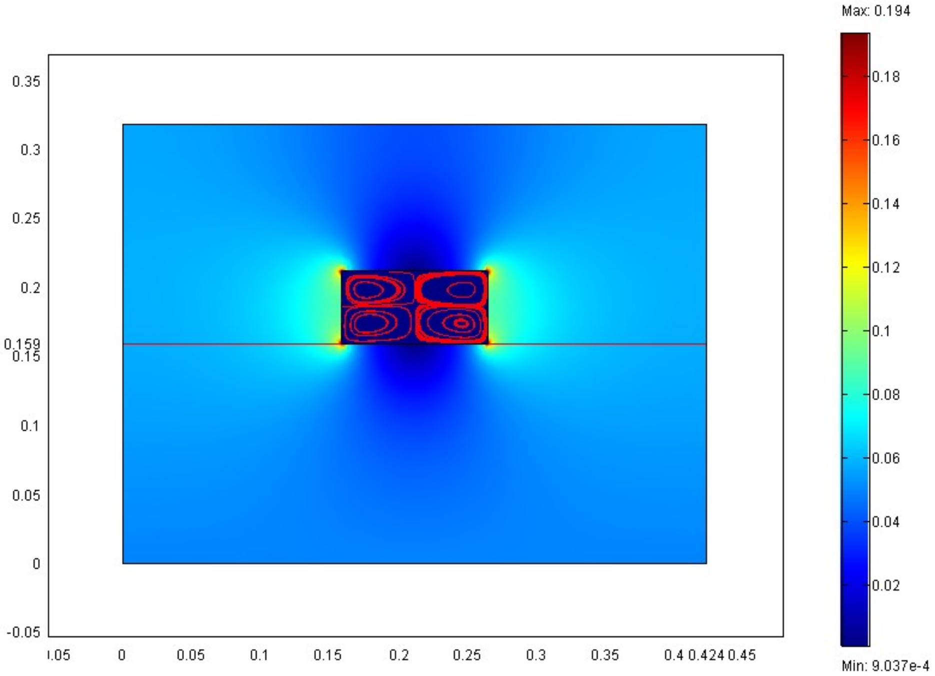

Figure 5.10: Rectangular cave model with surfaces indicating the conductive heat flux (Wm^{-2}), and streamlines indicating the velocity field (m s^{-1}). The model is the same as Figure 5.4 (H = 0.053 m), but it shows the entire model. The horizontal line indicates the transect used to derive Figure 5.11. Note: the four corners of the cave have high conductive heat flux.

The plot in Figure 5.10 displays the same model as in Figure 5.4, but it shows surfaces indicating the conductive heat flux (Wm^{-2}), and streamlines indicating the velocity field in the cave. In the plot, the heat conduction appears to be the most concentrated in the four corners of the cave, in which two cave walls are located closest to each other. The conductive heat flux was calculated along the horizontal transect indicated in Figure 5.10 and is shown in Figure 5.11. In the plot, conductive heat flux forms a sharp, almost parabolic line along the bottom wall of the cave with the minimum heat flux at the middle in which the two cave walls are located farthest from each other. The similar parabolic or U-shaped lines are observed when we take conductive heat fluxes along transects on the sides and top walls of the cave structure.

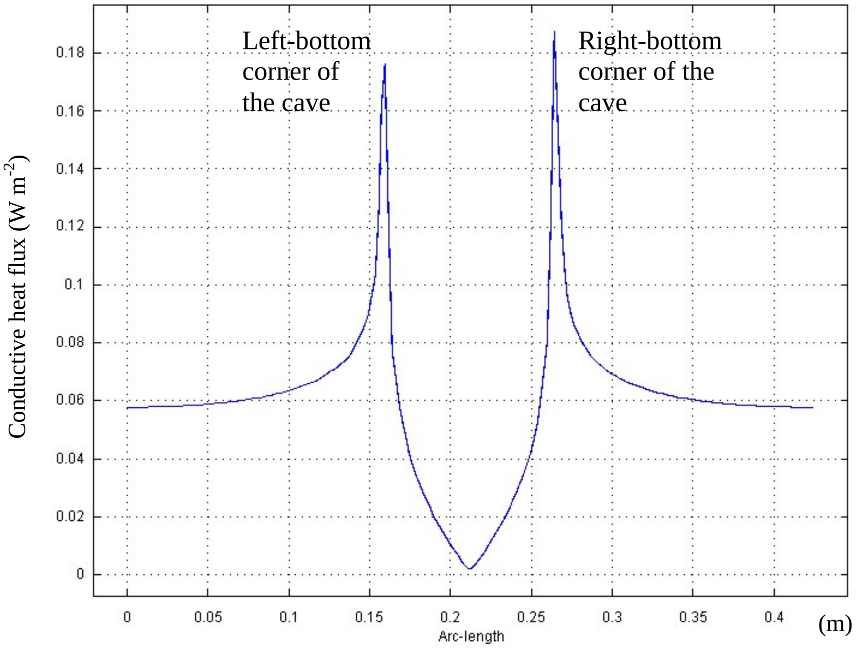

Figure 5.11: Plot of the magnitude of conductive heat flux (Wm^{-2}) in Figure 5.10 (H = 0.053 m) along the line from the middle of the left side to the middle of the right side boundary through the cave floor (indicated in Figure 5.10). The arc-length is the transect length indicated in Figure 5.10. Note that the conductive heat flux forms a sharp, almost parabolic line along the bottom wall of the cave with high values in the two corners.

In the rectangular cave models, the corners may be where the heat conduction is most concentrated. Where will the heat conduction be most concentrated in cases where a cave model does not have corners, e.g. like a large vug which can be considered a small, spherical cave? Figure 5.12 shows the heat conduction model with a spherical cave. The evaluation of the model is found in Table 5.4. The height of the circular cross-section of the cave is 0.053 m which is the same as the rectangular cave in Figure 5.10. Heat conduction appears to be more concentrated at the two sides than the top and bottom parts of the cave. Figure 5.13 shows the conductive heat flux along the horizontal transect from the middle of the left side boundary to the middle of the right side boundary though the cave center. Figure 5.14 shows the conductive heat flux along the vertical transect from the middle of the top boundary to the middle of the bottom boundary through the center. Note that in Figure 5.13, conductive heat flux is high in the side walls of the cave, whereas in Figure 5.14, the ceiling and floor have the same conductive heat flux as the center of the cave.

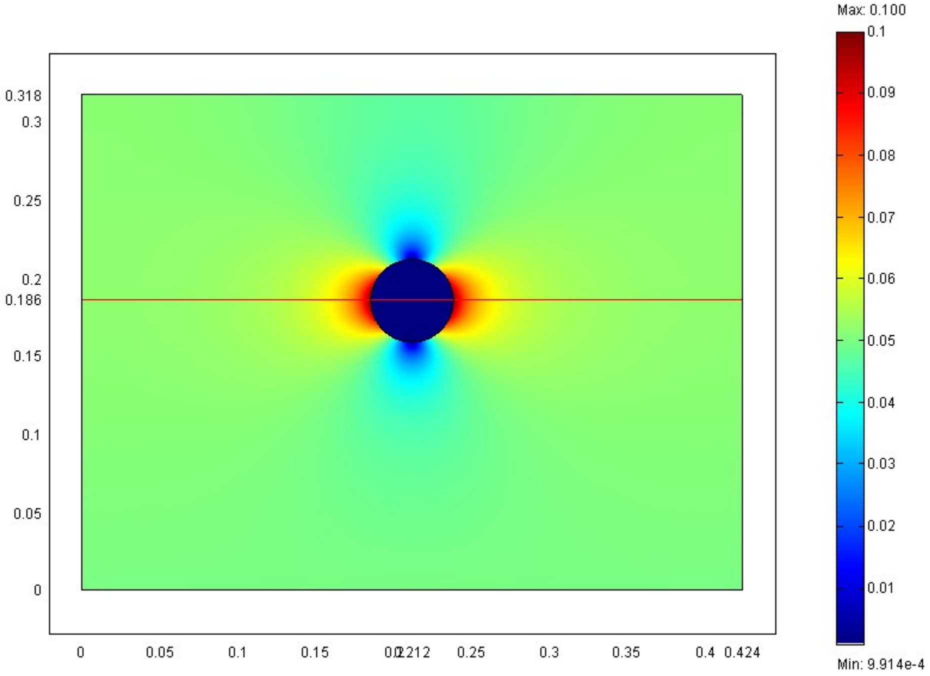

Figure 5.12: Circular cross-section cave model with surfaces indicating the magnitude of conductive heat flux (W m^{-2}). $Ra_1 = 17$, cave height $H = 0.053$ m, cave area = $\pi H^2/4$ and the length of the bottom boundary $L = 8H$. The horizontal line indicates the transect used to derive Figure 5.13.

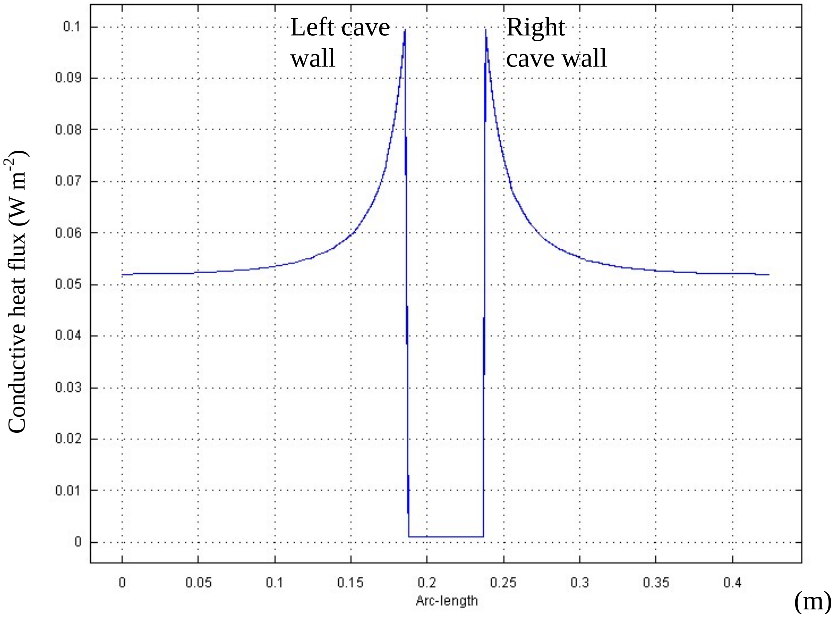

Figure 5.13: Plot of magnitude of conductive heat flux (Wm^{-2}) along the horizontal transect from the middle of the left side boundary to the middle of the right side boundary through the center of the circular cross-section cave (indicated in Figure 5.12). The arc-length is the transect length.

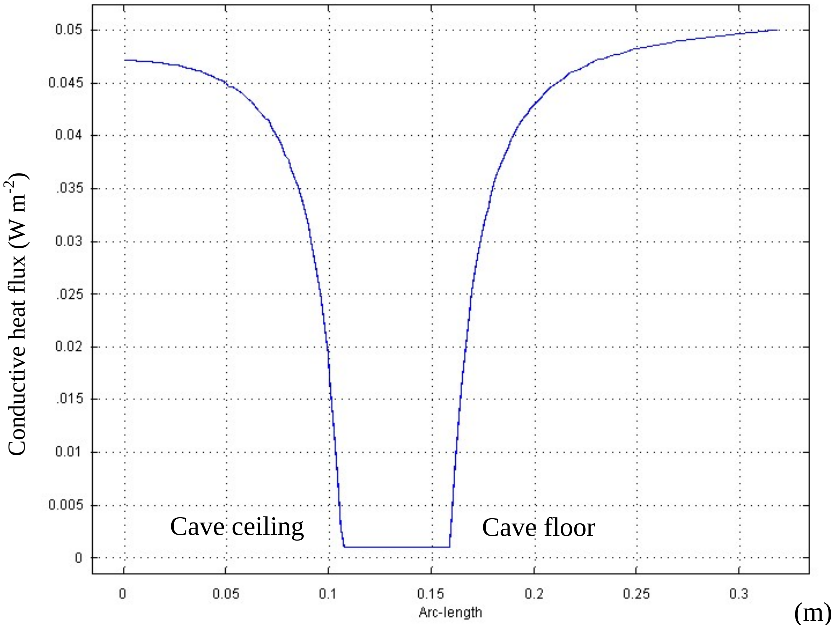

Figure 5.14: Plot of the magnitude of conductive heat flux (Wm^{-2}) along the vertical transect from the middle of the top boundary to the middle of the bottom boundary through the center of the cave. The arc-length is the transect length.

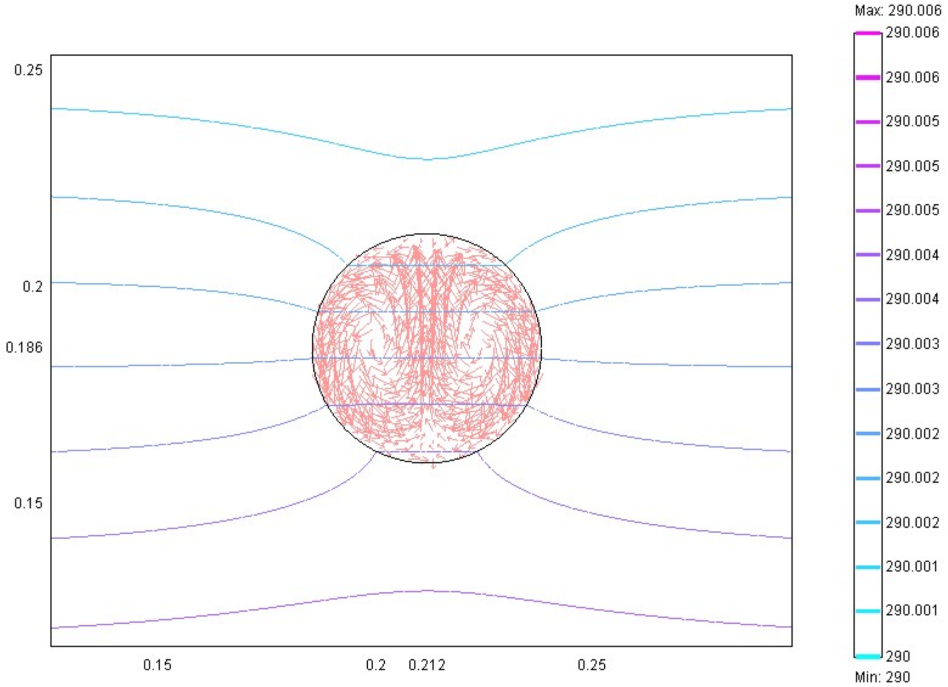

Figure 5.15: Circular cave model with contour lines indicating temperature (K), and arrows indicating the velocity field (m s^{-1}). The vicinity of the cave in Figure 5.12 is enlarged.

Figure 5.15 shows temperature contour lines in the vicinity of the circular cross-section cave, in which rock temperature and air temperature across the cave side walls are different, whereas they are the same across the cave ceiling and floor. Thus, the intensity of geothermal transfer varies in the side walls of this cave; whereas that of the side boundaries of the air-filled cavity-only models (Figure 5.2) is zero.

Therefore, the variation of heat transfer at the side walls of the circular cross-section cave model and at the four corners of the rectangular cave model could contribute to create organized flow patterns with ultra low velocities; the magnitude of the velocity field in the circular cave model (Figure 5.12) is 10^{-9} m s^{-1} and that of in the rectangular cave 10^{-6} m s^{-1} (Figure 5.10).

Table 5.4: Circular cross-section cave model. The length of the bottom boundary $L = 8H$ (m), where H is the height of the circular cave, and q is the heat flux of 0.05 $\mathrm{Wm^{-2}}$.

Model	*H (m)*	*Ra_1*	*Number of elements*	*Number of cells*	*Avg. velocity ($\mathrm{m\ s^{-1}}$)*	*Avg. temp. (K)*	*Boundary integration (Bi) ($\mathrm{Wm^{-1}}$)*	*Error* $\left\lvert\frac{Bi}{L\,q}\right\rvert 100(\%)$
F 5.12	0.053	17	4638	2	$6.265\mathrm{x}10^{-9}$	290.003	$-1.389\mathrm{x}10^{-7}$	$6.551\mathrm{x}10^{-6}$

5.2 Intensity of Heat Flux

Geothermal heat flux varies depending on the age of materials or timing of tectonic events (see Section 2.5). For example, geothermal heat flux near Carlsbad Cavern is about 0.045 $\mathrm{Wm^{-2}}$ [Mansure and Reiter, 1977]. That of Kartchner Cavern, AZ is about 0.074 to 0.085 $\mathrm{Wm^{-2}}$ [Buecher, 1999; Witcher et al., 1982]. This section examines how the intensity of geothermal heat flux affects air velocity, temperature and flow patterns inside caves.

Two types of models are created: one is a horizontally dominated cave (height x width = 0.225 m x 0.45 m); and the other is a vertically dominated cave (0.45 m x 0.225 m). The various heat fluxes are applied at the bottom boundary, and the spatial average values for velocity and temperature inside a cave are calculated. Figure 5.16 shows a model that has a horizontal cave with top, side, and bottom boundaries located at $2H$, $3H$, and $3H$, respectively, from a cave structure ($H = 0.225$ m). The bottom boundary has a heat flux of 0.06 $\mathrm{Wm^{-2}}$. Figure 5.17 illustrates a vertical cave model with top, side, and bottom boundaries located at $2H$, $3.5H$ and $5H$, respectively, from a cave structure. The bottom boundary has a heat flux of 0.06 $\mathrm{Wm^{-2}}$. We do not show other variations of heat fluxes here. Tables 5.5 and 5.6 summarize the models.

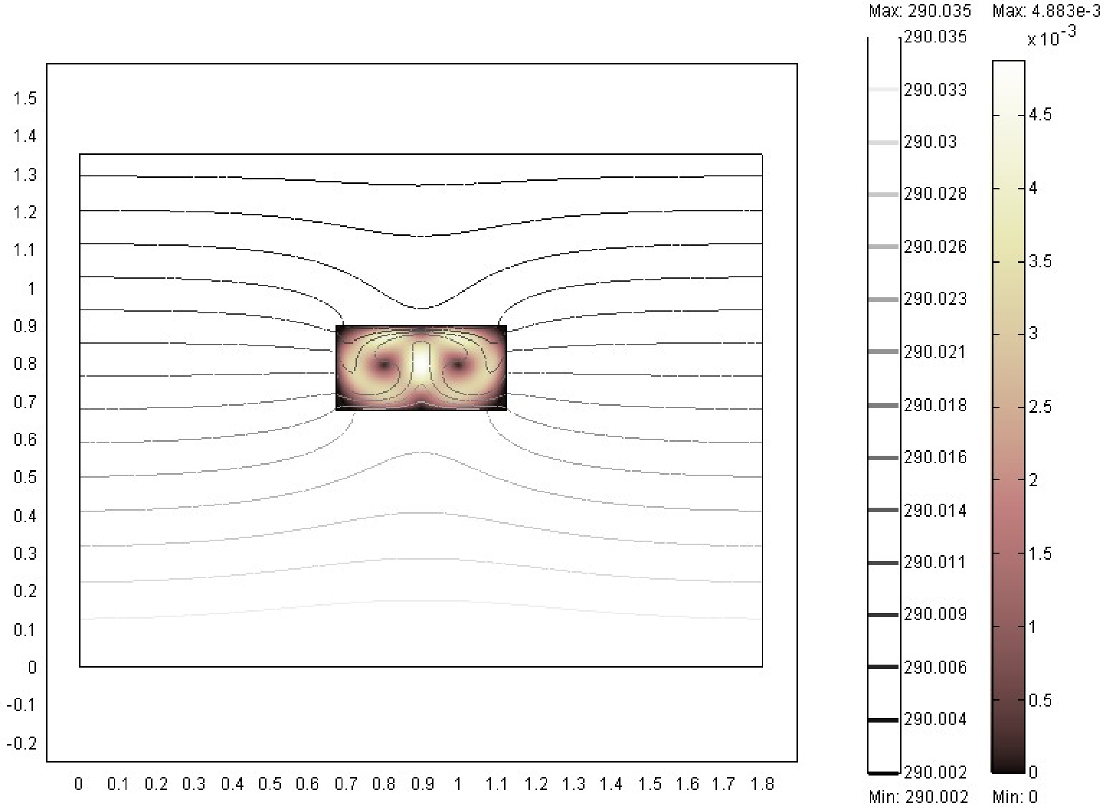

Figure 5.16: Horizontal cave model with contour lines indicating temperature (K), and surfaces indicating the velocity field (m s^{-1}). Heat flux on the bottom boundary = 0.06 Wm^{-2}. Cave height (*H*) = 0.225 m, and cave width =2*H*. The length of the bottom boundary *L* = 8*H*.

Table 5.5: Effects of intensity of heat flux for horizontal cave models. Ra_1 is based on the height of a cave *H* = 0.225 m and the heat flux *q*. The length of the bottom boundary *L* = 8*H*.

Bottom heat flux (q) (Wm^{-2})	*Ra_1*	*Number of elements*	*Number of cells*	*Avg. velocity (m s^{-1})*	*Avg. temp. (K)*	*Boundary integration (Bi) (Wm^{-1})*	*Error* $\left\|\frac{Bi}{L\,q}\right\|100(\%)$
0.05	5535	2550	4	9.921×10^{-4}	290.014	9.266×10^{-6}	1.030×10^{-2}
0.06	6642	2550	2	2.184×10^{-3}	290.016	1.071×10^{-5}	9.913×10^{-3}
0.07	7749	2550	4	1.194×10^{-3}	290.019	1.298×10^{-5}	1.030×10^{-2}
0.08	8856	2550	4	1.264×10^{-3}	290.022	1.485×10^{-5}	1.031×10^{-2}
0.09	9963	2550	4	1.319×10^{-3}	290.025	1.674×10^{-5}	1.033×10^{-2}
0.10	11069	2550	4	1.356×10^{-3}	290.027	1.866×10^{-5}	1.036×10^{-2}

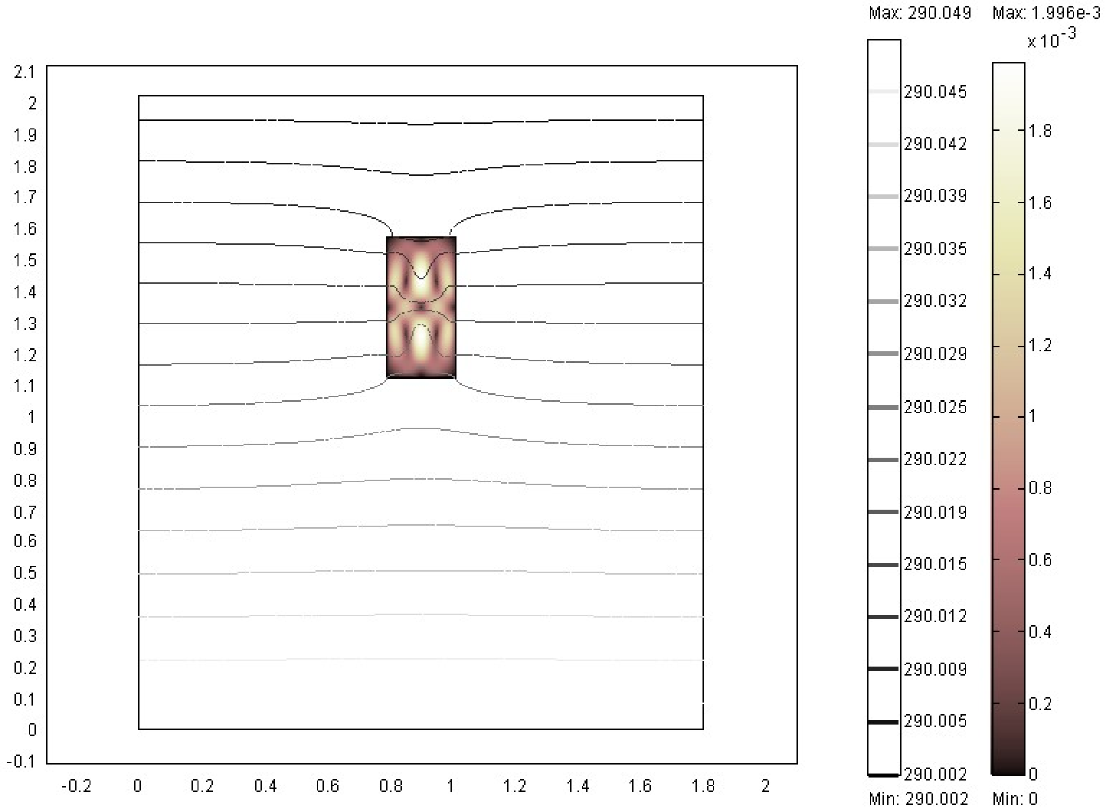

Figure 5.17: Vertical cave model with contour lines indicating temperature (K), and surfaces indicating the velocity field (m s^{-1}). Heat flux on the bottom boundary = 0.06 Wm^{-2}. Cave height (2*H*) = 0.45 m, and cave width (*H*) = 0.225 m. The length of the bottom boundary *L* = 8*H*.

Table 5.6: Effects of heat flux intensity for vertical cave models. Ra_1 is based on the width of a cave $W = H = 0.225$ m and the heat flux q. The length of the bottom boundary $L = 8H$.

Bottom heat flux(q) (Wm^{-2})	*Ra_1*	*Number of elements*	*Number of cells*	*Avg. velocity (m s^{-1})*	*Avg. temp. (K)*	*Boundary integration (Bi) (Wm^{-1})*	*Error* $\left\lvert\frac{Bi}{L\,q}\right\rvert 100(\%)$
0.05	5535	2582	4	6.337×10^{-4}	290.014	6.304×10^{-6}	7.004×10^{-3}
0.06	6642	2582	4	8.024×10^{-4}	290.017	7.531×10^{-6}	6.973×10^{-3}
0.07	7749	2582	4	9.470×10^{-4}	290.020	8.748×10^{-6}	6.943×10^{-3}
0.08	8856	2582	4	1.072×10^{-3}	290.023	9.961×10^{-6}	6.917×10^{-3}
0.09	9963	2582	4	1.182×10^{-3}	290.026	1.117×10^{-5}	6.897×10^{-3}
0.10	11069	2582	4	1.280×10^{-3}	290.029	1.239×10^{-5}	6.884×10^{-3}

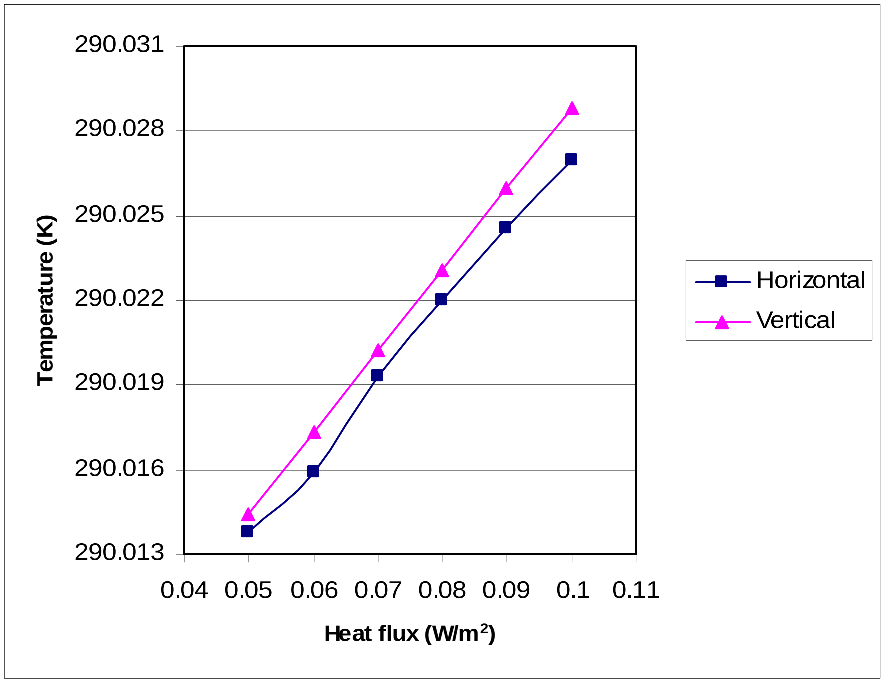

Figure 5.18: Average inside cave temperature versus heat flux at the bottom boundary.

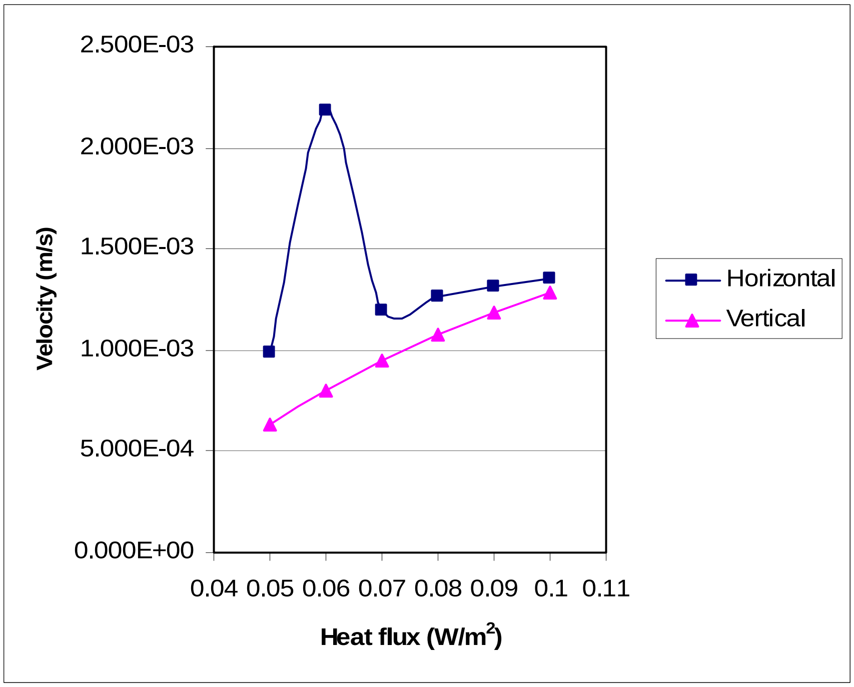

Figure 5.19: Average inside cave velocity versus heat flux at the bottom boundary.

Figures 5.18 and 19 summarize the effects of heat flux intensity on temperature and velocity, respectively. For both horizontal and vertical models, temperature and velocity increase as the heat flux on the bottom boundary increases. In terms of velocity however, the number of convection cells has significant influence. For example, the number of convection cells in a horizontal cavity with heat flux of 0.06 Wm^{-2} is two, which leads to a high velocity compared to the cases that produced four convection cells. For both types of models, the number of convection cells is usually similar (four), but occasionally they depart from this number for reasons that are unclear to us at present. In Figure 5.18, temperature of the vertical caves is slightly higher than that of the horizontal cavity, but there is an opposite relationship for velocity.

5.3 Geometry Effects

Geometry is an important factor that creates particular flow patterns inside caves. This section examines the effects of geometry on velocity, temperature and flow patterns using various, but simple geometries.

5.3.1 Entrance Passages

(1) Width of Entrance Passages

The large Natural Entrance of Carlsbad Cavern, NM descends more than 200 m underground following steep and narrow trails through a large trunk passage called the Main Corridor [Carlsbad Caverns, 2005a]. Not surprisingly, this large entrance passage appears to have a significant impact on the micrometeorology of Carlsbad Cavern. We would like to understand the relationship between the entrance width and the values for velocity and temperature in the entrance passage. Figure 5.20 is an example model in which the ratio of the width of cave entrance (*W*) to the height of the main cavity (*H* = 0.2 m) is 0.125. The width of the main cavity is 5*H*, and the height of the entrance passage is 3*H*. The distance between the side boundary and the cave structure is 7.5*H*, and between the bottom boundary and the cave structure is 8.5*H*. Figures 5.21 thru 5.26 show cave components in which the ratio of *W/H* was gradually increased as 0.25, 0.5, 0.75, 1 and 1.25, respectively, and the average velocity and temperature in the entrance passage are calculated. Evaluations are found in Table 5.7.

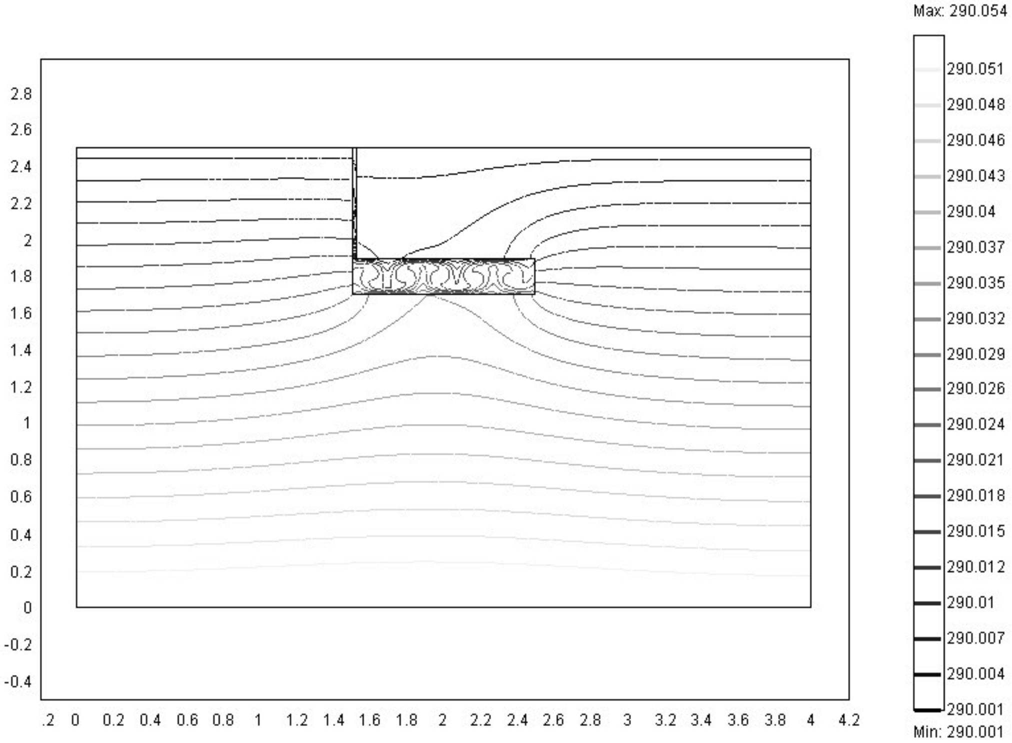

Figure 5.20: Width of entrance (W) is 0.125 *H*, where *H* is the main cavity height of 0.2 m. The length of the bottom boundary *L* = 20*H*. Model shows contour lines indicating temperature (K), and streamlines indicating the velocity field (m s^{-1}).

In Figure 5.20, a clear insulation effect of the main cavity is observed in the right hand side of the entrance passage (above the main cave), in which temperatures are lower than that in the left hand side of the entrance passage.

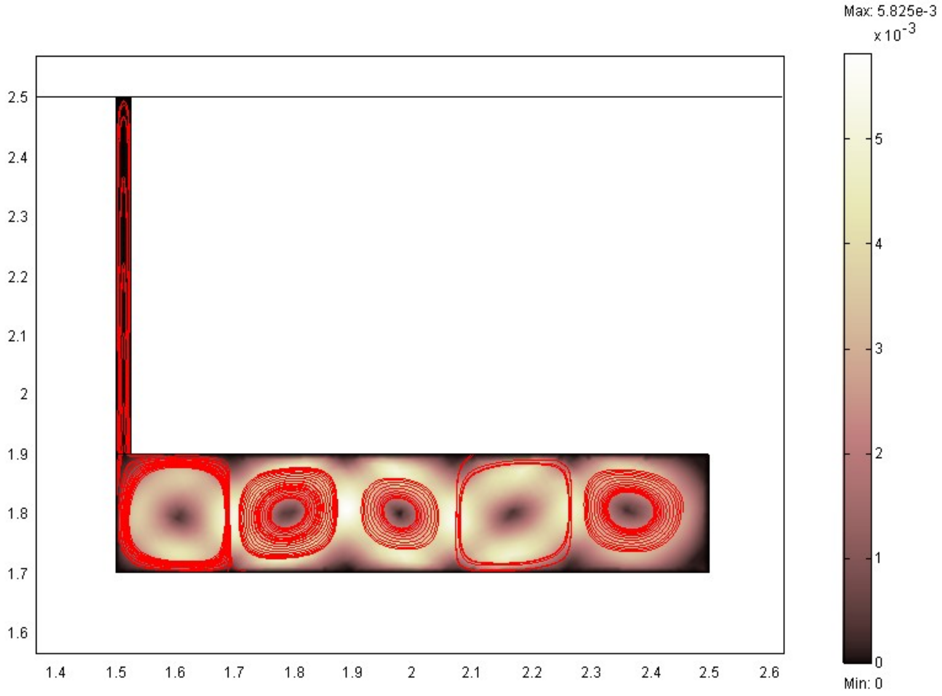

Figure 5.21: Width of entrance is 0.125*H*, where *H* is the main cavity height of 0.2 m. Model shows streamlines and surfaces indicating the velocity field (m s^{-1}).

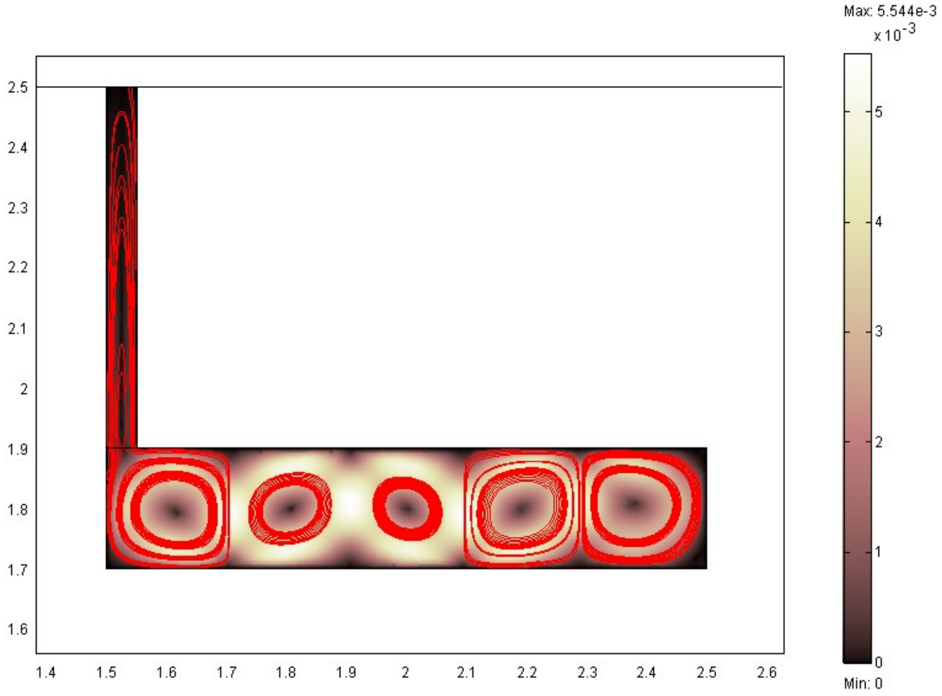

Figure 5.22: Width of entrance is 0.25*H*, where *H* is the main cavity height of 0.2 m. Model shows streamlines and surfaces indicating the velocity field (m s^{-1}).

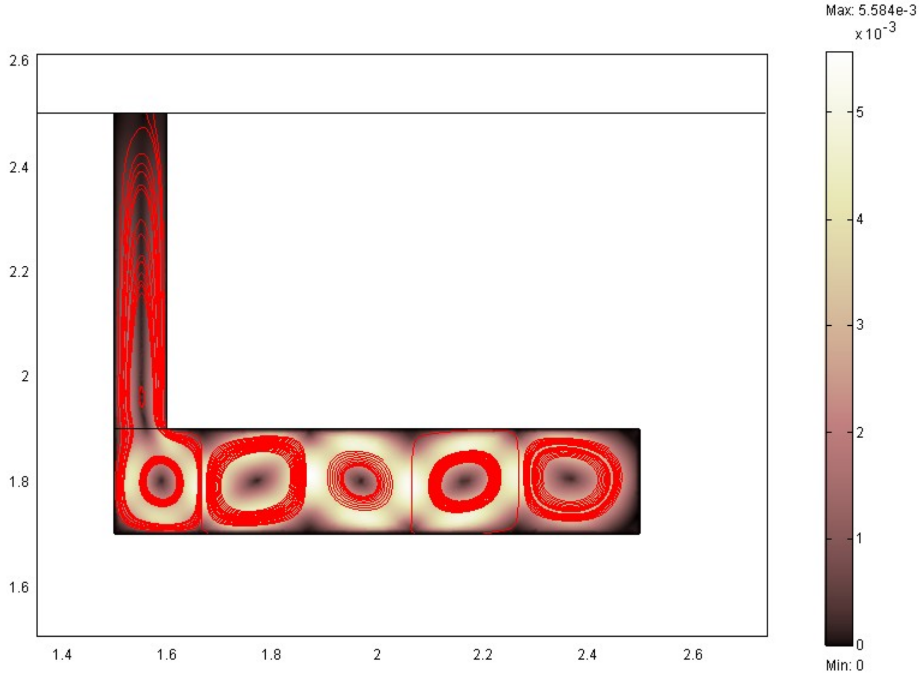

Figure 5.23: Width of entrance is 0.5*H*, where *H* is the main cavity height of 0.2 m. Model shows streamlines and surfaces indicating the velocity field (m s^{-1}).

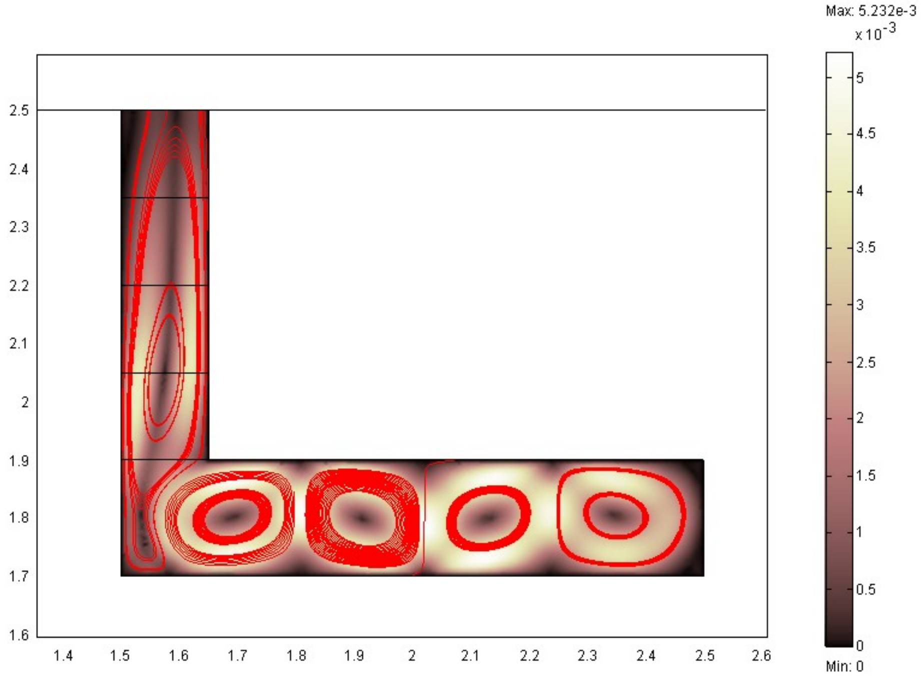

Figure 5.24: Width of entrance is 0.75*H*, where *H* is the main cavity height of 0.2 m. Model shows streamlines and surfaces indicating the velocity field (m s^{-1}).

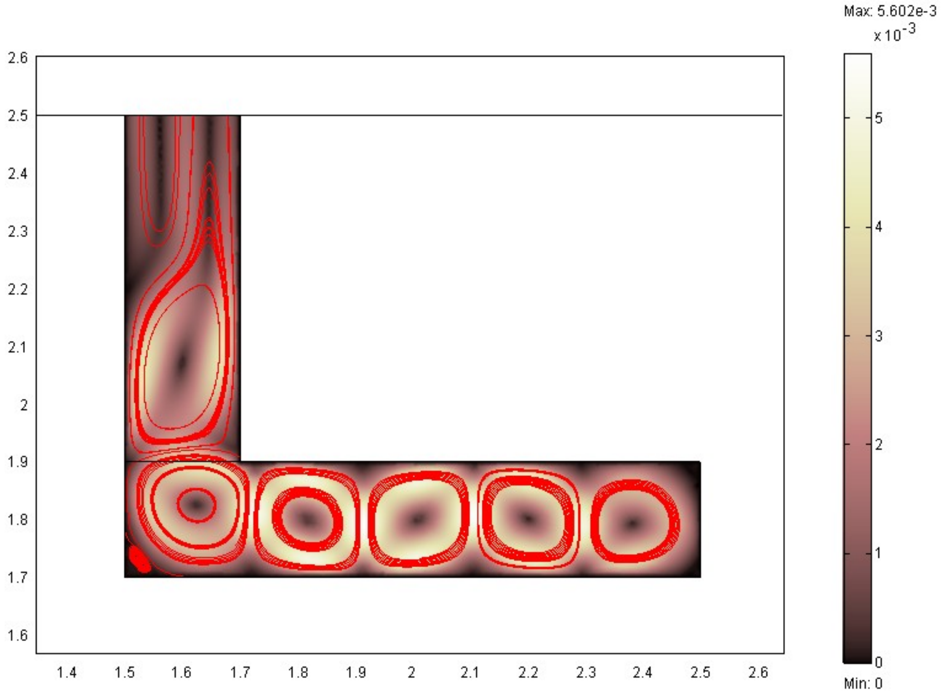

Figure 5.25: Width of entrance is 1*H*, where *H* is the main cavity height of 0.2 m. Model shows streamlines and surfaces indicating the velocity field (m s^{-1}).

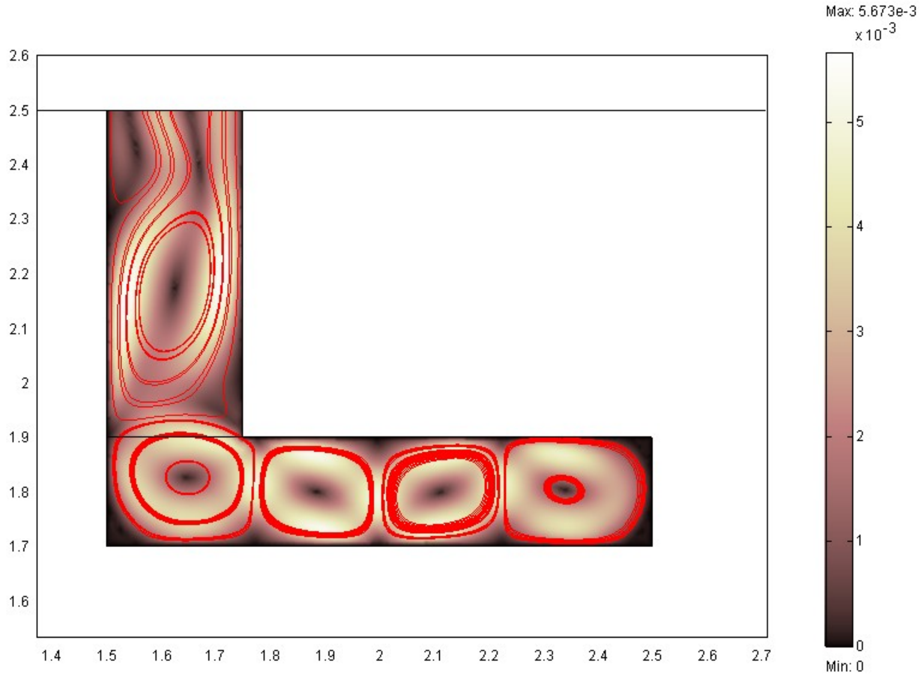

Figure 5.26: Width of entrance is 1.25*H*, where *H* is the main cavity height of 0.2 m. Model shows streamlines and surfaces indicating the velocity field (m s^{-1}).

Table 5.7: Entrance width effects. The height of the main cavity H = 0.2 m. The length of the bottom boundary $L = 20H$ (m), and q is the heat flux of 0.05 Wm^{-2}. Ra_1 = 3455 based on H.

Model	*W/H*	*Number of elements*	*Number of cells in the main cavity*	*Avg. velocity (ms^{-1})*	*Avg. temp. (K)*	**Boundary integration (Bi) (Wm^{-1})*	*Error* $\left\|\frac{Bi}{L\,q}\right\|100(\%)$
F 5.21	0.125	3263	5	$3.589\text{x}10^{-5}$	290.0050	$-1.333\text{x}10^{-4}$	$6.663\text{x}10^{-2}$
F 5.22	0.25	3003	5	$1.600\text{x}10^{-4}$	290.0051	$-1.193\text{x}10^{-4}$	$5.963\text{x}10^{-2}$
F 5.23	0.5	3092	5	$7.747\text{x}10^{-4}$	290.0057	$-7.830\text{x}10^{-5}$	$3.915\text{x}10^{-2}$
F 5.24	0.75	2860	4	$1.580\text{x}10^{-3}$	290.0059	$-1.062\text{x}10^{-4}$	$5.312\text{x}10^{-2}$
F 5.25	1	2962	5	$1.565\text{x}10^{-3}$	290.0063	$-3.054\text{x}10^{-4}$	$1.527\text{x}10^{-2}$
F 5.26	1.25	2870	4	$2.411\text{x}10^{-3}$	290.0057	$-9.822\text{x}10^{-4}$	$4.911\text{x}10^{-1}$

*Boundary integrations are taken as the normal conductive heat flux. This method is applied to all following models that have entrances (see the explanations presented flowing Table 5.9).

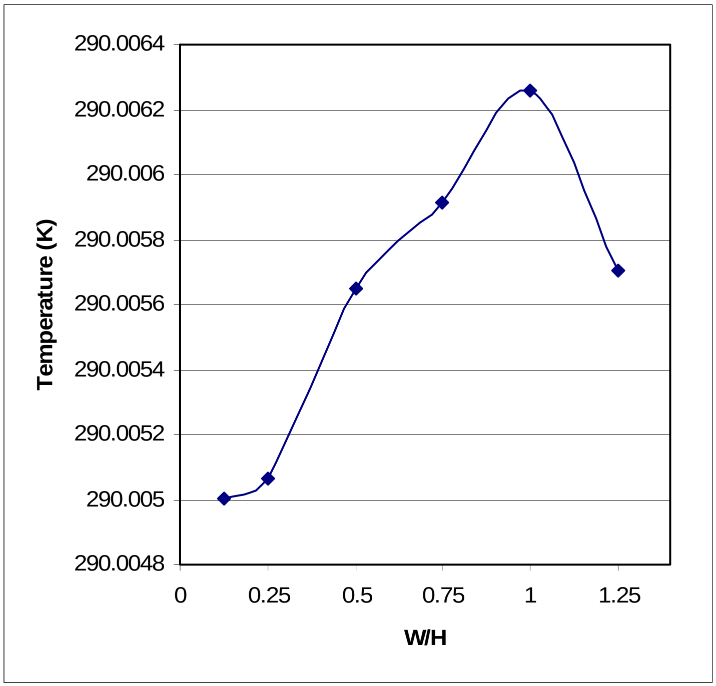

Figure 5.27: Average temperature in the entrance passage versus width of the entrance passage. W is the width of an entrance, and H = 0.2 m is the main cavity height.

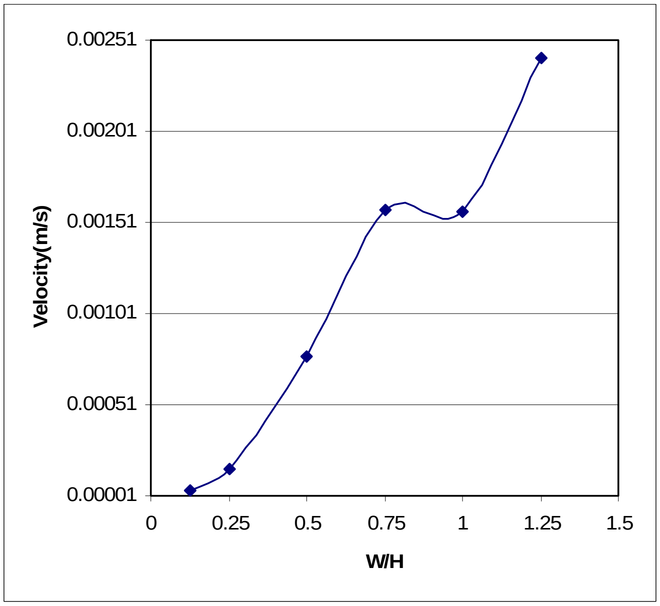

Figure 5.28: Average velocity field in the entrance passage versus width of the entrance passage. *W* is the width of entrance, and *H* = 0.2 m is the main cavity height.

Table 5.7, and Figures 5.27 and 5.28 summarize the relationship between the width of an entrance passage and the spatial average values for temperature and velocity. Both tend to increase as the entrance width increases, with several exceptions. In *W/H* = 1, the temperature is very high but the velocity is lower than that of *W/H* = 0.75. The number of convection cells in the main cavity is 5 when *W/H* = 1, whereas it is 4 when *W/H* = 0.75. In *W/H* = 1.25, the temperature is lower than that of *W/H* = 1, but the velocity is very high. The convection cell number in the main cavity is 4 when *W/H* = 1.25, whereas it is 5 when *W/H* = 1. The smaller number of main cavity convection cells appears to produce higher velocity, and the higher velocity appears to reduce temperature. The decrease in temperature in the larger entrance width could also be influenced by an increase in the air exchange between the surface and subsurface.

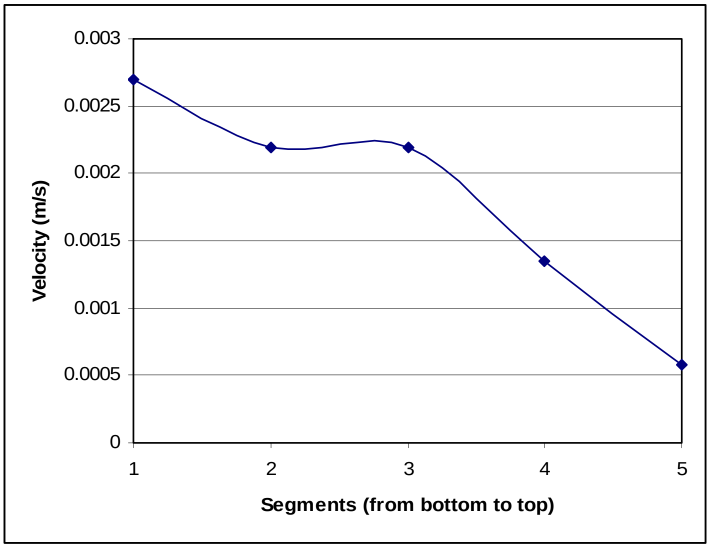

Figure 5.29: Average velocity field in each segment of Figure 5.24 from bottom to top (segment 1 is main cavity, and segments 2, 3, 4, 5 are 1/4, 2/4, 3/4, and 4/4 of the entrance passage, respectively).

Figure 5.29 shows the average velocity in each segment of Figure 5.24, in which *W/H* = 0.75. When there is no influence from surface weather conditions, velocity tends to decrease upward. This is a reasonable result because the source of energy is at the bottom, and energy gradually dissipates upward.

(2) Two Entrance Cases

Many caves have multiple entrances. For example, Carlsbad Cavern has the Natural Entrance and the Bat Cave Entrance (approximately half the diameter of the Natural Entrance). This section considers the effects of two entrances on velocity, temperature, and flow patterns in the entrance passages. Two types of models are created: large and small entrances are horizontally juxtaposed (Figure 5.30); and large and small entrances are rotated 45° so that the two entrances have a vertical relationship (Figure 5.31). Later in this section, the rotated model in Figure 5.31 is magnified so that we consider the effects of size.

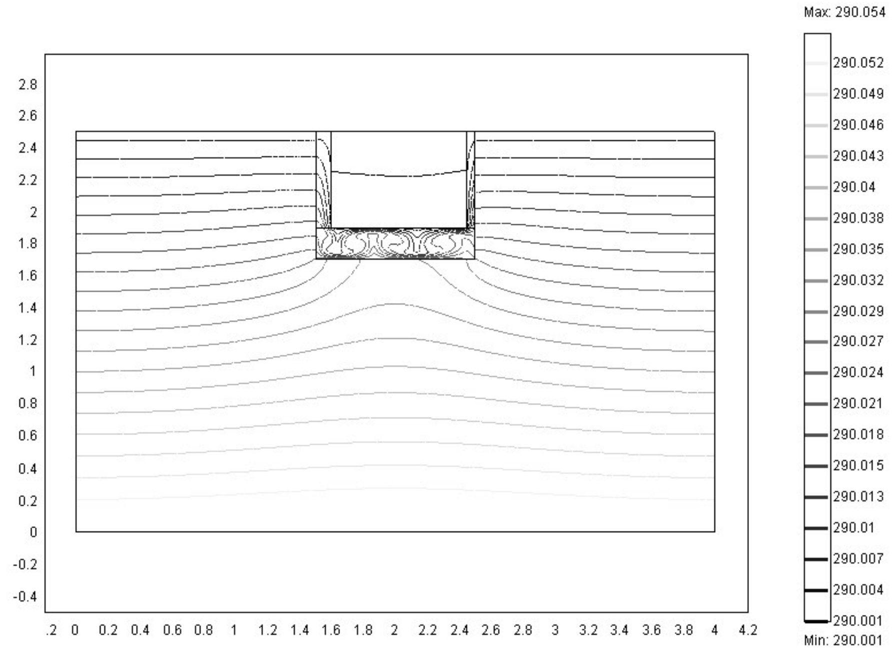

Figure 5.30: Horizontal cave model with two entrances. Height (*H*) and width of main cavity is 0.2 m and 5*H*, respectively. The large passage has a width of 0.5*H*, and height of 3*H*. The small passage has a width of 0.25*H* and height of 3*H*. The model shows contour lines indicating temperature (K).

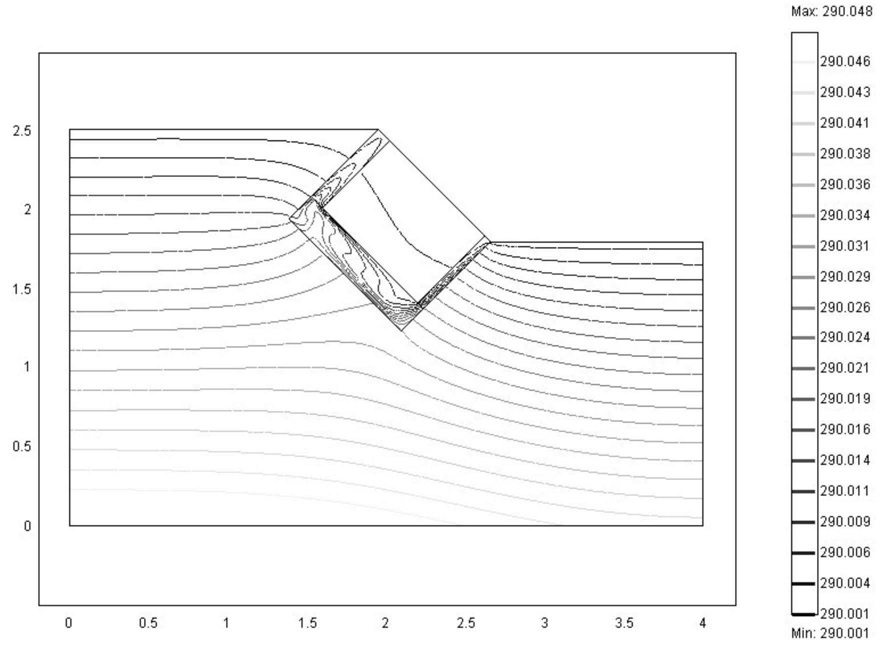

Figure 5.31: Tilted cave model with two entrances. The cave structure in Figure 5.30 is rotated clockwise by 45°. Height of main cavity (*H*) is 0.2 m and its width is 5*H*. The large passage has a width of 0.5*H*, and a height of 3*H*. The small passage has width of 0.25*H* and height of 3*H*. The model shows contour lines indicating temperature (K).

The model conditions are the same in Figures 5.30 and 5.31 but differ in cave geometries. In both models, a constant temperature of 290 K is assigned to the top boundaries, except for the cave entrances at which the boundary conditions of convective heat fluxes and normal flow with zero pressure are assigned. That is, air can move in or out through the boundary freely depending on the internal conditions. Note that temperatures of the area surrounded by the main cavity and the two entrances are low. Although there is a 2D exaggeration (see Section 4.1), here again, we can see the insulation effects of caves.

Figure 5.32 and 5.33 show arrows for the velocity field in the cave interiors in Figures 5.30 and 5.31, respectively. Both models have the same number of arrows (180), and the length of arrows indicates magnitude of velocity.

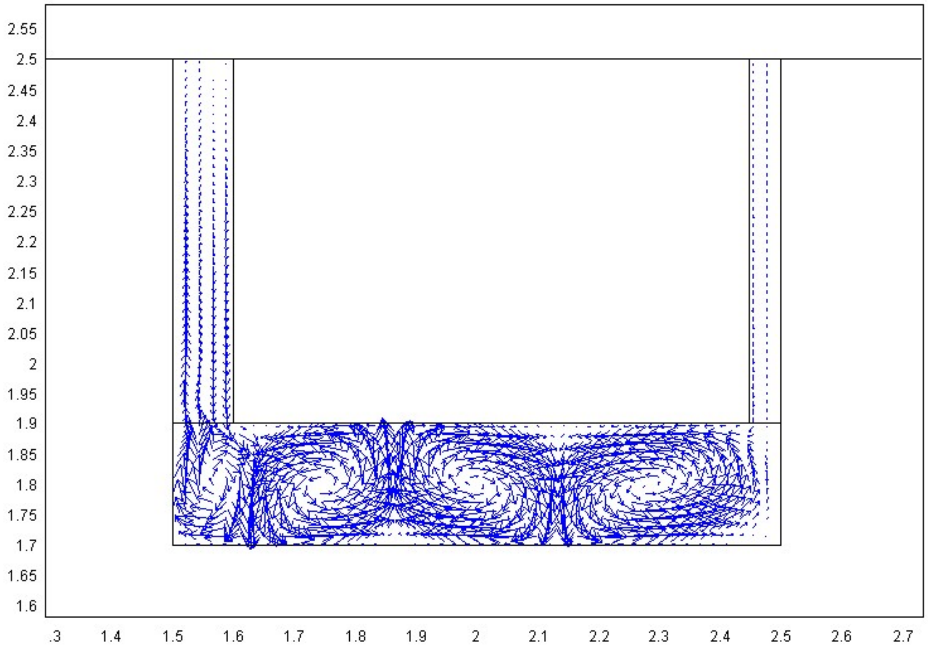

Figure 5.32: Horizontal model with two entrance passages showing arrows indicating the velocity field (m s^{-1}). The cave interior of Figure 5.30 is enlarged.

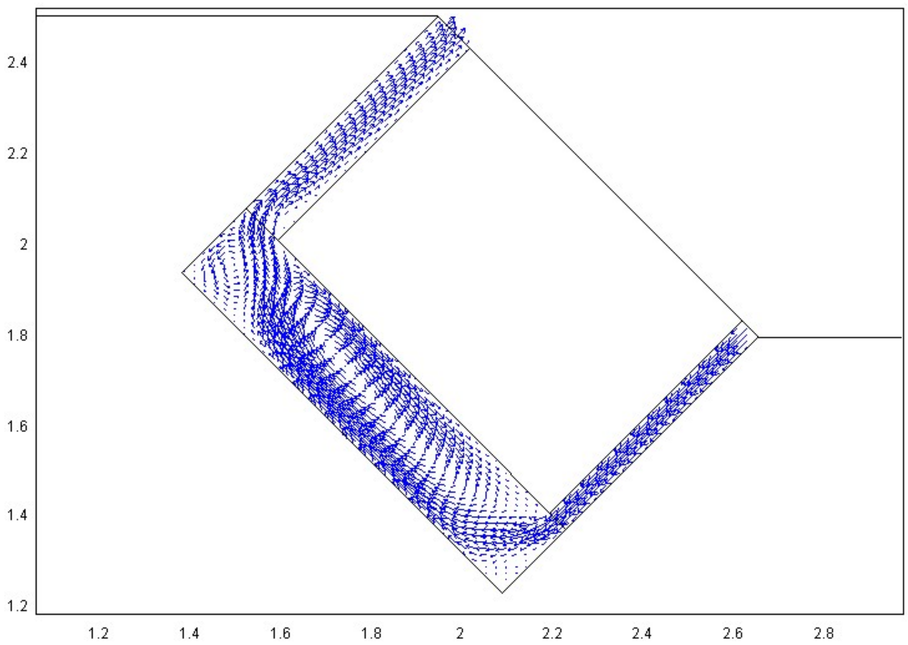

Figure 5.33: Tilted model with two entrances showing arrows indicating the velocity field (m s^{-1}). Large passage is above and small passage is below. The cave interior of Figure 5.31 is enlarged.

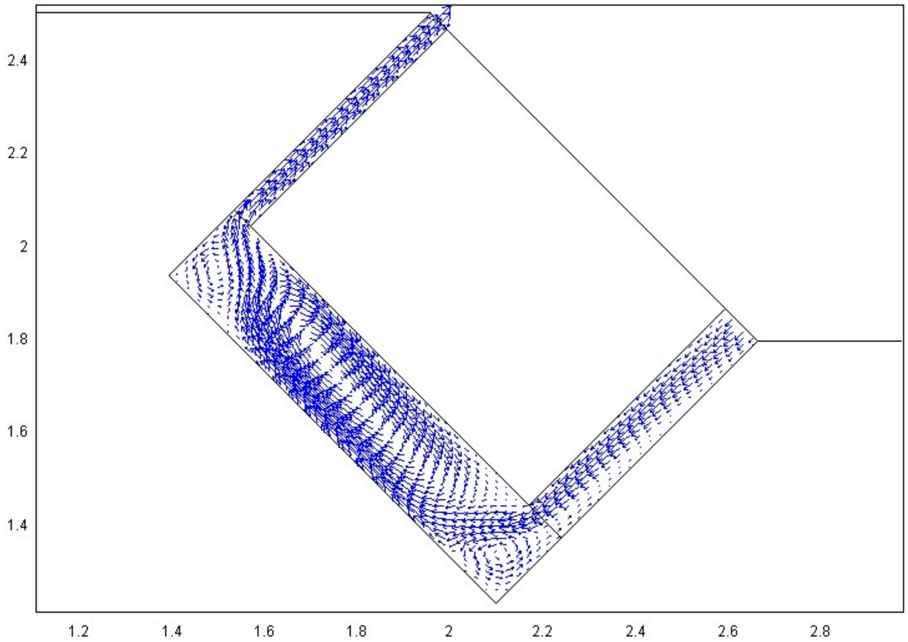

Figure 5.34: Tilted model with two entrances showing arrows indicating the velocity field (m s^{-1}). Small passage is above and large passage is below.

In Figure 5.32, four convection cells appear in the main cavity, and one elongated convection cell is observed in the larger entrance passage. The magnitude of velocity gradually decreases as the air ascends through the entrance passage. There are weak downward flows in the small passage. This flow pattern is changed dramatically when the cave is rotated 45°. In Figure 5.33, one elongated convection cell appears in the main cavity. Strong outward and inward flows are observed in the large and small passages, respectively. Figure 5.34 describes the situation in which the small passage is located above and the large passage below. From Figures 5.33 and 5.34, we can see that regardless of the width of entrance passages, the flow direction is inward in the lower passage and outward in the upper passage. If a cave is tilted (multiple entrance passages have some vertical relationships), air circulation is initiated. This circulation stems from internal factors, because there is no imposed flow component at the entrances, and the gravitational pressure gradient is ignored in our models. A summary of the models is found in Table 5.8 and Figures 5.35 and 5.36.

Table 5.8: Normal flow models with two entrances. The height of the main cavity H = 0.2 m, and the heat flux q is 0.05 Wm^{-2}. The length of the bottom boundary L = 20H. Ra_1 = 3455 based on H. L_a indicates a large entrance passage, and S a small entrance.

Model	*Number of elements*	*Ent.Pass.* L_a*=0.5H* *S=0.25H* *(H=0.2m)*	*Flow direction*	*Avg. velocity (ms^{-1})*	*Avg. temp. (K)*	*Boundary integration (Bi) (Wm^{-1})*	*Error* $\left\lvert\frac{Bi}{L\ q}\right\rvert 100(\%)$
F 5.32 (level)	4590	L_a (level) S (level)	in/out -	8.849x10^{-4} 3.048x10^{-4}	290.006 290.005	5.572x10^{-5}	2.786x10^{-2}
F 5.33 (tilt)	4508	L_a (above) S (below)	out in	2.297x10^{-3} 4.542x10^{-3}	290.004 290.006	-7.470x10^{-4}	3.735x10^{-1}
F 5.34 (tilt)	4543	L_a(below) S (above)	in out	1.795x10^{-3} 3.354x10^{-3}	290.006 290.002	-5.852x10^{-4}	2.926x10^{-1}

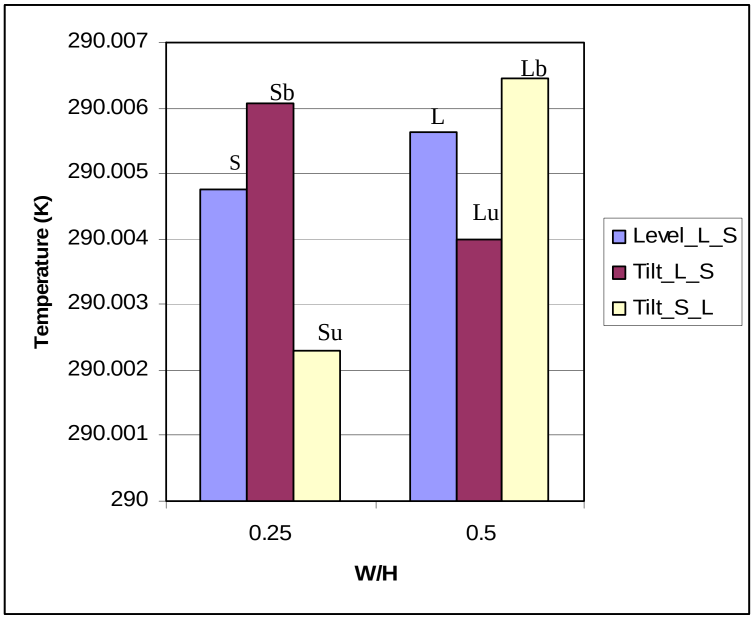

Figure 5.35: Average temperature of entrance passage versus width of entrance passage. In Level_L_S, a model is set level and the two side passages (*L*= *W/H* = 0.5 and *S*= *W/H* = 0.25, where *H* = 0.2 m) are horizontally juxtaposed. In Tilt_L_S, a model is tilted clockwise by 45° with *L* above (Lu) and *S* below (Sb). In Tilt_S_L, *S* is above (Su) and *L* is below (Lb). Note that when a model is level, the temperature is higher in a large entrance. When models are tilted, the lower entrance passages have higher temperatures.

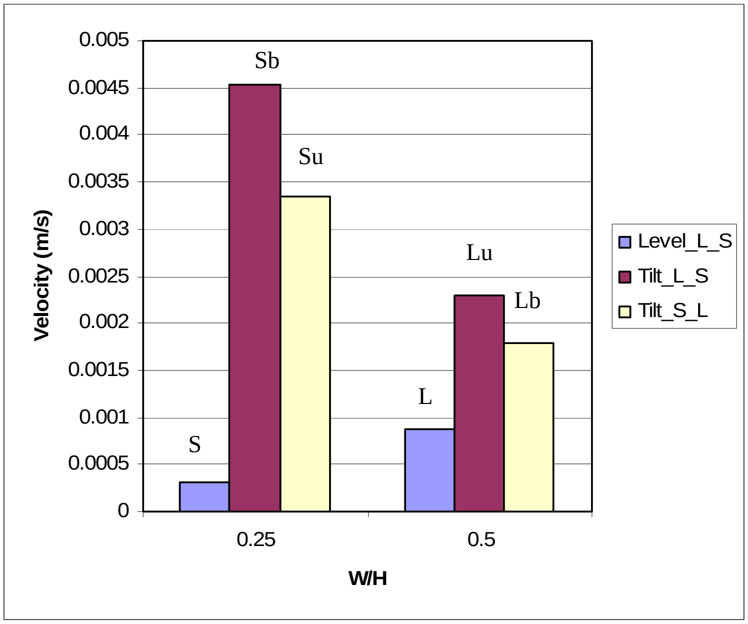

Figure 5.36: Average velocity field of entrance passage versus width of entrance passages. Note that when a model is level, the velocity field is higher in a large passage. When models are tilted, the higher velocity fields are observed in the small passages.

From Figures 5.35 and 5.36, we can see that when models are tilted, temperatures in the lower passages appear to be higher than that of the upper passages, but velocities are higher in the smaller passages regardless of their positions with respect to the larger passages. Can we observe the same phenomena in the models that have different size? Let's focus on the model configuration of Figure 5.33, in which the larger entrance passage is above, the smaller is below, and the height of the main cavity $H = 0.2$ m. We will increase the values for H from 0.2 m to 0.3 m and 0.4 m. Figure 5.37 shows the model whose H is 0.4 m (The figure for the model with $H = 0.3$ m is omitted).

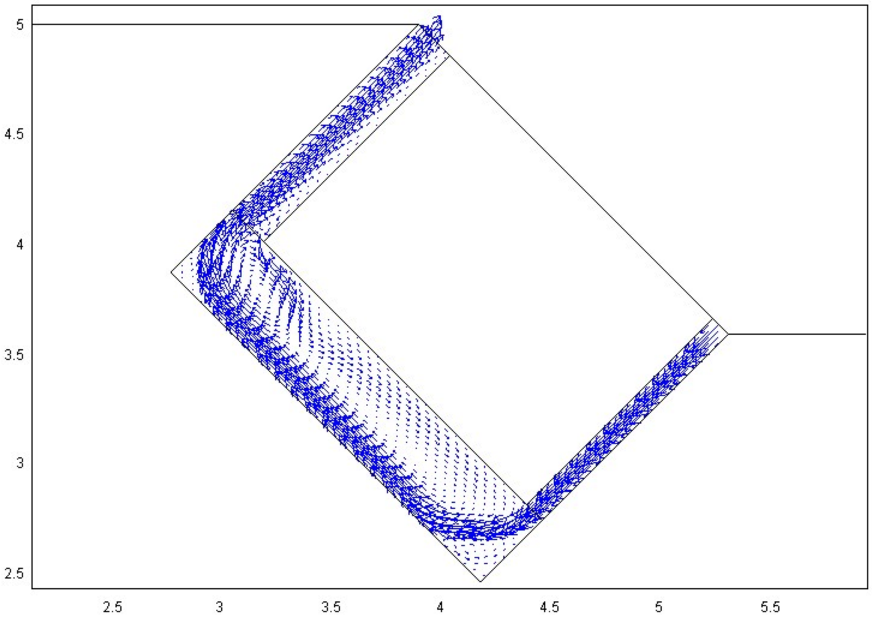

Figure 5.37: Large tilted model with two entrances showing arrows indicating the velocity field (m s^{-1}). Large passage is above and small passage is below. The height of the main cavity is 0.4 m. Relatively strong air circulation is observed.

In Figure 5.37, air circulation has become more effective, and the convection cell in the main cavity appears to be weaker compared to the smaller model in Figure 5.33. A summary of the models is found in Figures 5.38 and 39, and Table 5.9.

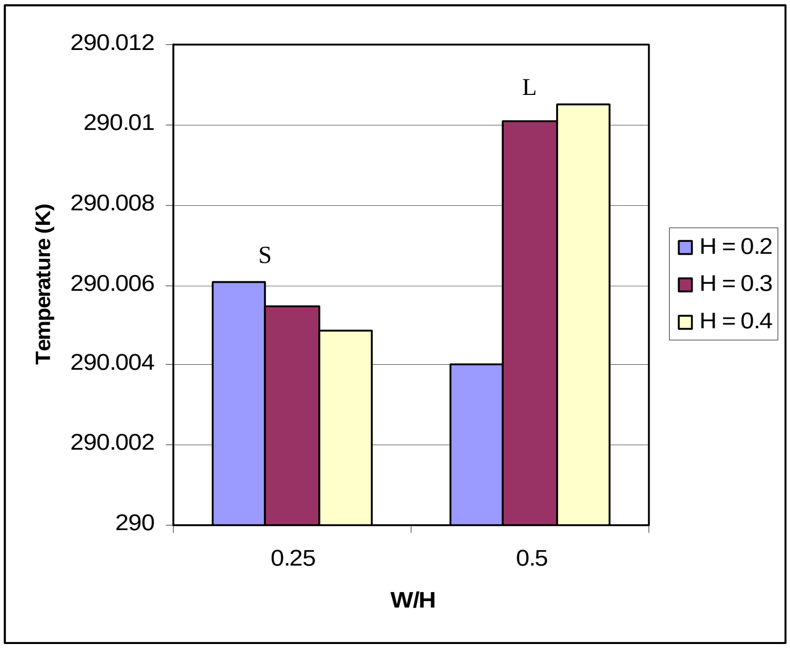

Figure 5.38: Effects of size on the average temperature in entrance passages (small passage *W/H* = 0.25 is located below, and large passage *W/H* = 0.5 above). *H* varies from 0.2 m to 0.3 m and 0.4 m. Note that in the larger models (*H* = 0.3 m and 0.4 m), temperatures are higher in the larger passages, and an opposite result is observed in the small model (*H* = 0.2 m).

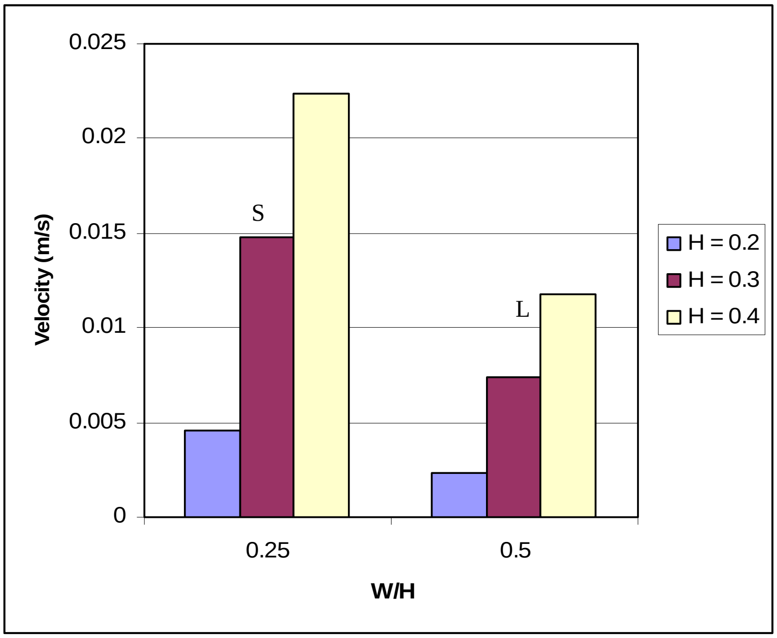

Figure 5.39: Effects of size on the average velocity field in entrance passages (small passage *W/H* = 0.25 is located below, and large passage *W/H* = 0.5 above). *H* varies from 0.2 m to 0.3 m and 0.4 m. Note that regardless of size of the models, the average velocity fields are higher in the smaller passages, and the phenomena are amplified as the size of the models increases.

In Figures 5.38, the average temperatures of the larger passages are higher than that of the smaller passages. An opposite result is observed in the small model. There is a possible explanation for this inverse result. We suggest that as the size of a model increases, the velocity of airflow within the small passage increases (Figure 5.39). This may thus reduce the average temperature of the small passage. The increase in the model size could also amplify the buoyancy forces, so that the warm air in the main cavity ascends more toward the larger passages. In turn, this could further raise their temperatures.

Table 5.9: Effects of size on models that are tilted and have two entrance passages. The length of the bottom boundary $L = 20H$, and q is the heat flux of 0.05 Wm^{-2}. L_a indicates a large entrance passage, and S a small entrance passage. The values for *a* and *b* are the normal conductive heat flux and the normal total heat flux (convective and conductive heat fluxes), respectively, integrated over the entire model boundary.

H (m)	*Number of elements*	*Ra_1*	*Flow direction L_a=0.5H S=0.25H*	*Avg. velocity ($m\ s^{-1}$)*	*Avg. temp. (K)*	*Boundary integration (Bi) (Wm^{-1})*	*Error* $\left\lvert \frac{Bi}{L\ q} \right\rvert 100(\%)$
0.2	4508	3455	(L_a) out (S) in	2.297×10^{-3} 4.542×10^{-3}	290.004 290.006	(a) -7.470×10^{-4} (b) -1.550×10^{-2}	0.3735 7.7510
0.3	7031	17492	(L_a) out (S) in	7.437×10^{-3} 1.480×10^{-2}	290.010 290.005	(a) -1.108×10^{-2} (b) -1.654×10^{-1}	3.692 55.133
0.4	8612	55285	(L_a) out (S) in	1.181×10^{-2} 2.237×10^{-2}	290.010 290.005	(a) -3.235×10^{-2} (b) -5.218×10^{-1}	8.088 130.450

In Table 5.9, errors based on the normal total heat flux *(b)* are unacceptably large and increase as the size of the models increases. The results appear to violate the conservation of energy. The values for boundary integration *(b)* were based on the normal total heat fluxes integrated over the entire model boundary. These models have entrances, so the normal total heat flux includes both convective and conductive heat fluxes (see explanations following Table 3.4). To identify the reasons for these large errors, we consider the convective heat flux and the conductive heat flux separately.

(2.1) Net Convective Heat Flux, Net Conductive Heat Flux, and Error Calculation

Table 5.10: Net convective flux and net conductive flux. B_{La} and B_S are the convective heat flux integrated over the large and small entrances, respectively. Bc is the conductive heat flux integrated over the entire model boundary. The length of the bottom boundary $L = 20H$, and q is the heat flux of 0.05 Wm^{-2}.

H (m)	*Convec. heat flux (B_{La}) (Wm^{-1}) outflow*	*Convec. heat flux (B_S) (Wm^{-1}) inflow*	*Net convec. heat flux ($A = B_{La} + B_S$) (Wm^{-1})*	*Net cnduc. heat flux (Bc) (Wm^{-1})*	*Normalized A* $\left\lvert\frac{A}{B_S}\right\rvert 100(\%)$	***Normalized Bc*** $\left\lvert\frac{Bc}{L\,q}\right\rvert 100(\%)$	*Error ($B_T=A+Bc$)* $\left\lvert\frac{B_T}{L\,q}\right\rvert 100(\%)$
0.2	79.475	-79.490	$-1.476\text{x}10^{-2}$	$-7.470\text{x}10^{-4}$	$1.856\text{x}10^{-2}$	**0.3735**	7.7510
0.3	388.280	-388.434	$-1.543\text{x}10^{-1}$	$-1.108\text{x}10^{-2}$	$3.973\text{x}10^{-2}$	**3.692**	55.133
0.4	782.248	-782.738	$-4.899\text{x}10^{-1}$	$-3.235\text{x}10^{-2}$	$6.259\text{x}10^{-2}$	**8.088**	130.450

Table 5.10 describes the boundary integration values and error calculations obtained by separating the convective heat flux (B_{La} and B_S) and the conductive heat flux (Bc) from the normal total heat flux (B_T). The models in Table 5.10 are the same as those in Table 5.9. In those models, the surface air enters into a cave through the small entrance, and escapes through the large entrance (see Figure 5.37). Convective heat is the heat transported by fluid flow (airflow in our case). We obtained the normal convective heat fluxes (B_{La} and B_S) separately from the two entrance boundaries. The models simulate steady state conditions, so if there is no error, $A = B_{La} + B_S = -Bc$ (conductive heat flux and convective heat flux are balanced). The net convective heat flux A was normalized by dividing by the inward convective heat flux B_S (at the small entrance). The negative values for A indicate that in the models the heat carried into the caves is larger than the heat carried out of the caves. However, the resulting normalized

net convective heat fluxes were sufficiently small, and inward and outward convective heat fluxes with respect the cave domains appear to be balanced.

The net normal conductive heat fluxes *Bc* were taken over the entire model boundary including the entrances. The values *Bc* are approximately 5 or 6 orders smaller than B_{La} or B_S, and one or two orders smaller than *A*. The magnitude of conductive heat flux is much smaller than that of convective heat flux. The normalized net conductive heat flux is relatively large compared to the normalized net convective heat flux, and it gets larger in larger models. The negative sign in *Bc* indicates that the entire amount of heat conducted into the model is larger than that conducted out of the models. The reasons for these results could be: 1) heat conducted into the caves is carried mostly by convection within the caves, so from the conductive heat flux perspective, the heat conducted into the caves does not move out of the caves; and 2) convective heat flux becomes larger with larger caves, which in turn induces more heat conduction into caves from the surroundings. Consequently, the models have net gain of conductive heat flux, and the gain becomes larger in larger models. However, the normalized net conductive heat fluxes are not extreme values, so the conductive heat fluxes entered into and escaped from the models are fairly balanced.

The *Errors* (the same as the errors based on *b* in Table 5.9) were calculated by the normal total heat flux ($B_{La} + B_S + Bc$) divided by the applied heat flux (*qL*) at the bottom boundary. The resulting errors are unacceptably large. This result is due to the fact that the net convective heat flux *A* is the difference between two large numbers (B_{La} and B_S). As discussed in the previous paragraph, the magnitude of convective heat flux is much larger than that of conductive heat flux. The net convective heat fluxes ($A = -4.9 \times 10^{-1}$

W m^{-1} when H = 0.4 m) are sufficiently small compared to the magnitude of convective heat fluxes (B_S = -783 W m^{-1} when H = 0.4 m), but they are large compared with the net conductive heat fluxes (Bc = -3.2 x 10^{-2} W m^{-1} when H = 0.4 m). The applied conductive heat flux (qL) is small compared to the convective heat flux (qL = -4.0 x 10^{-1} W m^{-1} and B_{La} = 782 W m^{-1} when H = 0.4 m). Errors are obtained by the sum of A (magnitude of 10^{-1}) and Bc (magnitude of 10^{-2}) divided by qL (magnitude of 10^{-1}). When H = 0.4m, A is larger than qL and, thus, the calculated errors become more than 100%. A is large because it is the difference between two large numbers (B_{La} and B_S). Errors may become larger with larger models since the larger numbers (B_{La} and B_S) also become larger.

Another normalized error which might be more applicable to these cases would be to take the net total flux over the entire boundary and divide by all inward fluxes (conduction from the bottom boundary qL and convection at the small cave entrance B_S). The resulting errors should be much smaller than the errors in Table 5.10, since we introduce the orders of magnitude larger number B_S in the denominator. However, sometimes the large entrances of models have noticeable inward flow components in addition to outward flow components. In that case, we cannot distinguish the inward and outward fluxes at the large entrance boundary. This may make the error calculation more complicated. Thus, to avoid such complications, we exclude the convective heat flux, and calculate errors based on the normal conductive heat flux integrated over the entire model boundary (errors based on a in Table 5.9, and *Normalized Bc* in Table 5.10).

(2.2) Summary of the Models with Two Entrances

From the models that have two entrances, we have observed: (1) that air circulation is effective when a model is tilted and the effect is amplified in the larger sized models; (2) in the tilted models, the small passages have higher velocity flows regardless of their positions with respect to the larger passages; (3) inflow occurs in the lower passage and outflow in the upper passage regardless of their size; and (4) the average temperature of the passages appears to depend on the average airflow velocity (the high flow velocity may reduce the temperature of the passage). These relationships were derived from small and very simple models. Of course, they could vary significantly depending upon the degree of tilt or the relative width of two entrance passages. Thus, we cannot generalize the relationships at this moment. However, we may be able to consider if the observed phenomena in the real systems can be explained at least in principle by those relationships found by the small computer models.

5.3.2 Presence of Speleothems

Speleothems are cave features created after the underground chamber has been formed. Such speleothems can be subaqueous in origin, i.e. formed in water, or subaerial, i.e. formed in air. Subaqueous speleothems are typically the result of slow-moving or still water, usually containing calcium carbonate, which has been dissolved from the limestone where the cave was formed. When this water enters the cave, a chemical change causes the calcium carbonate to precipitate, creating all manner of cave formations and features. Subaerial speleothems grow in air-filled cavity but often are moist structures and the carbonate chemistry briefly mentioned above is also important for these formations. Stalagmites grow up from the floor of a cave (e.g., Figure 5.40). Stalactites form hanging from the roof of a cave [Desert USA, 2004]. There are numerous other speleothem types produced in a variety of ways [Hill and Forti, 1997].

In this section, we will consider the effects of several of the most common speleothem types on temperature, velocity, and flow patterns. We create three types of highly simplified cave models: 1) cave with no speleothems (no), 2) cave with a stalagmite (bottom), and 3) a cave with a stalactite (up).

Most speleothems in carbonate caves are formed of the mineral calcite. The important properties of solid materials for our models are density (ρ) and thermal conductivity (k). The typical values for ρ and k of limestone are 2200 – 2800 kg m^{-3}, and 2 – 3.4 W m^{-1} K^{-1}, respectively (We have chosen 2500 kg m^{-3} and 2.5 W m^{-1} K^{-1} for our models) [Turcotte and Schubert, 1982, 432]. The density of mineral calcite is 2711 kg m^{-3} [Dean, 1999, 3.21], and its typical thermal conductivity is 3. 4 – 3.7 W m^{-1} K^{-1} [Bouguerra et al., 1997]. Those values of limestone and mineral calcite are similar compared to those of air (ρ = 1.201 kg m^{-3}, and k = 0.0255 W m^{-1} K^{-1}). Thus, the properties of limestone (see Table 3.3) are assigned to these speleothems for simplicity.

Figure 5.40: Hall of Giants [Carlsbad Caverns National Park, 2005b].

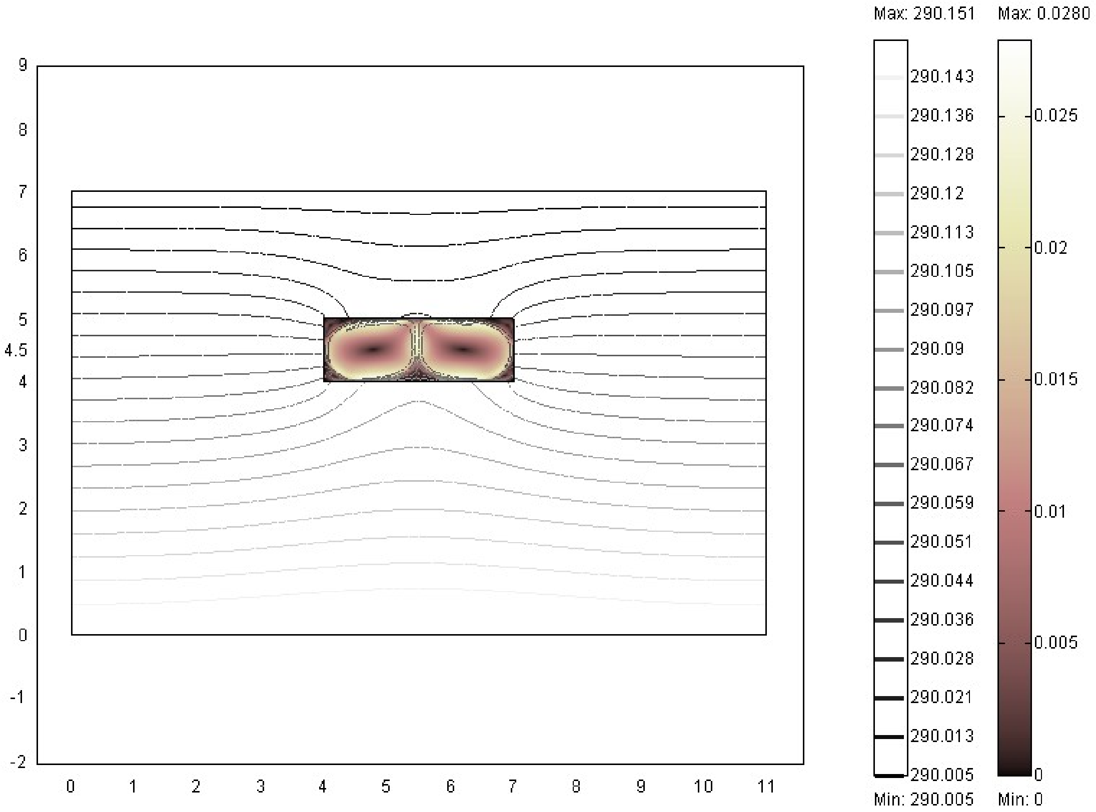

Figure 5.41: Cave model with contour lines indicating temperature (K) and surfaces indicating the velocity field (m s^{-1}). No speleothems are present. Height of the cave is 1m and width is 3 m.

The cave represented in Figure 5.41 has a height of H = 1 m, and a width of 3H; corresponding Ra_1 is $10^{6.33}$. The top, side, and bottom boundaries are located 2H, 4H, and 4H, respectively, from the cave. Figure 5.42 shows a temperature plot of the cave component in Figure 5.41. A stalactite and a stalagmite (their size is 1/40 of the cave area) are attached to the model of no-speleothems in Figure 5.41. Figures 5.43 and 5.44 indicate the temperature distribution inside caves with the stalactite and the stalagmite, respectively.

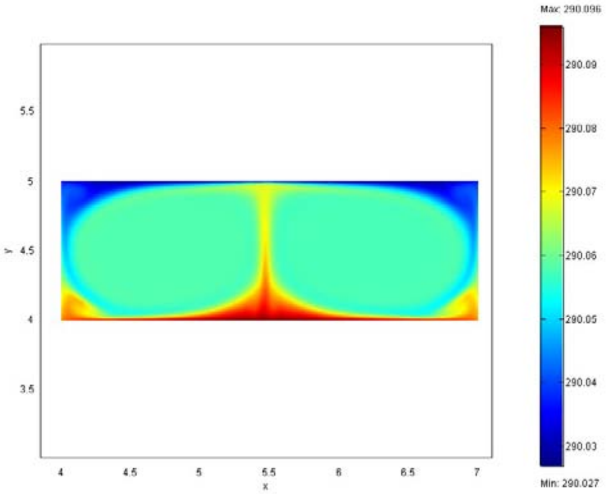

Figure 5.42: Cave with no speleothems with surfaces indicating temperature (K).

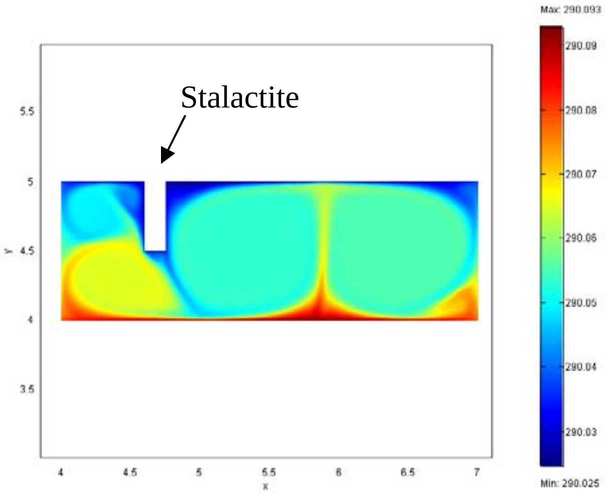

Figure 5.43: Cave with stalactite. Surfaces indicate temperature (K).

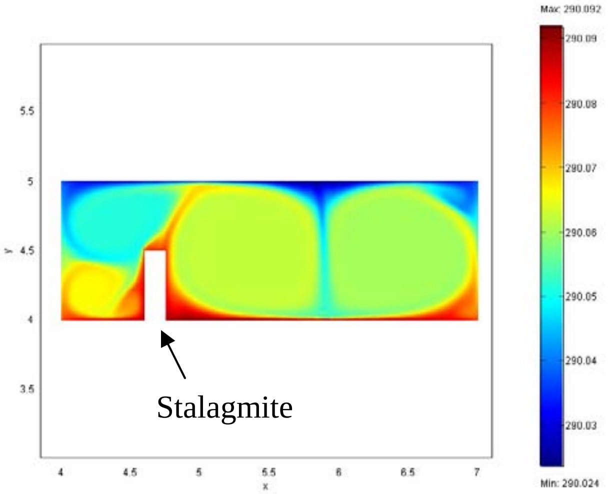

Figure 5.44: Cave with a stalagmite. Surfaces indicate temperature (K).

Table 5.11: Effects of speleothems. Height of caves H is 1m, and Ra_1 is $10^{6.33}$ based on H. The length of the bottom boundary $L = 11H$, and the length of the bottom q is the heat flux of 0.05 W m^{-2}.

Model	*Speleothem*	*Number of elements*	*Number of cells*	*Avg. velocity ($m\ s^{-1}$)*	*Avg. temp. (K)*	*Boundary integration (Bi) (Wm^{-1})*	*Error* $\left\lvert\frac{Bi}{L\,q}\right\rvert 100(\%)$
F 5.42	no	5961	2	1.233×10^{-2}	290.0583	1.165×10^{-3}	2.118×10^{-1}
F 5.43	up	6017	4	1.125×10^{-2}	290.0558	-4.133×10^{-4}	7.515×10^{-2}
F 5.44	bottom	6049	4	1.124×10^{2}	290.0600	1.471×10^{-4}	2.675×10^{-2}

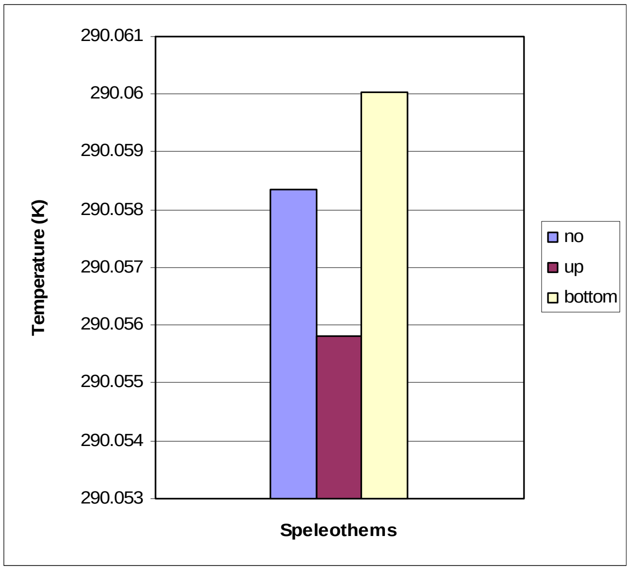

Figure 5.45: Average temperature versus presence of speleothems.

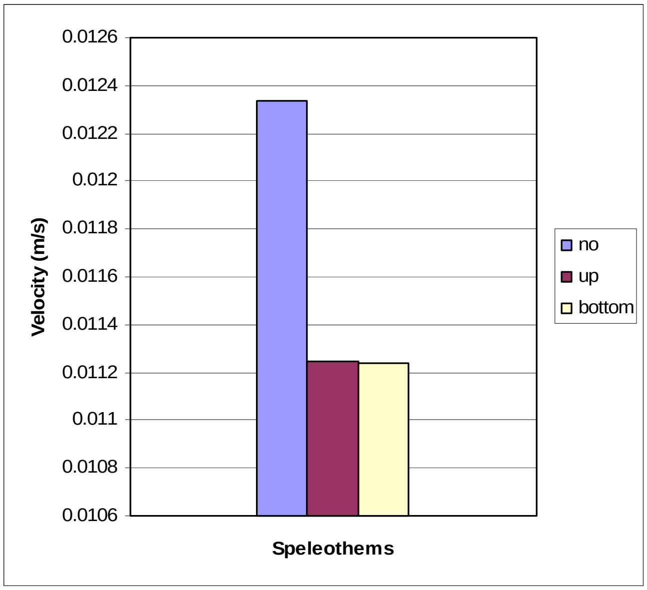

Figure 5.46: Average velocity field versus presence of speleothems.

Table 5.11 and Figures 5.45 and 5.46 summarize the model results. Limestone is a good thermal conductor compared to air. Thus, our models demonstrate that stalactites reduce the average temperature inside the cave because the area above the cave is cooler than the cave air, and heat in the cave is conducted out of the cave through the stalactites. Stalagmites raise cave air temperature because they conduct heat from the system below that is warmer than cave air. The average velocity fields, however, are lower in the models with speleothems than those without speleothems. The presence of speleothems creates a larger surface area. Additionally, the rough surface texture effectively creates eddies, which reduce mechanical energy. There are 2D exaggerations, and the presence of water is ignored (moving water may reduce air temperatures). Although there are more factors that create cave meteorology, we consider that the presence of speleothems could become one of the important factors governing cave air temperature and velocity.

5.3.3 Overlapped Cavities

Some caves have cavities that overlap each other. Carlsbad Cavern is one example of such a cave (the details of Carlsbad Cavern is discussed in Chapter 8). We would like to examine the effects of overlying cavities on the temperature and velocity of lower cavities. Figures 5.47 and 5.48 are 3D and 2D images of overlapped cavities, respectively.

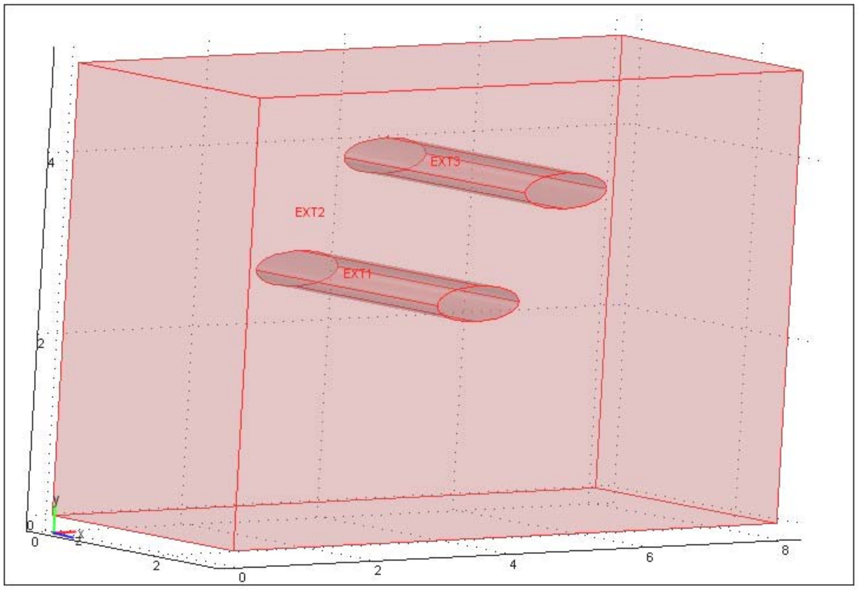

Figure 5.47: 3D image of overlapped cavities.

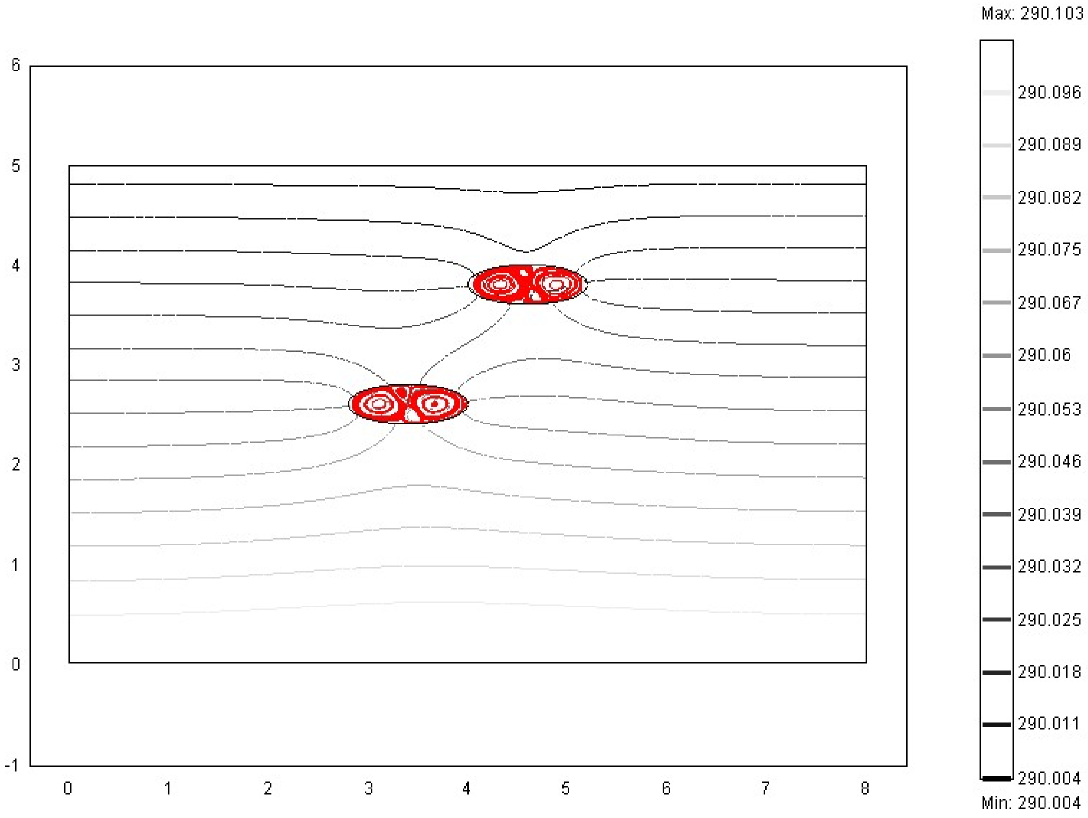

Figure 5.48: 2D image of overlapped cavities.

In Figure 5.48, the height (*H*) and width of the cavities are 0.4 m and 1.2 m, respectively. The height and width of the models are 5 m and 8 m, respectively. The vertical and horizontal distances between the two cavities are 3*H* from the centers of the cavities. The top is located 3*H* from the center of the upper cavity; and the bottom boundary 6.5*H* from the center of the lower cavity. The horizontal distances between the two overlapped cavities were changed by 0*H*, 1*H*, 2*H*, and 3*H* (Figure 5.48) to examine the relationships between the distance and the spatial average temperature and velocity field in the lower cavity. The model of a single cavity was created for comparison. Figures 5.49 thru 5.53 are enlarged images of the models. A summary of the models is found in Table 5.12 and Figures 5.54 and 5.55.

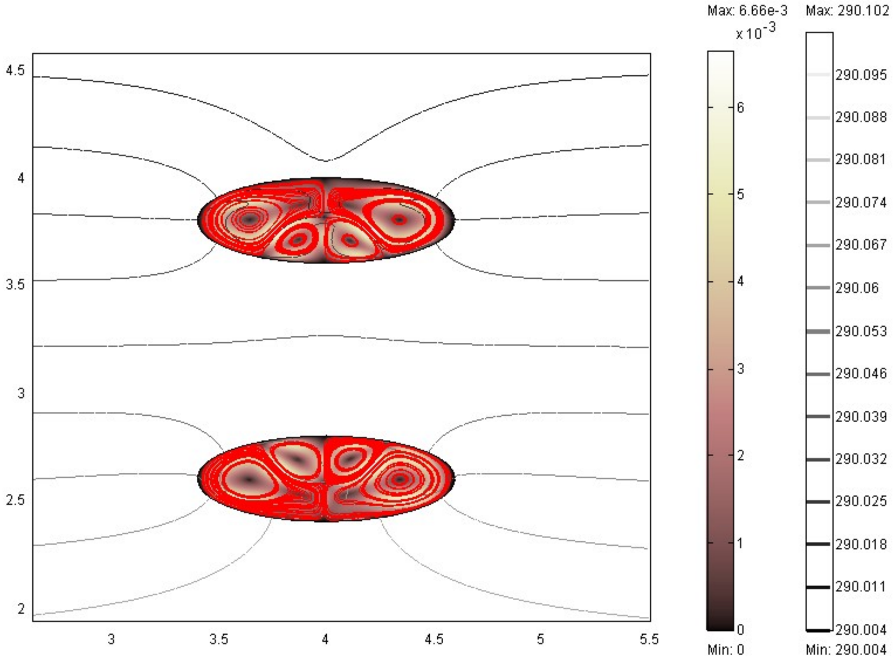

Figure 5.49: Overlapped cavities *D/H* = 0. The vertical and horizontal distances between cavities are 3*H* and 0*H*, where *H* = 0.4 m, the height of the cavities. The model shows contour lines for temperature (K), and surfaces and streamlines indicating the velocity field (m s^{-1}).

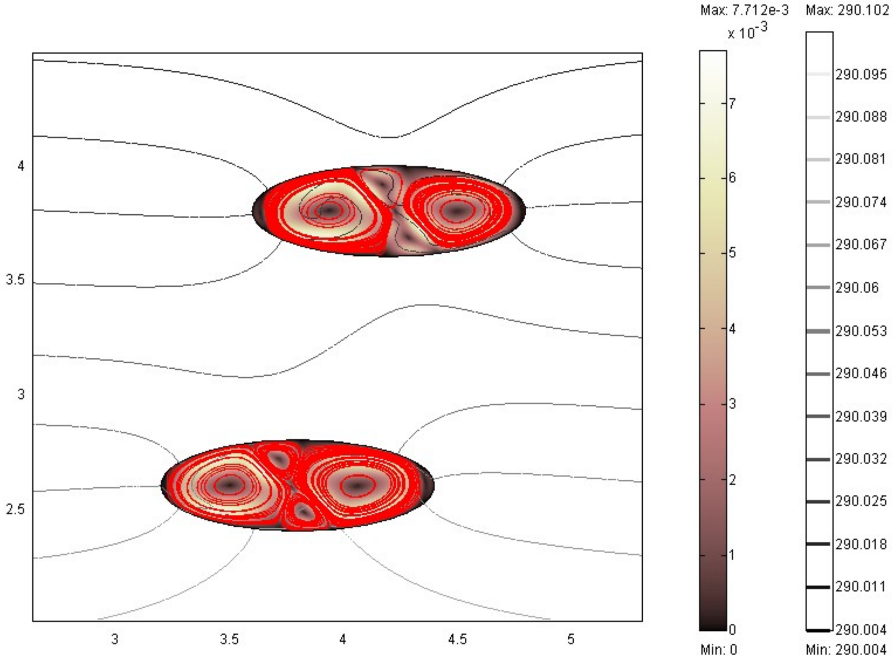

Figure 5.50: Overlapped cavities *D/H* = 1. The vertical and horizontal distances between cavities are 3*H* and 1*H*, where *H* = 0.4 m, the height of the cavities. The model shows contour lines indicating temperature (K), and surfaces and streamlines indicating the velocity field (m s^{-1}).

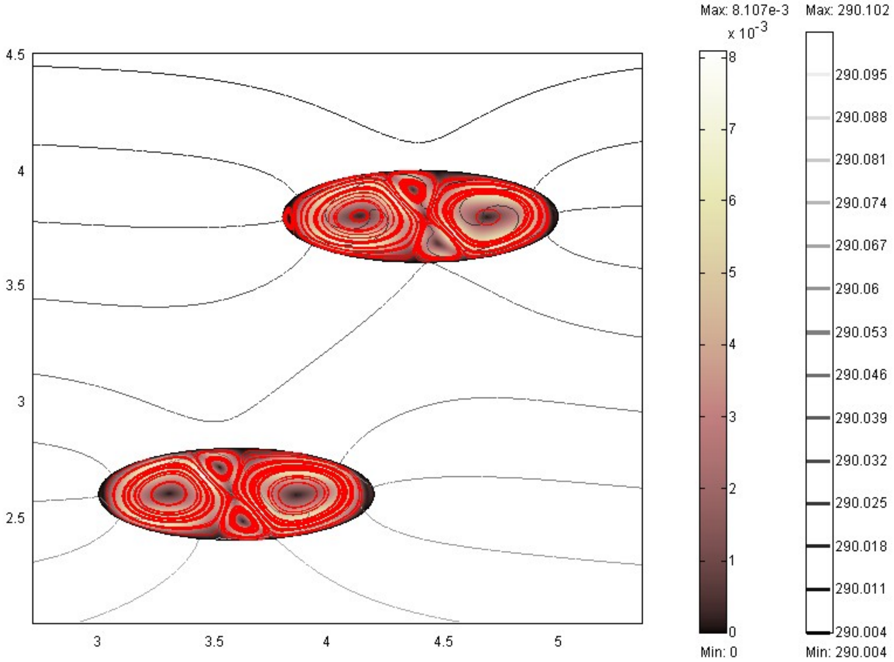

Figure 5.51: Overlapped cavities *D/H* = 2. The vertical and horizontal distances between cavities are 3*H* and 2*H*, where *H* = 0.4 m, the height of the cavities. The model shows contour lines for temperature (K), and surfaces and streamlines indicating the velocity field (m s^{-1}).

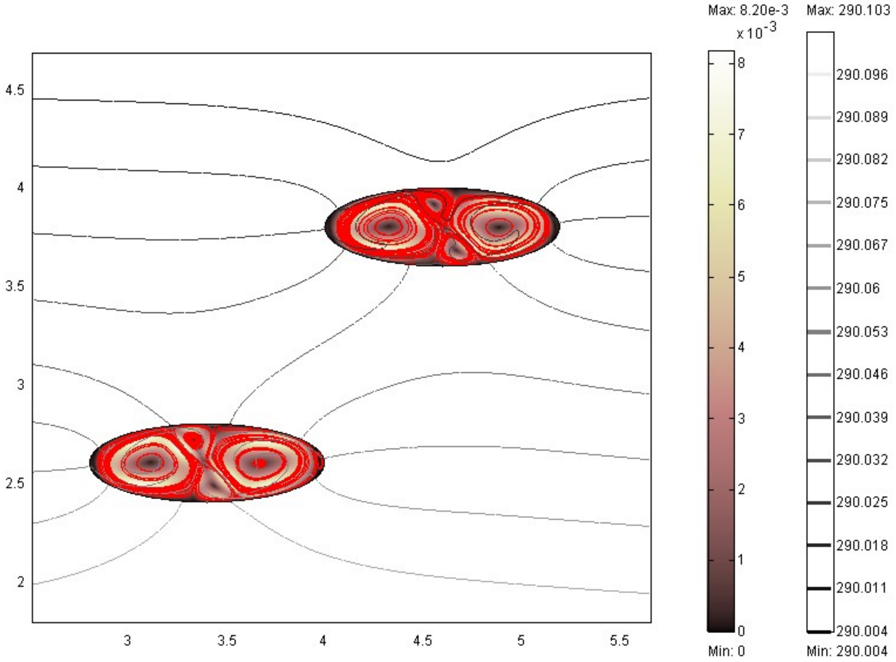

Figure 5.52: Overlapped cavities *D/H* = 3 (the same model as Figure 5.48). The vertical and horizontal distances between cavities are 3*H* and 3*H*, where *H* = 0.4 m, the height of the cavities. The model shows contour lines for temperature (K), and surfaces and streamlines indicating the velocity field (m s^{-1}).

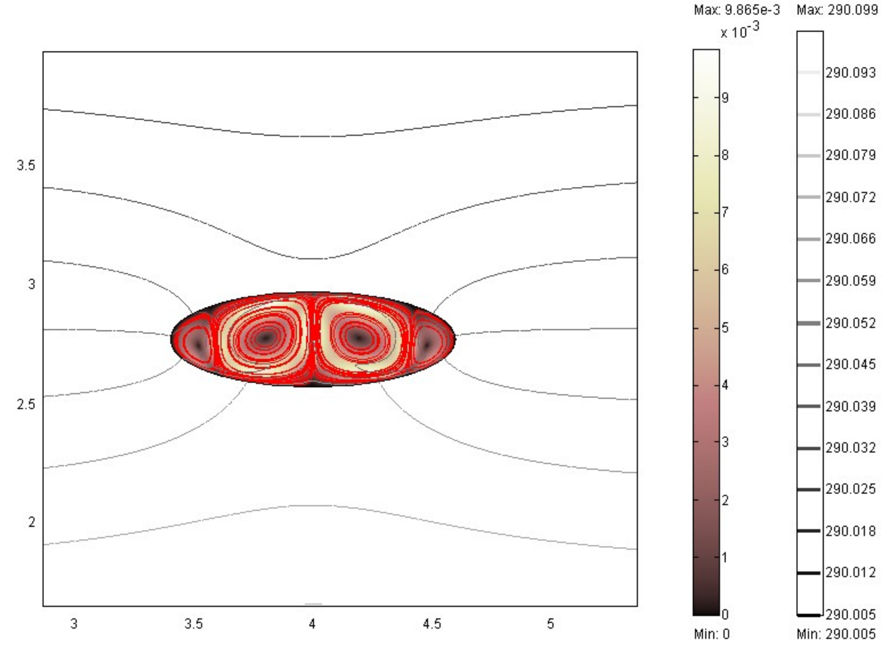

Figure 5.53: Single cavity (a lower cavity). The model shows contour lines for temperature (K), and surfaces and streamlines indicating the velocity field (m s^{-1}). The height of the cavity *H* is 0.4 m.

Table 5.12: Effects of overlapped cavities. Height of cavities H = 0.4 m, and Ra_1 is 55285 = $10^{4.74}$ based on H. The length of the bottom boundary $L = 20H$, and q is the heat flux of 0.05 Wm^{-2}. D is the horizontal distance between the two cavities.

Model	*D/H H=0.4m*	*Number of elements*	*Number of cells in the lower cavity*	*Avg. velocity (m s^{-1})*	*Avg. temp. (K)*	*Boundary integration (Bi) (Wm^{-1})*	*Error* $\left\lvert \frac{Bi}{L\,q} \right\rvert 100(\%)$
F 5.49	0	4831	4	$2.883\text{x}10^{-3}$	290.0552	$-8.628\text{x}10^{-5}$	$2.157\text{x}10^{-2}$
F 5.50	1	4870	4	$3.573\text{x}10^{-3}$	290.0550	$-1.002\text{x}10^{-4}$	$2.506\text{x}10^{-2}$
F 5.51	2	5024	4	$3.711\text{x}10^{-3}$	290.0547	$-5.553\text{x}10^{-5}$	$1.388\text{x}10^{-2}$
F 5.52	3	4908	4	$3.780\text{x}10^{-3}$	290.0542	$2.744\text{x}10^{-5}$	$6.859\text{x}10^{-3}$
F 5.53	single	4136	4	$4.411\text{x}10^{-3}$	290.0471	$1.464\text{x}10^{-6}$	$3.660\text{x}10^{-4}$

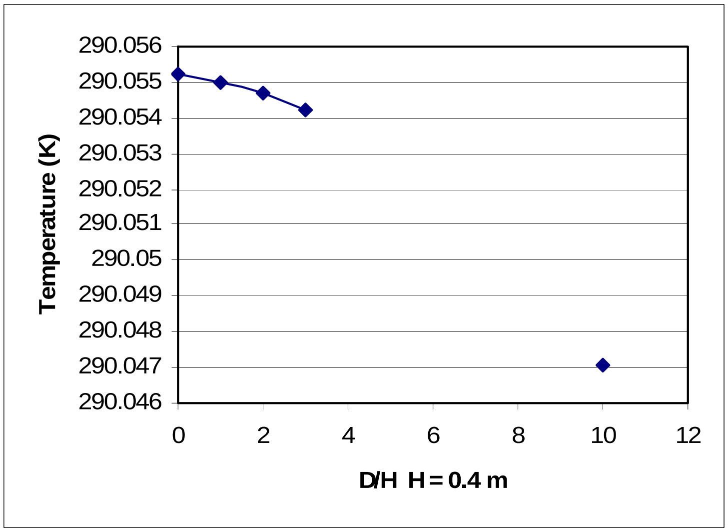

Figure 5.54: Average temperature of the lower cavity versus overlapped ratio. D/H =10 represents the single cavity model.

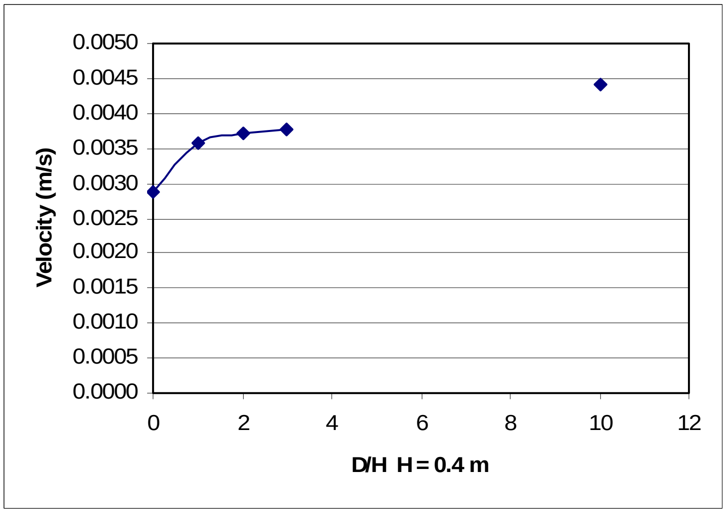

Figure 5.55: Average velocity field of the lower cavity versus overlapped ratio. D/H =10 represents the single cavity model.

The average temperature of the lower cavity drops as the horizontal distance between the two cavities increases, while the average velocity field appears to increase. The larger the distance, the less influence there is on the lower cavity from the overlying cavity, thus, there is an increase in the temperature gradient within the lower cavity. This could contribute to the higher velocity of the lower cavity. However, velocity depends on the number and shape of convection cells. That may be determined by the combination of multiple factors such as heat flux and shape or size of caves.

5.3.4 Flow Direction Controlled by Geometry

Geometries control flow directions. In Section 5.3.1, we saw that air circulation occurred when the model with two entrances was tilted. In this section, we provide more example models that describe flow directions controlled by geometry.

(1) Flow direction Controlled by Geometry

Two types of models of relevance are created: a horizontal tunnel is extended to both left and right sides of an entrance passage (Figure 5.56); and a horizontal tunnel is extended to the right side of an entrance passage (Figure 5.57). In both models, a lower tunnel and the main horizontal tunnel are connected at two points, by both narrow and wide downward passages. We will focus on the narrow passages to see whether slightly different geometries can create different flow directions. The bottom and side boundaries are located sufficiently far from a cave structure to avoid influence from constant boundary values on the temperature and velocity field.

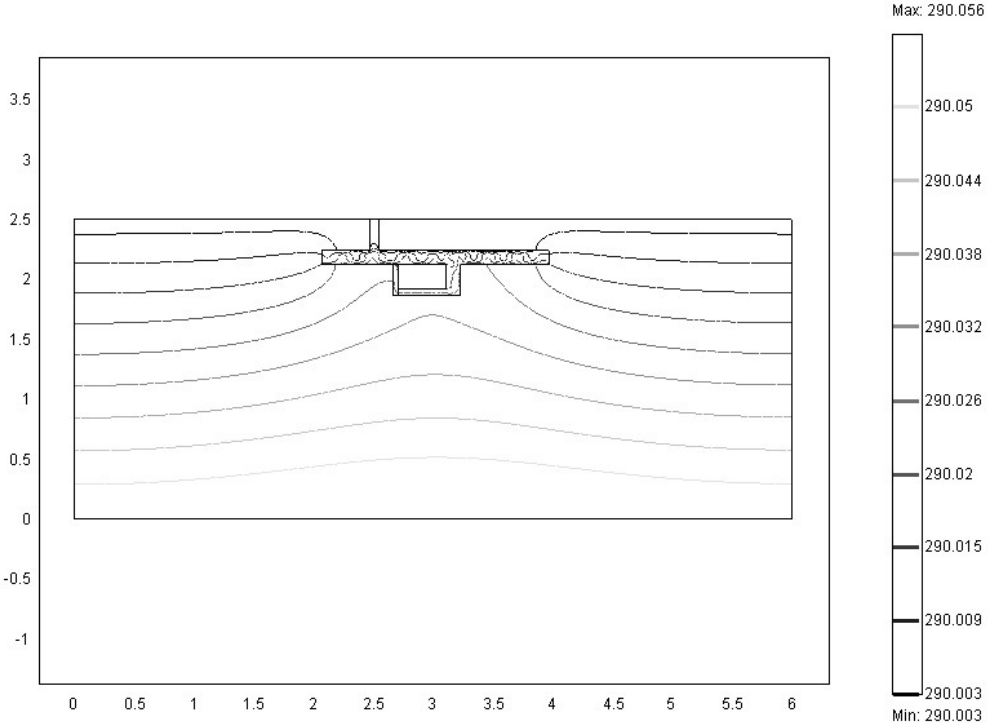

Figure 5.56: Horizontal tunnel is extended to both right and left sides of an entrance passage. Model displays contour lines representing temperature (K).

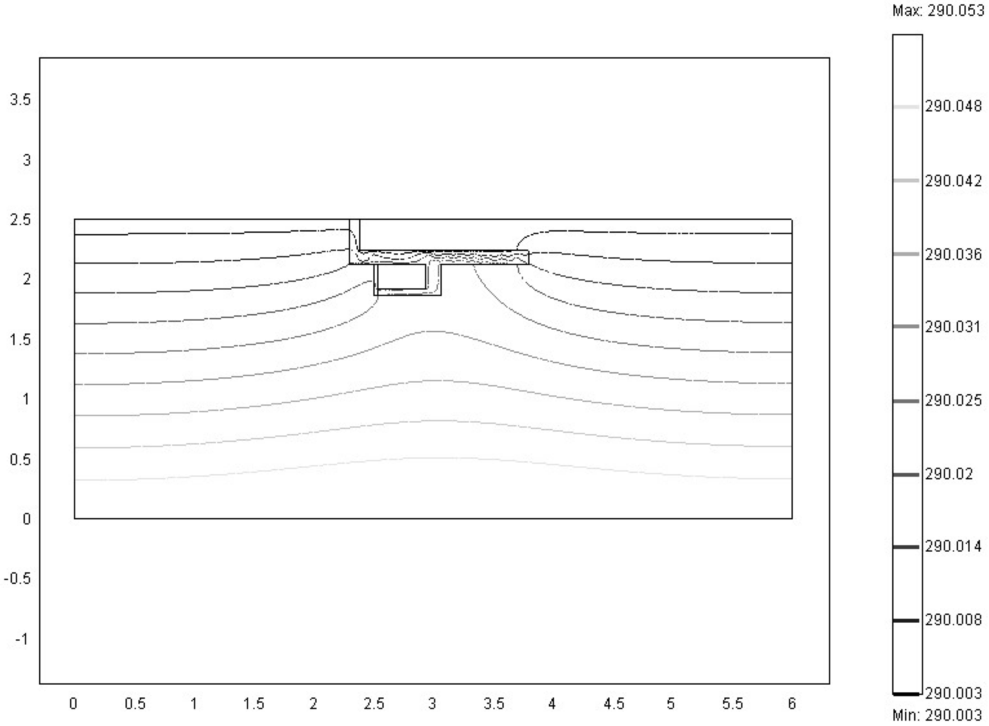

Figure 5.57: Horizontal tunnel is extended to the right side of an entrance passage. Model shows contour lines representing temperature (K).

Figures 5.58 and 5.59 show the velocity field of the caves in Figures 5.56, 5.57, respectively. In Figure 5.58, air circulation between the upper and lower tunnels is not produced, whereas clear air circulations are observed in Figure 5.59. Figures 5.60 and 5.61 show the vicinity of the narrow passages of Figures 5.56 and 5.57, with arrows and surfaces for the velocity field. In Figure 5.60, weak upward flows occur at the narrow passage, whereas in Figure 5.61, relatively strong downward flows appear. Table 5.13 summarizes the model results.

The small difference in cave geometry in these cases changed the flow direction at the narrow passage in the models. This change may be attributed to the difference in temperature at the left side of the narrow passage. Recalling Figures 5.56, the temperature at the left side of the narrow passage is similar to that at the right side of the large passage. On the other hand, in Figure 5.57, the temperature at the left side of the narrow passage is lower than that of the right side of the large passage. Because caves act as insulators, the presence of cavities long in the horizontal axis changes the thermal regime of the systems below the cavities. This effect could help to govern the direction of flow in caves.

Table 5.13: Flow direction controlled by geometry. Height of the upper tunnel $H = 0.12$ m, and Ra_1 is 448 based on H. The length of the bottom boundary $L = 50H$, and q is the heat flux of 0.05 Wm^{-2}. The flow directions and the average values for velocity and temperature are taken from the narrow passage that connects the upper and lower tunnels.

Model	*Number of elements*	*Flow direction at narrow passage*	*Avg. velocity* (ms^{-2})	*Avg. temp. (K)*	*Boundary integration (Bi)* (Wm^{-1})	*Error* $\left\lvert\frac{Bi}{L\,q}\right\rvert 100(\%)$
F 5.56	7108	up	$2.100\text{x}10^{-4}$	290.0237	$-6.201\text{x}10^{-6}$	$2.067\text{x}10^{-3}$
F 5.57	6341	down	$8.080\text{x}10^{-4}$	290.0194	$4.522\text{x}10^{-5}$	$1.507\text{x}10^{-2}$

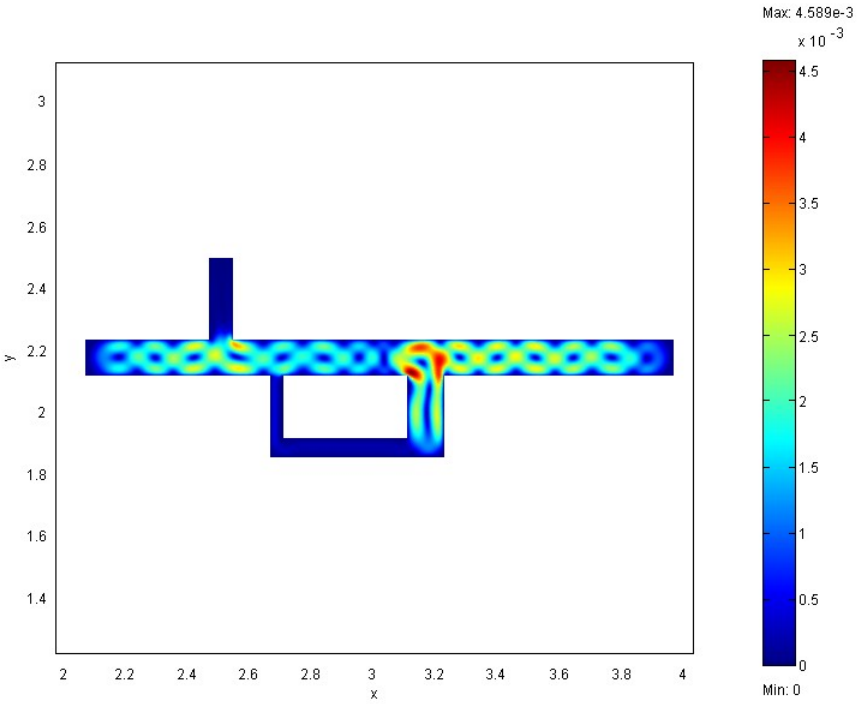

Figure 5.58: Cave domain plot of Figure 5.56, with surfaces indicating the velocity field (m s^{-1}).

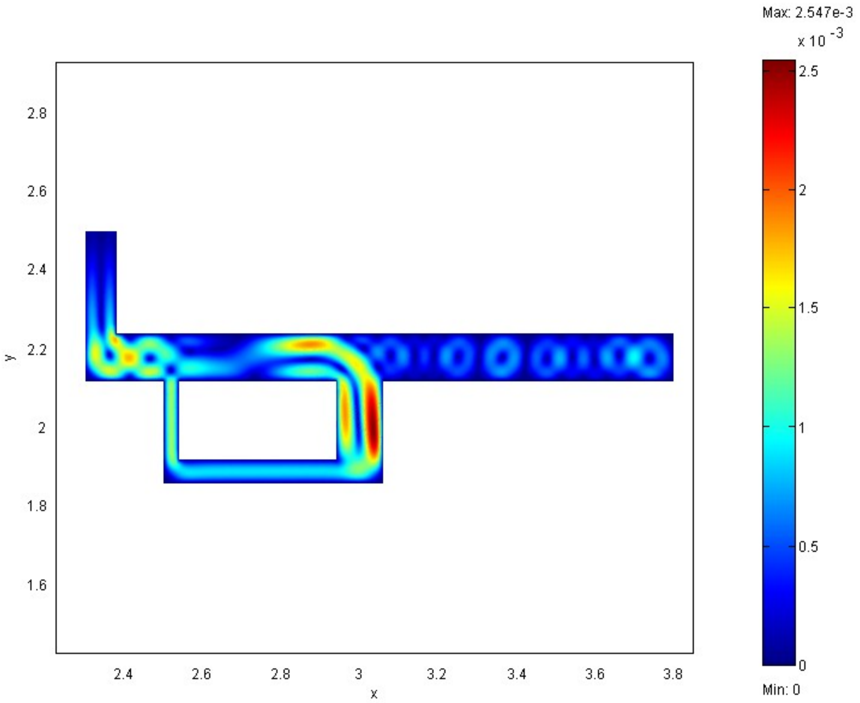

Figure 5.59: Cave domain plot of Figure 5.57, with surfaces indicating the velocity field (m s^{-1}).

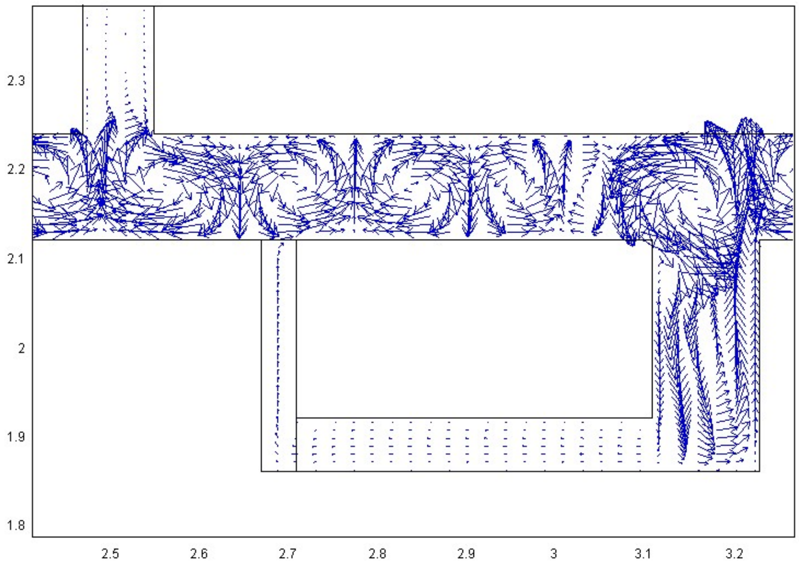

Figure 5.60: Enlarged image of the narrow passage of Figure 5.56, with arrows representing the velocity field (m s^{-1}). Weak upward flows are observed at the narrow passage. The arrows between the narrow passage and lower horizontal passage are not smooth due to different grid sizes that were applied.

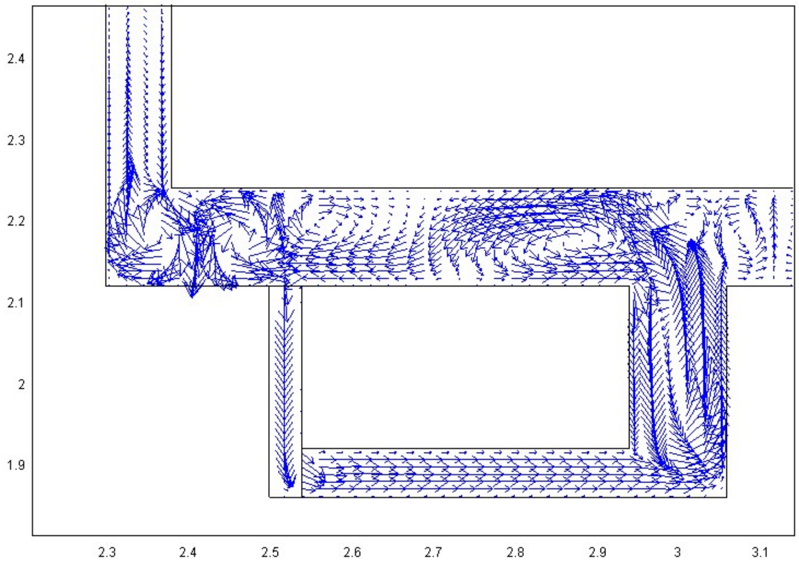

Figure 5.61: Enlarged image of the narrow passage of Figure 5.57, with arrows representing the velocity field (m s^{-1}). Relatively strong downward flows are observed at the narrow passage. The arrows between the narrow passage and lower horizontal passage are not smooth due to different grid sizes applied.

In Table 5.13, the calculated Rayleigh number Ra_1 based on the height of the upper horizontal tunnel (H = 0.12 m) is 448, which is relatively small. However, many convection cells appear in both models, and the average velocity in the narrow passage of Figure 5.57 is higher (8.080×10^{-4} m s^{-1}) than that of the model in Figure 5.7 (a rectangular cave, W/H = 2, Ra_1 = 830, H = 0.14 m, and the average velocity field is 4.28 x 10^{-4} m s^{-1}; see Table 5.3). The complex cave geometries with entrance passages that connect to the surface could further enhance air movements.

(2) Complex Cave Geometry and Air Movement

To examine the effect of complexity of cave geometry on air movement, we constructed two models that have simple rectangular cave geometries with H = 0.12 m, but their aspect ratios are different (W/H = 10 and 5). Figure 5.62 shows a model that has a simple horizontally long cavity extending to the side boundaries. The aspect ratio of the cave domain of this model is W/H = 10. The figure of the model with aspect ratio of 5 is omitted. Table 5.14 summarizes the models.

Table 5.14: The effects of complexity of cave geometry (1). Horizontally long cavity extends to the side boundaries. Height of the cavity H = 0.12 m, and Ra_1 is 448 based on H. The length of the bottom boundary L = 10H and 5H, respectively, and q is the heat flux of 0.05 Wm^{-2}.

Model (W/H) H=0.12m	*Number of elements*	*Number of convection cells*	*Avg. velocity* (*ms^{-2}*)	*Avg. temp. (K)*	*Boundary integration (Bi)* (*Wm^{-1}*)	*Error* $\left\lvert\frac{Bi}{L\,q}\right\rvert 100(\%)$
5	1622	5	4.043×10^{-3}	290.0480	-7.0214×10^{-6}	2.340×10^{-4}
10 (F5.62)	2876	10	4.125×10^{-3}	290.0469	-2.0794×10^{-4}	3.466×10^{-3}

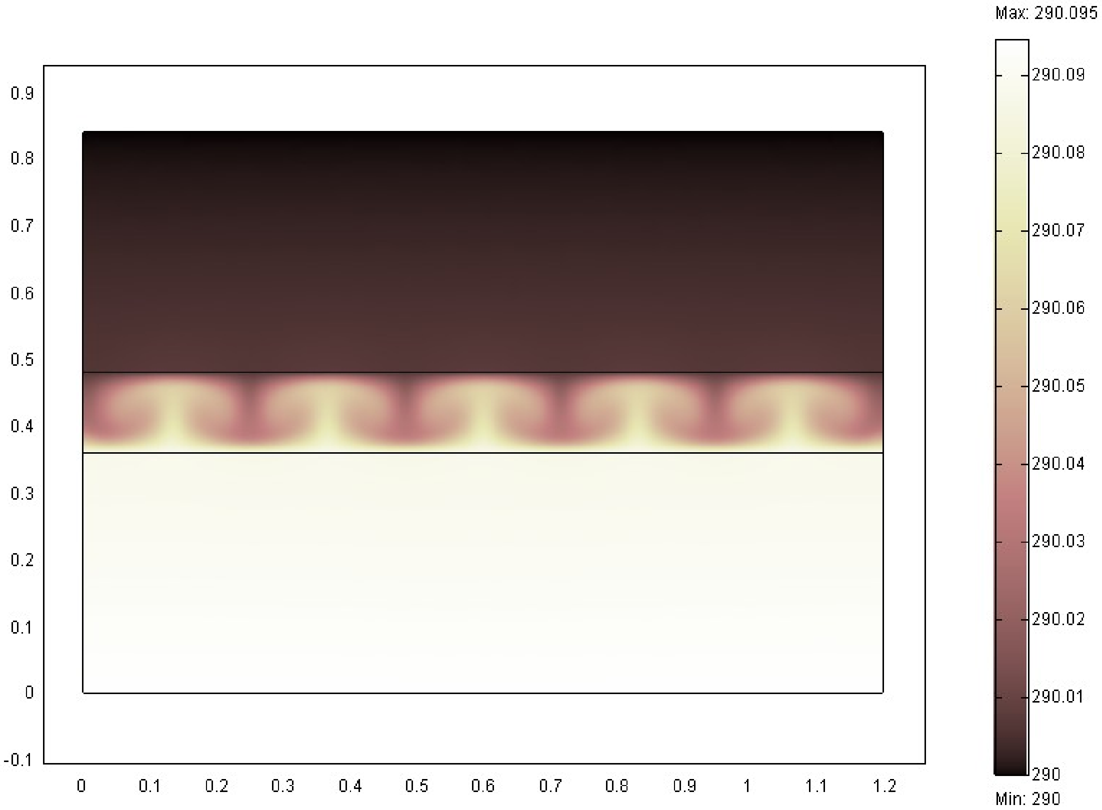

Figure 5.62: Horizontally long cavity extending to the side boundaries. The model shows surfaces indicating temperature (K). The height of cavity H = 0.12 m, and the width W = 10H. Ra_1 = 448 based on H.

In Table 5.14, the average velocity and temperature of both models are high compared to those taken from the narrow passages of the models in Figures 5.56 and 5.57. In these four models, Ra_1 = 448 based on H = 0.12 m, but Figure 5.56 and 5.57 have complex cave geometries, whereas the models described in Table 5.14 have simple cave geometries. Thus, we cannot verify the positive relationship between the average velocity and the complexity of cave geometry as discussed in the previous paragraph. The high average velocity in the models with simple cave geometries may be because caves are extended to the side boundaries, which result in the exaggeration of the values as discussed in Section 4.3. Clear insulation effects are observed in Figure 5.58, in which temperature is low above the cave structure, and high below. Temperature gradient is high because of this clear insulation effect, which results in higher velocity within the cavity. The numbers of convection cells are the same as the geometry aspect ratios. This indicates that in the models with a rigid-rigid boundary condition, the wavelength of the stable convection cell is 2 *H* [Furbish, 1995, 418].

We constructed two additional models to verify the positive relationship between the complexity of cave geometry and the average velocity within the cave. Figure 5.63 shows velocity magnitude in the long, main cavity of Figure 5.58, but with the rest of this complex cave masked out. Operationally this was handled by rerunning the model using FEMLAB features; the main cavity was surrounded by an internal boundary, regridded and rerun, allowing us to extract the main cavity plot shown in Figure 5.63. The velocity values in the main cavity of Figure 5.63 are influenced by the masked entrance passage and the lower passages. The flow patterns in the main cavity in Figure 5.63 are slightly different from Figure 5.58; this is caused by the additional internal boundaries in Figure 5.63, which produce slightly different grid sizes or shapes around the internal boundaries.

Figure 5.64 shows velocity magnitude in a long, main cavity, like that in Figure 5.58 or 5.63, but for a simulation that lacked the rest of this complex cave. That is, the cave consisted only of the main cavity. There was no entrance passage or the lower passages. This is a control model. All conditions between Figure 5.63 and 5.64 are the same, except that Figure 5.63 has the other cave structures (they are masked), whereas Figure 5.64 does not have other cave structures. We compared the velocity values in the main cavities between the two models. Table 5.15 summarizes the models.

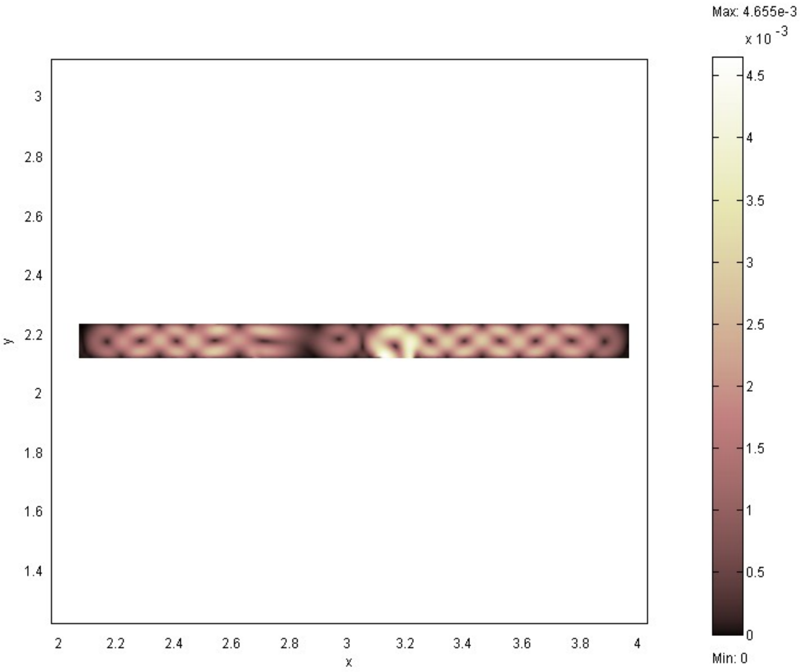

Figure 5.63: Velocity field with complex cave geometry. The model shows the domain plot of the main cavity in Figure 5.58, in which the entrance passage and the lower passages were masked. The model shows surfaces indicating the velocity field (m s^{-1}).

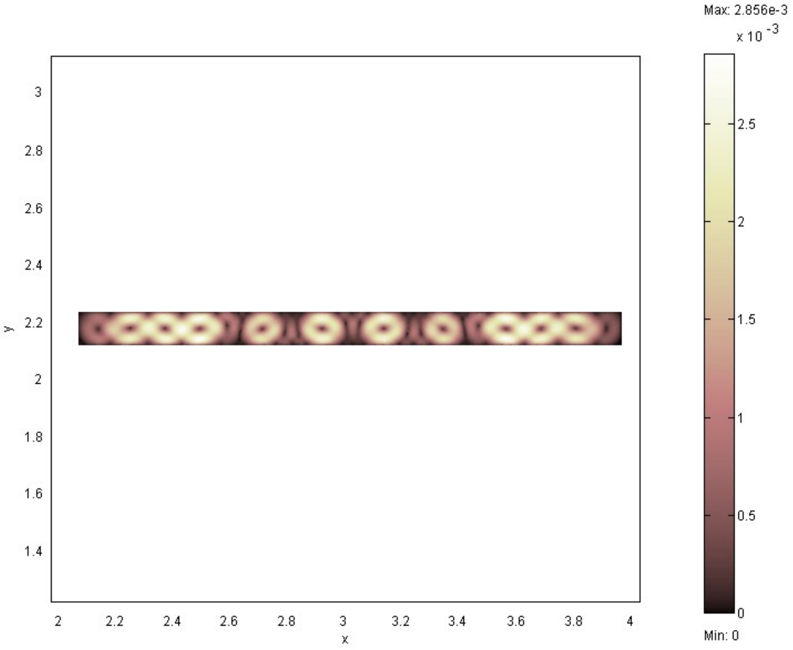

Figure 5.64: Velocity field without complex cave geometry (a control model). The model shows surfaces indicating the velocity field (m s^{-1}). The model was created by removing the entrance passage and the lower passages of the cave geometry in Figure 5.58. Thus, all conditions in Figures 5.63 and 5.64 are the same, except that Figure 5.63 has the masked other parts of the cave, whereas Figure 5.64 does not have other cave structures.

Table 5.15: The effects of complexity of cave geometry (2). The horizontally long cavities with/without complex cave structures are compared. Height of the upper tunnel H = 0.12 m, and Ra_1 is 448 based on H. The length of the bottom boundary $L = 50H$, and q is the heat flux of 0.05 Wm^{-2}.

Model *H=0.12m*	*Number of elements*	*Avg. velocity (ms^{-2})*	*Avg. temp. (K)*	*Boundary integration (Bi) (Wm^{-1})*	*Error* $\left\|\frac{Bi}{L\,q}\right\| 100(\%)$
F 5.63 (complex)	7064	1.434×10^{-3}	290.0122	4.0236×10^{-5}	1.341×10^{-2}
F 5.64 (simple)	3383	1.157×10^{-3}	290.0135	1.2024×10^{-4}	4.008×10^{-2}

In Table 5.15, we can see that the average velocity in the main cavity with complex cave geometry (Figure 5.63) is slightly higher than that of in the simple horizontally long cavity (Figure 5.64). However, the difference is very small, and at present, it is not clear that the complexity of cave geometry enhances air movement.

CHAPTER 6

MODELS WITH SURFACE INFLUENCE ASSOCIATED WITH CONSERVATION OF MASS

One of the components of our coupled model is the conservation of mass for air phase, the so-called continuity equation (see Chapter 3). If there is a surface influence on the flow system inside caves, how will the air mass be balanced? In this chapter, we will examine the surface influence by comparing the models without surface influence (normal flow at zero pressure boundary at an entrance boundary) and the models with surface influence (with a prescribed parabolic inflow or outflow component at an entrance boundary), focusing on the air mass balance and the relationship amongst the distributions of pressure, velocity field, and temperature within cave structures.

6.1 Inflow Simulation

When the surface weather condition near a cave entrance is a high pressure system, downward air currents occur, and the surface air could enter into the cave. We apply the parabolic velocity field expressed by:

$$v = (-5 \times 10^{-2})\, s\, (1 - s) \qquad (m\ s^{-1}) \tag{6.1}$$

where v is the vertical component of velocity, and s is expressed as $s = 0{:}1$ that FEMLAB automatically assigns to the boundary. In the steady laminar flow in a circular tube case, the velocity distribution is parabolic at any cross section. According to *Poiseulle's* *equation*, the mean velocity is given by $\bar{v} = \frac{R^2}{8\mu L}\Delta p$, where R is the tube radius, μ is the fluid viscosity, ∇p is the pressure gradient, which occurs over the length L; and the maximum velocity $v_{max} = 2\bar{v}$ [Young et al., 2004, 258]. These estimations of $\bar{v}$ and $v_{\max}$ are based on the Navier-Stokes equations for a tube. In our two-dimensional model, the equivalent Poiseulle model is for flow between parallel plates, where $\bar{v} = \frac{W^2}{12\mu L}\Delta p$ [Furbish, 1997, 68] and $v_{max} = \frac{3}{2}\bar{v}$ (based on equations 6.2 and 6.3), where W is the distance between walls. Based on equation (6.1), the mean velocity can be calculated by integrating the equation over $s = 0 : 1$:

$$\bar{v} = (-5 \text{x} 10^{-2})\int_0^1 s\,(1-s)\,ds \;=\; -\frac{5}{6} \text{ x } 10^{-2} \quad (m\, s^{-1}) \tag{6.2}$$

The maximum velocity of the parabolic velocity field occurs at its center $s = 0.5$.

$$v_{\max} = (-5 \text{x} 10^{-2})\; 0.5\,(1-0.5) = -1.25 x 10^{-2} \quad (m\, s^{-1}) \tag{6.3}$$

The negative sign of the velocity indicates that the flow direction is inflow, that is, air flows into a cave.

Figure 6.1 shows the velocity profile obtained along the large entrance boundary of the inflow model in Figure 6.6, in which the velocity profile of $v = (-5 \text{ x } 10^{-2})\, s\,(1 - s)$ was prescribed. The calculated maximum velocity agrees with that in Figure 6.1.

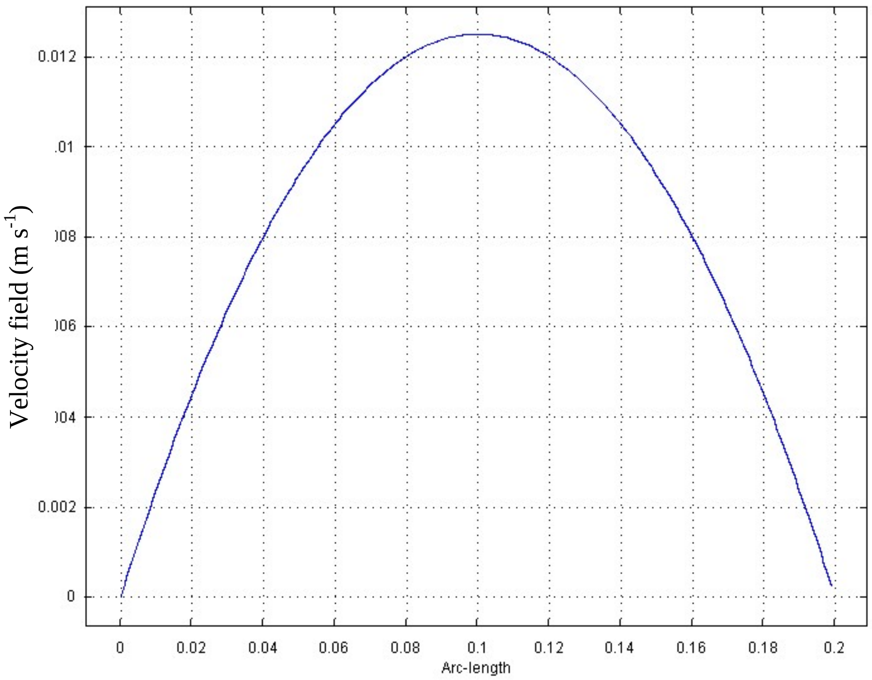

Figure 6.1: Velocity profile with $v = (-5 \times 10^{-2})\, s\, (1 - s)$, where s = 0:1. The profile was taken from the large entrance boundary in the inflow model in Figure 6.6. The maximum velocity about 1.25×10^{-2} (m s^{-1}) is observed in the center. Arc-length is the transect length along the entrance (m).

6.1.1 Models with Two Entrance Passages

(1) Horizontal Normal Flow model with Two Entrances

In Figure 6.2, the height of main cavity (*H*) is 0.3 m and its width is 5*H*. The height of the two passages is 3*H*. The width of the large entrance passages is 2/3*H* (0.2m) and that of the small passage is 1/4*H*. The side and bottom boundaries are located 7.5*H* and 8.5*H*, respectively, from a cave structure. The boundary condition of the normal flow with pressure zero is assigned to both entrances, so air can move freely through the entrances depending on the internal dynamics.

In Figure 6.2, the air mass is balanced in the large entrance having both inflow and outflow components, whereas in the small entrance, air movement appears not to be noticeable. As a result, the convection cells in the main cavity are not disturbed.

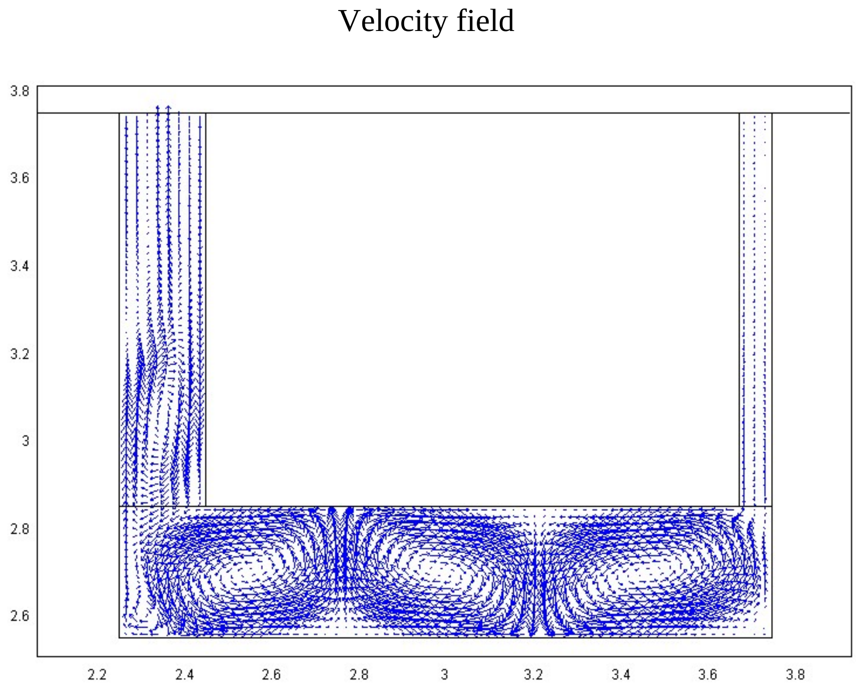

Figure 6.2: Horizontal normal flow model with two entrances showing arrows for the velocity field (m s^{-1}). The two entrances have the boundary condition of normal flow with zero pressure. Clear convection cells appear in the main cavity. Air circulation between the surface and the subsurface is not effective. Inflow and outflow components appear in the large entrance.

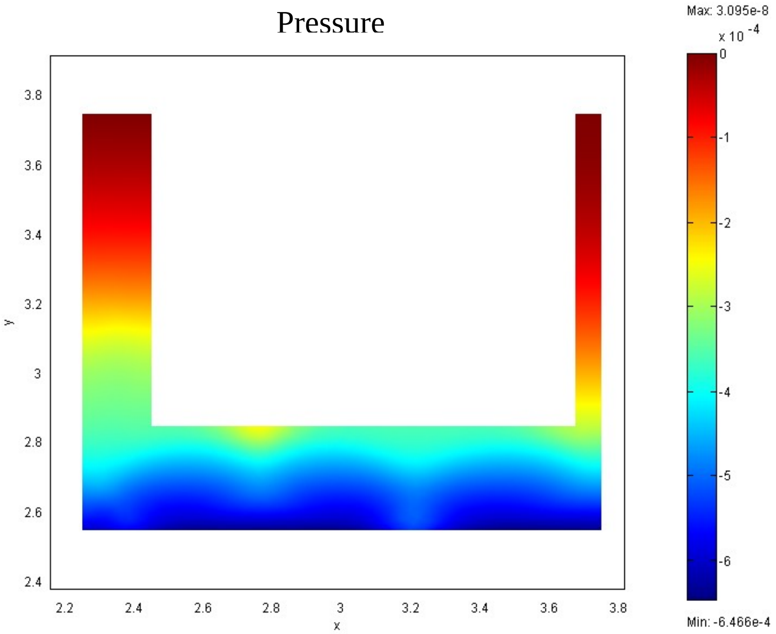

Figure 6.3: Horizontal normal flow model with two entrances showing the cave domain plot with surfaces indicating pressure (N m^{-2}). Pressure is high in the two entrance passages, and low in the main cavity. If flow is due to buoyancy force, air may be able to move from a low pressure region to a high pressure region.

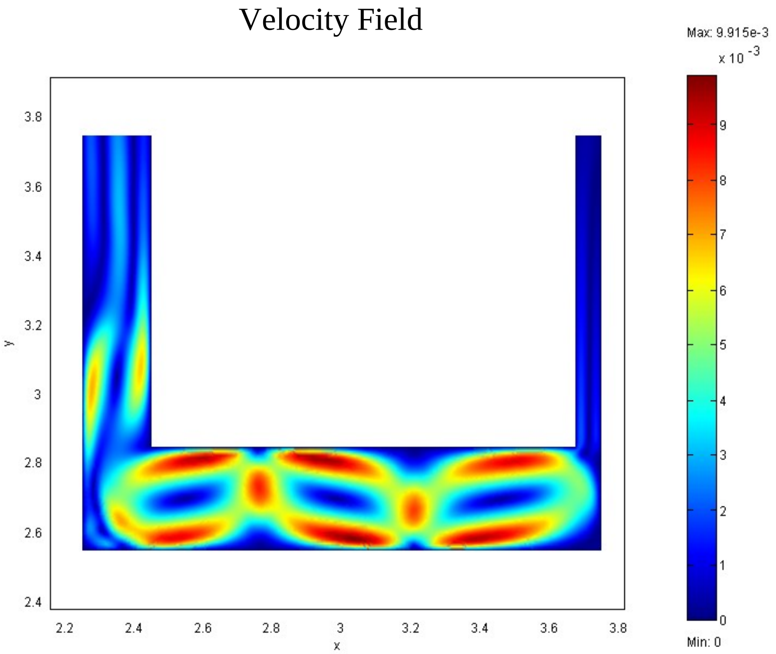

Figure 6.4: Horizontal normal flow with two entrances showing the cave domain plot with surfaces for the velocity field (m s^{-1}). There are clear convection cells in the main cavity.

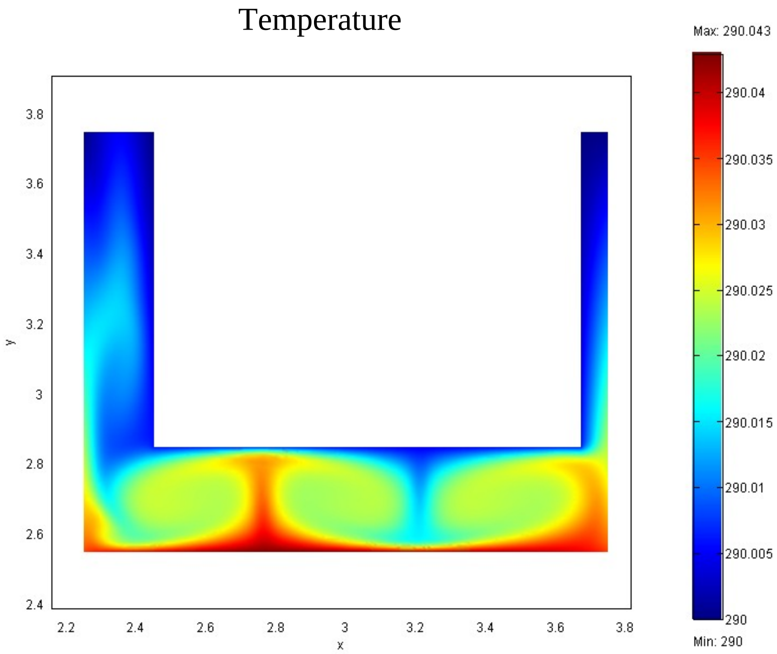

Figure 6.5: Horizontal normal flow model with two entrances showing the cave domain plot with surfaces indicating temperature (K).

Figures 6.3 and 6.4 show pressure and the velocity field plots, respectively. In the main cavity, pressure is low (Figure 6.3), and the velocity field is high (Figure 6.4), whereas the opposite situation is observed in the two entrance passages. Pressure and temperature (Figure 6.5) plots appear to have an inverse relationship, that is, the high temperature region (the main cavity) has low pressure. High temperatures result in high buoyancy forces, expressed by $F_y = \rho\, g\, \alpha\, (T-T_0)$, and the high buoyancy forces reduce the pressure. Let's rearrange the momentum equation (3.1) to understand how FEMLAB calculates the pressure term:

$$\nabla p = -\left[\rho \frac{\partial \mathbf{u}}{\partial t} + \rho(\mathbf{u} \cdot \nabla \mathbf{u})\right] + \nabla \cdot \left[\mu(\nabla \mathbf{u} + (\nabla \mathbf{u})^T)\right] + F \qquad (6.4)$$

From equation (6.4), it appears that ∇p increases as F increases, which is the opposite result of Figure 6.3. There may be a sign problem in this case. The general body forces are gravitational forces, expressed as $F = -\rho g \nabla h$, where h donates the height (relative to a specific datum) [Furbish, 1997, 266 and 274]. The negative sign of the equation indicates that the gravitational forces act downward. Our body forces are buoyancy forces that act upward. Thus, we may be able to rearrange equation (6.4) for the buoyancy forces (F_y) such as:

$$\nabla p = -\left[\rho \frac{\partial \mathbf{u}}{\partial t} + \rho(\mathbf{u} \cdot \nabla \mathbf{u})\right] + \nabla \cdot \left[\mu(\nabla \mathbf{u} + (\nabla \mathbf{u})^T)\right] - F_y \qquad (6.5)$$

Now, from the above expression, we can consider that an increase F_y appears to reduce the pressure gradient (∇p). The models have initial pressure as zero, and the expression ∇p indicates a pressure gradient caused by fluid flow. If there is no buoyancy force acting on the fluid, no flow occurs and ∇p becomes zero. If we assume that the terms in the first and the second brackets of the right side equation are constant C, and then $\nabla p = C - F_y$. As buoyancy forces increase, ∇p becomes more negative and, thus, reduces the fluid pressure.

(2) Horizontal Inflow Model with Two Entrances

All model conditions shown in Figure 6.6 are the same as Figure 6.2, except that the parabolic inflow is assigned to the large entrance. In Figure 6.6, the clear parabolic velocity field is observed in the large entrance. The introduced air circulates effectively, and disturbs the convection cells in the main cavity. Then the air moves out through the small entrance. The introduced forces at the large entrance overcome the buoyancy forces.

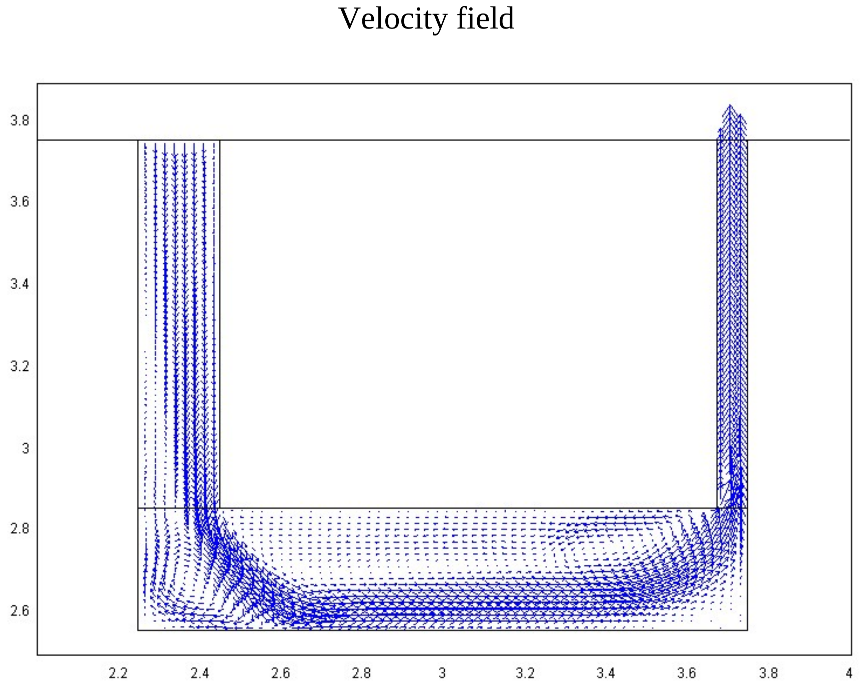

Velocity field

Figure 6.6: Horizontal inflow model with two entrances showing arrows indicating the velocity field (m s^{-1}). The prescribed inflow at the large entrance induces the parabolic outflow at the small entrance. Air circulates very well.

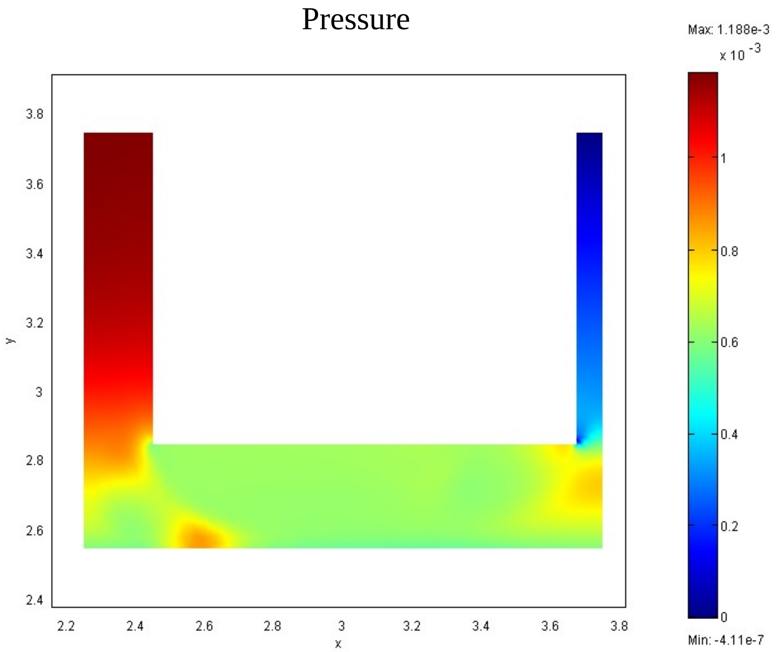

Pressure

Figure 6.7: Horizontal inflow model with two entrances showing the cave domain plot with surfaces indicating pressure (N m^{-2}). Pressure is high in the large entrance, and low in the narrow entrance. The flow system is dominated by viscous forces, and a flow direction is from high pressure to lower pressure regions.

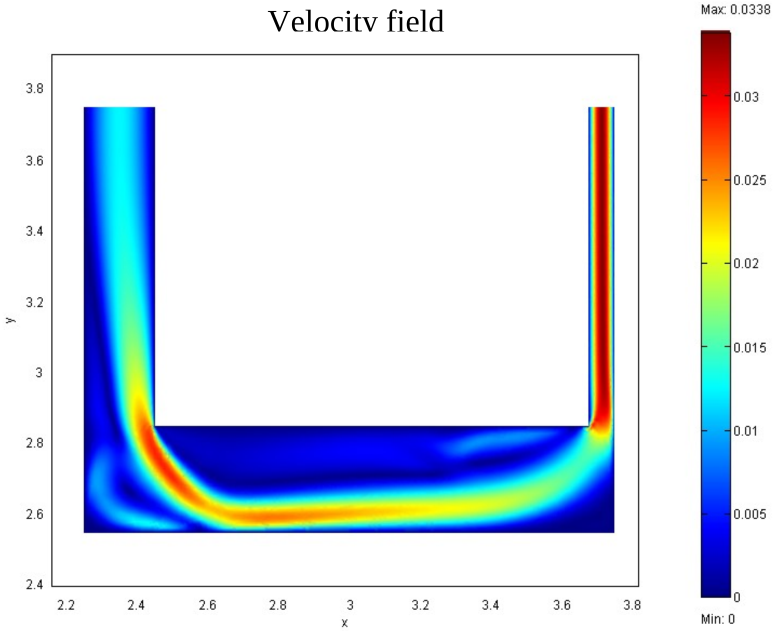

Figure 6.8: Horizontal inflow model with two entrances showing cave domain plot with surfaces indicating velocity field (m s^{-1}). Velocity field is high in the small entrance and low in the large entrance passage.

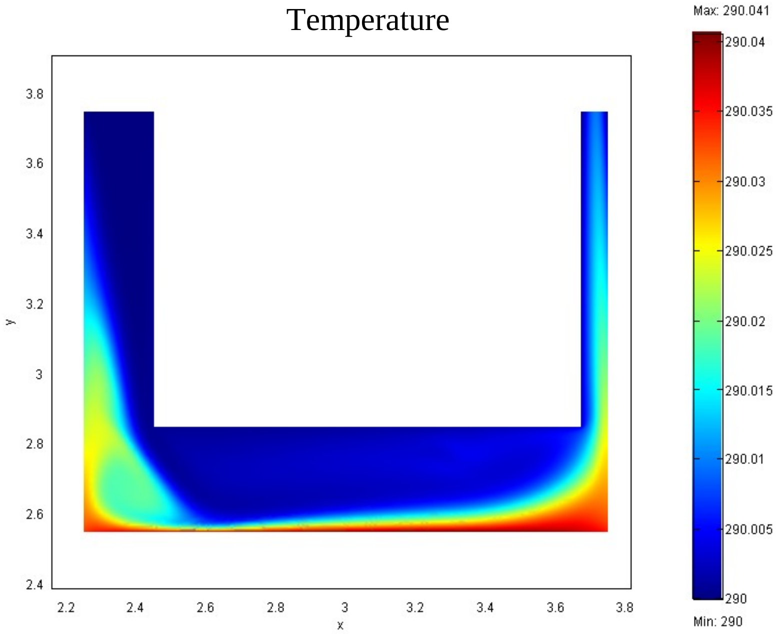

Figure 6.9: Horizontal inflow model with two entrances showing the cave domain plot with surfaces indicating temperature (K). Inflow components at the large entrance significantly changed the temperature regime in the main cavity.

The large entrance has high pressure (Figure 6.7) and low velocity fields (Figure 6.8). The opposite situation is observed in the small entrance. The prescribed inflow at the large entrance increases pressure in the large entrance and the pressure gradually decreases as air descends. Pressure becomes very low when the air escapes through the small entrance. The forces imposed on the large entrance boundary (parabolic inflow component) are viscous forces. From equation (6.5), we see that an increase in the viscous forces increases the pressure gradient. Pressure becomes very low when the introduced air descends toward the main cavity due to the viscous dissipation of mechanical energy and increase in buoyancy forces. Pressure becomes lower still when air ascends through the small entrance, also due to the viscous dissipation of mechanical energy. The high velocity in the small entrance can be roughly explained by the equation of continuity for incompressible fluid expressed by [Serway and Beichner, 2000, 470]:

$$A_1 v_1 = A_2 v_2 = \text{constant} \tag{6.6}$$

where A is the cross-sectional area through which fluids pass.

In Figure 6.9, temperature at the large entrance is lowest because the applied inflow component has the lowest temperature. The air circulation from the large to small entrances disturbs the buoyancy forces and, thus, thermal segregation occurs with high temperature at the lower part of the main cavity. Temperatures are low near the wall of the right side of the large entrance, the left side of the small entrance, and the top of the main cavity. This is because rock temperature in the area surrounded by the cave structure is low due to the insulation effects of the cave structure (see Figures 5.30 and 5.31).

(3) Tilted Normal Flow Model with Two Entrances

The tilted geometry with multiple entrances may be more realistic compared to the horizontal models. The models shown in Figure 6.2 were rotated at 45 degrees, and shown in Figures 6.10. Air circulated very effectively even without an imposed inflow component. The model does not have a gravitational pressure gradient. Thus, this air circulation is simply due to internal dynamics. The upper passage is large, where air mass is balanced by having both inflow and outflow components, whereas the small entrance has only the inflow component. Figures 6.11, 6.12 and 6.13 show the cave domain plots for pressure, velocity field and temperature, respectively. Flow occurs from the small entrance (high pressure) through the main cavity (low pressure) to the large entrance (high pressure). Because there is no imposed viscous force, buoyancy forces dominate in this system.

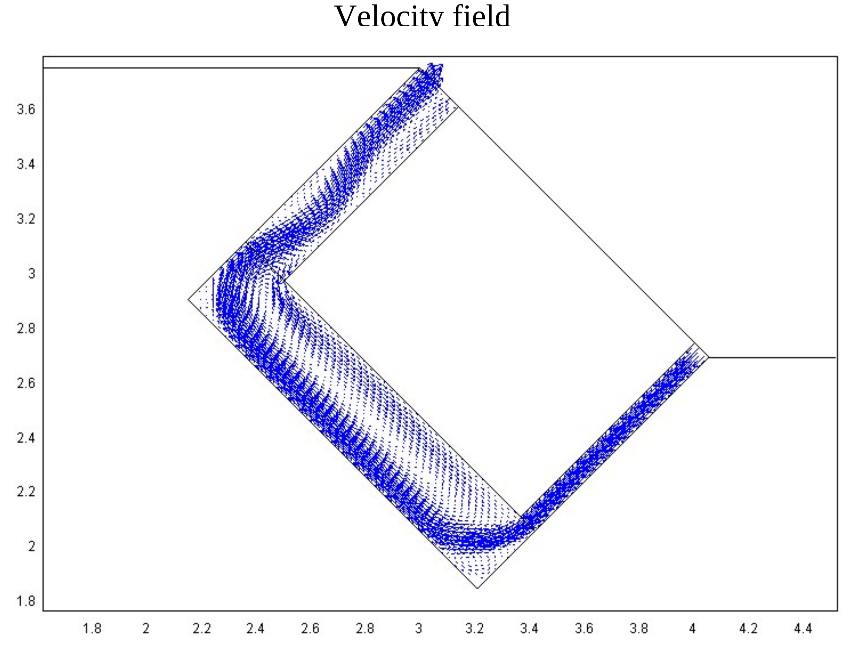

Figure 6.10: Tilted normal flow model with two entrances showing arrows indicating the velocity field (m s^{-1}). The model in Figure 6.1 was rotated by 45 degrees. The small entrance has inflow, and the large entrance has both inflow and outflow. Air circulation is effective.

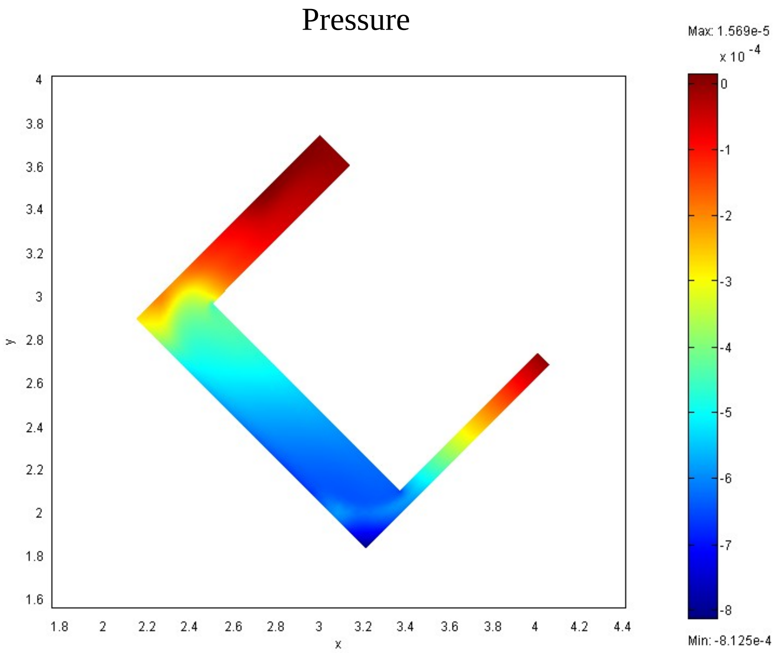
Pressure

Figure 6.11: Tilted normal flow model with two entrances showing the cave domain plot with surfaces indicating pressure (N m^{-2}). Flow occurs from the small entrance (high pressure) through the main cavity (low pressure) to the large entrance (high pressure).

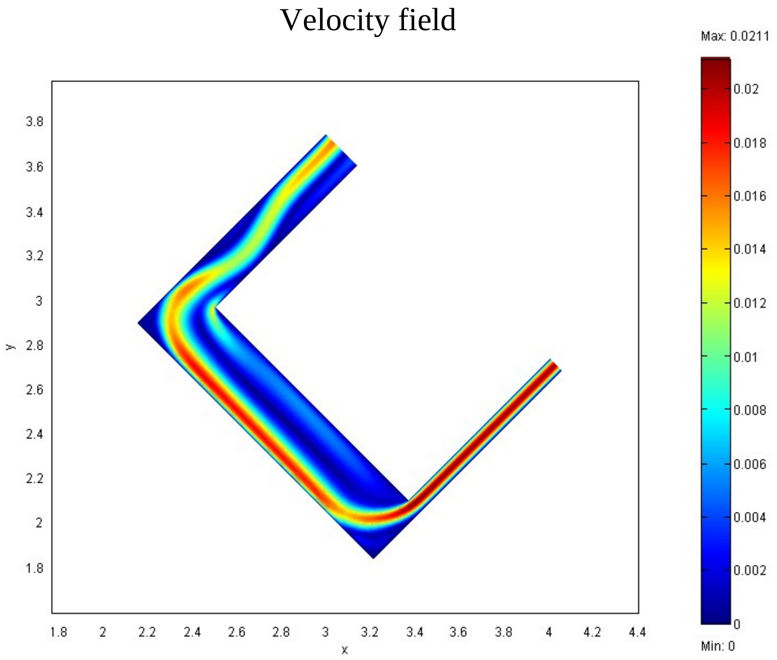
Velocity field

Figure 6.12: Tilted normal flow model with two entrances showing the cave domain plot with surfaces indicating the velocity field (m s^{-1}). The velocity field is high in the small passage and the lower part of the main cavity.

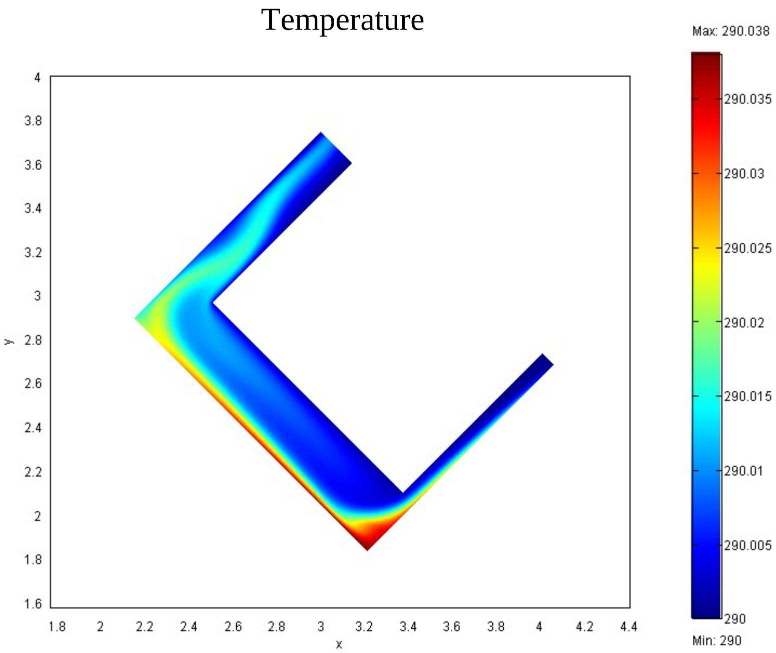

Figure 6.13: Tilted normal flow model with two entrances showing the cave domain plot with surfaces indicating temperature (K). Warm air in the main cavity ascends towards the large entrance and escapes through the left side of the large entrance, and cooler air descends from the small entrance and right side of the large entrance.

We assume that the original flow starts in the main cavity due to buoyancy forces. Some of the air in the main cavity moves toward the large entrance and escapes, resulting in the low pressure in the main cavity (less air). Cooler and denser surface air is introduced toward the main cavity through the small entrance, but it is not enough to maintain air mass in the main cavity. Therefore, cooler and denser air is also supplied through the available space of the large entrance. The two entrances have less buoyancy force, and cooler and denser air moves downward, creating relatively high pressure situations in the entrances.

(4) Tilted Inflow Model with Two Entrances

When parabolic inflow is prescribed for the large entrance (Figure 6.14), reverse air circulation occurs with respect to the normal flow model (Figure 6.10). Imposed viscous forces at the large entrance boundary overcome buoyancy forces. The flow direction is from high pressure to lower pressure regions (the large entrance – the main cavity – the small entrance). The physics behind these phenomena may be the same as the horizontal inflow model in Figure 6.6. In Figure 6.17, the temperature at the large entrance passage is low due to cooler air supplied into the passage. The cooler air appears not to be mixed well with warmer air in the main cavity, and escapes to the small entrance passage.

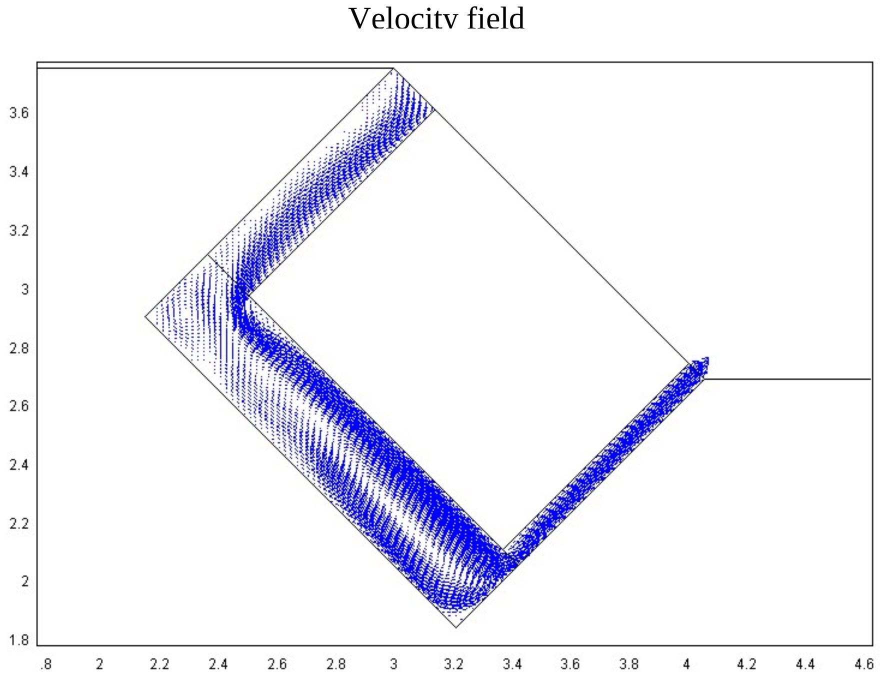

Figure 6.14: Tilted inflow model with two entrances showing arrows indicating the velocity field (m s^{-1}). Figure 6.6 was rotated at 45 degrees. The large entrance has parabolic inflow velocity field. Introduced inflow appears to be resisted by the outflow component of cave air at the entrance area.

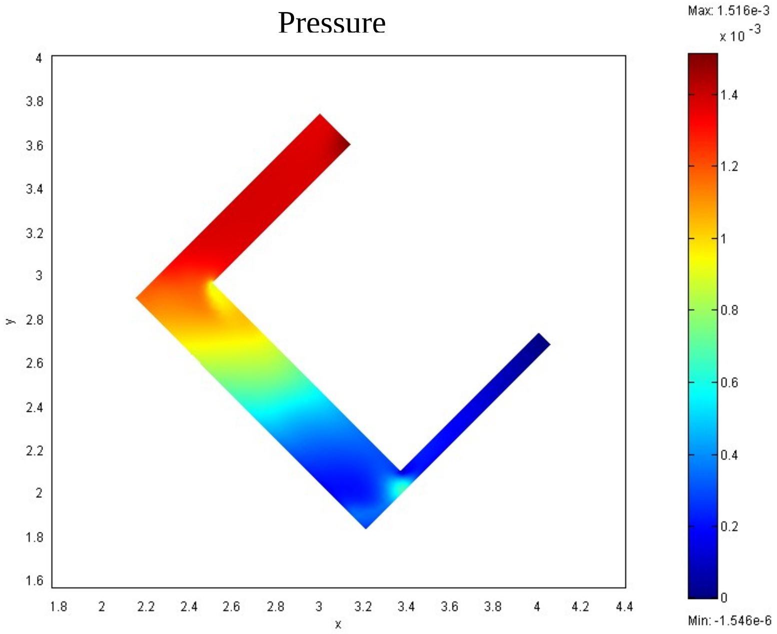

Pressure

Figure 6.15: Tilted inflow model with two entrances showing the cave domain plot with surfaces indicating pressure (N m^{-2}). Pressure is high in the large entrance passage and it becomes lower toward the small entrance passage through the main cavity.

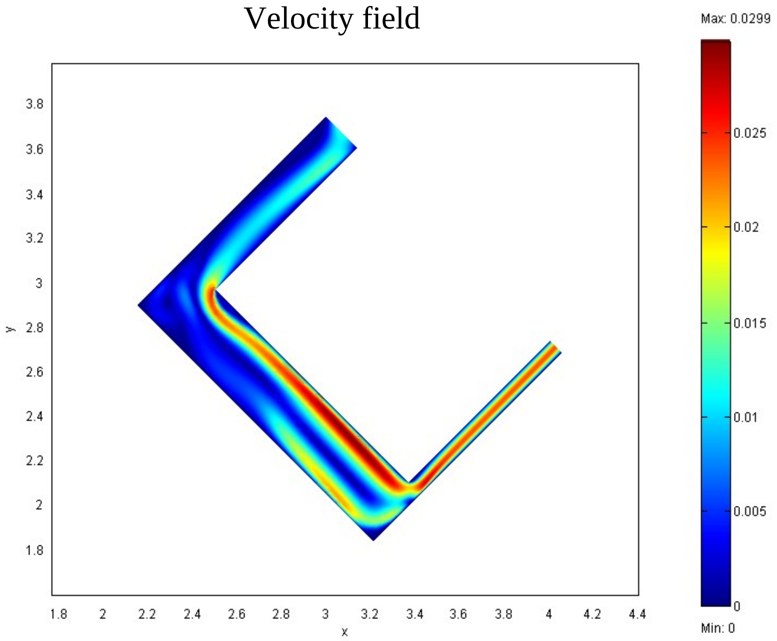

Velocity field

Figure 6.16: Tilted inflow model with two entrances showing the cave domain plot with surfaces indicating the velocity field (m s^{-1}). Velocities are high in the region from the upper part of the main cavity to the small entrance.

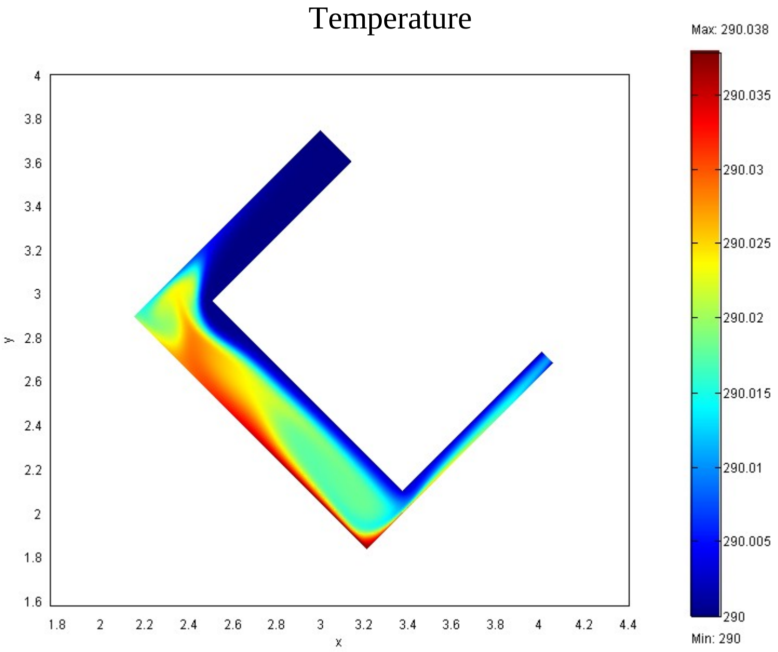

Figure 6.17: Tilted inflow model with two entrances showing the cave domain plot with surfaces indicating temperature (K). Temperature is low in the region from the large entrance passage to the upper part of the main cavity.

(5) Summary for the Models with Two Entrances

Naively one might think that fluid flow occurs from the high pressure region to the low pressure region. However, the pressure plots above show that sometimes flow can occur from the low pressure region to the high pressure region. This might be due to thermally induced buoyancy forces. We will discuss these flow directions with respect to pressure in Section 7.5.

Figures 6.18 thru 6.21 show the enlarged images of the large entrances of Figures 6.2, 6.6, 6.10 and 6.14, respectively. Air mass is balanced mostly at the large entrance by having both inflow and outflow components (Figures 6.18 and 6.20). When the tilted model has prescribed inflow at the large entrance (Figure 6.21), the outflow components of cave air (Figure 6.20) resists the introduced air. On the other hand, the small entrance tends to have a single flow direction (see Figures 6.2, 6.6, 6.10 and 6.14). Table 6.1 and Figures 6.22 thru 6.25 summarize the modeling results.

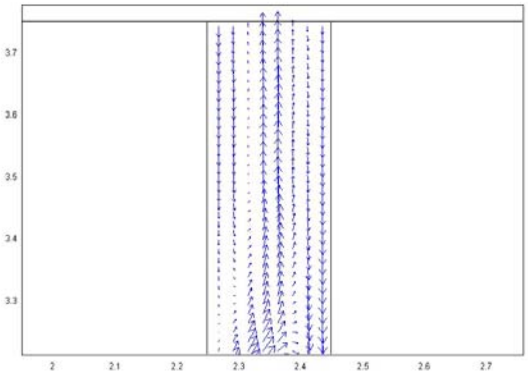

Figure 6.18: Horizontal normal flow model with two entrances. The large entrance of Figure 6.2 is enlarged. Both inflow and outflow are observed.

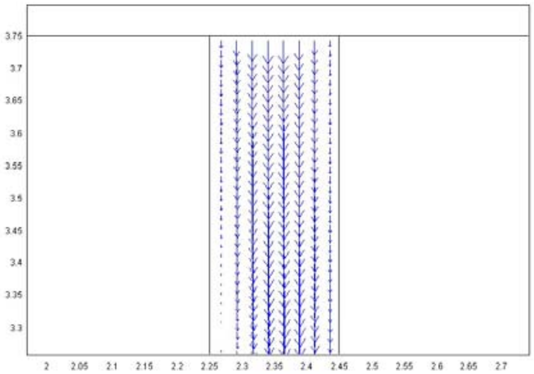

Figure 6.19: Horizontal inflow models with two entrances. The large entrance of Figure 6.6 is enlarged. Clear parabolic inflow is observed.

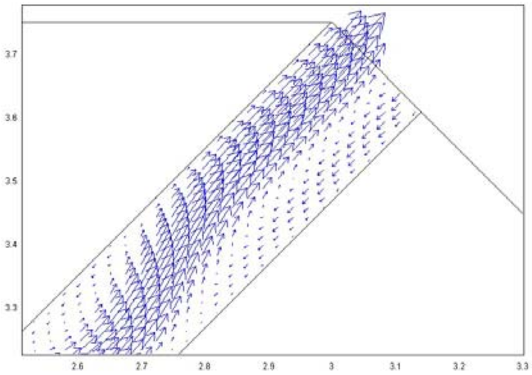

Figure 6.20: Tilted normal flow model with two entrances. The large entrance of Figure 6.10 is enlarged. Both inflow and outflow are observed, but the outflow component is strong.

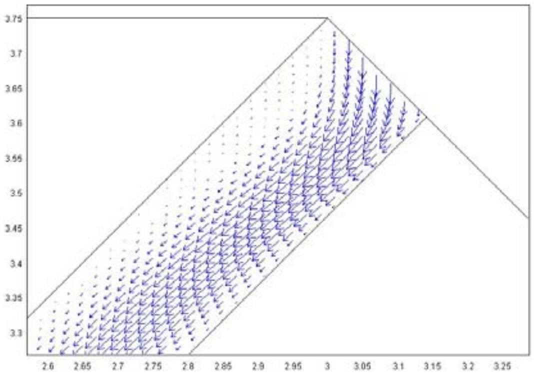

Figure 6.21: Tilted inflow model with two entrances. The large entrance of Figure 6.14 is enlarged. The applied inflow is resisted by the outflow component of cave air.

Table 6.1: Inflow and normal flow models with two entrances. Ra_1 = 17492 based on the height of the main cavity H = 0.3m. The q is heat flux of 0.05Wm^{-2}. The length of the bottom boundary L = 20H. L_a indicates a large entrance passage, S a small entrance and M a main cavity.

Model	*Number of elements*	*Ent.Pass.* *L_a=0.67H* *S=0.25H* *M = H* *(H=0.3m)*	*Flow direction*	*Avg. velocity (m s^{-1})*	*Avg. temp. (K)*	*Boundary integration (Bi) (Wm^{-1})*	*Error* $\left\|\frac{Bi}{L\,q}\right\|100(\%)$
F 6.2 normal	8513	L_a (level)	in/out	2.291x10^{-3}	290.009	-4.072x10^{-3}	1.357
		S (level)	-	6.334x10^{-4}	290.007		
		M (level)	3 cells	4.504x10^{-3}	290.024		
F 6.6 inflow	8513	L_a (level)	in	8.828x10^{-3}	290.004	-1.810x10^{-2}	6.035
		S (level)	out	2.224x10^{-2}	290.010		
		M (level)	circulate	8.462x10^{-3}	290.010		
F 6.10 normal	8450	L_a (above)	in/out	6.250x10^{-3}	290.009	-1.289x10^{-2}	4.295
		S (below)	in	1.356x10^{-2}	290.006		
		M (tilted)	circulate	6.744x10^{-3}	290.012		
F 6.14 inflow	8450	L_a (above)	in/out	6.217x10^{-3}	290.001	-1.265x10^{-2}	4.216
		S (below)	out	1.573x10^{-2}	290.010		
		M (tilted)	circulate	9.840x10^{-3}	290.018		

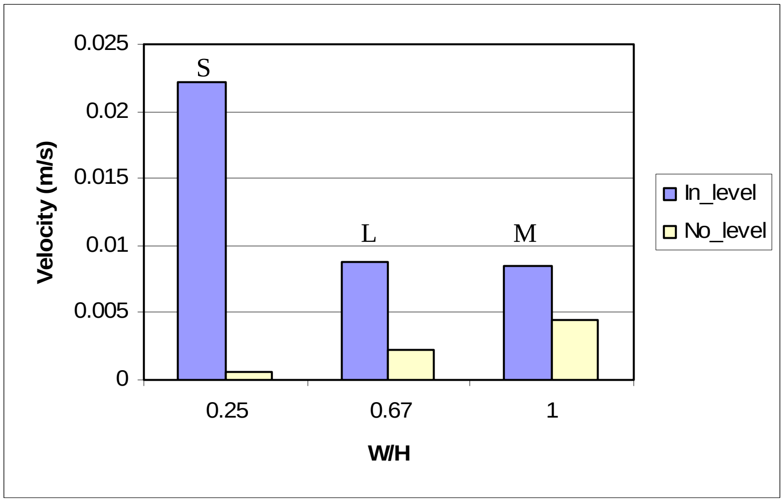

Figure 6.22: Plot of the average velocity field in Figures 6.2 (No_level) and 6.6 (In_level). Imposed inflow at the large entrance increases the average velocity in the entire model. One of the highest average velocity fields amongst all simulations in this chapter is observed in the small entrance (S).

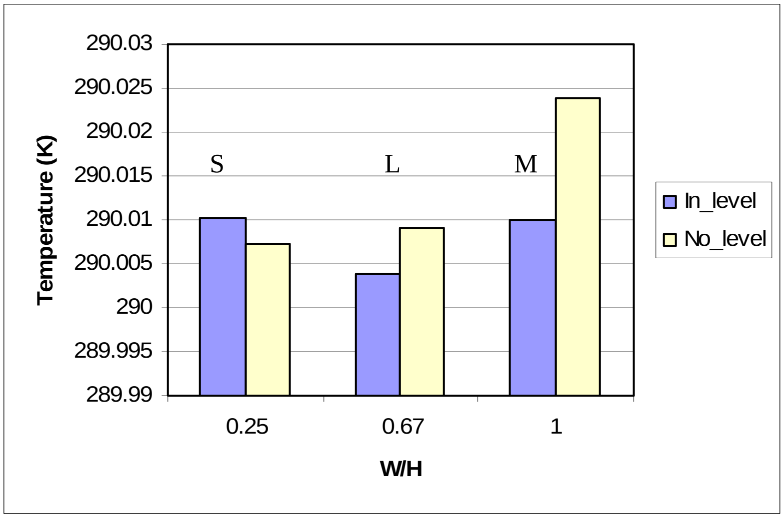

Figure 6.23: Plot of the average temperature in Figures 6.2 (No_level) and 6.6 (In_level). The imposed inflow at the large entrance reduced temperatures in the main cavity (M) and the large entrance passages (L), and increased in the small passage (S).

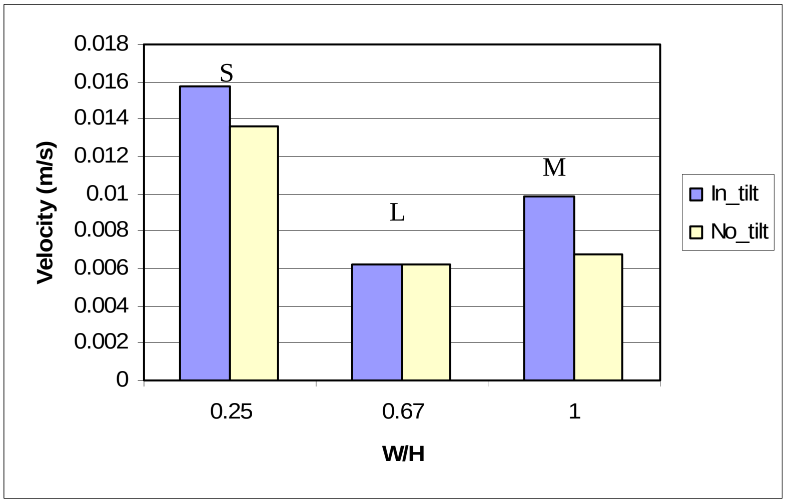

Figure 6.24: Plot of the average velocity field in Figures 6.10 (No_tilt) and 6.14 (In_tilt). The introduced inflow increased the velocity field at the small (S) entrance passage and the main cavity (M).

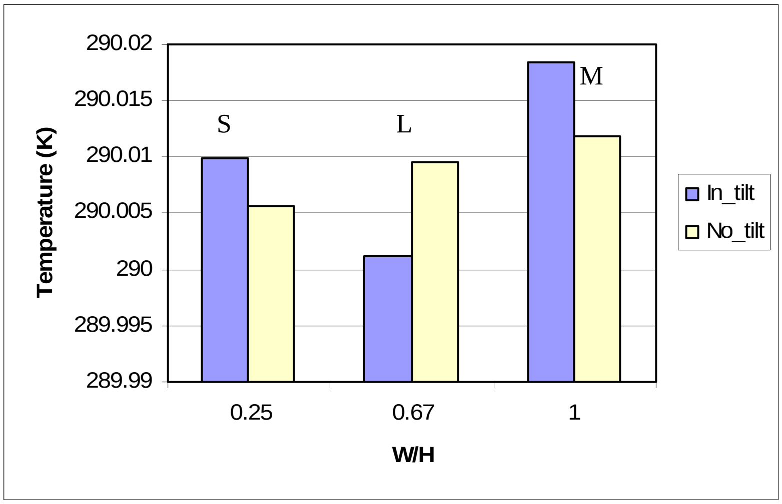

Figure 6.25: Plot of the average temperature in Figures 6.10 (No_tilt) and 6.14 (In_tilt). The imposed inflow increased the average temperature at the small entrance passage (S) and the main cavity (M), and largely reduced it at the large entrance passage (L).

6.1.2 Models with Single Entrance Passage

Normal flow, inflow, and outflow simulations were conducted using the cave models with single entrance. However, the inflow and outflow models did not converge. Thus, only normal flow models are presented here. Later in this section, we will discuss why the inflow or outflow simulations of the model with a single entrance did not produce a unique solution.

(1) Horizontal Normal Flow Model with Single Entrance

Airflow may not be effective when caves have only one entrance. In such a case, how is the air mass balanced? Figure 6.26 shows the modeling result with the cave geometry of Figure 6.2 without the small entrance. In Figure 6.26, the entrance of the model has both inflow and outflow components. The flow pattern of this single entrance is similar to that of the model with two entrances in Figure 6.2, except for the number of convection cells in the main cavities; three in Figure 6.2 and four in Figure 6.26. Figures

6.27 thru 6.29 show the plots of pressure, velocity field and temperature, respectively. The relationships amongst pressure, velocity field and temperature seem to be similar to those of the horizontal normal flow model with two entrances (Figure 6.3 thru 6.5).

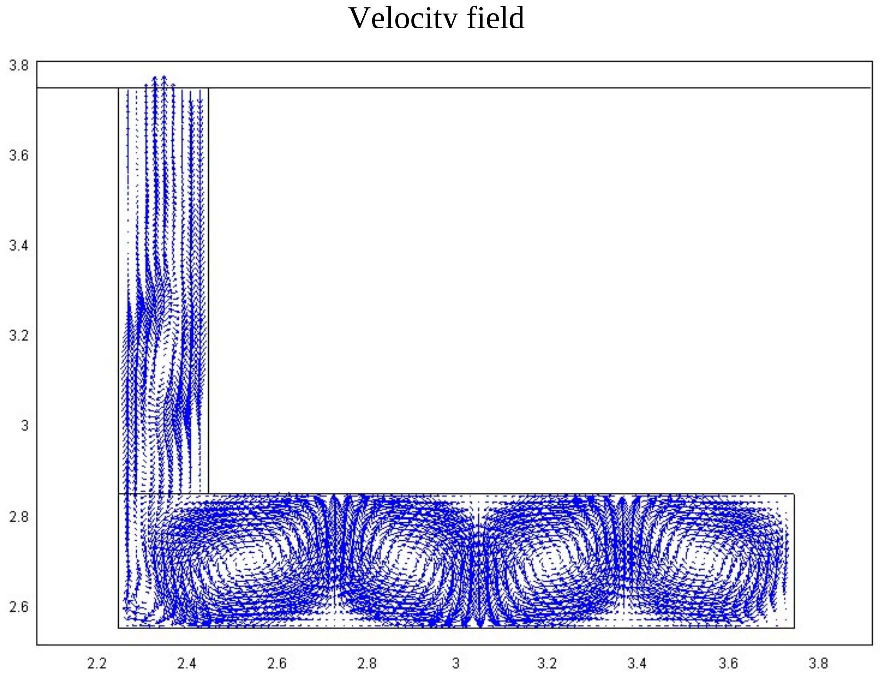
Velocity field

Figure 6.26: Horizontal normal flow model with single entrance. The model shows arrows indicating the velocity field (m s^{-1}). Both inflow and outflow are observed at the entrance. Clear convection cells appear in the main cavity.

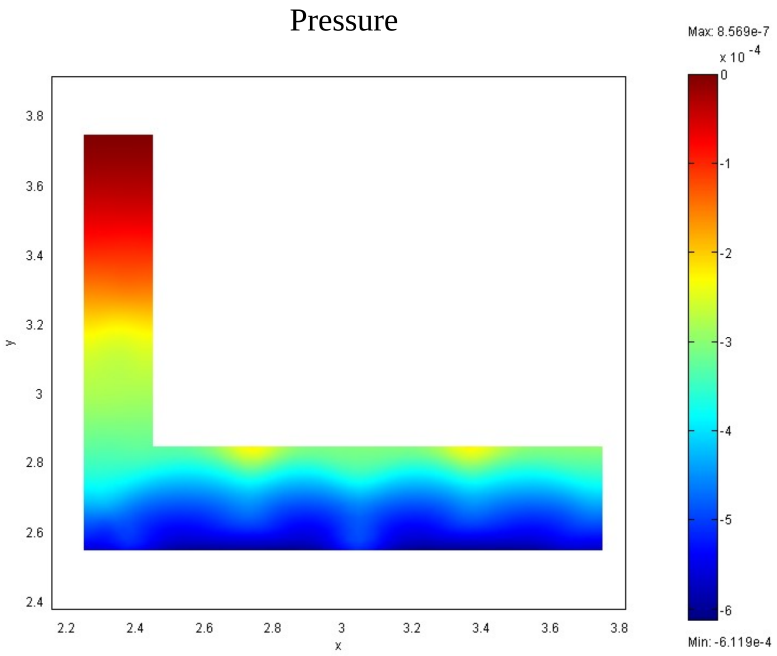
Pressure

Figure 6.27: Horizontal normal flow model with single entrance showing the cave domain plot with surfaces indicating pressure (N m^{-2}).

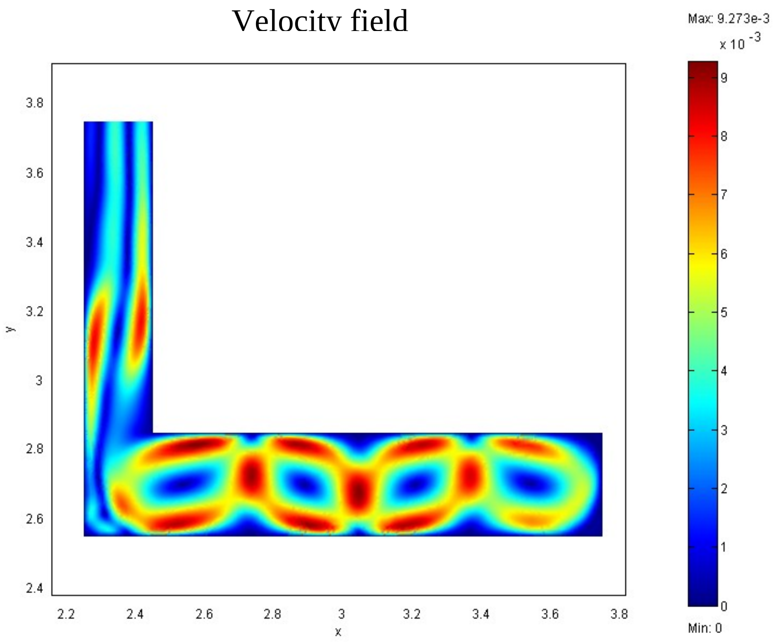
Velocity field

Figure 6.28: Horizontal normal flow model with single entrance showing the cave domain plot with surfaces indicating the velocity field (m s^{-1}).

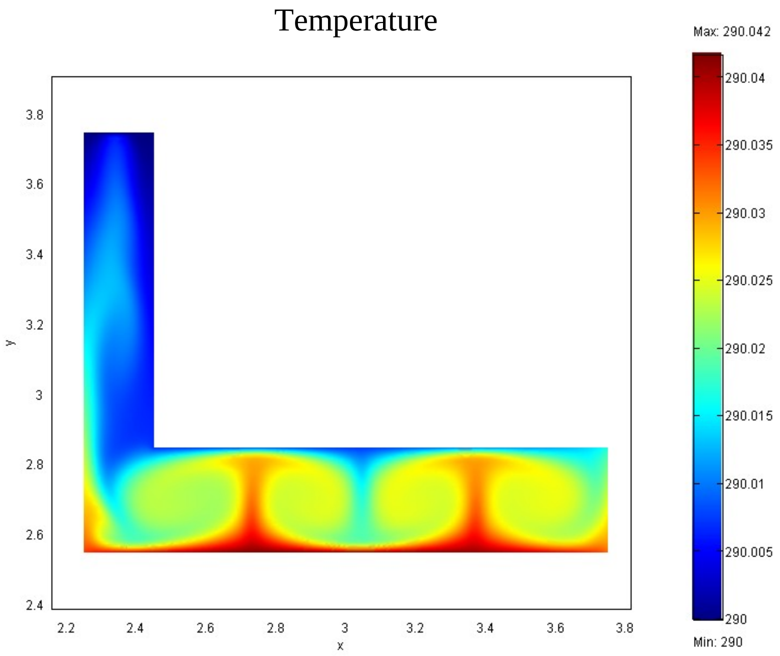

Figure 6.29: Horizontal normal flow model with single entrance showing the cave domain plot with surfaces indicating temperature (K).

(2) Tilted Normal Flow Model with Single Entrance

Air circulation is not effective when caves have only one entrance, especially when a model is tilted (Figure 6.30). Convection cells tend to circulate within the same region, and air exchange takes place only in the vicinity of the entrance. The relationships amongst pressure (Figure 6.31), velocity (Figure 6.32) and temperature (Figure 6.33) are the same as those of the horizontal normal flow model with single entrance (see Figures 6.27 thru 6.29). With depth, the pressure decreases, and the velocity and temperature increase. Pressure, velocity and temperature influence each other, creating stronger convection cells in the deeper sections of the cave model. One convection cell ascends, but when it meets the entrance passage ceiling, the second convection cell is created, thus reducing the velocity field.

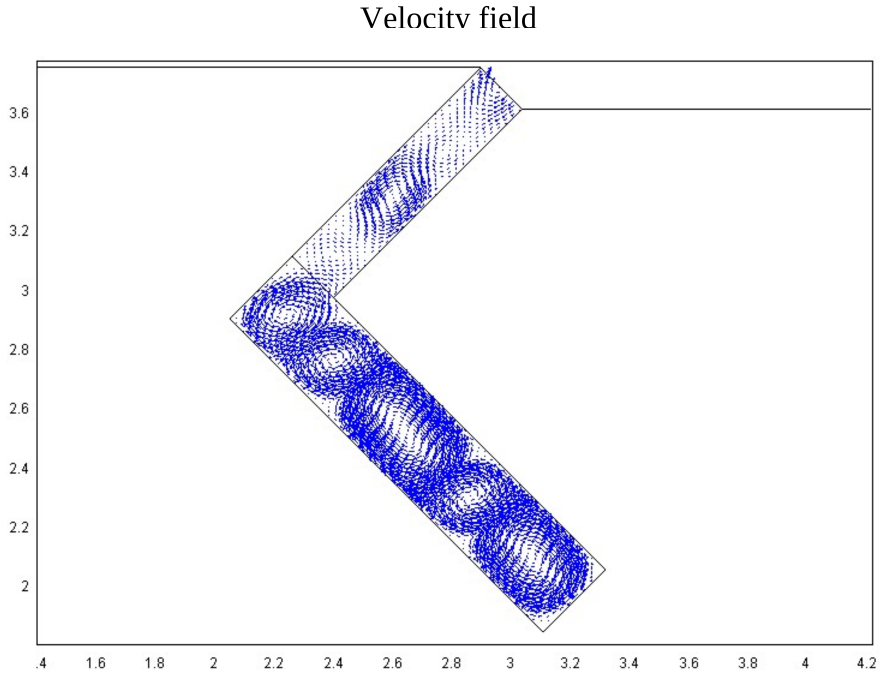

Figure 6.30: Tilted normal flow model with single entrance showing arrows indicating the velocity field (m s^{-1}). Clear convection cells appear in the main cavity.

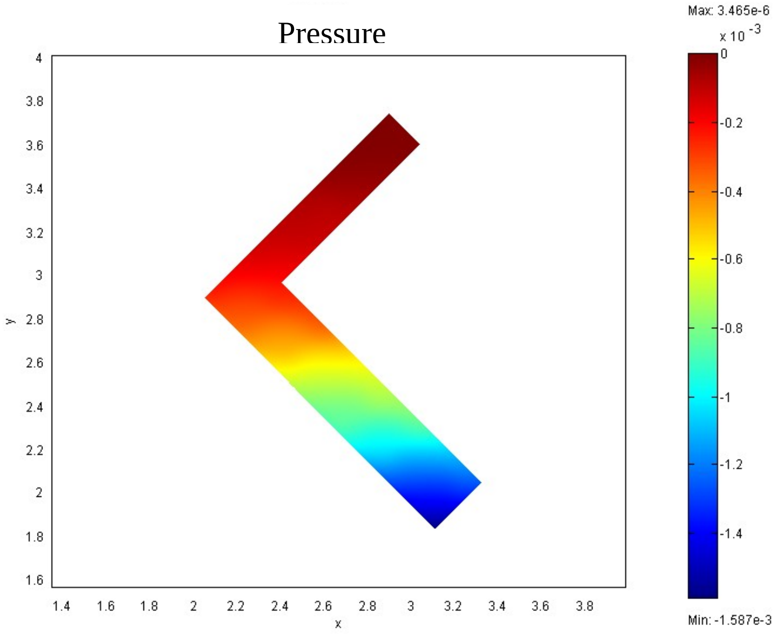

Figure 6.31: Tilted normal flow model with single entrance showing the cave domain plot with surfaces for pressure (N m^{-2}).

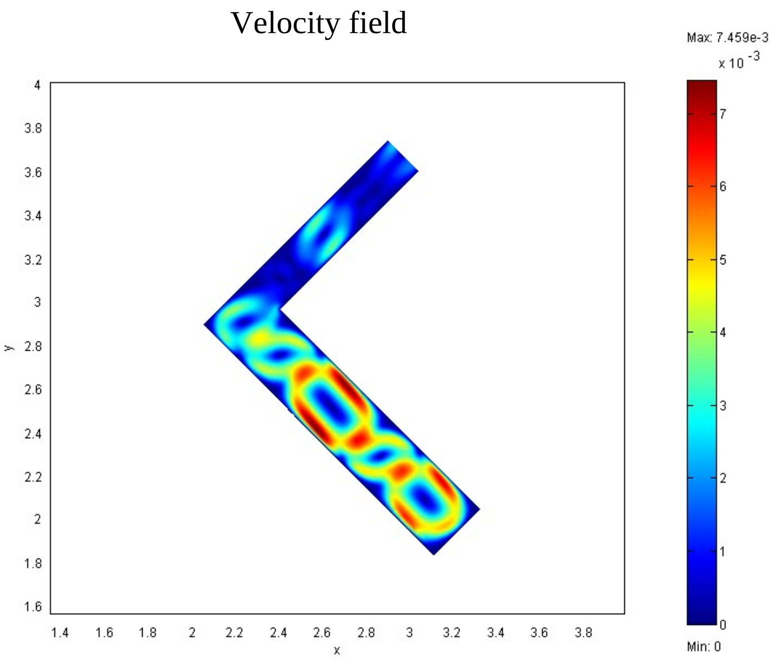

Figure 6.32: Tilted normal flow model with single entrance showing the cave domain plot with surfaces indicating velocity field (m s^{-1}).

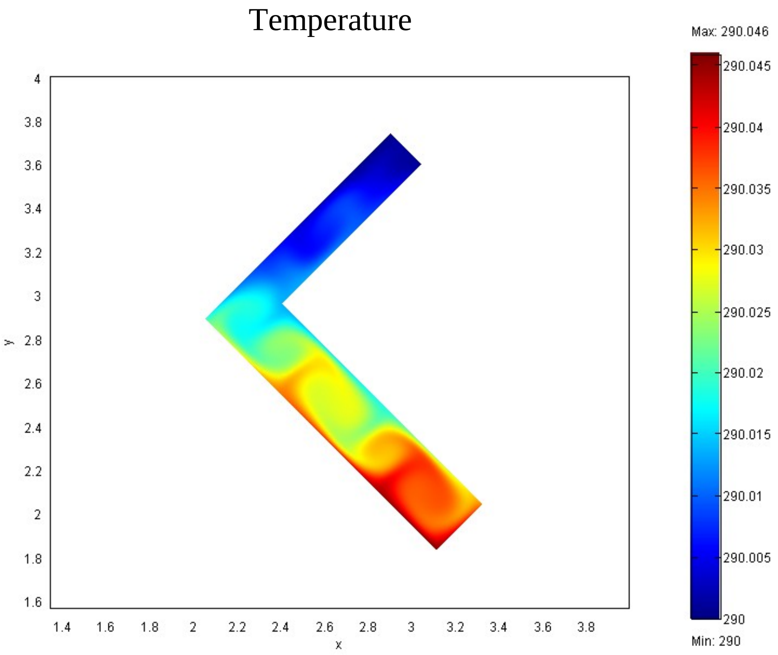

Figure 6.33: Tilted normal flow model with single entrance showing the cave domain plot with surfaces indicating temperature (K). The deeper parts have higher temperatures.

Figures 6.34 and 6.35 are the enlarged images of the entrances of Figures 6.26 and 6.30, respectively. Table 6.2 and Figures 6.36 and 6.37 summarize the modeling results.

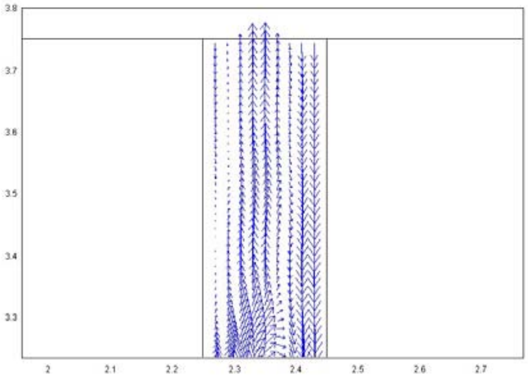

Figure 6.34: Horizontal normal flow model with single entrance. The entrance in Figure 6.26 is enlarged. Both inflow and outflow are observed.

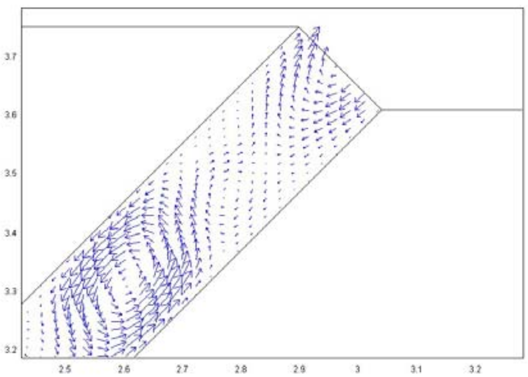

Figure 6.35: Tilted normal flow model with single entrance. The large entrance of Figure 6.30 is enlarged. Air exchange occurs only in the vicinity of the entrance.

Table 6.2: Normal flow models with single entrance. Ra_1 = 17492 based on the height of the main cavity H = 0.3m. The q is heat flux of 0.05Wm^{-2}. The length of the bottom boundary L = 20H. L_a indicates a large entrance passage, and M a main cavity.

Model	*Number of elements*	*Ent.Pass.* *L_a=0.67H* *S=0.25H* *M = H* *(H=0.3m)*	*Flow direction*	*Avg. velocity ($m\ s^{-1}$)*	*Avg. temp. (K)*	*Boundary integration (Bi) (Wm^{-1})*	*Error* $\left\|\frac{Bi}{L\,q}\right\|100(\%)$
F 6.26 normal	4465	L_a (level) M (level)	in/out 4 cells	3.040×10^{-3} 4.502×10^{-3}	290.009 290.024	-2.810×10^{-3}	9.367×10^{-1}
F 6.30 normal	4379	L_a (above) M (tilted)	in/out 5 cells	9.971×10^{-4} 3.209×10^{-3}	290.007 290.028	-2.788×10^{-3}	9.293×10^{-1}

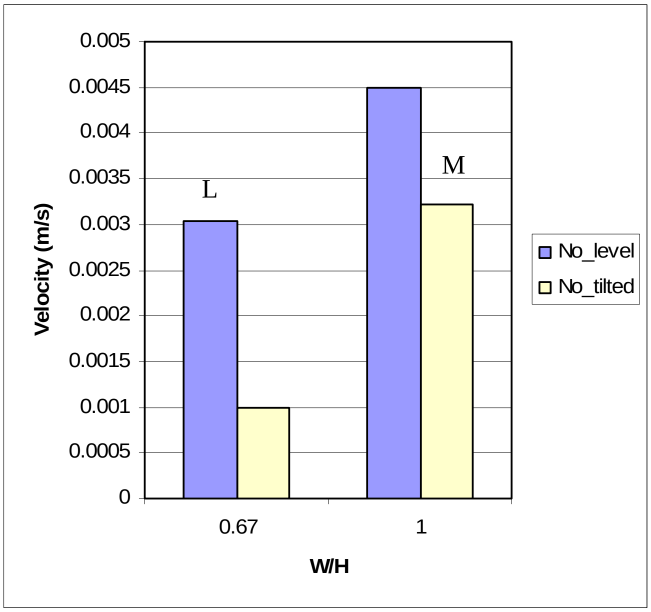

Figure 6.36: Plot of the average velocity field in Figures 6.26 (No_level) and 6.30 (In_level). The average velocities are low in the tilted model.

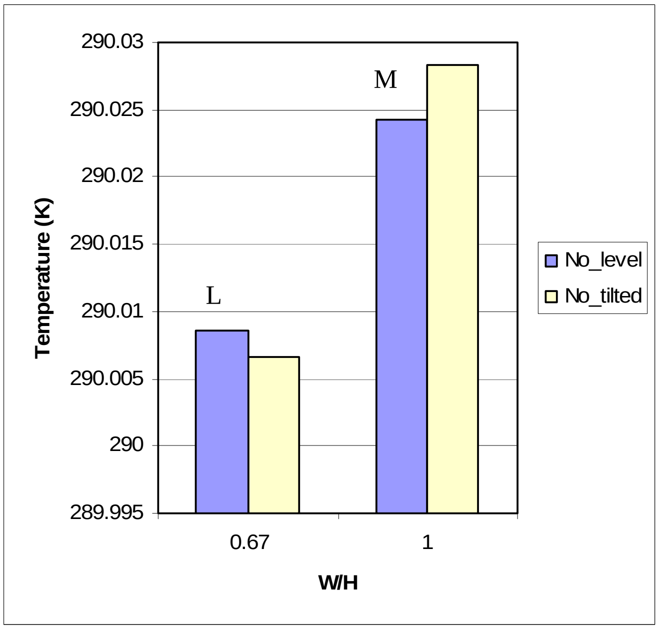

Figure 6.37: Plot of the average temperature in Figures 6.26 (No_level) and 6.30 (In_level). The temperature at the main cavity of the tilted model is high.

(3) Why Cave Models with Inflow and Outflow Simulations Failed to Produce a Unique Solution

The model with a single entrance did not produce a solution when parabolic inflow or outflow fields were applied to the single entrance. Our models have the continuity equation for an incompressible fluid. The introduced inflow or outflow violates the conservation of mass, because there is no exit for the introduced additional air mass, or there is no available open space to supply the surface air to compensate for the outgoing cave air.

If a cave has a single entrance, it may be difficult for the surface air to enter into the cave simply due to high surface barometric pressure, unless compressibility and transient flow are accounted for. On the other hand, buoyancy can easily lead fluid to enter or exit a single cave entrance, as we saw in Chapter 5. To help us understand the airflow of this cave geometry, we conducted simple laboratory demonstrations.

A small flask, representing a cave, was filled with dyed water. A water-filled larger container represented the surface atmosphere. The small flask was submerged into the larger container to observe the water exchange between the flask and the container. Figure 6.38 shows this experiment, in which no water exchange took place between the flask and the container.

In Figure 6.39, after the dyed-water-filled flask was submerged into the container, the container water was mixed vigorously to create currents, resulting in the slow water exchange between the flask and the container. In Figure 6.40, the water in the flask was warmed slightly, and submerged into the container to create a density driven flow. Soon after the flask submerged, water exchange took place actively. Among these three experiments, the thermally-induced density driven flow (Figure 6.40) is the most efficient in terms of water exchange between the two systems.

For air to exchange between the surface and the cave with a single entrance (assuming that there are no other connections to the surface, such as fractures or pore spaces within the vadose zone) requires buoyancy effects or air currents at the surface, because air currents cause unstable situations. Although, it may depend on the intensity of the instability at the surface, we can see from the simple laboratory experiments that the instability at the surface appears not to effectively initiate the exchange of air. In contrast, the thermally induced density driven flow may be most efficient at inducing air exchange. Our flow models simulated this density driven flow with buoyancy forces as the body forces.

Figure 6.38: Equilibrium state. No water exchange takes place.

Figure 6.39: Mechanically forced currents in the container. Water exchange takes place slowly.

Figure 6.40: Density driven flow. Water temperatures in the container and in the flask are 17.6°C and 33.1°C, respectively. Vigorous water exchange takes place.

Our models simulated the steady state of an incompressible fluid flow. In real cave situations, however, cave airflow will often be transient, because the surface weather conditions are always changing (both in terms of velocity and temperature) and, thus, the intensity of instability at the surface is also changing all the time. Based on the simple experimental result in Figure 6.40, fluctuation of temperature at the surface particularly may induce transient conditions inside a cave, even if it has a single entrance. Air can be treated as an incompressible fluid in flow system, but on local scales, such as in caves, air could be temporarily compressed as discussed in Section 2.4. Transients (especially induced by fluctuation of the surface temperature) together with compressibility of air (in local scale flow systems) will cause some air exchange between the surface and the subsurface. We did not model these situations.

6.2 Outflow Simulation

When there is a low pressure system near cave entrances, upward air currents occur and some cave air may be sucked out to the surface. In this section we impose the parabolic outflow velocity field at cave entrances. The parabolic outflow is expressed by:

$$v = (5 \times 10^{-2})\, s\, (1 - s) \qquad m\, s^{-1} \tag{6.7}$$

where a positive sign indicates outflow (see Section 6.1).

(1) Horizontal Outflow Model with Two Entrances

All model conditions shown in Figure 6.41 are the same as Figure 6.1 (normal model) except that the parabolic outflow velocity field is prescribed at the large entrance. In Figure 6.42, clear parabolic outflow and inflow velocity fields are observed in the large and small entrances, respectively. Imposed viscous forces overcome buoyancy forces, resulting in the effective air circulation between the surface and the subsurface.

Figures 6.42 thru 6.44 show the plots of pressure, velocity field and temperature, respectively. As a result of the prescribed outflow at the large entrance, pressure within the large entrance and the main cavity become low, but pressure is high in the small entrance. These phenomena are due to the applied viscous forces (as outflow components) to the large entrance, in an opposite direction from the gravitational force. In equation (6.5), we can change the sign of the viscous force from positive to negative, which results in lowering the pressure gradient by the viscous forces. Pressure becomes lowest in the main cavity due to the combined effects of the prescribed outflow component at the large entrance and buoyancy forces. Both of them act in the opposite direction from the gravitational forces. The low pressure at the main cavity induces the movement of surface air through the small entrance to the main cavity with relatively high velocity. Pressure in the small entrance passage becomes high as the flow that acts as positive viscous forces in equation (6.5) is downward.

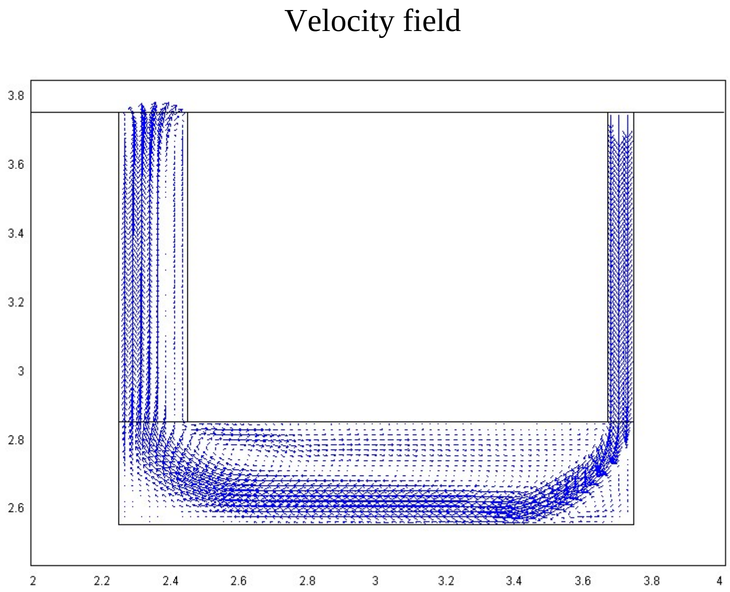

Figure 6.41: Outflow model with two entrances showing arrows indicating the velocity field (m s^{-1}). Parabolic outflow is applied at the large entrance. Air circulates effectively.

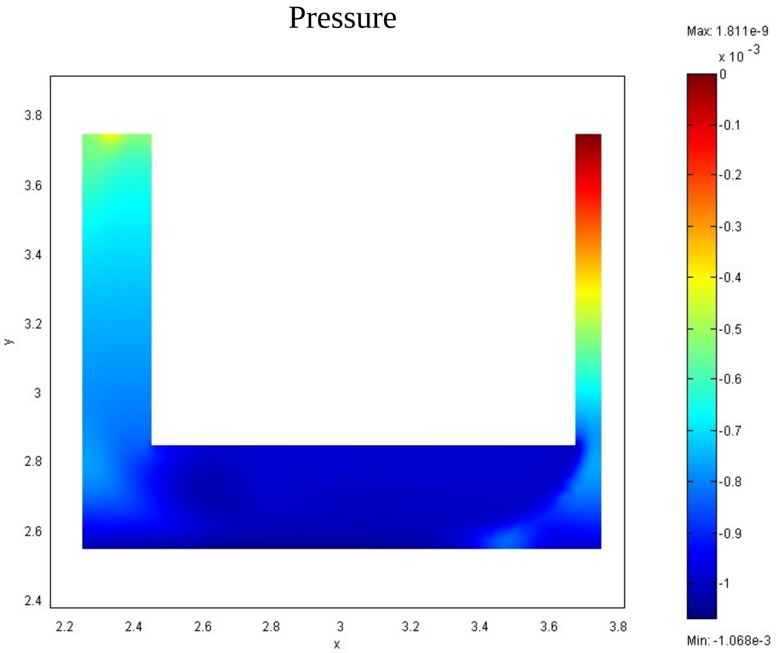

Figure 6.42: Horizontal outflow model with two entrances showing the cave domain plot with surfaces indicating pressure (N m^{-2}). Flow occurs from the high pressure to low pressure regions.

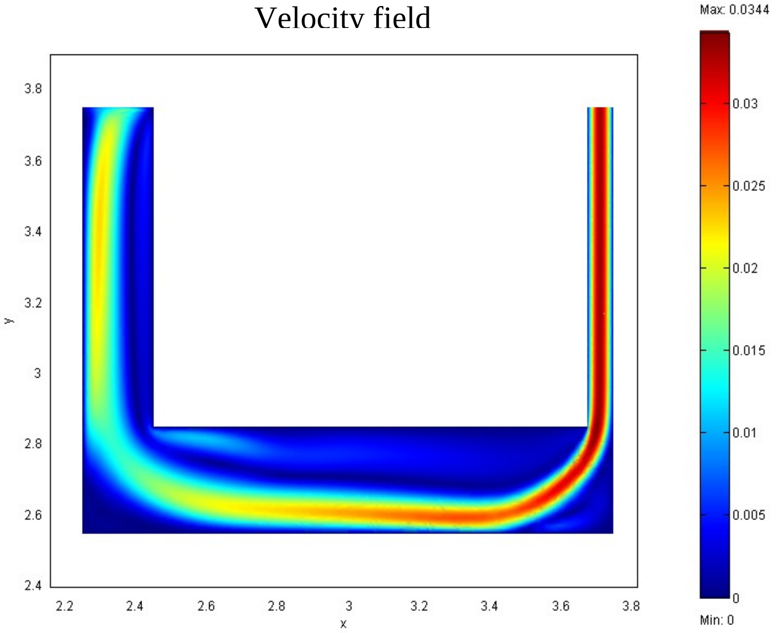

Figure 6.43: Horizontal outflow model with two entrances showing the cave domain plot with surfaces indicating the velocity field (m s^{-1}). A high velocity field is observed at the small entrance.

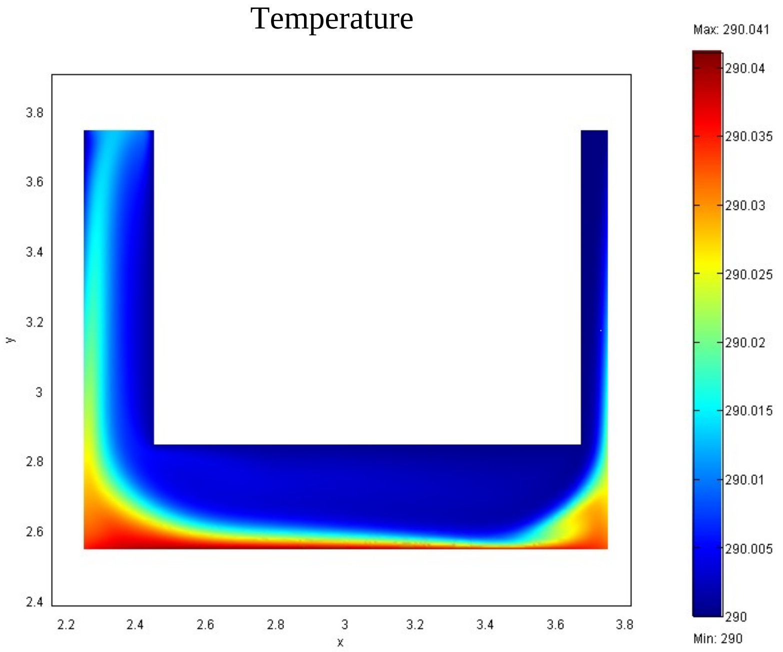

Figure 6.44: Horizontal outflow model with two entrances showing the cave domain plot with surfaces indicating temperature (K). Thermal segregation is observed with high temperatures in the lower parts of the main cavity and low temperatures in the upper parts of the main cavity and the two entrance passages.

(2) Tilted Outflow Model with Two Entrances

All model conditions shown in Figure 6.45 are the same as Figure 6.10 (tilted normal model) except that the parabolic outflow velocity field is applied to the large entrance. The flow patterns are very similar to those of the normal flow model, but they are slightly different in the entrance area. Plots of pressure, velocity field and temperature in Figures 6.46 thru 6.48 are also similar to those of the normal flow model (see Figures 6.11 thru 6.13). The physics behind this model may be similar to that of the normal flow model.

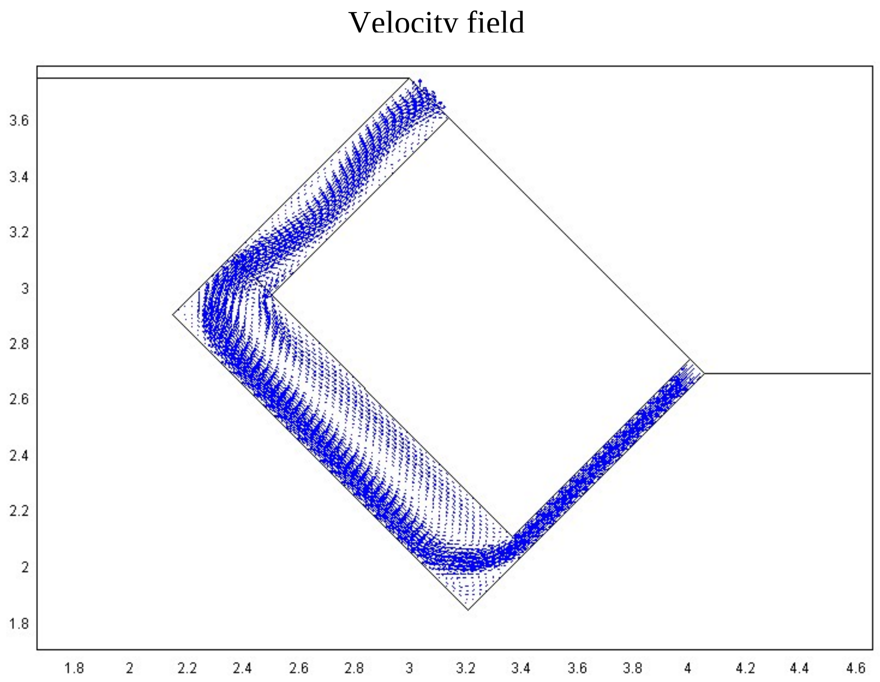

Figure 6.45: Tilted outflow model with two entrances showing arrows for velocity field (m s^{-1}). Parabolic outflow is applied at the large entrance, which appears to slightly stimulate air circulation, but the overall flow pattern is very similar to that of the tilted model with normal flow (Figure 6.10).

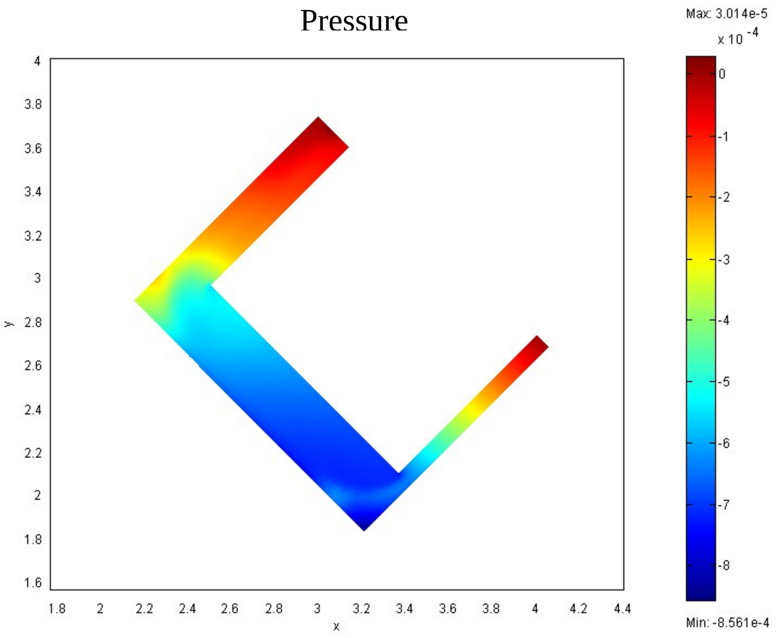

Figure 6.46: Tilted outflow model with two entrances showing the cave domain plot with surfaces indicating pressure (N m^{-2}).

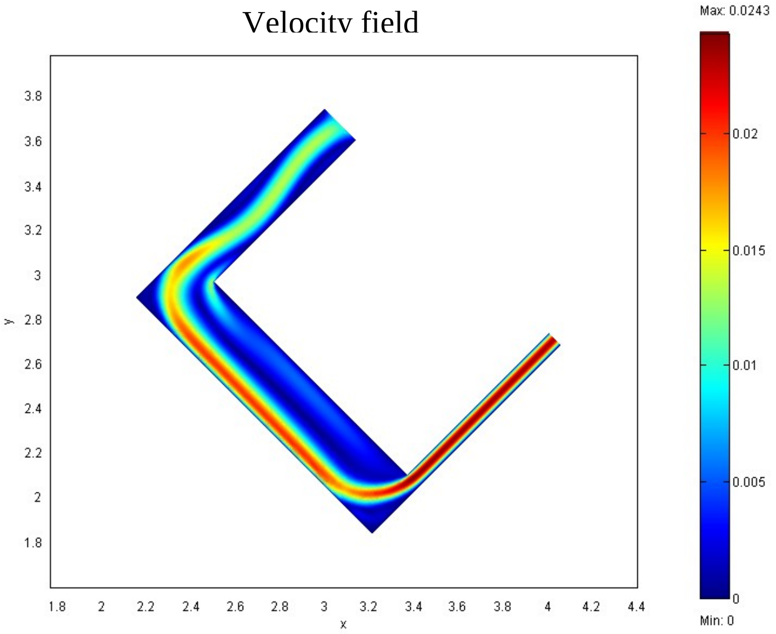

Figure 6.47: Tilted outflow model with two entrances showing the cave domain plot with surfaces indicating the velocity field (m s^{-1}).

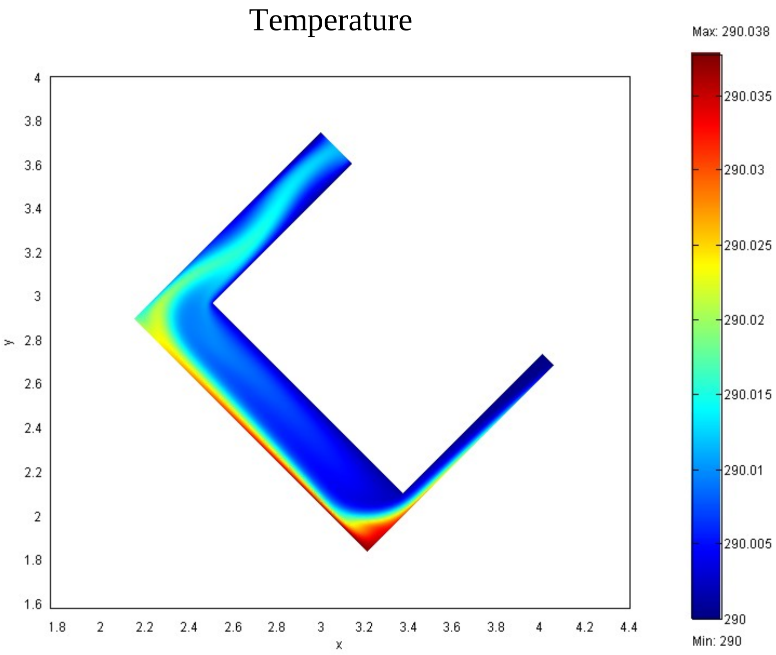

Figure 6.48: Tilted outflow model with two entrances showing the cave domain plot with surfaces for temperature (K).

(3) Summary for Outflow Simulation

Figures 6.50 and 6.52 show the enlarged images of the large entrances of Figures 6.41 and 6.45, respectively, displayed with the normal flow models in Figures 6.49 and 6.51 (the same models with Figures 6.18 and 6.20) for comparison.

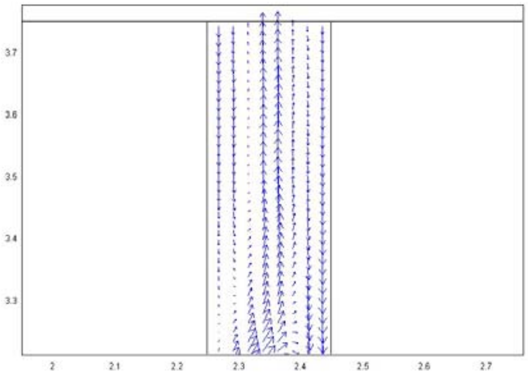

Figure 6.49: Horizontal normal flow model with two entrances. The large entrance of Figure 6.2 is enlarged. Both inflow and outflow are observed.

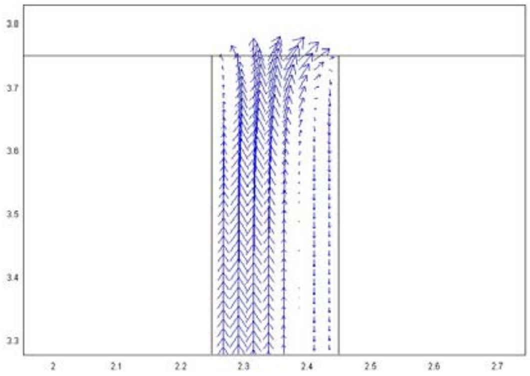

Figure 6.50: Horizontal outflow model with two entrances. The large entrance of Figure 6.41 is enlarged. Clear parabolic outflow is observed at the entrance, but the inflow component also appeared at the right side.

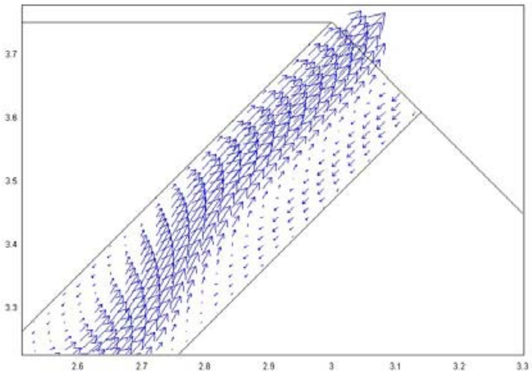

Figure 6.51: Tilted normal flow model with two entrances. The large entrance of Figure 6.10 is enlarged. Both inflow and outflow are observed, but the outflow component appears to be strong.

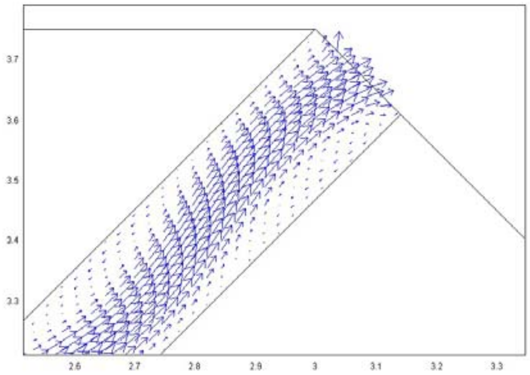

Figure 6.52: Tilted outflow model with two entrances. The large entrance of Figure 6.45 is enlarged. Imposed parabolic outflow slightly changed flow patterns.

Table 6.3: Outflow and normal flow models with two entrances. *Ra_1* = 17492 based on the height of the main cavity *H* = 0.3m. The *q* is heat flux of 0.05Wm^{-2}. The length of the bottom boundary *L* = 20*H*. *L_a* indicates a large entrance passage, *S* a small entrance and *M* a main cavity.

Model	*Number of elements*	*Ent.Pass. L_a=0.67H S=0.25H M = H (H=0.3m)*	*Flow direction*	*Avg. velocity ($m\ s^{-1}$)*	*Avg. temp. (K)*	*Boundary integration (Bi) (Wm^{-1})*	*Error* $\left|\frac{Bi}{L\ q}\right|$100(%)
F 6.2 normal	8513	L_a (level)	in/out	2.291x10^{-3}	290.009	-4.072x10^{-3}	1.357
		S (level)	-	6.334x10^{-4}	290.007		
		M (level)	3 cells	4.504x10^{-3}	290.024		
F 6.41 Out-flow	8513	L_a (level)	in/out	9.733x10^{-3}	290.009	-2.622x10^{-2}	8.739
		S (below)	in	2.222x10^{-2}	290.002		
		M (level)	circulate	8.631x10^{-3}	290.009		
F 6.10 normal	8450	L_a (above)	in/out	6.250x10^{-3}	290.009	-1.289x10^{-2}	4.295
		S (below)	in	1.356x10^{-2}	290.006		
		M (tilted)	circulate	6.744x10^{-3}	290.012		
F 6.45 Out-flow	8450	L_a (above)	in/out	6.656x10^{-3}	290.010	-1.487x10^{-2}	4.955
		S (below)	in	1.572x10^{-2}	290.005		
		M (tilted)	circulate	7.316x10^{-3}	290.011		

Figures 6.53 thru 6.56 summarize the outflow models. In the horizontal models with two entrances, when the large entrance has a prescribed outflow, air circulation becomes effective (Figure 6.53). This leads to lower temperatures in the main cavity and the small entrance (Figure 6.54). In this horizontal cave geometry, when the outflow component is applied to the large entrance, the air mass is balanced by increasing the inflow velocity at the small entrance and having both small inflow and large outflow components at the large entrance (Figure 6.50).

In the tilted models with two entrances, the prescribed outflow at the large entrance is not enough to alter the average velocity field and temperature of the normal flow model (Figures 6.55 and 6.56). The tilted normal model in Figure 6.10 already has air circulation that is in the same flow direction as the outflow simulation (Figure 6.45). However, the applied outflow produced slightly different flow patterns in the vicinity of the large entrance (Figures 6.51 and 6.52). Nonetheless, the overall flow pattern is very similar between the normal flow and outflow simulations (Figure 6.10 and 6.45). Therefore, in this case, the air mass is balanced by altering the flow patterns in the vicinity of the entrance.

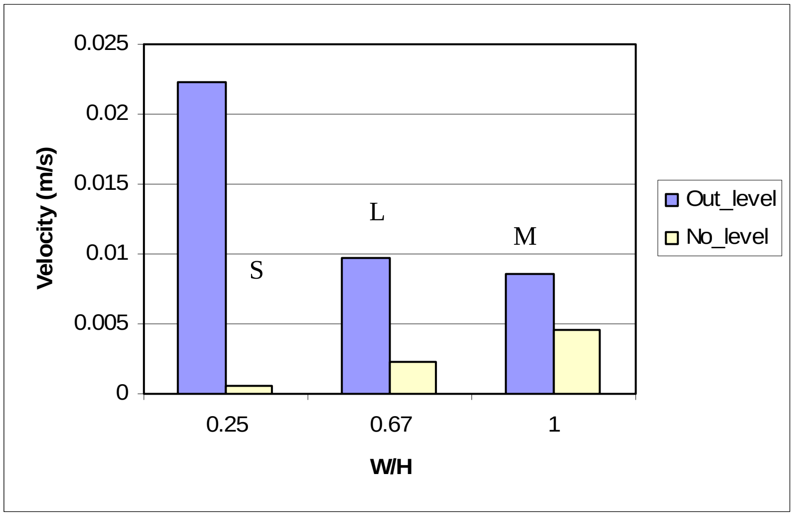

Figure 6.53: Plot of the average velocity field of Figures 6.2 (No_level) and 6.41 (Out_level). Imposed outflow increased the average velocities.

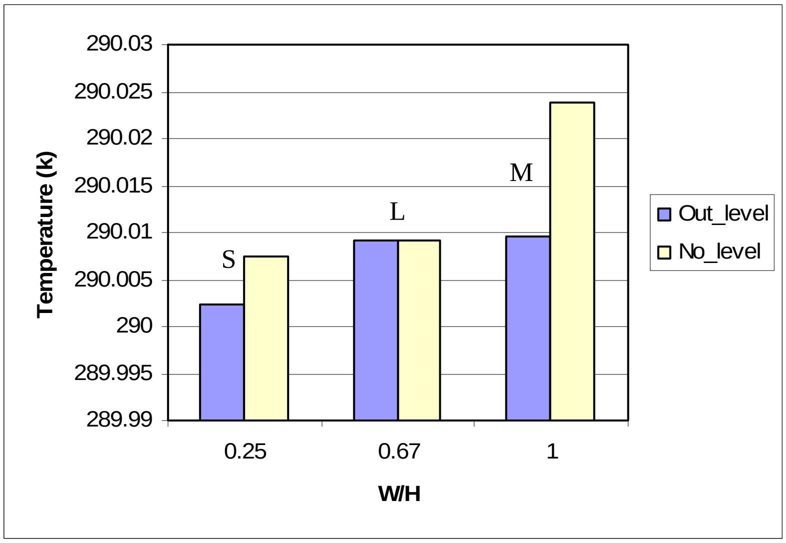

Figure 6.54: Plot of the average temperature of Figures 6.2 (No_level) and 6.41 (Out_level). Imposed outflow reduced the average temperature of the small entrance passage (S) and the main cavity (M), but did not change in the large entrance (L).

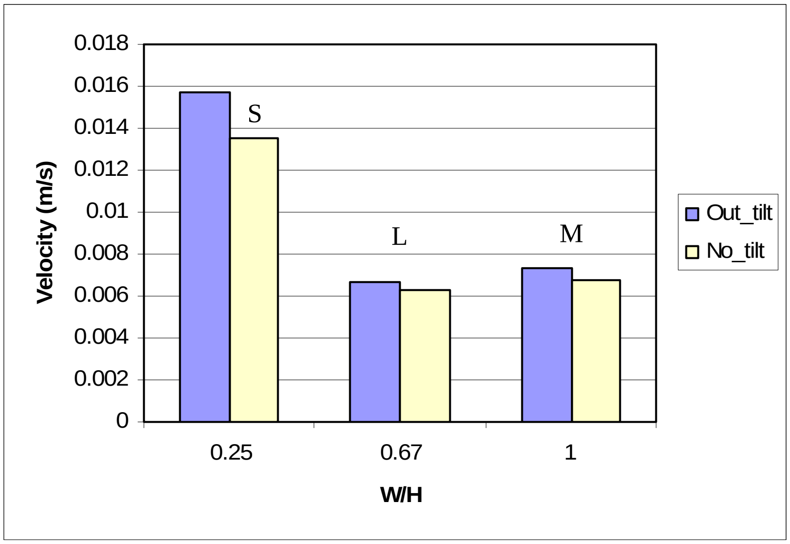

Figure 6.55: Plot of the average velocity field of Figures 6.10 (No_tilt) and 6.45 (Out_tilt). The imposed outflow increased the average velocity in all parts of the cave only very slightly.

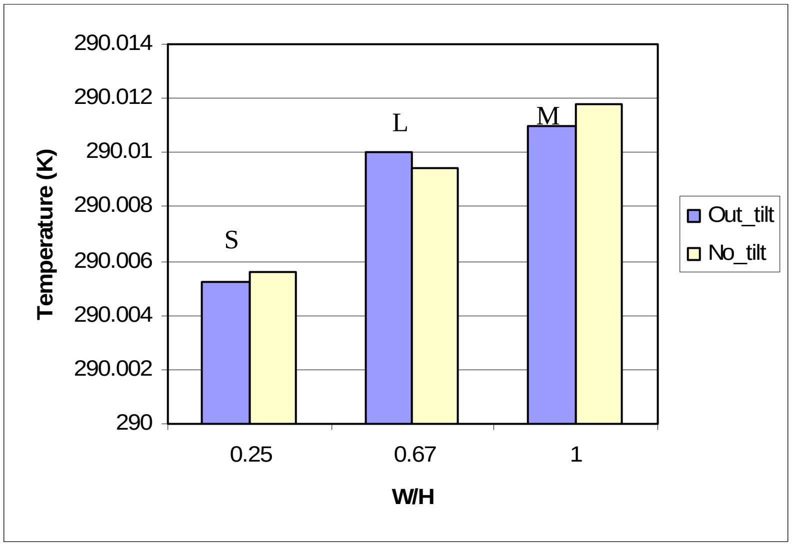

Figure 6.56: Plot of the average temperature of Figures 6.10 (No-tilt) and 6.45 (Out_tilt). The imposed outflow slightly increased the average temperature at the large entrance passage (L), and reduced it at the small (S) passage and the main cavity (M).

6.3 When the Surface Air is Warmer than the Cave Air

The top boundaries of the all models (except entrances) are prescribed with the lowest temperature so that geothermal heat travels through the bottom to the top boundaries. The temperature of the cave entrance inflowing components is influenced by the temperature at top boundaries, which are the lowest in the simulation; that is, any introduced surface air is always cooler than the cave air. Consequently, the models simulate a condition of winter or night. We would like to know what happens when hot surface air is introduced with the inflow at the surface entrance.

The model geometry of Figure 6.57 is the same as Figure 6.10 (the tilted normal flow model with two entrances) but a warmer temperature of 290.1 K (a higher temperature than its bottom temperature of about 290.07 K) was prescribed at the entrance boundaries, instead of the convective heat flux boundary condition for the heat balance equation. The normal flow with zero pressure boundary condition was kept for the flow equations. By having these boundary conditions, cooler cave air or warmer surface air can move freely through the entrance boundaries depending on the internal dynamics (the intensity and direction of buoyancy forces in the main cavity). Figures 6.58 thru 6.61 are the cave domain plots showing arrows indicating velocity field (Figure 6.58), surfaces for pressure, velocity, and temperature (Figures 6.59 thru 6.61, respectively). Figures 6.62 and 6.63 show enlarged images of the large entrances in Figures 6.10 and 6.58, respectively. Both models have 250 arrows, so the same lengths were used for the velocity vectors in the two plots. From these figures, we can see that even when the surface air is warmer than the cave air, air exchange can take place between the surface and the subsurface, when the cave has sufficient buoyancy forces. Figures 6.64 and 6.65, and Table 6.4 summarize the modeling results.

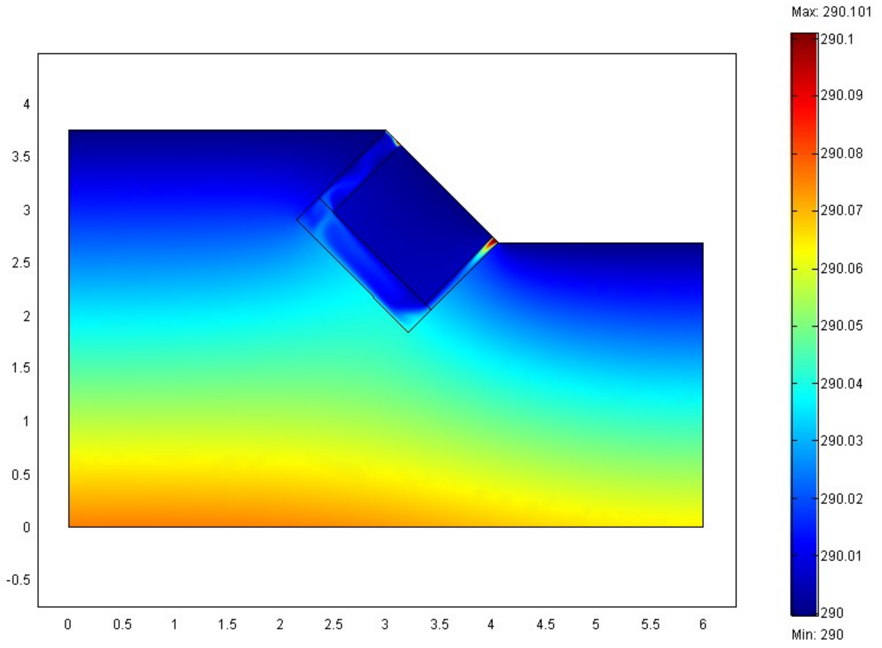

Figure 6.57: Tilted normal flow model with two entrances, to which the highest temperature of 290.1 K was prescribed. The model shows surfaces indicating temperature (K).

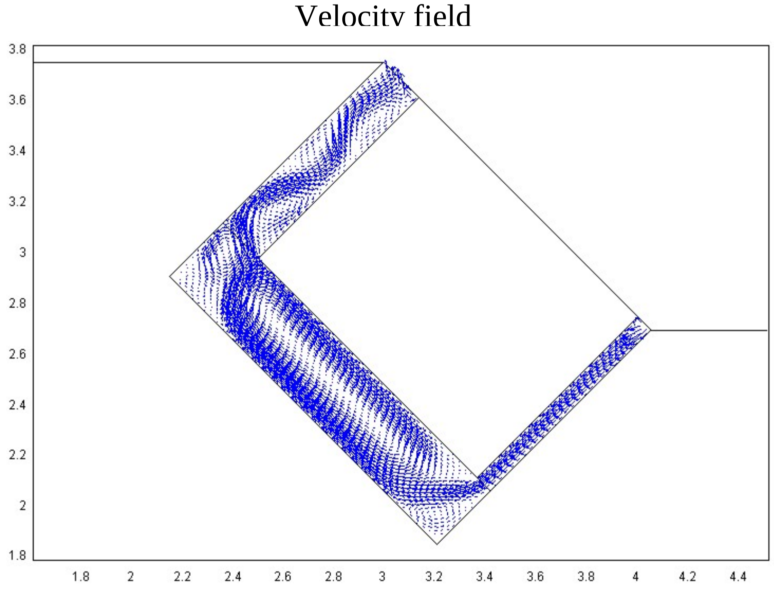

Figure 6.58: Tilted normal flow model with two entrances, to which the highest temperature (K) is prescribed. The model shows arrows indicating the velocity field (m s^{-1}).

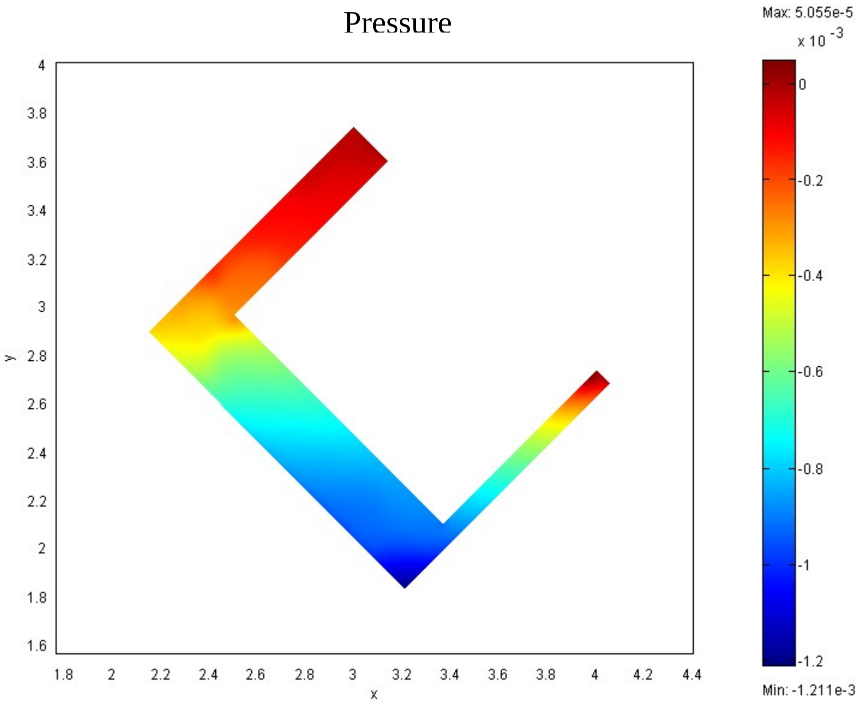

Figure 6.59: Tilted normal flow model with two entrances, to which the highest temperature (K) is prescribed. The model shows surfaces indicating the pressure (N m^{-2}). The pressure distribution is similar to that in Figure 6.11 (convective flux at its entrance boundaries).

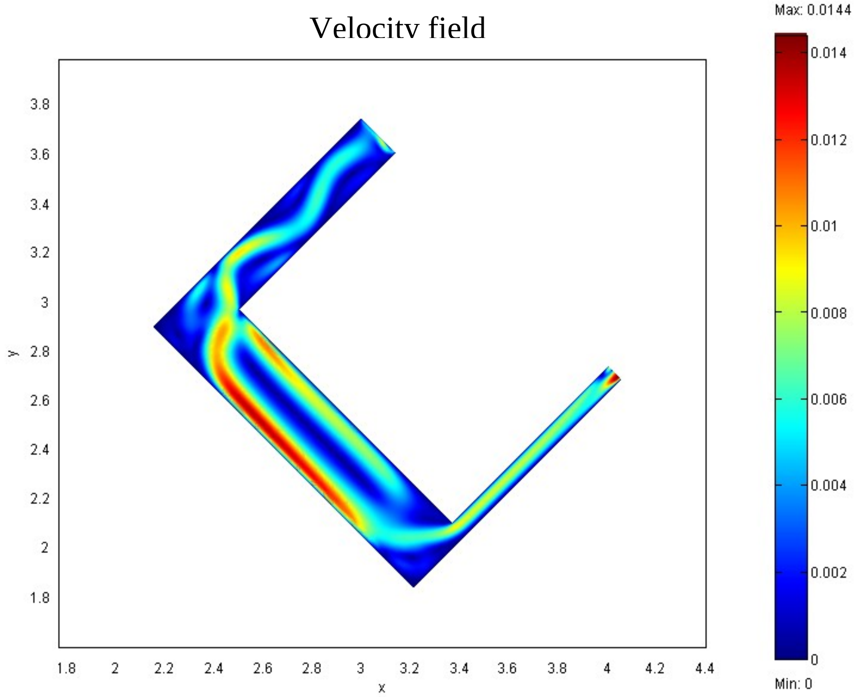

Figure 6.60: Tilted normal flow model with two entrances, to which the highest temperature (K) is prescribed. The model shows surfaces indicating the velocity field (m s^{-1}). Air circulation in the main cavity appears to be stronger than that in Figure 6.12 (convective flux at its entrance boundaries).

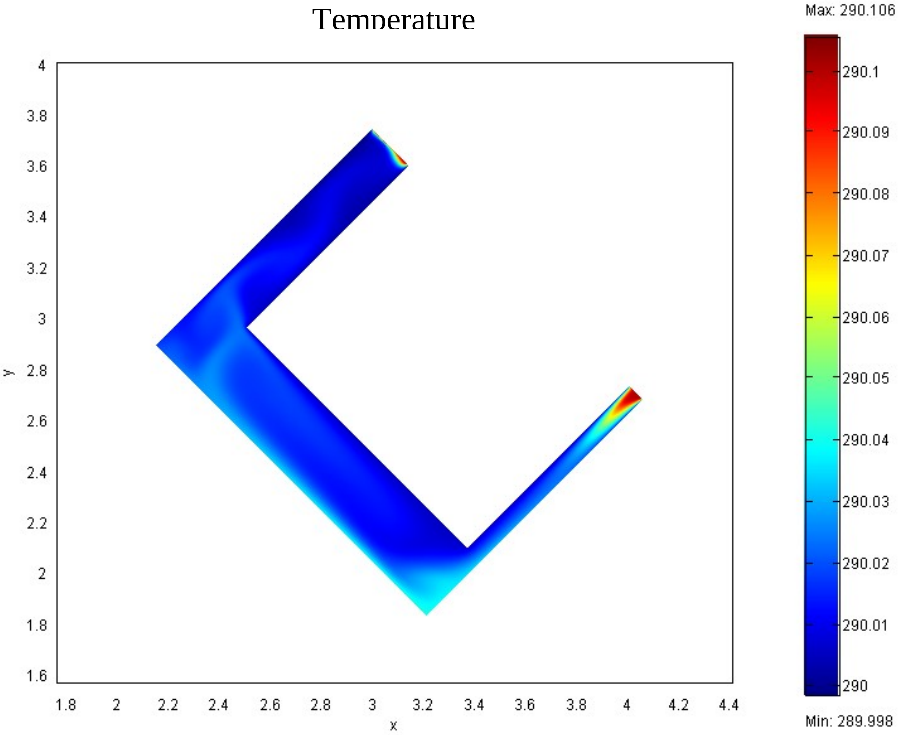

Figure 6.61: Tilted normal flow model with two entrances, to which the highest temperature (K) is prescribed. The model shows surfaces indicating the temperature (K). Note that the warmer surface air is introduced into the cave by internal dynamics.

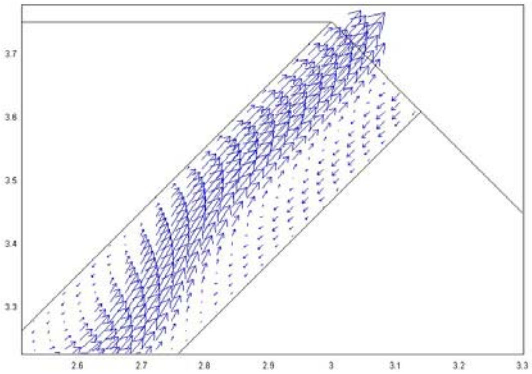

Figure 6.62: Tilted normal flow model with two entrances. The large entrance of Figure 6.10 is enlarged (the same images as Figures 6.20 and 6.51). Both inflow and outflow are observed, but the outflow component appears to be strong.

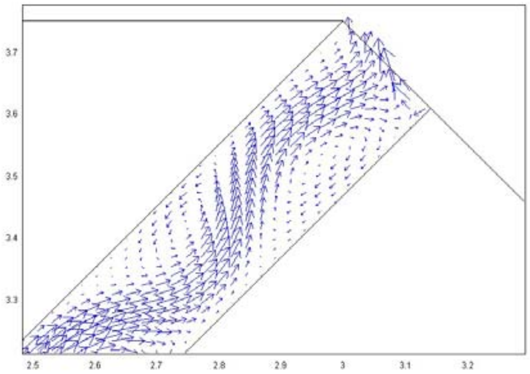

Figure 6.63: Tilted normal flow model with two entrances, to which the highest temperature is prescribed. The large entrance of Figure 6.58 is enlarged. Both inflow and outflow components appear to become weak compared to those in Figure 6.62.

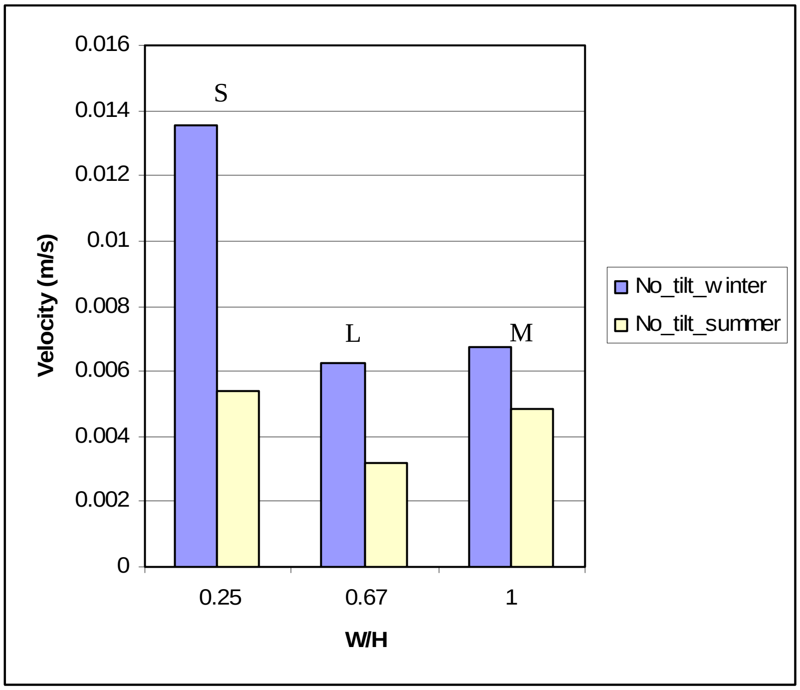

Figure 6.64: Plot of the average velocity field of Figure 6.10 (No-tilt_winter) and 6.57 (No_tilt_summer). The imposed high temperature at the entrance boundaries reduces the velocity in all parts of the cave.

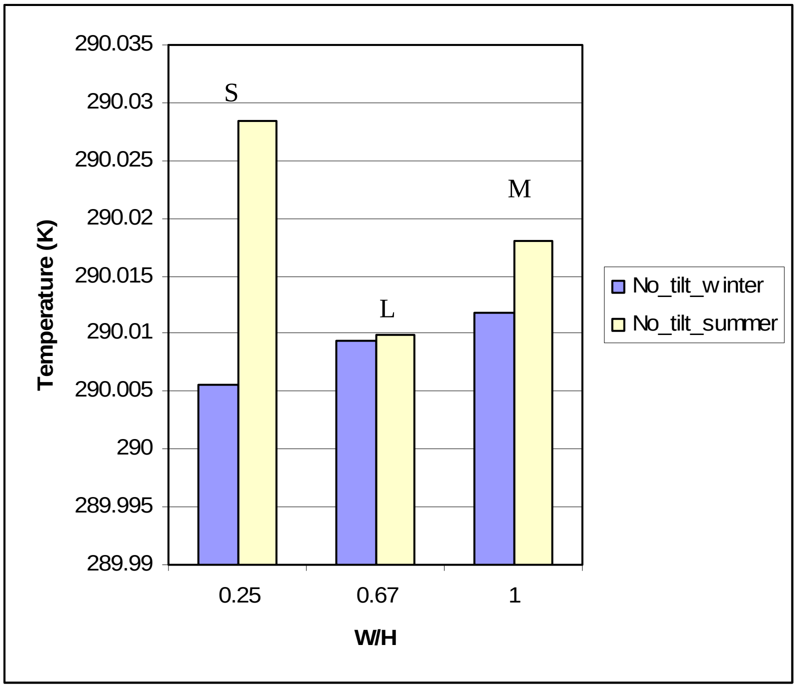

Figure 6.65: Plot of the average temperature of Figure 6.10 (No_tilt_winter) and 6.57 (No_tilt_summer). The imposed high temperature at the entrances increases the temperature in all parts, especially in the small entrance (S) of the cave.

Table 6.4: Normal flow models with two entrances. Models simulated winter and summer conditions. Ra_1 = 17492 based on the height of the main cavity H = 0.3m. L_a indicates a large entrance passage, S a small entrance and M a main cavity. The q is heat flux of 0.05Wm^{-2}. The length of the bottom boundary $L = 20H$. α is the applied heat flux by assigning the highest temperature at the two entrances ($\alpha = 0$ for F 6.10, and 1.5756 Wm^{-1} for F6.57).

Model	*Number of elements*	*Ent.Pass.* L_a*=0.67H S=0.25H M = H (H=0.3m)*	*Flow direction*	*Avg. velocity* (m s^{-1})	*Avg. temp. (K)*	*Boundary integration (Bi)* (Wm^{-1})	*Error* $\left\lvert \frac{Bi}{L\,q+\alpha} \right\rvert 100(\%)$
F 6.10 normal winter	8450	L_a (above)	in/out	6.250x10^{-3}	290.009	-1.289x10^{-2}	4.295
		S (below)	in	1.356x10^{-2}	290.006		
		M (tilted)	circulate	6.744x10^{-3}	290.012		
F 6.57 normal summer	8450	L_a (above)	in/out	3.196x10^{-3}	290.010	1.425x10^{-1}	7.597
		S (below)	in	5.390x10^{-3}	290.028		
		M (tilted)	circulate	4.897x10^{-3}	290.018		

In Table 6.4, an error of F.6.57 was obtained by the normal conductive heat flux error (*Bi*) divided by the total applied heat fluxes: $L\,q$ (bottom boundary) + 1.5756 Wm^{-1} (two entrances boundaries).

CHAPTER 7

WHAT THE SIMPLE AND SMALL CAVE MODELS CAN EXPLAN

The models in this study represent mathematical solutions of the Navier-Stokes equations and the heat balance equation. Although the models are very simple and small, and they do not include some elements such as humidity, presence of water movement, or gravitational pressure gradient, the models are useful to identify to first order important factors that are acting on cave micrometeorology. This chapter summarizes the modeling and seeks to identify the factors that we can apply to explain real cave meteorological conditions.

7.1 Air-filled Caves Act as Insulators

Due to low thermal conductivity of air compared to that of rocks, air-filled caves act as insulators regardless of occurrence of convection cells. Therefore, the presence of caves changes the temperature regime of the surrounding rocks. The model boundaries have constant heat flux or temperature. When the boundaries are too close to a cave structure, the thermal regime of the rock between the boundaries and the cave structure would have been changed by both the insulation effect of the cave and the constant values at the boundaries. Consequently, the constant values at the model boundaries change the temperature and velocity within the cave structures. Thus, we need to set the model boundaries far enough away from cave structures, where the insulation effect of caves is negligible and, thus, we can safely assign constant values for temperature or heat flux.

In general, the geothermal gradient has little or no effect on surface temperatures except in rare cases, however, in the subsurface the geothermal gradient does exert an influence on temperature. As a rule of thumb, the average temperature of a cave is expected to be similar to the average surface temperature at the cave’s elevation [Moore and Sullivan, 1978]. However this is an oversimplification. Where there are large cave systems, the rock temperature above the cave structures may be lower than it would be without caves because the caves redirect geothermal heat (see Figures 5.30 and 5.31). The average temperature at the Natural Entrance passage of Carlsbad Cavern is about 10°C (based on Figure 8.25), which is very low compared to the surface average temperature of 17°C in this region (based on Figure 8.4). This low temperature in the entrance passage could be partially attributed to the insulation effects of the large and multiple cave structures of Carlsbad Cavern below the entrance passage. Of course, another contributing factor may be the cave acting as a cold trap as winter air can flow in and end up in the lower passages. Perhaps the truth will prove to be a combination of both phenomena.

7.2 Geothermal Heat Produces Convection Cells

Recalling equation (2.7), Rayleigh number (*Ra*) describes the ratio of thermally induced buoyancy forces, which drive convective fluid flow, to the viscous forces inhibiting fluid movements expressed by:

$$Ra = \frac{\rho^2 \, g \, C_p \, \alpha \, \Delta T \, L^3}{\mu \, k}$$

where ρ (kg m^{-3}) is the fluid density, g is the gravitational acceleration (m s^{-2}), C_p is the specific heat at constant pressure (J kg^{-1} K^{-1}), α is the coefficient of thermal expansion (K^{-1}), ΔT is the temperature difference (K), L is the characteristic length (m,) μ is the dynamic fluid viscosity (N s m^{-2}), and k is the thermal conductivity of the fluid (Wm^{-1}K^{-1}). Recalling equation (2.9), in this study, we employed the modified Rayleigh number (Ra_1) to deal with thermal properties of two materials (rock and air) and heat flux q_r instead of temperature difference ΔT expressed by:

$$Ra_1 = \frac{\rho_a^2 \; g \; c_{pa} \; \alpha_a \; q_r \; L^4}{\mu_a \; k_a \; k_r}$$

where the subscripts $_a$ and $_r$ refer to air and rock, respectively.

Because of the low viscosity of air and the isolation of the cave within a rock mass, convection cells occur even though the applied heat flux is low (such as a geothermal flux of 0.05 Wm^{-2}). In conventional models of rectangular enclosures heated from below, the critical Rayleigh number (Ra_c) of 1708, refers strictly to an infinite horizontal layer with rigid (no-slip) and isothermal top and bottom boundaries [Bejan, 1995, 254]. The Ra_c for an air-filled cavity with a constant temperature of 290 K at the top boundary and a geothermal flux of 0.05 Wm^{-2} at the bottom boundary lies between 1670 and 1800 (using equation 2.10). The corresponding characteristic lengths for our other parameters (the height of the cavities) are 0.053 m and 0.054 m, respectively (see Figures 5.1 and 5.2). The Ra_c for an air-filled cavity with no rock surrounding it but with isothermal top boundary and a constant heat flux bottom boundary is very close to that of the theoretical value with isothermal top and bottom boundaries (1708).

Unlike air-filled cavity models, the boundaries of cave models are located far from the cave structures and, thus, cave walls do not have constant thermal conditions. The thermal variation of side walls of caves is especially significant (see Section 5.1.2). This thermal variation on cave walls may cause instability of the air in terms of heat transfer, creating organized flow patterns with ultra low velocities, such as the spatial average velocity field of 10^{-9} m s^{-1} observed in Figure 5.5. However, with such low velocity fields, the temperature contour lines do not indicate any convection. The contour lines of the air-filled cavity-only models begin to indicate convection when the magnitude of the spatial average velocity field shifts to 10^{-4} m s^{-1} from a lower order, such as 10^{-7} m s^{-1} (Figure 5.2). We assume that at Ra_{1c} (critical Rayleigh number for cave models) the order of the average velocity field shifts to 10^{-4} m s^{-2} from lower orders. The Ra_{1c} for the simple rectangular cave model with the aspect ratio of $W/H = 2$ could lie between 617 and 830 (corresponding characteristic lengths are 0.13 m and 0.14 m, respectively, see Figures 5.6 and 5.7). At $Ra_{1=}$ 830, the temperature contour lines begin to curve with the concave profile pointing up at the center.

When caves have more complicated structures such as the presence of entrance passages, then convection cells can occur with lower Ra_1 such as 448 (corresponding characteristic length is 0.12 m, see Figures 5.58 and 5.59). However, it is not clear that the complexity of cave geometry enhances air movement (see Table 5.15). In addition, the reader will recall the horizontal normal flow model with two entrances in Figure 6.2. The convection cells created in the main cavity (Ra_1 =17492) can move up to the large entrance passage, whereas they cannot move to the small entrance passage. This may be because the width of the small entrance is too short compared to the wavelength of the convection cells created in the main cavity. Thus, Ra_{1c} strongly depends on cave geometries.

7.3 Intensity of Heat Flux Affects Average Temperature and Velocity Field

Mean continental heat flow ranges from 0.04 Wm^{-2} on the stable cratons to 0.07 Wm^{-2} in Tertiary tectonic provinces [Ingebritsen and Sanford, 1998, 176-177]. The intensity of heat flux and the average temperatures inside caves appear to be proportional (Figure 5.18). The average velocity field also increases with an increase in heat flux, except when the models produce the different number of convection cells. The average velocity field is affected by the number of convection cells. A high velocity field is observed in the models with a small number of convection cells (Figure 5.19). The number of convection cells may be determined by the combination of geometry and intensity of heat flux, but we have not yet determined the details of these mechanisms.

7.4 Geometries Control Cave Micrometeorology

In the models, air and heat flow patterns or cave temperatures are regulated strongly by cave geometries. Under the same height of entrance passages, the wider the entrance passages, the higher the velocity field and temperature (Figure 5.27) within the passage, but too high a velocity can actually reduce the temperature. The decrease in the temperature in the larger entrance width could also be affected by the temperature in the top boundaries adjacent to the entrance, in which the lowest temperature is applied. The average velocity field decreases as cave air ascends along an entrance passage (Figure 5.29).

In internal dynamics models in Chapter 5, air circulation is not effective in a horizontal model with two entrances (Figure 5.32), but it is initiated when the model is tilted and the effect is amplified further in the larger sized models (Figures 5.33, 5.34, and 5.37). In the tilted models with two entrances, the small passage has a higher velocity regardless of the vertical positions with respect to the larger passages (Figure 5.36). Inflow occurs in the lower passage and outflow in the upper passage regardless of their size (Table 5.9). This may be largely due to the preferential flow direction of the main cavity, that is, towards the upper cavity. The average temperatures of the passages appear to partially depend on the average velocity of the passages (too high a velocity can reduce the temperature of the passage).

Speleothems are good thermal conductors; stalactites and stalagmites could lower or raise, respectively, cave air temperature (Figure 5.45). However, we have ignored the effects of water movement that is usually associated with creation of speleothems, and moving water may well alter air temperature.

The presence of overlying cavities increases the temperature of underlying cavities, even when the cavities are not perfectly overlapped (Figure 5.54). On the other hand, the average velocity field of underlying cavities appears to be slightly reduced by the presence of overlying cavities due to a decrease of the thermal gradient within the underlying cavity (Figure 5.55).

A small difference in cave geometry can change the flow direction. In the example models of Figures 5.56 and 5.57, the flow directions (upward or downward) of the narrow passage were altered depending on whether or not a horizontally long passage was attached to the left side of the narrow passage. Because caves act as insulators, the presence of the horizontally long cavities raises the temperature of the system below them, which could change the flow directions in cavities below the tunnels.

7.5 Airflow Occurs Both from High to Low and Low to High Pressure Regions

Naïve models of fluid flow assume that flow occurs from the high pressure region to the low pressure region. However, the pressure plots in Chapter 6 show that sometimes the flow can occur from the low pressure region to the high pressure region. Perhaps, if the viscous force dominates in the flow system models (such as fluids flow due to the prescribed inflow), then fluid flow can occur from the high pressure region to the low pressure region. However, if it is a thermally-induced buoyancy-driven flow (such as in natural convection), then the flow can be in both directions, that is; fluids flow from the high to low pressure regions, or from low to high pressure regions depending on fluid density and geometry.

These models ignore the gravitational pressure gradient. However, this treatment is not a serious flaw, because we focus on the thermally-induced density-driven flow that occurs as a result of the density difference between neighboring parcels of air, whose gravitational pressure gradient is negligible. Neglecting the gravitational pressure gradient lets us focus on the internal dynamics. For example, without a gravitational pressure gradient, air circulates within the cave structures in the tilted models with two entrances. These flows are a result of the thermally-induced buoyancy forces, the conservation of mass (with air as an incompressible fluid), and the cave geometries. The presence of a gravitational pressure gradient between the two entrances would facilitate these air circulations when there is a difference in temperature between the cave and the open atmosphere [Bögli, 1980, 218].

7.6 Cave Air Moves in Order to Conserve Air Mass

Models are simulated in steady state, and air is treated as an incompressible fluid. Thus, the air mass inside cave structures should remain constant. Because the gravitational pressure gradient was neglected in our models, the air mass inside caves should be determined mostly by air temperature and volume of the caves (the elevation factor is neglected). The most enlarged image of the large entrance passages of the models in Chapter 6 describes concurrent inflow and outflow components. On the other hand, the small entrances of models with two entrance passages tend to produce a single flow direction. The large entrances may be the places where the air mass is balanced having both inflow and outflow components. Our models simulate the density-driven flows associated with thermally-induced buoyancy forces as body forces. Thus, these inflow and outflow components are created by the air density difference as well as by the conservation of mass. The lighter, warm cave air moves up and escapes through the entrance, and the same amount of denser, cool surface air moves down into the caves. Note that the surface influence can be introduced by having inflow components caused by the internal dynamics: thermally-induced buoyancy forces, conservation of mass, and cave geometries (e.g., a large entrance passage, or multiple entrances).

In the steady state, incompressible fluid flow simulation, the introduced and escaped air mass should be the same. However, unlike our models, real cave systems could be transient and, thus, the rate of air escape could be different from the rate of incoming air. This could lead to an imbalance of air mass inside caves. If caves have excess air mass, temporarily, excess air pressure would be created locally, triggering a movement of air to areas of lower pressure. Eventually, excess air moves out through available openings. The reverse phenomenon can be observed if caves have less air pressure than the exterior. When an open space is large enough, two flow directions (in and out) can be observed in a single opening, or if it is small, unidirectional flow can occur. Thus, we consider that: 1) cave air mass is largely conserved; 2) cave air moves to conserve the appropriate air mass in terms of temperature, volume of cave, and elevation; and 3) the internal dynamics (thermally-induced buoyancy forces, conservation of mass, and cave geometries) alone, without the fluctuation of the surface weather systems, can introduce surface air into caves.

CHAPTER 8

APPLICATIONS OF THE MODELS

In the previous chapters, we have identified some possible factors that affect cave internal meteorological dynamics. In this chapter, we will apply the results of modeling to suggest possible explanations for some observed phenomena within two well-known New Mexico caves, Carlsbad Cavern and Lechuguilla Cave.

8.1 Carlsbad Cavern, New Mexico

Carlsbad Cavern is a well-known, very large cave system in southeastern New Mexico. The map in Figure 8.1 describes elevations of the cave structure and Figure 8.2 is a vertical cave profile. The elevations on these maps were roughly estimated based on Hill [1987, Sheets 2 and 3]. Our primary focus areas within Carlsbad Cavern are Natural Entrance, Bat Cave, Left Hand Tunnel, Lower Cave, and Lake of the Clouds. According to Hill [1987, 24], there are four main levels of horizontal cavern development that have occurred in Carlsbad Cavern: 1) 60 m below Natural Entrance (Bat Cave level); 2) 120 m (New Section level); 3) 230 m (Big Room level); and 4) 260 m (Lower Cave level).

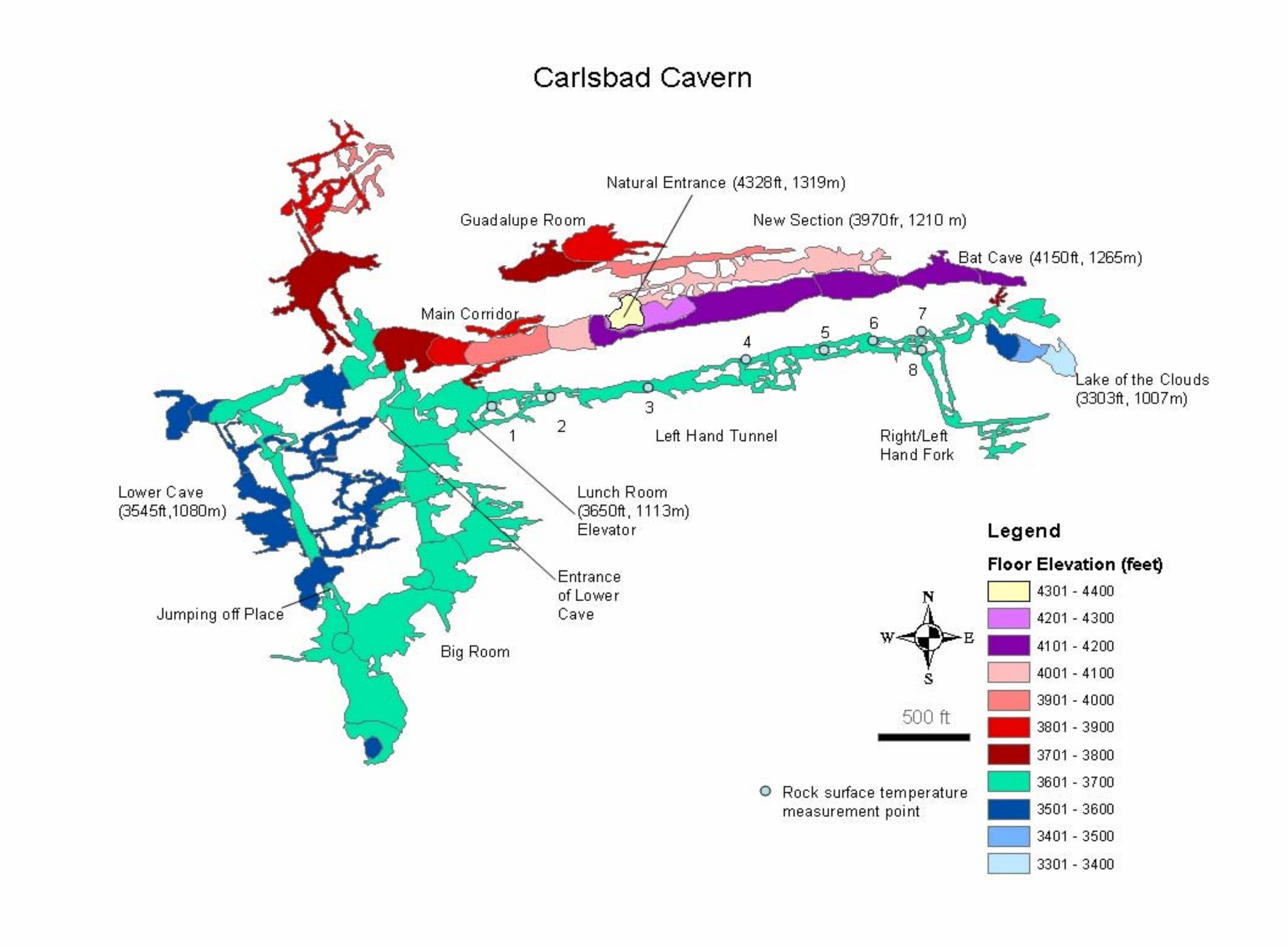

Figure 8.1: Carlsbad Cavern elevation map. Elevations were roughly estimated based on Hill [1987, Sheet 2] to help us visualize the vertical relationships within the cave structure. The numbers along the Left Hand Tunnel are the rock surface temperature measurement points that were conducted on October 25, 2003 and December 10, 2004.

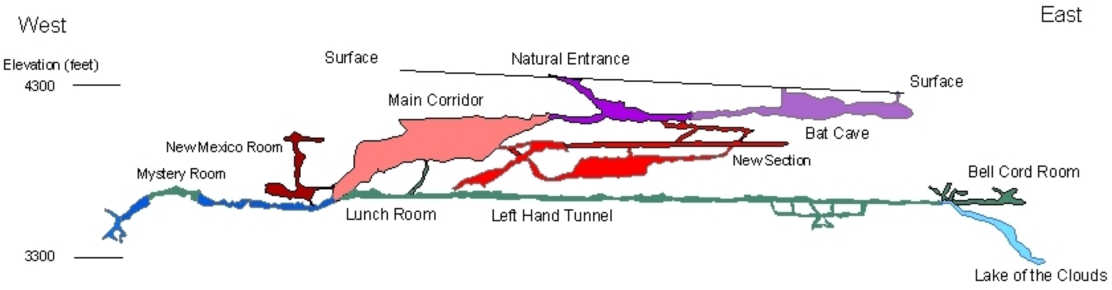

Figure 8.2: Vertical profile of Carlsbad Cavern based on Hill [1987, Sheet 3].

McLean [1971] provides a map for cave soil temperature distribution within Carlsbad Cavern [Hill, 1987, 26] (Figure 8.3). The soil temperatures were obtained using a thermistor probe, which was inserted in the cave soil (floor) to a depth of about 3-4 cm and allowed 1-2 minutes to stabilize [McLean, personal communication, 2005]. The following discussion regarding the temperature of Carlsbad Cavern is largely based on this map. Figure 8.4 is a plot of the monthly average temperature and precipitation at the surface of Carlsbad Cavern from January 1935 to April 2004.

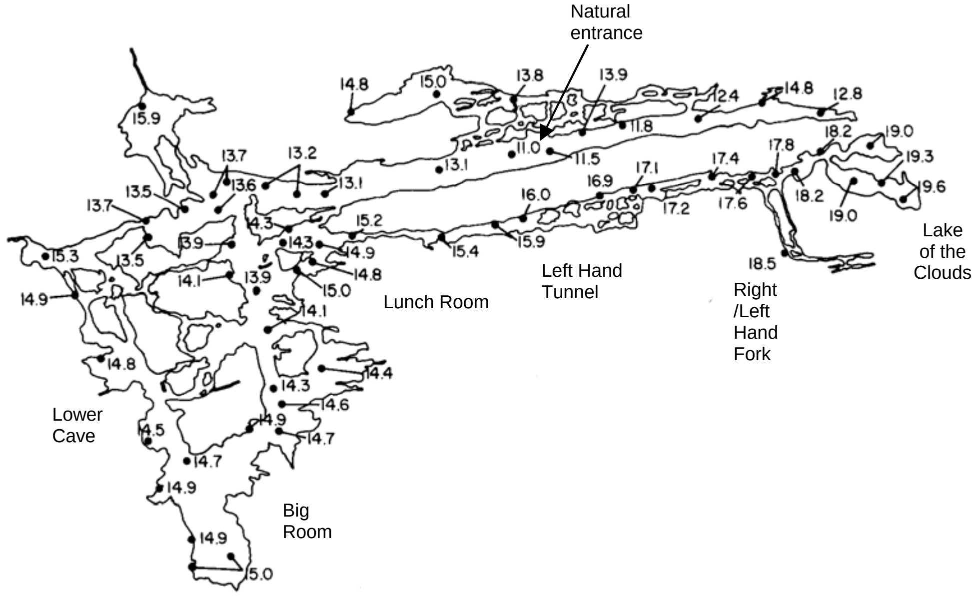

Figure 8.3: Cave-soil temperature (°C), Carlsbad Cavern, in September 1969 [Mclean, 1971; Hill 1987, 26].

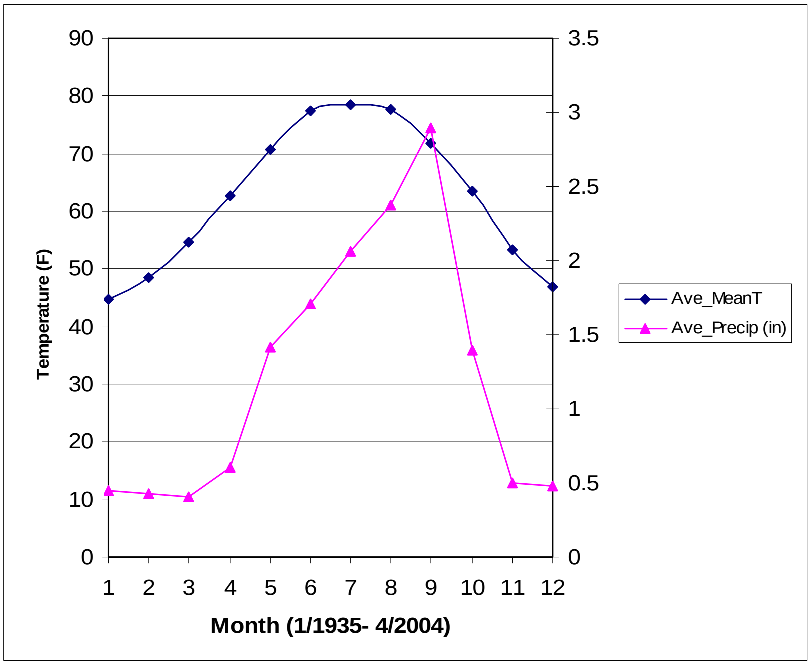

Figure 8.4: Carlsbad Caverns National Park, New Mexico – 69 year surface temperature and precipitation data summary (January 1935- April 2004). The average temperature is the daily mean temperature, and the average precipitation includes inches of monthly rain and melted snow, but snowfall depth is not included [Carlsbad Caverns Bat Cave Draw Weather Station, 2004; Burger, 2004a].

8.2 High Temperatures in Left Hand Tunnel

Left Hand Tunnel, located approximately 210 m below the Natural Entrance, is a horizontally long tunnel that connects the Lunch Room area (north of the Big Room, in which there is an elevator) and the Lake of the Clouds area. The length of the tunnel is about 1000 m. The height varies, but it is approximately 10 m.

Observations:

In Figure 8.3, we see that soil temperatures increase along Left Hand Tunnel from about 15°C near the Lunch Room to 19.6°C at the Lake of the Clouds. On October 25, 2003, we collected rock surface temperatures at the ceiling and the floor along Left Hand Tunnel from the Lunch Room area to the Right Hand Fork area, using an infrared thermometer (the measurement positions are found on the map in Figure 8.1). The results are shown in Table 8.1. On December 10, 2004, we repeated the measurements of rock surface temperature. At this time, however, the second bridge (Point 6) had been removed due to the weathering of the bridge material and we could not go farther. We collected rock surface temperature data from ceiling, floor and two mid-points between ceiling and floor to consider the vertical rock surface temperature variations. The results are shown in Table 8.2.

The measurement points in Table 8.2 roughly correspond to those in Table 8.1, but they are not exactly the same. The rock surface temperature data between 2003 and 2004 are slightly different, which may reflect differences in the measurement points within the same area, or other measurement errors. In Table 8.2, we see small vertical temperature variations. With a few exceptions the temperatures at the ceiling are slightly higher than those in lower parts of passages. Observed rock surface temperatures in 2003 and 2004 were slightly higher than the soil temperatures of McLean‘s study in 1969, but they show the same tendency that temperatures increase along Left Hand Tunnel toward the Lake of the Clouds.

Table 8.1: Rock surface temperatures (°C) along Left Hand Tunnel toward Lake of the Clouds (October 25, 2003).

Measurement point	1	2	3	4	5	6	7	8
Ceiling	16.4	16.2	16.6	17.6	18.7	19.3	19.4	20.04
Floor	15.6	16.2	16.2	17.2	18.5	18.8	18.9	19.8

Point 1 is the entrance of Left Hand Tunnel at Lunch Room; Point 2 is gate to Left Hand Tunnel, Point 3 is 1st Bridge; Point 4 is the Iron Pool area; Point 5 is the end of the visitor’s trail; Point 6 is 2nd Bridge; Point 7 is the left side of the Right Hand Fork area; and Point 8 is the right side of the Right Hand Fork area. (The measurement points are found on the map in Figure 8.1.)

Table 8.2: Rock surface temperatures (°C) along Left Hand Tunnel toward Lake of the Clouds (December 10, 2004).

Measurement point	1	2	3	4	5	6	7	8
Ceiling	15.6	16.2	16.8	18.3	19.1	-	-	-
Middle up	15.6	16.2	17.0	17.6	18.9	-	-	-
Middle low	15.4	16.2	16.8	18.1	18.7	-	-	-
Floor	15.4	16.0	16.8	17.8	18.8	-	-	-

The measurement points are found on the map in Figure 8.1. For description of measurement points, see Table 8.1.

In Table 8.1, Points 7 and 8 are in the Right Hand Fork area that is the end of Left Hand Tunnel, where the tunnel splits to left and right. The left side of the Right Hand Fork area (Point 7) is a known access passage leading to the Lake of the Clouds, and the right side (Point 8) is a narrow downward trending maze. It is interesting that rock surface temperatures in the right side are higher than those on the left side of this area. According to Burger [personal communication, 2004b] in Carlsbad Caverns National Park, the narrow maze may be connected to the Lake of the Clouds or other unknown cave structures below. Anecdotally, when a park ranger went down the maze, he felt warm air flowing up from the deeper point of the narrow maze [Burger, personal communication, 2004b].

In our models, we have ignored humidity effects and considered that the humidity may have less impact on altering convection cells, and rather airflow may actually change the local humidity. However, humidity has significant impacts in terms of altering cave features. Popcorn lines are observed along Left Hand Tunnel (Figure 8.5). Popcorn is a nodular-shaped coralloid speleothem (Figure 8.6). One of the characteristics of the popcorn line in Carlsbad Cavern is that it is associated with distinct corrosion. Above the line, speleothems and bedrock are highly corroded, whereas below the line they are not corroded [Hill, 1987, 54 - 55].

Three atmospheric conditions in a cave are thought to be necessary before condensation-corrosion can occur: 1) a high CO_2 level in the air; 2) a high amount of moisture in the air; and 3) a temperature gradient between the air masses in different passages [Hill, 1987, 89]. The third condition may be necessary to induce air exchange between these passages with warm airflow along upper portions, and cooler airflow along lower parts of the passages. Hill [1987, 91] reports that carbon-dioxide levels along Left Hand Tunnel are consistently higher near the ceiling than they are near the floor (the reasons are unknown).

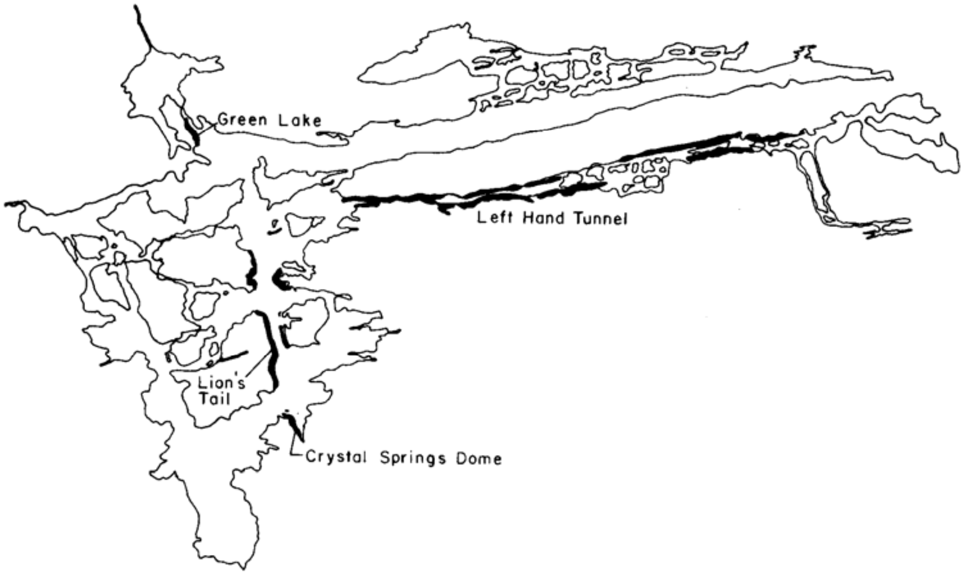

Figure 8.5: Distribution of the popcorn line in Carlsbad Cavern [Hill, 1987, 55].

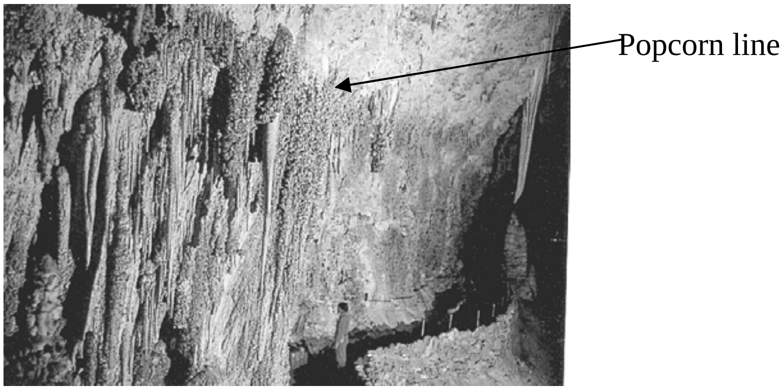

Figure 8.6: Popcorn line in Big Room [Hill, 1987, 105]. Above the line speleothems and bedrock are highly corroded, whereas below the line they are not corroded. Photo by Alan Hill.

Burger [2004a] has collected continuous humidity data in Left Hand Tunnel from the upper and lower parts of the area between the first bridge (Point 3 on Tables 8.1 and 8.2) and Iron Pool area (Point 4) of Left Hand Tunnel. The map in Figure 8.7 shows his monitoring stations.

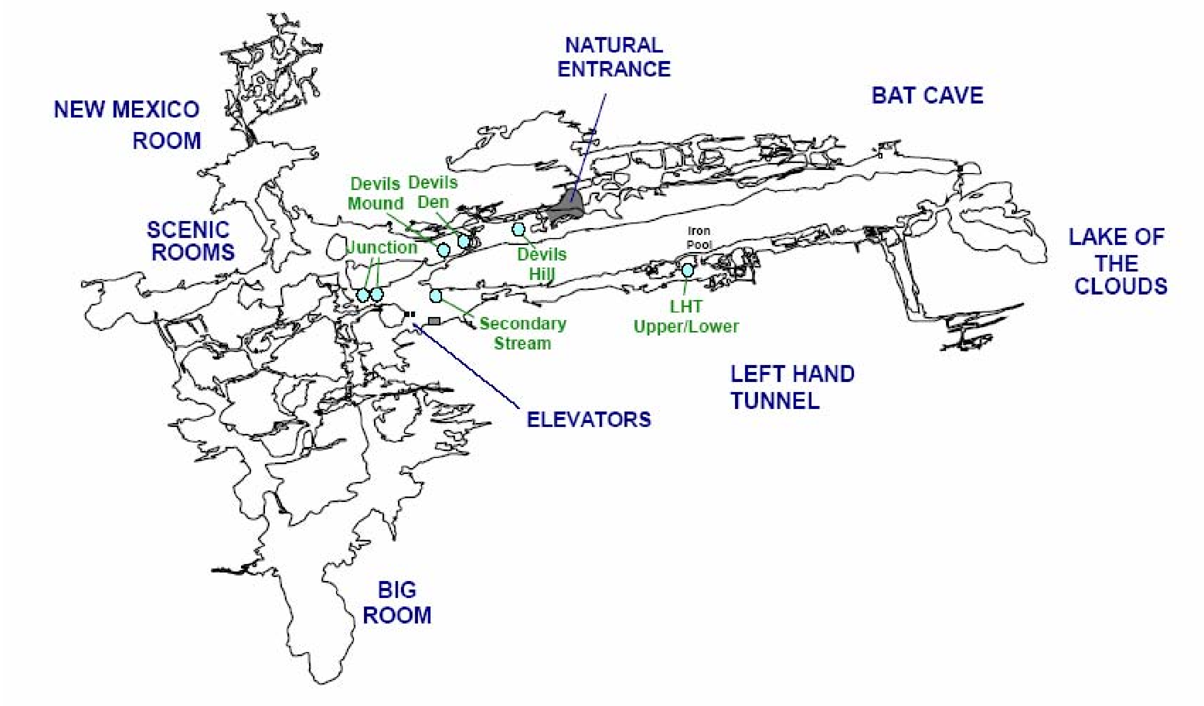

Figure 8.7: Burger’s monitoring stations [Burger, 2004a].

According to Burger's data, the relative humidity (RH) of the upper part of Left Hand Tunnel ranges from 95% to 100% (Figure 8.8), whereas that of the lower part ranges from 88% to 96% (Figure 8.9). While warm, moist air migrates along the ceiling from the Lake of the Clouds area towards the Big Room the air temperature decreases, leading to condensation of moisture from the air. Hence, condensation-corrosion is expected to occur preferentially near the ceiling of Left Hand Tunnel. The condensed moisture drops to the lower part of the passage, evaporates, and deposits calcium carbonate, which results in the formation of popcorn at the lower part of the tunnel.

In Figure 8.9, we see that the lower part of Left Hand Tunnel shows seasonal humidity fluctuations. Low humidities occur in winter or spring and high humidities occur in summer or fall seasons. The highest RH is observed in November and the lowest RH in February (RH is low in December thru March). In contrast, at the surface, the highest average precipitation is observed in September and the lowest in November thru March (see Figure 8.4). Left Hand Tunnel is far from the Natural Entrance, so it could take on the order of a month or more to be influenced by the surface weather conditions. There is an elevator at the Lunch Room that is located at the left end of Left Hand Tunnel. The humidity fluctuation, (especially in the winter season) could also reflect the influence from the elevator in the Lunch Room. On the other hand, there is no significant fluctuation in terms of air temperature. Temperature could be less sensitive to small seasonal changes compared to humidity because of the enormous thermal mass of the rock; or it could reflect some measurement errors.

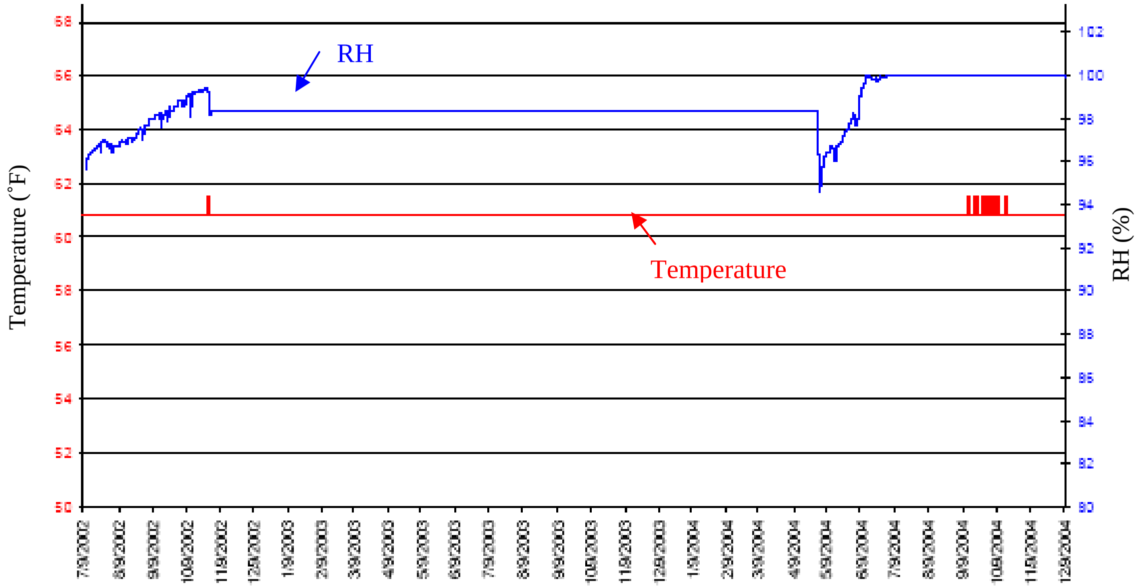

Figure 8.8: Humidity and temperature collected every two hours at the upper part of the Iron Pool area of Left Hand Tunnel [Burger, 2004a].

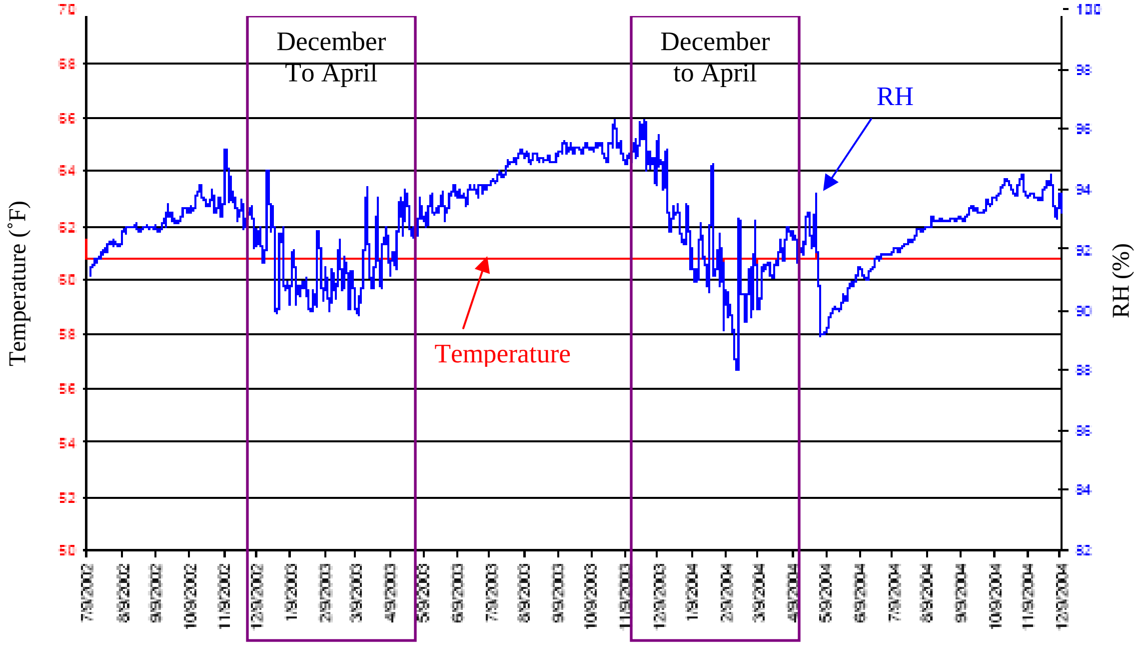

Figure 8.9: Humidity and temperature collected every two hours at the lower part of the Iron Pool area of Left Hand Tunnel [Burger, 2004a]. RH tends to be low from December to April.

Application of the modeling:

Temperatures in Left Hand Tunnel are high and increase towards the Lake of the Clouds. We consider three factors in this observation: 1) the effect of overlying cavities; 2) the effect of air circulation around the Right Hand Fork and Lake of the Clouds or unknown cavities below; and 3) air exchange between the Big Room and the Left Hand Tunnel.

From the models in Chapter 5, we suggested that the presence of overlying cavities raises temperatures in lower cavities, even when the cavities are not perfectly overlapped. There are multiple overlying cavities (Bat Cave and an area of New Section and Guadalupe Room) above Left Hand Tunnel (Figures 8.1 and 8.2). Although they are not perfectly overlapped with each other, they may contribute to raising the temperatures in Left Hand Tunnel. Figure 8.10 shows the conduction model that represents a similar relationship amongst these overlapped cavities. The model size is 2000 m x 6000 m (height x width). Since the conduction simulation is linear, our computer can produce large-scale models very easily.

Figure 8.11 is the domain plot of the cave component in which heat is transferred only by conduction. Figure 8.12 is the domain plot of the cave component in which the Navier-Stokes equations were applied, so heat transfer occurs by convection and conduction. Figure 8.13 shows the velocity field in which clear convection cells appear in the Main Corridor area. The model size in Figure 8.12 is 3 m x 9 m. Since the convection and conduction simulation is non-linear, there is a limitation in scale. Evaluations for the models are found in Table 8.3.

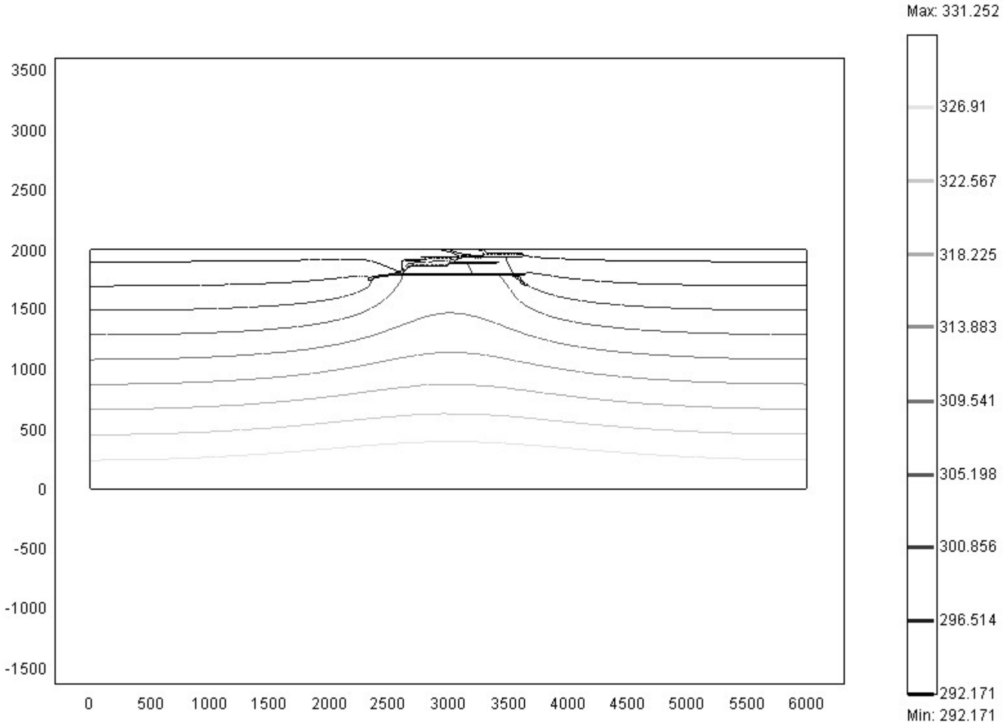

Figure 8.10: Conduction model with geometry similar to Carlsbad Cavern. Model shows contour lines indicating temperature (K). The model size is 2000m x 6000m, and that of the cave component is about 300m x 1320m.

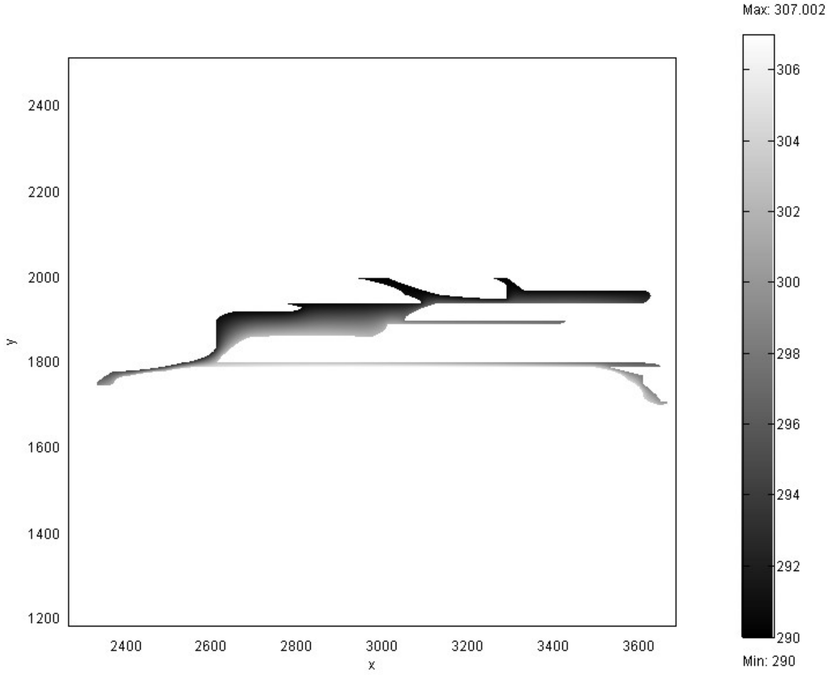

Figure 8.11: Domain plot of the cave component of the conduction model in Figure 8.10. Model shows surfaces indicating temperature (K). The temperature along Left Hand Tunnel is higher than in the other parts of the cave model.

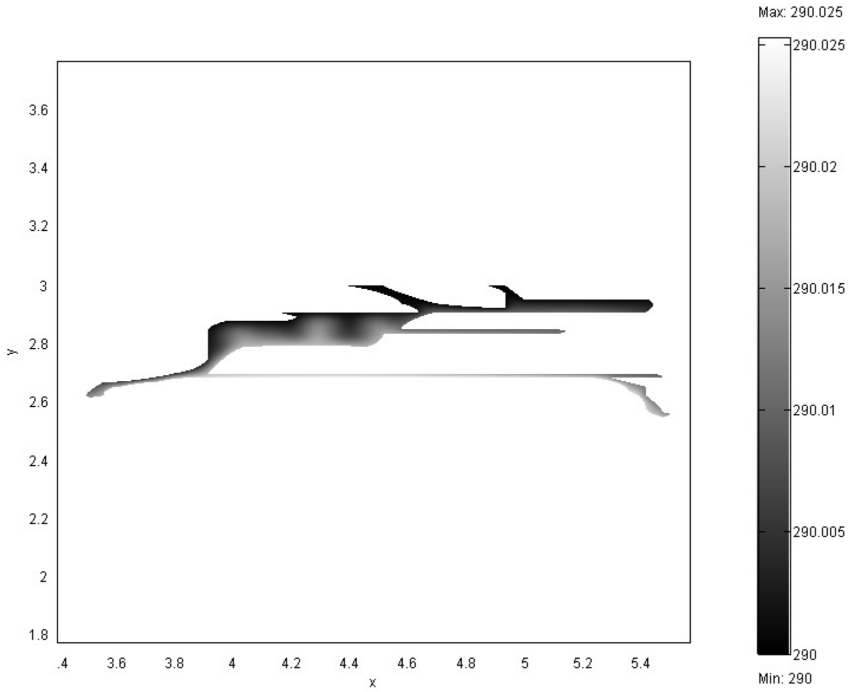

Figure 8.12: Convection and conduction model with geometry similar to Carlsbad Cavern. Model shows the domain plot of the cave component with surfaces indicating temperature (K). The model size is 3m x 9m, and that of the cave component is about 0.46m x 2m. The temperature along the Left Hand Tunnel is higher than that of other parts of the cave model.

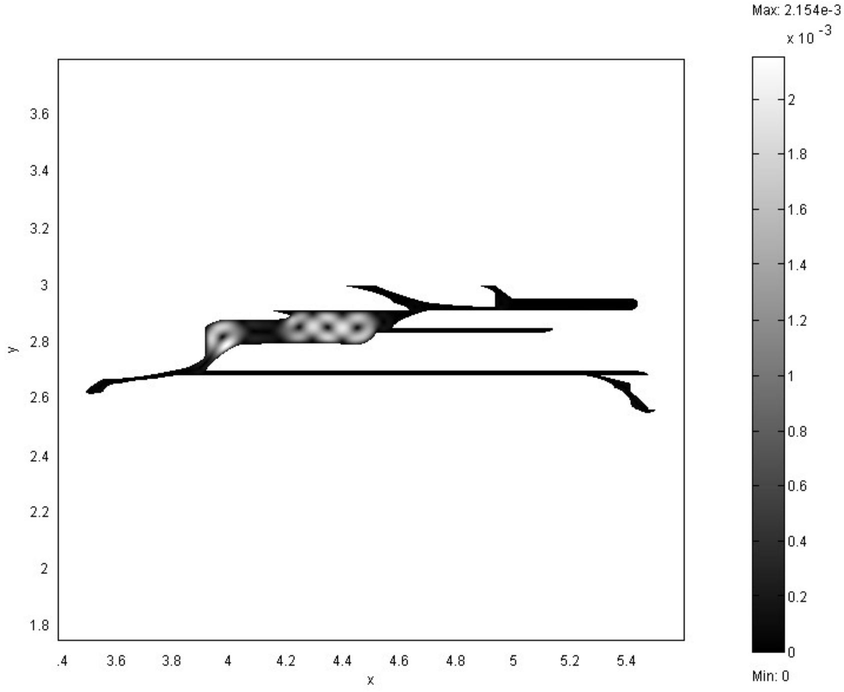

Figure 8.13: Convection and conduction model with geometry similar to Carlsbad Cavern. The same model as Figure 8.12, but with surfaces indicating the velocity field (m s^{-1}). Clear convection cells appear in the Main Corridor area.

When we consider the horizontal temperature variation of the models, we see that the temperatures along Left Hand Tunnel appear to have a proportional relationship with the volume of air above the tunnel. Both Figures 8.11 and 8.12 indicate that temperatures along Left Hand Tunnel are higher than that of other parts of the cave (the largest volume of air above Left Hand Tunnel). This is especially true of the area under the Main Corridor. On the other hand, the temperatures in the area of the left side of Left Hand Tunnel are low where there are no overlying cavities.

Air circulation between Right Hand Fork and Lake of the Clouds or unknown cavities below could also contribute to a rise in temperature in Left Hand Tunnel. The Lake of the Clouds is located at the deepest point of this cave system. When we consider geothermal heating, it is reasonable that the temperatures are higher in the deeper parts of the cave. For example, in the borehole AEC-8 at the WIPP site, the temperatures increase with depth even though there are some variations in terms of geothermal heat flux (Figures 2.2 and 2.3). Sass [1984] provided temperature profiles from the surface to about 200 m depth in wells at the Brantley Dam site on the Pecos River near Carlsbad. The report also shows that temperatures increase with depth, having some variations in heat flux. Thus, we expect the highest air temperature to be at the Lake of the Clouds. In addition, gravitational compression of moist air changes the temperature by about 0.5 to 0.65°C per 100 m [Dingman, 2002, 590] although our particular models neglect gravitational compression. The vertical distance between the surface and the Lake of the Clouds is about 300 m, so the gravitational compression could raise the air temperature about 1.5 to 1.95°C relative to the air temperature at the surface.

If multiple passages are connected to the Lake of the Clouds or unknown cavities below, air circulation may be initiated. The upward flow of air in the narrow maze of Right Hand Fork observed by a park ranger is reasonable, because Left Hand Tunnel (a horizontally long tunnel) traps heat and raises the temperature below it (see Figures 5.58 and 5.60). Warm air from the Lake of the Clouds or unknown cavities below is mixed with air that already exists in Left Hand Tunnel. While air is mixing, heat is transferred from warmer air to cooler air and, thus, temperatures of Left Hand Tunnel increase towards the Lake of the Clouds.

The left end of Left Hand Tunnel is connected to the Lunch Room, a northern portion of the Big Room (Figures 8.1 and 8.2), in which temperatures are about 14°C to 15°C. Left Hand Tunnel’s temperature ranges from 15°C to 19.6°C. There may be air exchange between the Big Room and the Left Hand Tunnel due to the difference of air density. The temperature plots of normal models with two entrances in Chapter 6 indicate that warm cave air ascends toward the large entrances, and the cool surface air descends into the cave through the entrances (e.g., Figures 6.4, and 6.12). Cool, dryer air in the Big Room may flow into Left Hand Tunnel along the lower parts of the passage, and warm, wetter air in Left Hand Tunnel may flow out towards the Big Room along the upper parts of the passage. This air exchange may also enhance increase in the temperature along Left Hand Tunnel. The temperatures at the upper reaches tend to be slightly higher than those of the lower parts of the tunnel. This air exchange may also partially contribute to the formation of the popcorn line along Left Hand Tunnel.

Table 8.3: Evaluations for Figures 8.10 and 8.12. The lengths of the bottom boundaries *L* are 6000 m and 9 m, respectively. Heat flux $q = 0.05\ \mathrm{Wm}^{-2}$.

Model	*Size H(m) x W(m)*	*Model type*	*Number of elements*	*Degrees of freedom*	*Solution time (s)*	*Boundary integration (Bi) (Wm^{-1})*	*Error* $\left\lvert\frac{Bi}{L\,q}\right\rvert 100(\%)$
F 8.10	2000 x 6000	Conduction (linear)	26809	111928	16.25	$-5.939\mathrm{x}10^{-2}$	$1.980\mathrm{x}10^{-2}$
F 8.12	3 x 9	Convection Conduction (non-linear)	29593	124447	425.078	$-1.504\mathrm{x}10^{-4}$	$3.342\mathrm{x}10^{-2}$

8.3 Downward Airflow at Entrance of Lower Cave and Main Corridor-Big Room Junction Area

Observations:

The Lower Cave in Carlsbad Cavern (Figure 8.14) is located about 260 m below the surface and about 30 m below the Big Room. Lower Cave and the Big Room are connected by multiple passages in a complex manner. However, there are two known connections: the Entrance of Lower Cave, where there are narrow ladders (Figure 8.15); and the Jumping Off Place, a wide cliff located to the southeast relative to the Entrance of Lower Cave (see Figure 8.1). The bottom of Jumping Off Place is Lower Cave. This author visited the area in May, 2003. When our team descended the narrow ladders at the Entrance of Lower Cave, we clearly felt air flowing down towards it. On December 10, 2004, the author measured this downward flow as $0.4\ \mathrm{m\ s}^{-1}$, in which a dangling handkerchief was tilted by approximately 15 to 30°.

According to Forbes [2000], the annual air temperature around Rookery Pool at Lower Cave ranges from 12.4°C to 14.3°C, whereas that of Longfellow’s Bathtub at the Big Room ranges from 13.0°C to 15.3°C. Considering geothermal heating, we expect higher temperatures in the deeper parts of a cave as discussed in the previous section.

Geothermal heating alone may not be enough to explain the observed slightly lower temperatures in the Lower Cave.

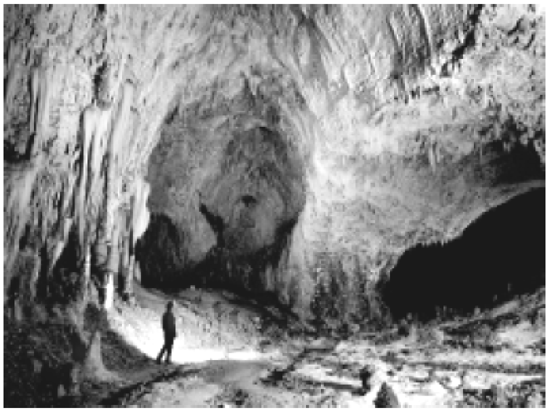

Figure 8.14: Lower Cave of Carlsbad Cavern. Photo by *A.N. Palmer* [Palmer, A. N. and Palmer M. V., 2000].

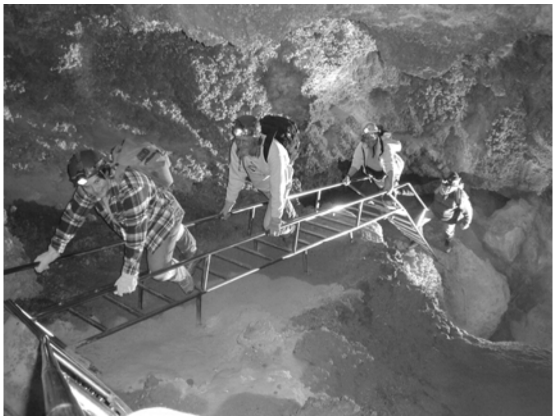

Figure 8.15: Narrow ladders at Entrance of Lower Cave. Photo by Kenneth Ingham, 2002.

Burger [2004a] has provided the data from his continuous monitoring of air temperature and humidity around the Entrance of Lower Cave and the Main Corridor-Big Room Junction (Figures 8.16 thru 8.18). The Main Corridor is a steep, large trunk passage descending approximately 200 m from the Natural Entrance following a steep, narrow passage (Figures 8.1 and 8.2). According to Burger [personal communication, 2004b] downward airflow and fog events are often observed at the Main Corridor-Big Room Junction area year round.

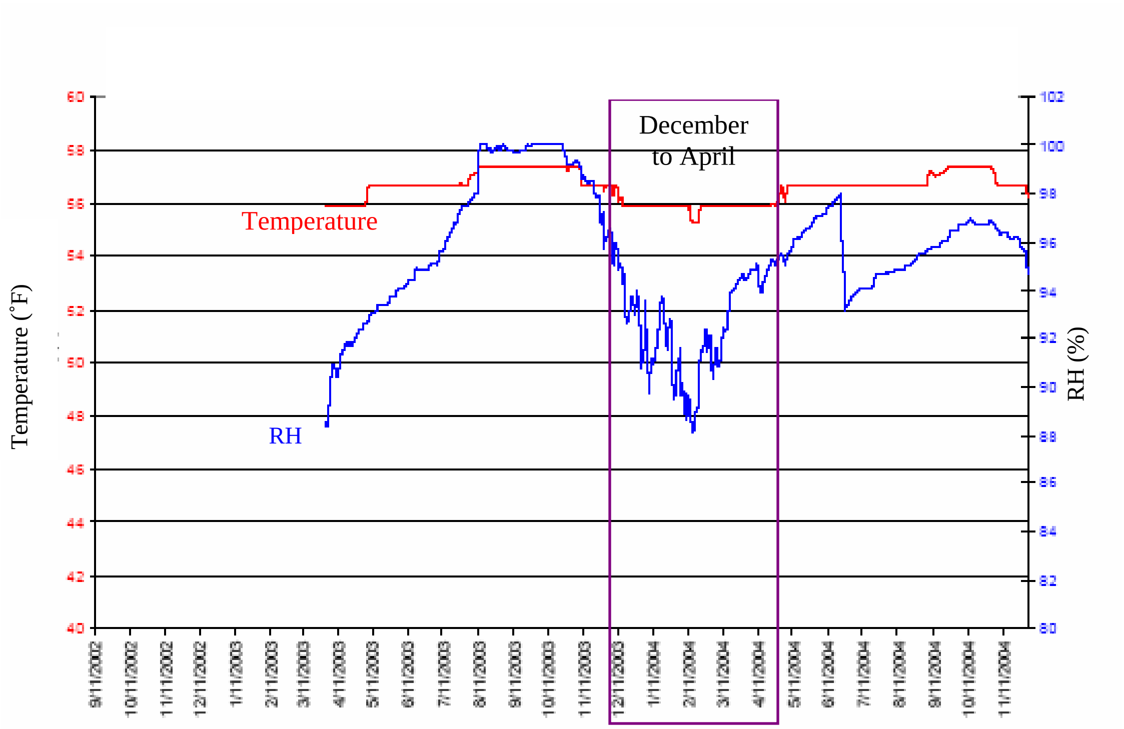

Figure 8.16: Temperature and humidity collected every two hours at the Big Room-Main Corridor Junction. There are two stations indicated as 'Junction' on the map in Figure 8.7, and this a right hand side station of the two [Burger, 2004a].

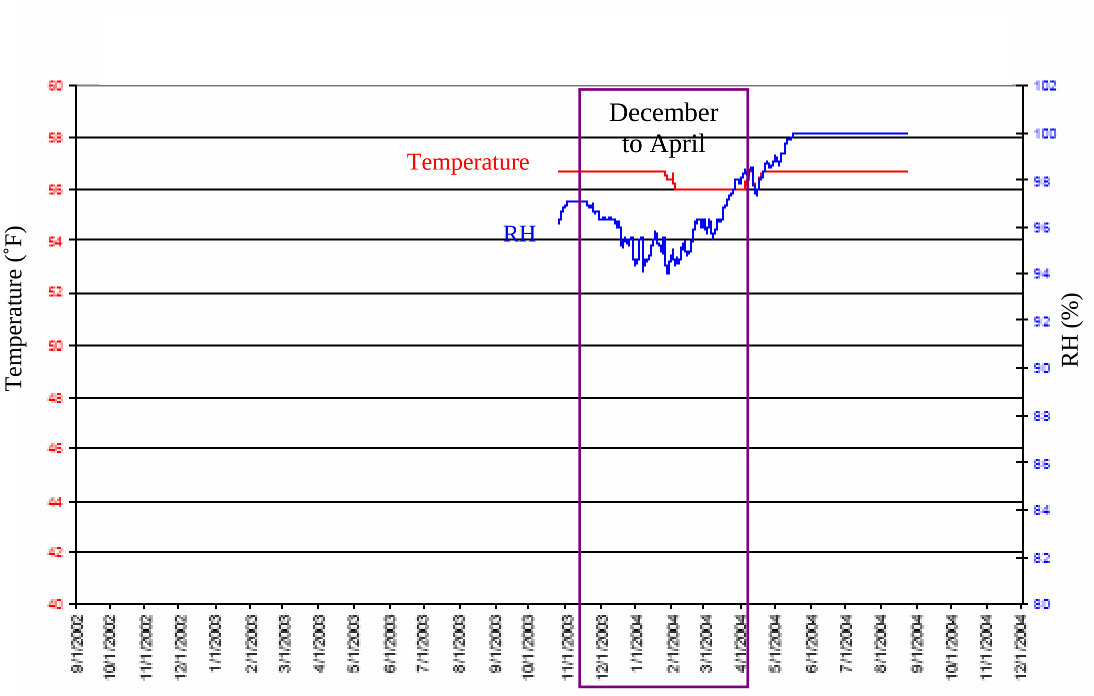

Figure 8.17: Temperature and humidity collected every two hours at the Lower Cave-Trapdoor. There are two stations indicated as 'Junction' on the map in Figure 8.7, and this a left hand side station of the two [Burger, 2004a].

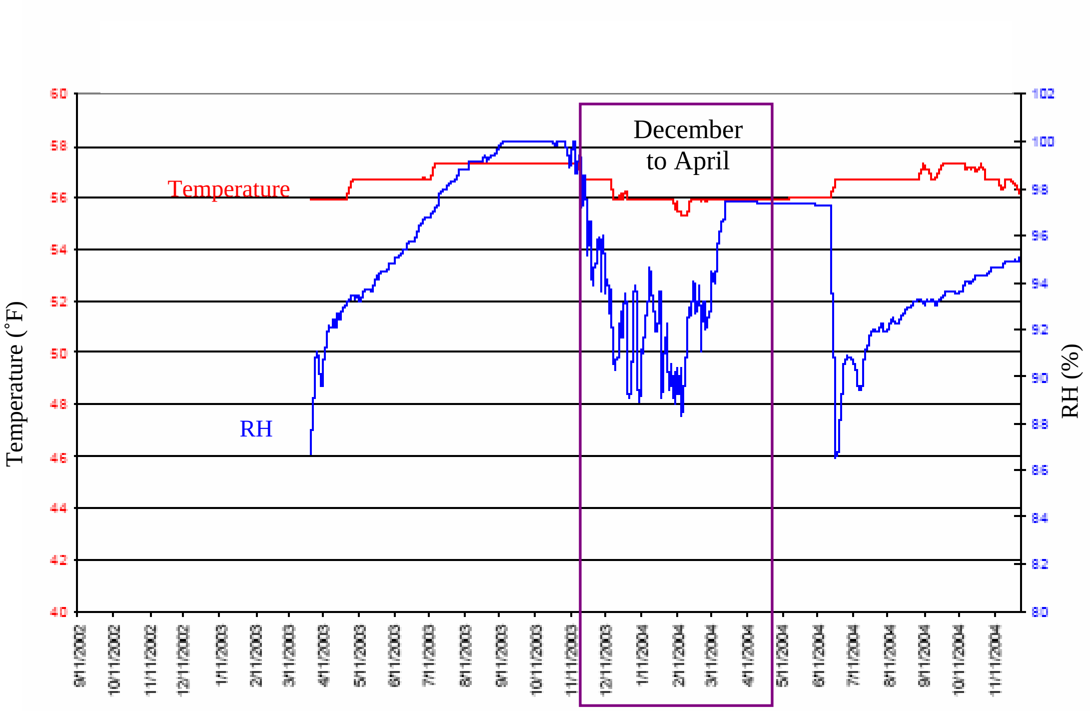

Figure 8.18: Temperature and humidity collected every two hours at the NY Skyline indicated as 'Secondary Stream' on the map in Figure 8.14 [Burger, 2004a].

In Figures 8.16 thru 8.18, there are clear seasonal variations in humidity. Low humidity occurs in winter and spring seasons and high humidity is measured in summer and fall. (There are a few exceptions in that low humidity was observed in June and July of 2004 at NY Skyline and Main Corridor-Big Room Junction; reasons for these anomalously low humidities are unknown). Temperature also shows seasonal variation with the same tendencies as the humidity variation. However, these humidity and temperature fluctuations are small compared with those of the surface. Carlsbad Cavern is located in an arid area with a summer monsoon, so the high seasonal fluctuations of the surface temperature and humidity are expected (Figure 8.4).

There appear to be direct surface influences at the Main Corridor-Big Room Junction, at the Entrance of Lower Cave (trapdoor), and at the NY Skyline (Secondary stream), although these areas are approximately 200 m below the surface. The seasonal variations of humidity are similar to those in Left Hand Tunnel, that is, the relative humidity is high from August to November, and low from December to March. On the surface, the maximum average precipitation is observed in September, and there is low precipitation from November to March. This direct influence from the surface weather conditions on the Main Corridor-Big Room Junction area could indicate that the density driven flow system dominates here. When the surface air is colder and dryer (denser) than the cave air (lighter), significant air exchange takes place (see Figure 6.40). In addition, geometries in this area could allow surface influence. This area is connected to the surface in three ways: by the Main Corridor, by the NY Skyline (Secondary Stream), and by an elevator. The combination of these three connections could overcome the great vertical distance from the surface and allow the surface weather conditions to affect the cave.

Application of modeling:

In our models, flow directions are largely controlled by cave geometries (see Section 5.34). Recalling Figures 5.57, 5.59 and 5.61, the downward flow is observed at the narrow passage, in which there is no horizontally long tunnel attached to the upper left of the narrow passage. Figure 8.18 uses the same model conditions as Figures 5.57, 5.59, and 5.61, but it shows the vicinity of the cave structure with contour lines indicating temperature and surfaces indicating the velocity field. This geometry produced a lower temperature at the left side of the narrow passage and a higher temperature at the right side of the larger passage, creating air circulation.

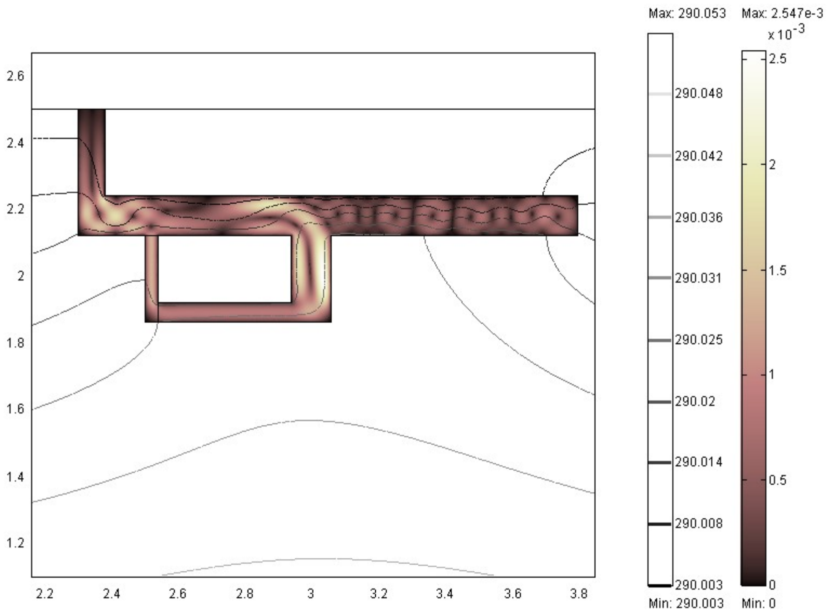

Figure 8.19: Flow controlled by geometry. Model is the same as Figure 5.57, but it shows contour lines indicating temperature (K) and surfaces indicating the velocity field (m s^{-1}). Note that the temperature at the left side of the narrow passage is lower than in the right side of the large passage.

As in Figure 8.19, it is possible that the geometries of Lower Cave and the Big Room area promote air circulation between Lower Cave and the Big Room with a downward flow at the Entrance of Lower Cave, and a lower temperature at Lower Cave. However, it is difficult to image the three dimensional geometry of Carlsbad Cavern from the 2D elevation map or the vertical profile (Figures 8.1 and 8.2).

Meanwhile, the apparent permanent downward flow at the Main Corridor-Big Room Junction [Burger, personal communication, 2004b] indicates that internal dynamics (the thermally-induced buoyancy forces and the conservation of mass) are at work here. Convection cells occur if an entrance passage is large enough (see Figures 5.25 and 5.26). Figure 8.20 is the same model as Figure 5.25, but it shows contour lines indicating temperature and arrows indicating the velocity field. A clear convection cell (with both upward and downward flow components) is observed in the entrance passage of Figure 8.20. This convection cell is created by the thermally-induced buoyancy forces and the entrance size. The size of the Main Corridor of Carlsbad Cavern and geothermal heating are enough to create convection cells. Thus, the observed apparent permanent downward flow in this region could be the downward flow component of a convection cell.

We can also consider the downward flow at Main Corridor-Big Room Junction area from the conservation of mass viewpoint. Figure 8.20 is a good example of mass balance, in which downward flow occurs at both left and right sides of the entrance passage, and upward outflow occurs in the center. Because of thermally-induced buoyancy forces, some of the warm cave air escapes through the entrance, and the same amount of cool surface air enters into the cave to conserve cave air mass.

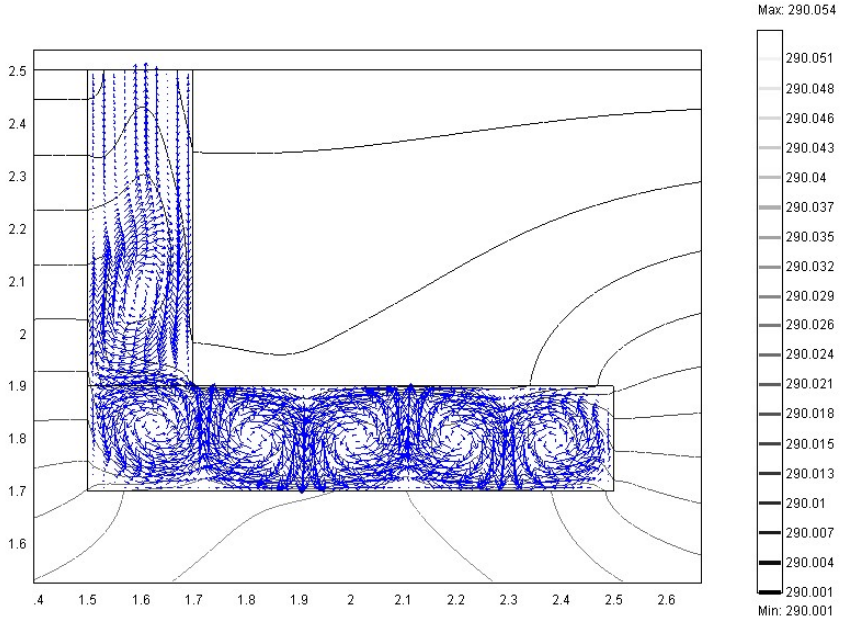

Figure 8.20: Normal flow model with single entrance. The width of the entrance is the same as the height of the horizontal cavity. It is the same model as in Figure 5.25, but it shows contour lines for temperature (K) and arrows for the velocity field (m s^{-1}). Note that a clear convection cell is observed at the entrance passage.

When there are multiple entrance passages that have a vertical relationship amongst them, air circulation is promoted. The reader will recall the tilted normal flow model with two entrances shown in Figure 6.10. Figure 8.21 is the same model as Figure 6.10, but it shows surfaces indicating temperature and arrows indicating the velocity field. Figure 8.22 is the same image as Figure 6.20, in which the large entrance passage of Figure 6.10 was enlarged. Air circulation is effective in the tilted model with two entrances. This air circulation is created due to thermally induced buoyancy forces in the main cavity. The air in the main cavity preferentially moves towards the large entrance, creating low pressure in this region, which in turn triggers inflow at the small entrance. In the large entrance of the model, the cave air flows out through the ceiling and the surface air flows into the cave through the floor to conserve cave air mass (Figure 8.21).

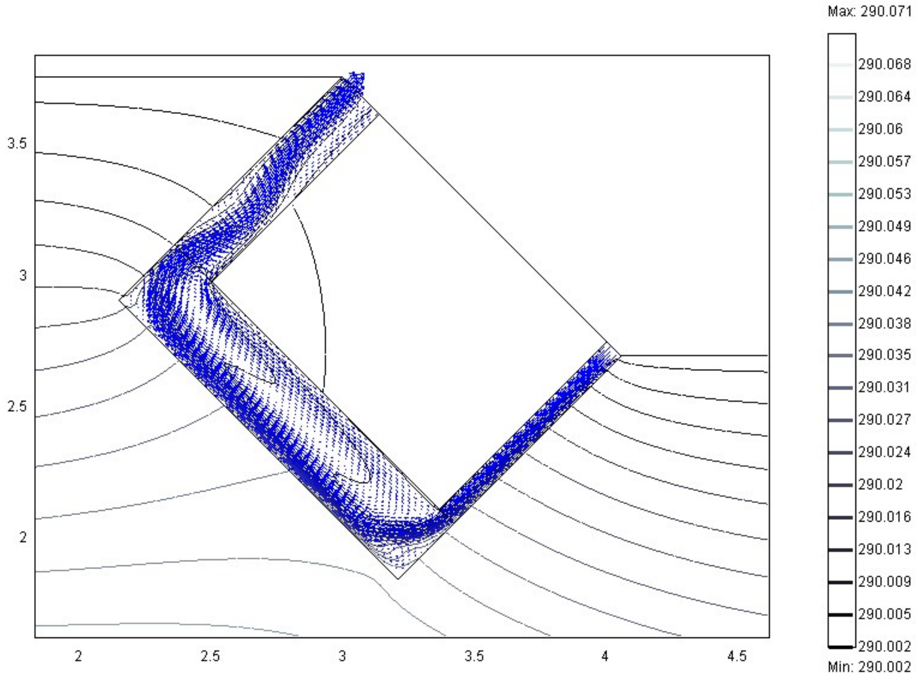

Figure 8.21: Tilted normal flow model with two entrances. This is the same model shown in Figure 6.10, but it displays contour lines indicating temperature (K) and arrows indicating the velocity field (s m^{-1}).

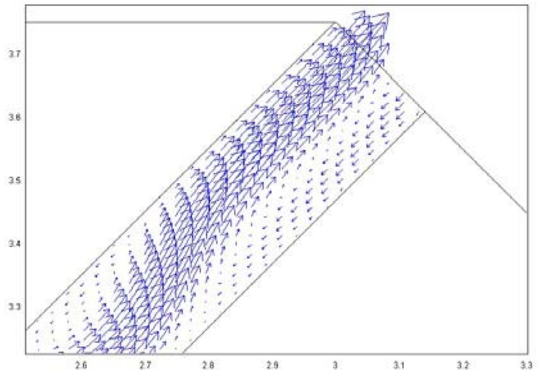

Figure 8.22: Tilted normal flow model, the same image as Figure 6.20. The large entrance of Figure 6.10 is enlarged. Both inflow and outflow are observed, but the outflow component appears to be the strongest.

Although, our models have neglected the gravitational pressure gradient, the tilted models show air circulation due to the internal dynamics. In real cave systems, when they have multiple entrances, the difference in elevation of the entrances becomes an important factor that initiates air circulation in addition to the cave internal dynamics. The surface air enters into a cave through the lower entrance (higher static pressure) and escapes though the upper entrance (lower static pressure) [Bögli, 1980, 218]. Thus, even when the surface air is warmer than the cave air, the warmer surface air may be able to enter into caves supported by particular cave geometries.

If warmer surface air enters into a cave (e.g., in summer) due to particular cave geometries (e.g., caves with multiple entrances that are located at different elevations), then the incoming warm air is cooled while descending. Considering the typical human height, we only feel this downward cooler airflow, and we cannot feel the outgoing cave airflow because it takes place at the ceiling. When surface air is cooler than the entrance passage (e.g., in winter), then the cooler air happily sinks along the floor, and we feel this cooler air flow, but again we cannot feel warmer air escaping through the ceiling.

Thus, the apparent permanent downward flow at the Main Corridor-Big Room Junction area can be explained by cave internal dynamics: the thermally-induced buoyancy forces, the conservation of mass, and the cave geometry. Because the Entrance of Lower Cave is close to the Main Corridor, the cooler air may preferentially sink into Lower Cave through its entrance, which could partially be attributable to the lower temperatures of this region compared to the Big Room area located about 30 m above.

According to Burger [personal communication, 2004b], fog events are often observed at the Main Corridor-Big Room Junction area year round. Fogging in the subsurface occurs in two situations: 1) when cave walls are cooler than the dew point temperature of the incoming air; or 2) as a result of decompressive cooling of humid ascending cave air [McPherson, 1993, 514]. The passage from the Natural Entrance to the Main Corridor-Big Room Junction is the coolest area of Carlsbad Cavern (see Figure 8.3; see also Figures 8.16 thru 8.18 and 8.27 thru 8.29), so fogging can be expected.

To increase our understanding of the meteorological conditions of the area of the Main Corridor-Big Room Junction, we must also monitor vertical humidity variations. Forbes [1998] conducted a relative humidity (RH) study within Torgac Cave, New Mexico. He assessed vertical variations in RH in the Tray Room, located approximately 75 m from the Main Entrance by suspending kaolinite clay samples for five weeks (between January 7, 1995 and February 11, 1995) at 30 cm intervals (Figure 8.23), and subsequently performing laboratory analyses of the water activity and gravimetric water content of the clay samples. As a result, Forbes identified a large variation in RH over the monitored vertical interval of 3.5 m (Figure 8.24). He infers that the lowest humidity zone probably corresponds to the zone of maximum airflow.

Figure 8.23: The Tray Room in Torgac Cave, NM. Kaolinite clay samples were suspended at 30 cm intervals to monitor vertical variations in relative humidity [Forbes, 1998].

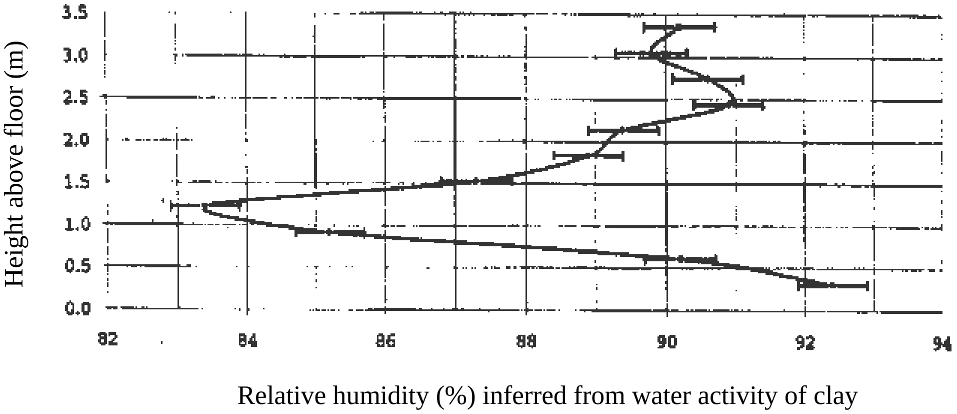

Figure 8.24: Vertical variations of relative humidity in the Tray Room of Torgac Cave [Forbes, 1998].

The seasonal humidity variations within Main Corridor-Big Room Junction and Entrance of Lower Cave area of Carlsbad Cavern (Figures 8.16 thru 8.18) could also have vertical variations. As in Forbes' hypothesis, if humidity is very sensitive to airflow, then observation of both vertical and horizontal humidity variations could help us visualize the flow patterns of the area.

8.4 Inflow and Outflow Components at the Natural Entrance of Carlsbad Cavern, and Temperature and Humidity Variations Near the Entrance Area

There are two known cave entrances in Carlsbad Cavern; the Natural Entrance and the Bat Cave Entrance. The Natural Entrance (Figure 8.25) is a large external opening through which visitors (including bats and swallows!) enter the cave. The Bat Cave Entrance is located east with respect to the Natural Entrance (see Figure 8.2). The size of the Bat Cave Entrance is approximately half that of the Natural Entrance [Burger, 2004b].

Figure 8.25: The Natural Entrance of Carlsbad Cavern. Photo by Val Hildreth-Werker.

Observations:

On 11 January 1970 at 8:00 pm, McLean [1971] observed inflow and outflow components at the Natural Entrance of Carlsbad Cavern (Figure 8.26).

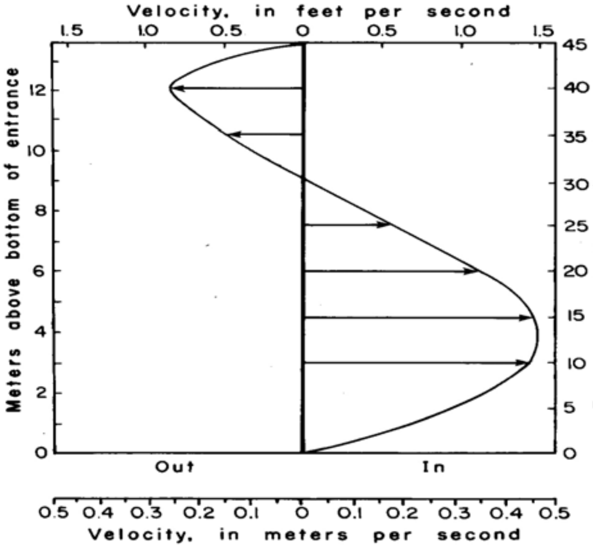

Figure 8.26: Airflow velocity at the Natural Entrance of Carlsbad Cavern [McLean, 1971; Hill, 1987, 29].

In Figure 8.26, we can see that a large inflow component is observed in the lower part of the entrance, and a small outflow component in the upper part. The plot seems to describe well the ventilation conditions at this period of time (in winter at night). The surface air is colder and drier, thus, heavier than cave air. The heavier surface air sinks into the cave along the lower parts of the entrance, and the lighter cave air moves out along the ceiling.

Burger's meteorological monitoring [2004a] (Figures 8.27 thru 8.29; see also Figure 8.7) at the vicinity of the Natural Entrance of Carlsbad Cavern also clearly shows the direct influence from surface weather conditions. Both temperature and humidity are low in winter and spring seasons, and high in summer and fall seasons.

There is no significant trend in terms of the fluctuation of humidity amongst the other monitoring stations. The relative humidity (RH) at Devils Hill ranges from 90.5% to 100%, at Devils Den from 88% to 100%, and at Devils Mound from 89% to 100%. The RH at Main Corridor-Big Room Junction ranges from 88% to 100%, at NY Skyline 86.5% to 100%, and from 88% to 96% at lower part of Left Hand Tunnel. (The relatively larger fluctuation in the New York Skyline could be attributed to the air circulation around this region.) However, the temperature gradually increases, and the fluctuations gradually become smaller as the distance from the surface increases. The fluctuations of temperature at Devils Hill, Devils Den, and Devils Mound are 46° F to 56° F (7.8° C to 13.3° C), 52°F to 56° F (11.1°C to 13.3°C), and 52.5°F to 56°F (11.4°C to 13.3°C), respectively. Temperatures at the Main Corridor-Big Room Junction and NY Skyline range from 55°F to 57°F (12.8°C to 13.9°C). An apparently constant temperature of 61°F (16.1°C) is observed near the Iron Pool in Left Hand Tunnel.

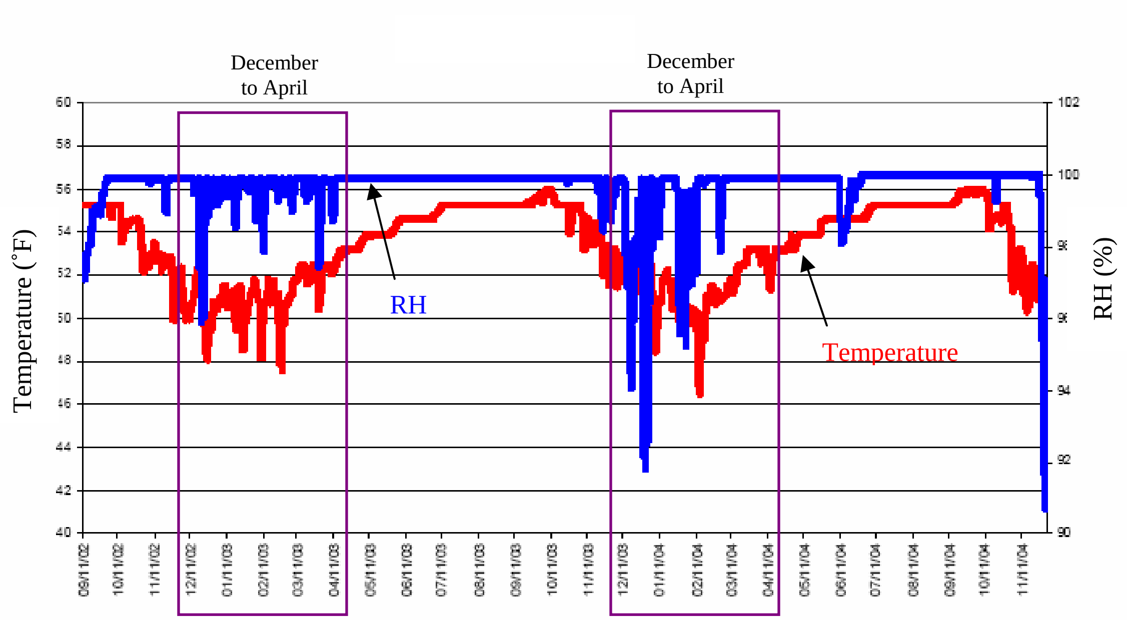

Figure 8.27: Temperature and humidity collected every two hours at Devils Hill [Burger, 2004a].

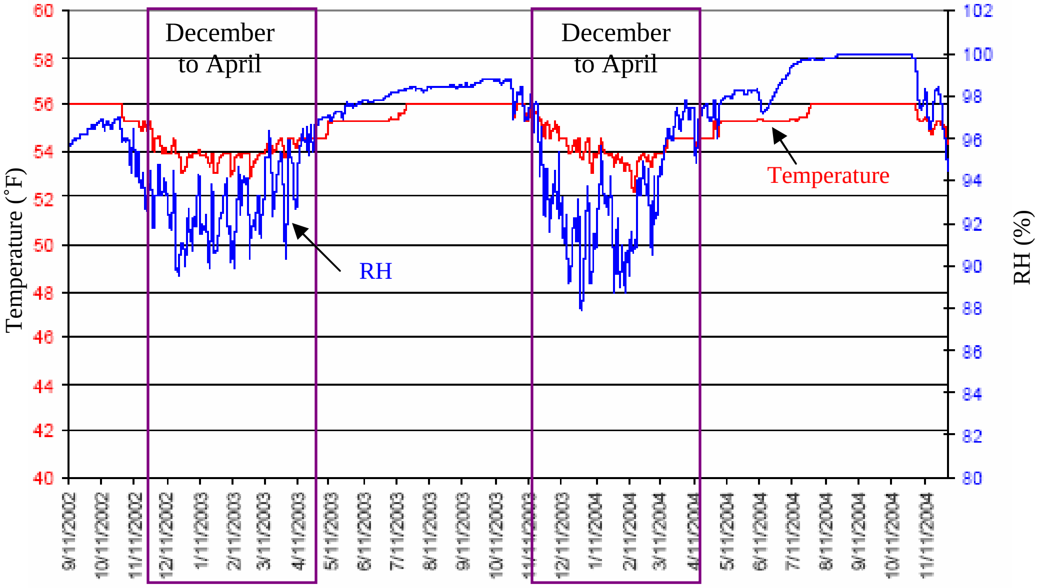

Figure 8.28: Temperature and humidity collected every two hours at Devils Den [Burger, 2004a].

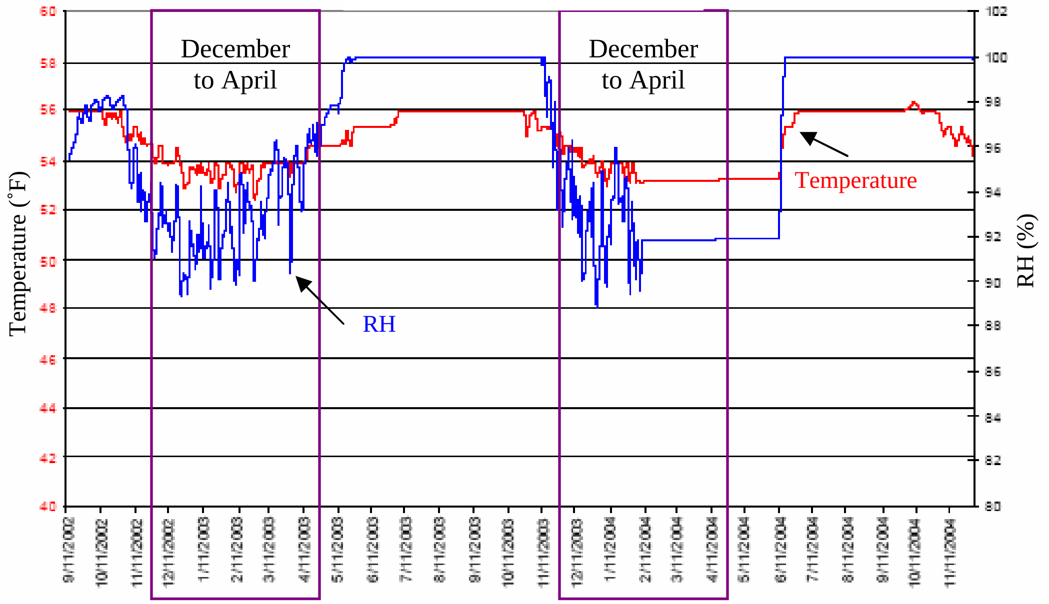

Figure 8.29: Temperature and humidity collected every two hours at Devils Mound [Burger, 2004a].

Application of modeling:

Most enlarged images of the large entrance passages of the models in Chapters 5 and 6 describe inflow and outflow components. On the other hand, the small entrances of models with two entrance passages tend to have single flow directions. In Section 7.6, based on modeling results, we concluded that cave air mass is largely conserved. If cave entrances are large enough, two flow directions at the same time can be observed to conserve cave air mass. The Natural Entrance of Carlsbad Cavern is large enough to have both outflow and inflow components.

The seasonal variations of humidity and temperature in this area appear to indicate that the thermally-induced, density-driven flow dominates in this cave. Since this area is close to the Natural Entrance, it experiences the surface influence slightly earlier than other deeper parts. These seasonal variations can also be explained by cave internal dynamics as described in the previous section.

8.5 Strong Outflow at the Culvert of Lechuguilla Cave

About four miles from Carlsbad Cavern, is another enormous cave system, Lechuguilla Cave, whose surveyed passage is over 161 km long and over 457 m of vertical extent. It is the deepest and the third longest cave in the U.S [Crane, 2000, 51; Schneiker, 2002].

Richards [2001] reports an excellent episode that illustrates meteorological conditions in the entrance area of deep, large cave systems. In the Lechuguilla entrance pit (Figure 8.30), there was a narrow culvert that was deployed in May of 1986 (Figure 8.31). The counter-balanced lid and seal was placed to add security and to prevent constant exchange of air (sometimes by winds up to 26.8 m s^{-1}). The interior of the culvert was always either wet or dry depending on whether the cave was exhaling or inhaling. The extreme fluctuations of humidity in response to the placement of a very narrow air conduit into an extremely large cavity system dramatically illustrates some of the principles that we have discussed in this study. This constant variation of "climate" in the interior of the Lechuguilla Cave entrance culvert created a very hostile environment and the perfect conditions to promote corrosion on metal surfaces. For safety purposes, the management of Carlsbad Caverns National Park's Cave Resource Office decided to replace it with a combined non-corrosive airlock and culvert. Stainless steel was chosen as a non-corrosive material. The replacement project started in February 1999, and ended in Jun 2001. Thus, we can see that micrometeorological factors are more than simply of academic interest. They can play an important role in development of best practices in cave resource management issues.

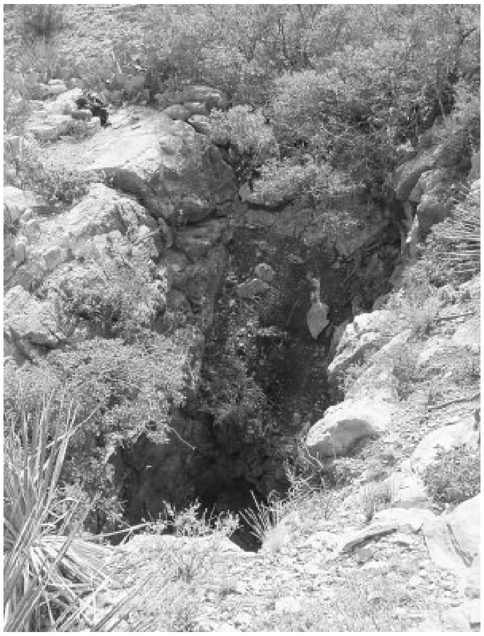

Figure 8.30: Lechuguilla Cave entrance pit [Alger, 2002]

Figure 8.31: Paul Burger at the dig culvert of Lechuguilla Cave; wind measured at 17.9 m s^{-1} (Photo by Stan Allison) [Reames et al., 1999, 48].

Observations:

In Figure 8.31, a strong wind can be seen blowing out from Lechuguilla Cave through the culvert with a velocity of 17.9 m s^{-1}. In this case, the pressure inside the cave is probably higher than that of the surface. According to Richards [2001], and direct observations by numerous cavers, the reverse flow is also observed.

Application of modeling:

We can consider this pressure difference between the surface and the cave in light of three different aspects: 1) the low pressure system at the surface; 2) the high pressure inside the cave due to internal dynamics; and 3) the combination of the low pressure system at the surface and the high pressure inside the cave.

The common explanation of this phenomenon may be that cave air flows out due to the low-pressure system at the surface, that is, the pressure difference between the surface and the subsurface occurs only due to the fluctuation of the surface. However, the phenomenon could also be partly explained by internal dynamics (the combination effects of thermally-induced buoyancy forces, conservation of mass, and cave geometry) assuming 1) that there are calm surface weather conditions near the cave entrance, 2) that the flow system is transient due to the cave's extremely large size, and 3) that it has unknown multiple entrances. Two possibilities are considered below.

(1) High air pressure is created inside the cave due to internal dynamics

Temporarily, excess air pressure could be created inside the cave. Perhaps excess air may have accumulated in the system due to the combination of presence of unknown multiple entrances that are located at different elevations, and variations of recent surface weather conditions near these multiple openings. Such a situation could create a transient flow state inside the cave. When the airlock of the culvert was removed, the inside excess cave air moved out through the culvert to conserve cave air mass. Because it is a narrow culvert, compared to the immense volume of the cave, a strong unidirectional airflow occurred at high speed.

(2) Air circulation ensues when the culvert is opened

Cave air may be non-circulating due to Lechuguilla's particular cave geometry (e.g., its single entrance). When the airlock of the culvert is removed, air circulation suddenly is allowed between the cave and the surface similar to that shown in the tilted model with two entrances. The flow shown in Figure 8.30 is outward, so there could be another entrance in the lower part of the cave below the level of the culvert (e.g., Figure 5.34), or there could be high barometric pressure near unknown openings above (e.g., Figure 6.14).

The outward flow through the culvert would be amplified if a low pressure system at the surface accompanied the high pressure temporarily created inside cave.

8.6 Other Examples

From the modeling viewpoint, convection cells are expected inside caves. There is an important report that suggests the occurrence of convection cells in deeper parts of caves. Cunningham and LaRock [1991] studied the Radon (Rn) levels within Lechuguilla Cave as a health-oriented Rn assessment of the cave for the National Park Service (NPS). They identified six discrete zones throughout the cave where Rn levels are being diluted via convective ventilation, fresh air entering from the known entrance, fresh air from unknown surface connections, or all of the above. According to these authors, “Correlations between Rn concentration and outside temperature, barometric pressure, and entrance airflow can be demonstrated only in the area of the entrance passage….Convective air circulation is proposed for deeper and more remote areas of the cave and may be driven by internal cave temperature differences.”

Boston [personal communication, 2004], a microbiologist and cave researcher, provides another unpublished example that implies the occurrence of convection cells in deeper parts of caves. In Australia, C. Waring, a cave microclimate specialist, and his colleagues observed a one-day cycle time of methane and carbon dioxide at a particular cave [Waring et al., 2004]. Waring considered that the activity of cave microorganisms could produce this one-day cycle. However, according to Boston, such a short cycle of methane and carbon dioxide concentrations is probably too fast from the microbiological perspective in a low nutrient environment. She considers that the presence of convection cells is a much more likely cause of the observed phenomenon in that particular Australian cave.

8.7 Possible Future Work

Our modeling efforts appear to be a first attempt to capture the basic physical processes involved in cave micrometeorology. Based on this study, we would like to suggest several possible avenues of future work that would help us understand cave systems.

(1) Monitoring of the Vertical Humidity Variations

From the monitoring data within Carlsbad Cavern provided by Burger [2004a], we can see that humidity could be very sensitive to small fluctuations of flow. As mentioned in Section 8.3, monitoring the vertical humidity variations may be very useful to estimate flow patterns even when such flow cannot be directly measured. Good places to observe the vertical humidity variation in Carlsbad Cavern are Left Hand Tunnel and the Big Room where the popcorn lines are prominent and consistent. We may be able to correlate the occurrence of popcorn lines with humidity variations and airflow patterns.

We have tried to simulate the air exchange between two big chambers that are connected by a horizontally long, narrow tunnel, each with a different temperature, as is the relationship amongst the Big Room, Left Hand Tunnel, and Lake of the Clouds. However, the model did not produce a unique solution. Further refinements in modeling, perhaps creating a code specifically to handle these types of simulations, are necessary to handle these types of complex geometrical arrangements. Incorporation of the available monitoring data into such future models would also be very fruitful.

(2) Exploring Evaporation and Condensation in Subsurface Heat Flow Systems

Humidity is an important factor in cave meteorology. However, based on Rayleigh number and the autoconvective lapse analyses with dry and moist air, we suggested that humidity does not have an important role in altering the internal convection cells that we modeled (see Section 2.6). In our analyses we calculated fluid properties (ρ, C_p, μ, k, α, and R) for both dry and moist air under the pressure of 100 kPa and temperature of 20˚C, and established that humidity does not change these fluid properties significantly. However, there is a more complicated issue concerning phase behavior and latent heat transfer. Wilson [personal communication, 2005] suggests that, "We need to model the movement of moisture, and its condensation and evaporation. It is also strongly coupled to heat transport, which must now add latent heat condensation and evaporation to the heat transfer model (perhaps as a source/sink term)."

McLean [1976] studied evaporation effects within Carlsbad Cavern, to evaluate the revolving doors installed in 1972 at the lower lobby of the elevator shaft in the Lunch Room. Reviewing McLean's report will be helpful when we focus on evaporation and condensation. He measured the variation in the evaporation rate with nonstandard plastic pans (rectangular shaped, 79,400 mm^2 in area, and about 150 mm deep). The collected data were analyzed in various ways (e.g., by correlating the distance from the elevator, number of visitors and lightning). McLean concluded that 1) the greatest reduction in evaporation (34 %) occurred for the pans nearest the elevator shaft; 2) evaporation in the cave increased due to both increased energy inputs by the cave lighting system and increased visitor traffic.

To incorporate the movement of moisture in cave micrometeorological models we will need to employ coupled thermohydrologic models of water and heat transfer in the porous and fractured rock surrounding the cave, and gas, heat, and moisture transfer in the cave atmosphere. For example, phase change (evaporation, condensation) in the cave and on its walls will influence convective heat transfer in the cave. This change of phase comes from the temperature difference between the fluid and the wetted solid surface [Bejan, 1995, 403]. Studying these areas may give us clues in how to incorporate the effects of evaporation and condensation in cave micrometeorological models, and then eventually we can correlate the modeled micrometeorology with the secondary mineral deposition.

Yucca Mountain, Nevada, is a potential civilian high-level radioactive waste repository for the United States. The Yucca Mountain Project, especially its hydrology projects, are also studying humidity effects in drift scale flow systems in the vadose zone, because the movement of moisture and its condensation and evaporation control the corrosion rates of waste packages, as well as mobilization and transport of radionuclides [Salve and Kneafsey, 2005] (see Section 1.3). We must consider the progress of these projects as providing useful analogs to cave micrometeorology.

(3) Monitoring Pressure Variations

As discussed in Section 8.5, strong inflow or outflow winds are sometimes observed in the culvert of Lechuguilla Cave. Of course the surface barometric pressure has an important role in this phenomenon. However, we can also consider the contributions of the cave internal dynamics to these strong unidirectional flows. Based on the model simulations with a single entrance and the simple laboratory experiments, we hypothesize that to have a strong unidirectional flow at a narrow entrance, there is a high possibility that the cave has other connections to the surface. If a cave has multiple connections to the surface, the flow should be transient and, thus, internal pressure will vary with time and in different parts of the complex cave maze geometry.

The monitoring of the small but measurable pressure variations within the cave and the surface barometric pressure would be useful to examine the hypotheses that Lechugilla Cave is connected to the surface in multiple ways, and that flow is transient. Cunningham and LaRock [1991] identified six discrete zones throughout the cave where radon levels are being diluted via convective ventilation, fresh air entering from the known entrance, fresh air from unknown surface connections, or all of the above. Those six zones would be excellent places to observe the pressure variations with time.

There is another good opportunity to monitor the cave pressure fluctuations and their possible effects on speleothems. Cave balloons are spherical or ovate, thin-walled speleothems with gas inside of a mineralized, bag-like pouch [Hill, 1987, 118]. Cave balloons are believed to be extremely short-lived structures. Some of the best cave balloons observed occur in the Left Hand Tunnel of Carlsbad Cavern. Several mechanisms that might produce cave balloons have been hypothesized including microbially produced gases [Canaveras et al., 2001] and emission of gases from groundwater or percolation of gases through fractures [Polyak and Guven, 2000]. It would be an interesting exercise to see if cave pressure fluctuations could be correlated with the formation of cave balloons.

Mining engineering studies have included various pressure surveys. We may be able to apply their pressure survey methods. For example, Wala et al, [2001] performed a mine ventilation survey in the 705-m deep Cayuga Mine, NY, using the direct- pressure measuring method. At this mine, the natural ventilation pressure (NVP) has significant effects on the ventilation system. These investigators determined that during the summer, the power generated by NVP works against the fan, while in the winter it works with the fan.

(4) Finding a Correlation of the Pressure Fluctuations among Cave Rock, Cave Core, and the Surface

The present study was conducted by assuming that cave rocks are impermeable and, thus, cave walls are disconnected from the surface. Under this assumption, we identified geothermal heating, cave geometries, and thermal properties of rock and air as the important internal factors that produce airflow inside caves. However, there are important reports (subsurface temperature measurements, and water level measurement in unconfined aquifers) that suggest that cave walls are porous and/or fractured and actually connected to the surface.

Subsurface temperature data taken in both the saturated and unsaturated zones help in a variety of studies, including geothermal resources investigation, defining the thermal regime of the earth's crust and upper mantle, calculating ground surface temperature changes that may be associated with climate change, and considering subsurface heat transfer processes [Reiter, 2004]. Measuring subsurface temperatures requires that a sensor be lowered down a hole into the earth in a manner that will least disturb the *in situ* temperature. Subsurface temperature measurement becomes difficult when the hole is filled with air; because 1) sensor response time is very slow, and 2) the problems of well bore convection in large-diameter wells and diurnal barometric changes may provide greater uncertainties. Reiter [2004] reported a new temperature-logging system, with a relatively fast time constant in air, that provides accurate temperature measurements in a continuous logging mode. The temperature data described in Figure 2.2 are the results of subsurface temperature measurement using this new logging system. Reiter concludes that with this instrumentation there is no noticeable free convection in the piezometer tubing, or airflow in the piezometer because of atmospheric pressure change. According to this investigator, “The lack of noticeable airflow in the piezometer resulting from atmospheric pressure change is consistent with the piezometer being sealed and isolated from the formation except at the screened interval, which for the piezometer logged was at the 212-m depth, about 152 m below water level.”

Barometric pressure fluctuations also influence water level data in unconfined aquifers. Hubbell et al. [2003] present a well completion method designed to reduce the effects of barometric pressure fluctuations on measured water levels. According to the authors, “Temporal fluctuations in barometric pressure can significantly complicate measurement of water level in unconfined aquifers, particularly where the vadose zone is thick or contains low permeability zones. First, water levels are commonly measured using differential pressure transducers referenced to barometric pressure at the wellhead. Second, unsealed observation wells provided a direct connection to atmospheric pressure changes, while the surrounding aquifer is partially buffered by the intervening vadose zone materials. Thus, water levels in the well may not be at equilibrium with the aquifer, leading to inaccurate measurements…. Low air permeability materials in the vadose zone can restrict communication to the atmosphere. As a result, gas pressure in the vadose zone will change more slowly and to a lesser extent than barometric pressure.

Conversely, gas pressure in an unsealed well will equilibrate almost instantaneously to changes in barometric pressure. Where gas pressure in the vadose zone exceeds atmospheric pressure, water will move from the aquifer into an unsealed well bore, creating an unnaturally high water level, and vice versa."

The proposed well configuration by Hubbell et al. [2003], called the isobaric well, seals the interior of the well from atmospheric pressure, and vents the reference side of the water level pressure transducer to the gas phase pressure above the water table. These authors explain, "By sealing the well bore against atmospheric pressure, the well is only connected to the atmosphere through the portion of the screen above the water table." Therefore, gas pressure within the well bore will equilibrate to the surrounding media, and water levels within the well will accurately reflect conditions in the surrounding aquifer.

The above two reports presume that the vadose zone is connected to the atmosphere. Most caves are located in the vadose zone, so according to this premise caves are connected to the atmosphere through their entrances and the cave walls. Perhaps caves are excellent places to examine the premise that the vadose zone is connected to the atmosphere. If we can take pressure fluctuation measurements directly against the cave wall rock (just inside the cave wall), and compare with those within the cave core, and then if we can identify the difference in the pressure fluctuations between the rock and the cave core, and correlate the surface barometric pressure fluctuations, we may be able to identify another very important mechanism of cave airflow.

There is a potentially excellent place to conduct the pressure fluctuation measurements against the cave wall rocks. V. Werker and J. Werker have installed photomonitoring stations in the cave walls, ceilings, and floors in Lower Cave of Carlsbad Cavern. These are approximately 10-mm stainless steel tubes machined to accept the monorod that positions the camera properly. Most of the photomonitoring tubes are covered with a white or black nylon cap to keep debris out [Werker, personal communication, 2005]. According to Werker [1999], "Photomonitoring is the process of establishing a system of photo stations so the same photographs can be easily repeated at defined time intervals and archived to record visitor impact, vandalism, formation growth and decline, water levels, trail conditions, etc."

Because there are already small holes in the cave wall of the photomonitoring stations of the Lower Cave, we do not need to create additional holes within the cave wall rock to measure its pressure fluctuation. At present, there are stainless steel tubes in the holes. Because stainless is an impermeable material, the holes are disconnected from the atmosphere. Thus, to conduct the pressure measurements directly against the cave wall rock, we need to remove the tubes from the rock. It is not certain whether or not removing the tubes is possible. However, we may need to find the correlation of pressure fluctuations among the cave wall rock, the cave core and the surface; because the pressure difference between the cave wall rock and the cave core may be one of major factors of internal airflow in addition to the geothermal heating and cave geometries.

(5) Potentially Interesting References for Future Work

The Buddhist cave temples at Yungang, China, are subjected to rapid soiling caused by the deposition of airborne particles onto the thousands of statues in those caves. Christoforou et al. [1994 and 1996] studied air exchange within these Buddhist cave temples. The purpose of their study was to characterize the exposure of the grottoes to air pollutants in a manner that will establish a basis for the future protection of the grottoes from air pollution damage. The authors have developed a computer-based model that can predict air flows into and out of the temples. According to the authors, “The model can be used to predict air flows through the caves in the presence of increased resistance to air flow such as may occur following the future installation of filtration systems for particle removal at the caves.”

CHAPTER 9

CONCLUSION

Micrometeorological modeling by the finite element method was conducted using FEMLAB computer software. The thermal properties of limestone and air, and geothermal flux are applied to the models. The models coupled the incompressible Navier-Stokes equations (air phase only) with the thermal energy convection and conduction equation using the finite element method. The models simulated thermally-induced density-driven flow, assuming steady state and limestone as an impermeable rock, and ignoring the gravitational pressure gradient. Although, the constructed models are limited in scale and have highly simplified geometries compared to real cave systems, the models have identified some important factors that are likely affecting internal dynamics and may be heuristically applied to attempt to understand the micrometeorological behavior of real caves.

Air-filled caves act as insulators because the thermal conductivity of air is very small compared to that of rock. Natural convection occurs inside caves due to the relative thermal properties of air and rock, geothermal heat, and cave geometry. Humidity is an important factor in caves, and it may assist air to move upward because moist air is lighter than dry air. However, the Rayleigh number and instability analyses indicate that humidity has less impact than other factors (such as cave geometry) on flow dynamics in the moderate cave meteorological condition (e.g., cave air temperature of 20˚C). Rather, airflow may change the local humidity. Considerations for future studies include latent heat transport, and evaporation and condensation. Intensity of geothermal heat flux affects air temperature and flow velocity inside caves. Cave geometry exerts an important influence on cave meteorology, and it can control flow patterns.

Cave air moves to conserve air mass. However, unlike our steady state models, real cave systems could experience transient states and, thus, the rate of air escape could be different from the rate of incoming air. If caves have excess air mass, temporarily, an excess pressure of air may be created locally, triggering a movement of air to areas of lower pressure. As a result, if a cave entrance is large enough, inflow and outflow components can be observed at a single entrance. Thus, cave internal dynamics (combined effects of thermally-induced buoyancy force, conservation of mass, and cave geometries) can cause processes that have been attributed only to the surface influence. The models can provide useful explanations for certain phenomena that have been observed in Carlsbad Cavern and Lechuguilla Cave, New Mexico.

To our knowledge, this modeling effort is the first attempt to capture the dynamical behavior of such cave micrometeorological systems. Thus, as a preliminary attempt, there may be other interpretations of the modeling results. We believe that computer modeling can be a very useful tool to assist understanding of the dynamics of cave interiors. Modeling combined with detailed and continuous site monitoring in real caves, and attempts to include vertical variations of humidity, cave pressure fluctuations, and additional salient aspects of cave geometries, will be especially fruitful.

An important ultimate application of cave studies is to "Protect caves as natural resources." The study of cave micrometeorology is an important part of realizing this goal. Modeling is a powerful tool of cave micrometeorological studies that may be useful for these purposes. For example, Neville [Bat Conservation International, 2001, 2 and 21-23] studied cave micrometeorology to help restore a hibernatory population of endangered Indiana bats (Figure 9.1). We are looking forward to seeing cave meteorological modeling further promote the restoration of endangered bats and assist where possible in similar future cases of critical cave management issues.

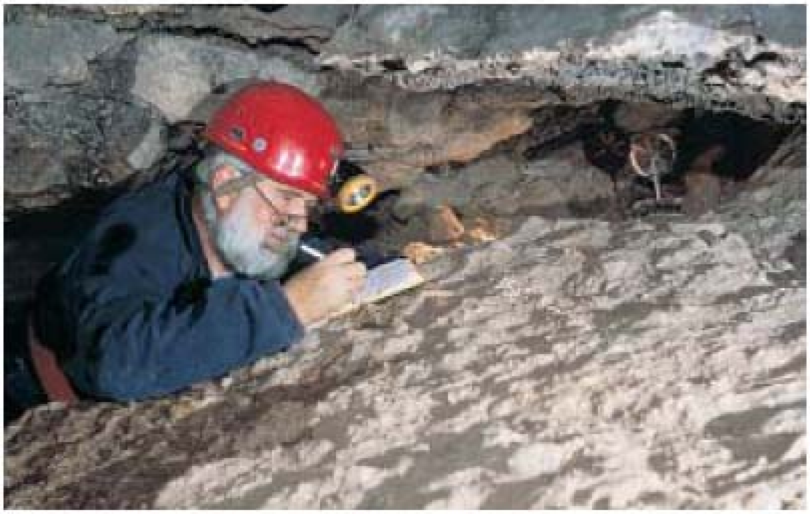

© Elaine Acker, BCI 1916-5107

Figure 9.1: Neville Michie studies the microclimate in Saltpetre Cave in Carter Caves State Resort Park, Kentucky. The information gathered will be used to help restore a once large hibernating population of endangered Indiana bats (*Myotis sodalis*) [Bat Conservation International, 2001, 2 and 21-23].

BIBLIOGRAPHY

Alger, B. K., Lechuguilla Cave expedition, 2002. http://www.lubbockareagrotto.org/Reports/2002LechuguillaTrip.htm (accessed February 16, 2005).

Barroll, M. W., and Reiter, M., Analysis of the Socorro hydrogeothermal system: Central New Mexico, *Journal of Geophysical Research,* Vol. 95, No. B13, pp. 21949 – 21963, December 10, 1990.

Bat Conservation International, Annual report 2000 – 2001, Austin, TX, 2001. Also available online at http://www.batcon.org/anreport/ar2000-2001.pdf.

Bejan, A., Convection heat transfer, 2nd ed, Wiley, New York, 1995.

Bejan, A., Shape and structure, from engineering to nature, Cambridge University Press, United Kingdom, 2000.

Bish, D. L., Thermal behavior of natural zeolites, In Natural Zeolites '93, ed. DW Ming, FA Mumpton, pp. 259–69, Brockport, NY: Int. Commun, 1995.

Blake, K. R., Poulikakos, D. and Bejan, A., Natural Convection near 4 °C in a horizontal water layer heated from below, *Phys. Fluids*, Vol. 27, pp. 2608-2616, 1984.

Bodenschatz, E., Pesch, W., and Ahlers, G., Resent developments in Rayleigh-Bénard Convection, Annual Review of Fluid Mechanics, Vol. 32: 709-778, 2000. Also available online at http://arjournals.annualreviews.org/doi/full/10.1146/annurev.fluid.32.1.709;jsessionid=iWEAevnR9ln_.

Bögli, A., Karst hydrology and physical speleology, Springer-Verlag, Berlin Heidelberg New York, 1980.

Boston, P. J. (Director, Cave and Karst Studies Program, New Mexico Tech), in discussion with the author, September 2004.

Bourguerra, A., Laurent, J. P., Goual, M. S., and Queneudec, M., The measurement of the thermal conductivity of solid aggregates using the transient plane source technique, *J. Phys. D: Appl. Phys.* 30 (1997) 2900-2904, 1997. Also available online at http://ej.iop.org/links/q44/qSpw95J6BhfFHpZFGQqbeQ/d72018.pdf.

Buecher, R. H., Microclimate study of Kartchner Caverns, Arizona, *Journal of Cave and Karst Studies 61 (2): 108-120*, 1999. Also available online at http://www.caves.org/pub/journal/PDF/V61/v61n2-Buecher.pdf.

Burger, P. (Carlsbad Cavern National Park)_a, Temperature and humidity data within Carlsbad Cavern, provided by Burger to the author, December 16, 2004.

Burger, P. (Carlsbad Cavern National Park)_b, in discussion with the author, December 10, 2004.

Buscheck, T. A., Nitao, J. J., and Ramspott, L. D., Localized dryout: an approach for managing the thermal-hydrological effects of decay heat at Yucca Mountain, *Mater. Res. Soc. Symp. Proc.* 412:715–22, 1996.

Busse, F. H., Non-linear properties of thermal convection, *Rep. Prog. Phys*., Vol. 41, pp. 1929-1967, 1978.

Canaveras, J. C., Sanchez-Moral, S., Soler, V., and Saiz-Jimenez, C., Microorganisms and microbially induced fabrics in cave walls, Geomicrobiol, J. 18(3): 223-240, 2001.

Carlsbad Caverns Bat Cave Draw Weather station, 69 year temperature and precipitation data summery [January 1935-April 2004], 2004.

Carlsbad Caverns National Park_a, Natural entrance self-guide route, 2005, http://www.nps.gov/cave/tour-ne.htm (accessed January 13, 2005).

Carlsbad Caverns National Park_b, Carlsbad Caverns photos, 2005, http://homepage.mac.com/stepheda/CarlsbadCaverns/PhotoAlbum145.html (accessed January 16, 2005).

Carson, J. E., Soil temperature and weather conditions, Argonne National Laboratory, The University of Chicago, November 1961.

Catton, I., Natural convection in enclosures, In Proc. Sixth Intl. Heat Transfer Conf., volume 6, pp. 13-31, Toronto, Aug. 7-11, 1978.

Cave Research Foundation, The quadrangle maps of Carlsbad Cavern, New Mexico. New Carlisle, Ohio, Cave Research Foundation: 18pp, 1992.

Chapman, D. S., and Pollack, H. N., Global heat flow: A new look, *Earth and Planetary Science Letters 28, 23-32*, 1975.

Christoforou, C. S., Salmon, L. G., and Cass, G. R., Deposition of atmospheric particles within the Buddhist cave temples at Yungang, China, *Atmospheric Environment* Vol, 28, No.12, pp 2081-2091, 1994.

Christoforou, C. S., Salmon, L. G., and Cass, G. R., Air exchange within the Buddhist cave temples at Yungang, China, *Atmospheric Environment* Vol, 30, No.23, pp 3995-4006, 1996.

Christon, M. A., Gresho, P. M and Sutton, S. B., Computational predictability of time-dependent natural convection flows in enclosures (including a benchmark solution), *Int. J. Numer. Meth. Fluids*, 40: 953-980, 2002.

COMSOL AB_a, FEMLAB 3: FEMLAB user's guide, 2004.

COMSOL AB_b, FEMLAB 3: FEMLAB modeling guide, 2004.

COMSOL AB_c, FEMLAB 3.1: Chemical engineering module user's guide, 2004.

COMSOL AB_d, FEMLAB 3.1: FEMLAB user's guide, 2004.

Crane, C., Carlsbad Caverns National Part: Worlds of wonder, Carlsbad Caverns Guadalupe Mountains Association, 2000.

CRWMS M&O (Civilian Radioactive Waste Management System Management and Operating Contractor), *Impact of Radioactive Waste Heat on Soil Temperatures*, BA0000000-01717-5700-00030, Rev. 0. Las Vegas, Nevada, 1999.

Cunningham, K. L., and LaRock, E. J., Recognition of microclimate zones through radon mapping, Lechuguilla Cave, Carlsbad Caverns National Park, New Mexico, *Health Physics* Vol. 61. No.4 (October), pp. 493-500, 1991.

Dean, J. A., Lange's handbook of chemistry, 15th ed., McGraw-Hill Inc., 1999.

Desert USA, Speleothems, http://www.desertusa.com/mag99/feb/papr/speleothems.html, (accessed October 13, 2004).

Dingman, S. L., Physical hydrology – 2nd ed., Prentice-Hall, Inc., Upper Saddle River, New Jersey 07458, 2002.

Earth Observatory, The highs and lows of the NAO. http://earthobservatory.nasa.gov/Study/NAO/NAO_2.html, (accessed October 13, 2004).

Farnetani, C. G, and Samuel, H., Lagrangian structures and stirring in the Earth's mantle, Earth and Planetary Science Letters 206 (2003) 335-348, 2003. Also available online at http://www.geology.yale.edu/~hs344/WORK/PAPERS/Lagrange.pdf.

Forbes, J., Air temperature and relative humidity study: Torgac Cave, New Mexico, *Journal of Cave and Karst Studies 60(1):27-32*, 1998. Also available online at http://www.caves.org/pub/journal/PDF/V60/V60N1-Forbes.pdf.

Forbes, J.R., Geochemistry of Carlsbad Cavern pool waters, Guadalupe Mountains, New Mexico, *Journal of Cave and Karst Studies 62(2): 75-79*, 2000. Also available online at http://www.caves.org/pub/journal/PDF/V62/v62n2-Forbes.pdf.

Furbish, D. J., Fluid physics in geology: an introduction to fluid motions on Earth's surface and within its crust, Oxford University Press, Inc., New York, 1997.

Gelfgat, A. Y., Stability and slightly supercritical oscillatory regimes of natural convection in a 8:1 cavity: solution of the benchmark problem by global Galerkin method, *Int. J. Numer. Meth. Fluids*, 44: 135-146, 2004.

Ghassemi, M., Keshavarz, A., and Fathabadi, J., Numerical investigation of turbulent natural convection in a triangular shaped enclosure, The 6th ASME-JSME Thermal Engineering Joint Conference, TED-AJo3-662, March 16-20, 2003.

Hao, Y., Nitao, J. J., Buscheck, T. A., Sun, Y., and Lee, K. H. Thermohydrologic modeling: Coupling Navier-Stokes models of gas, moisture, and heat flow in underground engineered systems with porous-media models in fractures rocks: H21E-1053 0800h (Abstract of 2004 AGU conference), 2004.

Hemp, R., Psychrometry, Environmental Engineering in South African Mines, Chapter 18, 435-63, Mine Ventilation Society of South Africa, 1982.

Hill, C. A., and Forti, P., Cave minerals of the world, 2nd ed., National Speleological Society, Huntsville, AL, 1997.

Hill, C. A., Geology of Carlsbad Cavern and other caves in the Guadalupe Mountains, New Mexico and Texas, *New Mexico Bureau of Mines & Mineral Resources, Bulletin 117*, 1987.

Hirsch, C., Numerical computation of internal and external flows (Wiley series in numerical methods in engineering): v.1. Fundamentals of numerical discretization, John Wiley & Sons Ltd, 1988.

Hubbell, J. M., Sisson, J. B., Nicholl, M. J., and Taylor, R. G., Well design to reduce barometric pressure effects on water level data in unconfined aquifers, *Vadose Zone Journal* 3: 183-189, 2004.

Huq, P., and Stretch, D. D., Critical dissipation rates in density stratified turbulence, *Phys. Fluids* 7 (5), May 1995.

Ingebritsen, S.E., and Sanford, W.E., Groundwater in geologic processes, Cambridge University Press, 1998.

Jernigan, J. W., and Swift, R. J., A mathematical model of air temperature in Mammoth Cave, Kentucky, *Journal of Cave and Karst Studies* 63 (1): 3-8, 2001.

Lasance, C. J. M., The thermal conductivity of moist air, Electronics Cooling: the central resource for practitioners in the field of electronics thermal management, 2003, http://www.electronics-cooling.com/html/2003_november_techdata.html (accessed November 12, 2004).

Mansure, A., and Reiter, M., An accurate equilibrium temperature log in AEC No. 8, a drill test in the vicinity of the proposed Carlsbad Disposal site, Open File Report No. 80, 1977.

Markatos, N. C. and Pericleous, K. A., Laminar and turbulent natural convection in an enclosed cavity, *Int. j. Heat Mass Transfer*, vol. 27, No. 5, pp. 755-772, 1984.

McLean, J. S., The microclimate in Carlsbad Caverns, New Mexico, *U.S. Geological Survey, Open File Report 71-198, 67pp*, 1971.

McLean, J. S., Factors altering the microclimate in Carlsbad Cavern, New Mexico, *U.S. Geological Survey, Open File Report 76-171 pp*, 1976.

McLean J. S., e-mail message to the author, May 15, 2005.

McPherson, M. J., Subsurface ventilation and environmental engineering, Chapman & Hall, 1993.

Moore, G. W. and Sullivan, G. N., Speleology: The study of caves, Revised second edition. Teaneck, N.Y. Zephyrus Press: 150 pp, 1978.

Nepstad, J., and Pisarowicz, J., Wind Cave temperature & humidity variations, National *Speleological Society Bulletin* 51 (2): 125-128, 1989. http://www.nps.gov/wica/NSS_Bulletin.htm (accessed October 23, 2004).

Or, D, and Ghezzehei, T. A., Dripping into subterranean cavities from unsaturated fractures under evaporative conditions, Water Resources Research, Vol. 36, No.2, pp. 381-393, February 2000.

Palmer, A. N., and Palmer, M. V., Hydrochemical interpretation of cave patterns in the Guadalupe Mountains, New Mexico, *Journal of Cave and Karst Studies 62(2):91-108*, 2000. Also available online at http://www.caves.org/pub/journal/PDF/V62/v62n2-Palmer.pdf.

Paul, M. R., and Catton, I., The relaxation of two-dimensional rolls in Rayleigh-Bébard convection, *Phys. of Fluids,* Vol. 16, No 5, pp. 1262-1266, May 2004.

Polyak, V. J., and Guven, N., Authigenesis of trioctahedral smectite in magnesium-rich carbonate speleothems in Carlsbad Cavern and other caves of the Guadalupe Mountains, New Mexico, Clays and Clay Minerals 48 (3): 317-321, 2000.

Potter, M. C., and Wiggert, D. C., Mechanics of fluids -2nd ed., Prentice Hall, Upper Saddle River, NJ 07458, 1997.

Reames, S., Fish, L., Burger, P., and Kambesis, P., Deep secrets: discovery & exploration of Lechuguilla Cave, Cave Books, 1999.

Reddy, J. N., and Gartling, D. K., The finite element method in heat transfer and fluid dynamics, 2nd ed., CRC Press LLC, 2001.

Reiter, M., Continuous temperature logging in air across the deep vadose zone, *Vadose Zone Journal* 3: 982 – 989, 2004.

Reiter, M., (New Mexico Bureau of Mines and Mineral Resources), in discussion with the author, March 14, 2005.

Reiter, M., and Jordan, D. L., Hydrogeothermal studies across the Pecos River Valley, southeastern New Mexico, *GSA Bulletin*; June 1996; v. 108; no. 6 p, 747-756, 1996.

Richards, J. M., Lechuguilla Cave culvert replacement project, 2001 National Cave and Karst Management Symposium, 2001, http://www.nckms.org/pdf/RICHARDS.pdf (accessed February 16, 2005).

Rowling, J., Cave entrances – wind effects, the University of Sydney Australia, 2001, http://karst.planetresources.net/entrances_wind_effects.htm (accessed February 24, 2005).

Salve, R., and Kneafsey, T. J., Vapor-phase transport in the near-drift environment at Yucca Mountain, Water Resources Research, Vol. 41, W01012, doi: 10.1029/2004WR003373, 2005.

Sandia National Laboratories, and D'Applonia Consulting Engineers, Basic data report for Drillhole AEC8 (Waste Isolation Pilot Plant – WIPP), *SAND79-0269, Unlimited Release, UC-70,* 1983.

Sass, J. H., Thermal studies at the Brantley Damsite on the Pecos River near Carlsbad, New Mexico, United States Department of The Interior Geological Survey, Open-file Report 84-663, 1984.

Schmidt, E., and Grigull, U., Properties of water and stream in SI-units, Springer-Verlag Berlin Heidelberg New York R. Oldenbourg München, 1979.

Schneiker, H., The Lechuguilla air circulation study, 2002. Also available online at http://www.hdssystems.com/LechProposal.pdf.

Sclater, E. J., Jaupart, C., and Galson, D., The heat flow through oceanic and continental crust and the heat loss of the Earth, *Reviews of Geophysics and Space Physics 18*, 269-311, 1980.

Seway, R. A., and Beichner, R. J., Physics for scientists and engineers, fifth ed., Sanders College Publishing, 2000.

Spiegel, E. A., and Veronis, G., On the Boussinesq approximation for a compressible fluid, *Astrophysical Journal* 131:442-47, 1960.

Spinelli, G., Hydrogeologic processes class lecture notes 3, Spring semester 2004, New Mexico Tech, 2004.

Turcotte, D. L., and Schubert, G., Geodynamics: applications of continuum physics to geological problems, John Wiley & Sons, 1982.

Valentine, G. A., Zhang, D., and Robinson, B. A., Modeling complex, nonlinear geological processes, Annual Review of Earth and Planetary Sciences, Vol. 30: 35-64 (Volume publication data May 2002), 2002. Also available online at http://arjournals.annualreviews.org/doi/full/10.1146/annurev.earth.30.082801.150140.

Wala, A. M., Stoltz, J. R., Thompson, E., and Pattee, S, Natural ventilation pressure in a deep salt mine – a case study, preprinted number 00-158, presented at the SME Annual Meeting, Feb 28-Mar 1, 2000, Salt Lake City, UT. Revised manuscript received and accepted for publication May 2001.

Waring, C., Griffith, D., Wilson, S., Parkes, S., James, J., and Stone, D., Limestone cave respiration studies for understanding speleothem isotope accumulation records, Abs. 293-27. 32nd International Geological Congress, Florence, Italy, 20-28 August, 2004.

Werker, V. H., e-mail message to the author, May 12, 2005.

Werker, V. H., Photographic Definitions: Terms for Documentation, Inventory and Monitoring, http://www.acave.us/cd/b_conservation/how-to_cons/photo_definitions.htm, (accessed May 21, 2005).

Wilkening, M. H., and Watkins, D. E., Air exchange and Rn^{222} concentrations in the Carlsbad Caverns: Health Physics, v. 31, 139-145 pp, 1976.

Wilson, J. L., Conceptual model: unpublished notes on model of convection in cavities (e.g. caves), New Mexico Tech, provided by Wilson to the author, November 27, 2004.

Wilson, J.L., e-mail message to the author, May 5, 2005.

Witcher, J. C., Stone, C. and Hahman, W. R., Map of the geothermal resources of Arizona, Arizona Bureau of Geology and Mineral Technology, Single sheet map with text, 1982.

Yang, K. T., Natural convection in enclosures, In S. Kakaç, R. K. Shah, and W. Aung, editors, Handbook of Single-Phase Convective Heat Transfer, chapter 13, Wiley-Interscience, New York, 1987.

Young, D. F., Munson, B. R., and Okiishi, T. H., A brief introduction to fluid mechanics, 3rd ed., John Wiely & Sons, 2004.